

**Rational Design and Synthesis of Low-Dimensional Halide  
Perovskites with Improved Ambient Air Stability for  
Optoelectronic Applications**

By

**Prachi Prasad Kour**

**10CC19J26009**

A thesis submitted to the  
Academy of Scientific & Innovative Research  
for the award of the degree of  
DOCTOR OF PHILOSOPHY  
in  
SCIENCE

Under the supervision of  
**Dr. Shatabdi Porel Mukherjee**



**CSIR- National Chemical Laboratory, Pune**



Academy of Scientific and Innovative Research  
AcSIR Headquarters, CSIR-HRDC campus  
Sector 19, Kamla Nehru Nagar,  
Ghaziabad, U.P. – 201 002, India

**April-2023**

## Certificate

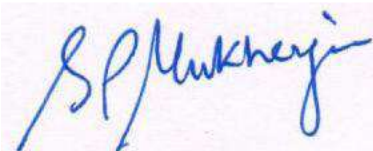
This is to certify that the work incorporated in this Ph.D. thesis entitled, "Rational Design and Synthesis of Low-Dimensional Halide Perovskites with Improved Ambient Air Stability for Optoelectronic Applications", submitted by Ms. Prachi Prasad Kour to the Academy of Scientific and Innovative Research (AcSIR), in partial fulfillment of the requirements for the award of the Degree of Doctor of Philosophy in Science, embodies original research work carried out by the student. We further certify that this work has not been submitted to any other University or Institution in part or full for the award of any degree or diploma. Research material(s) obtained from other source(s) and used in this research work has/have been duly acknowledged in the thesis. Image(s), illustration(s), figure(s), table(s) *etc.*, used in the thesis from other source(s), have also been duly cited and acknowledged.



Ms. Prachi Prasad Kour

Research Student

Date : 29/03/2023



Dr. Shatabdi Porel Mukherjee

Research Supervisor

Date : 29/03/2023

## Statements of Academic Integrity

I, Ms. Prachi Prasad Kour, a Ph.D. student of the Academy of Scientific and Innovative Research (AcSIR) with Registration No. 10CC17J26019 hereby undertake that the thesis entitled “Rational Design and Synthesis of Low-Dimensional Halide Perovskites with Improved Ambient Air Stability for Optoelectronic Applications” has been prepared by me and that the document reports original work carried out by me and is free of any plagiarism in compliance with the UGC Regulations on “*Promotion of Academic Integrity and Prevention of Plagiarism in Higher Educational Institutions (2018)*” and the CSIR Guidelines for “*Ethics in Research and in Governance (2020)*”.



Signature of the Student

Date : 29/03/2023

Place : Pune

---

It is hereby certified that the work done by the student, under my supervision, is plagiarism free in accordance with the UGC Regulations on “*Promotion of Academic Integrity and Prevention of Plagiarism in Higher Educational Institutions (2018)*” and the CSIR Guidelines for “*Ethics in Research and in Governance (2020)*”.



Signature of the Supervisor

Date : 29/03/2023

Place : Pune

*Dedicated to  
my mother*

Content	Page no
Acknowledgement: .....	i
Abbreviations: .....	iv
Synopsis: .....	vi

---

## CHAPTER-1

---

### Classification, Properties and Applications of Perovskites: A Brief Overview

	<b>Summary</b>	<b>1</b>
<b>1.1.</b>	<b>Introduction</b>	<b>2</b>
<b>1.2.</b>	<b>Perovskite systems</b>	<b>3</b>
<b>1.3.</b>	<b>Types of Perovskite systems</b>	<b>6</b>
1.3.1.	Oxide Perovskites	<b>6</b>
1.3.2.	Halide Perovskites	<b>8</b>
1.3.2. (a)	Inorganic Halide Perovskites	<b>10</b>
1.3.2. (b)	Hybrid Organic- Inorganic Perovskites (HOIPs)	<b>11</b>
<b>1.4.</b>	<b>Properties of HOIPs</b>	<b>14</b>
<b>1.5.</b>	<b>Applications of HOIPs</b>	<b>15</b>
1.5.1.	Metal Ion Detection	<b>16</b>
1.5.2.	Photocatalysis	<b>18</b>
1.5.3.	Photodetector	<b>21</b>
<b>1.6.</b>	<b>Problems With HOIPs Structure</b>	<b>24</b>
1.6.1.	Environmental Instability in HOIPs	<b>24</b>

1.6.1. (a)	Effect of water	24
1.6.1. (b)	Effect of Oxygen	25
1.6.1. (c)	Effect of Atmospheric gases	26
1.6.1. (d)	Effect of Solvents	26
1.6.2.	Lead toxicity	28
<b>1.7.</b>	<b>Strategies to enhance the applicability of HOIPs Systems</b>	<b>29</b>
1.7.1.	Low-Dimensional HOIP Structures	29
1.7.2.	Lead-free HOIPs	35
1.7.3.	Nanocomposite Formation	39
<b>1.8.</b>	<b>Characterization Techniques</b>	<b>41</b>
1.8.1.	X-ray Diffraction (XRD)	41
1.8.2.	Single Crystal XRD	42
1.8.3.	UV-visible absorption spectroscopy	43
1.8.4.	Photoluminescence (PL) spectroscopy	43
1.8.5.	Transmission electron microscopy (TEM)	44
1.8.6.	Scanning electron microscopy (SEM)	46
1.8.7.	X- Ray Photoelectron Spectroscopy (XPS) and Ultraviolet photoelectron spectroscopy (UPS)	47
1.8.8.	Thermogravimetric Analysis and Differential Scanning Calorimetry (TGA-DSC)	50
<b>1.9.</b>	<b>References</b>	<b>51</b>

---

**CHAPTER-2**


---

**Zwitterionic Cysteamine linker based 2D Organic-Inorganic Perovskitoid for Metal Ion Detection and Photodetector Applications**

	<b>Summary</b>	<b>55</b>
<b>2.1.</b>	<b>Introduction</b>	<b>56</b>
<b>2.2.</b>	<b>Experimental Section</b>	<b>59</b>
2.2.1.	Synthesis of (cysteammonium) <sub>7</sub> Pb <sub>4</sub> I <sub>15</sub> (compound 1)	<b>59</b>
2.2.2.	Synthesis of (cysteammonium) <sub>2</sub> PbI <sub>4</sub> (compound 2)	<b>59</b>
2.2.3.	Preparation of compound 1 and FLBP (Few Layer Black Phosphorous) nanocomposite	<b>59</b>
2.2.4.	Metal-oleate Synthesis	<b>60</b>
2.2.5.	Photo-detector fabrication	<b>60</b>
<b>2.3.</b>	<b>Results and Discussion</b>	<b>60</b>
2.3.1.	Crystallographic Information	<b>65</b>
2.3.2.	TGA - DSC	<b>73</b>
2.3.3.	Optical Spectroscopy	<b>75</b>
2.3.4.	Analysis and Insights based on Density Functional Theory	<b>78</b>
<b>2.4.</b>	<b>Applications of the Perovskitoid Phase</b>	<b>80</b>
2.4.1.	Self-powered photodetector using compound 1 crystals	<b>80</b>
2.4.2.	Perovskitoid/FLBP interfacing and metal ion detection	<b>82</b>
2.4.2. (a)	Ni <sup>2+</sup> ion concentration dependence of PL intensity	<b>86</b>
2.4.2. (b)	Mechanism of Selective Ni <sup>2+</sup> ion sensing	<b>87</b>

<b>2.5.</b>	<b>Conclusions</b>	<b>88</b>
<b>2.6.</b>	<b>References</b>	<b>89</b>
	<b>Appendix</b>	<b>93</b>

---

### CHAPTER-3

---

#### Lead-Free Low Dimensional Mn- and Cu- based Hybrid Organic and Inorganic Perovskites for Pb<sup>+2</sup> Metal Ion Detection

	<b>Summary</b>	<b>96</b>
<b>3.1.</b>	<b>Introduction</b>	<b>97</b>
<b>3.2.</b>	<b>Experimental Section</b>	<b>99</b>
3.2.1.	Synthesis of (TEA) <sub>2</sub> CuBr <sub>4</sub> and (TEA) <sub>2</sub> MnBr <sub>4</sub>	<b>99</b>
3.2.2.	Synthesis of (TBA)CuBr <sub>2</sub> and (TBA) <sub>2</sub> MnBr <sub>4</sub>	<b>99</b>
3.2.3.	Nanoparticle (NP) solutions synthesis	<b>100</b>
3.2.4.	Synthesis of Metal-oleate solutions	<b>100</b>
3.2.5.	Metal-ion Detection Application	<b>100</b>
<b>3.3.</b>	<b>Results and Discussion</b>	<b>101</b>
3.3.1.	Structural Characterizations	<b>103</b>
3.3.2.	IR Spectroscopy	<b>104</b>
3.3.3.	XPS	<b>105</b>
3.3.4.	Nanoscale Microscopy	<b>107</b>
3.3.5.	Optical Spectroscopy	<b>110</b>
<b>3.4.</b>	<b>Metal Ion Detection</b>	<b>113</b>



3.4.1.	Post - Pb <sup>2+</sup> detection characterizations	118
3.4.2.	Proposed Mechanism	120
<b>3.5.</b>	<b>Conclusions</b>	<b>120</b>
<b>3.6.</b>	<b>References</b>	<b>121</b>
	<b>Appendix</b>	<b>125</b>

---

## CHAPTER-4

---

### 3D/0D Perovskite@COF Nanocomposite for Photocatalysis of Model Molecule in Water

	<b>Summary</b>	<b>127</b>
<b>4.1.</b>	<b>Introduction</b>	<b>128</b>
<b>4.2.</b>	<b>Experimental Section</b>	<b>129</b>
4.2.1.	Synthesis of Ethidium Bromide COF (EB-COF:Br)	129
4.2.2.	Synthesis of CsPbBr <sub>3</sub> @EB-COF:Br	130
4.2.3.	Synthesis of CsPbBr <sub>3</sub> /Cs <sub>4</sub> PbBr <sub>6</sub> @EB-COF:Br	130
4.2.4.	Synthesis of CsPbBr <sub>3</sub> -Cs <sub>4</sub> PbBr <sub>6</sub> without COF	130
4.2.5.	Water stability	131
4.2.6.	Photocatalytic experiments	131
<b>4.3.</b>	<b>Results and Discussion</b>	<b>131</b>
4.3.1.	Structural Characterizations	133
4.3.2.	Optical Spectroscopy	136

4.3.3.	IR Spectroscopy	137
4.3.4.	BET	138
4.3.5.	CHN Analysis	139
4.3.6.	Nanoscale Microscopic Imaging	139
4.3.7.	XPS	141
4.3.8.	TGA	143
<b>4.4.</b>	<b>Heterogeneous Photocatalytic Performance</b>	<b>144</b>
4.4.1.	Photocatalyst Recyclability	149
4.4.2.	Post-catalysis Characterizations	151
4.4.3.	Total Organic Carbon (TOC) Analysis and Measurement	151
<b>4.5.</b>	<b>Conclusions</b>	<b>153</b>
<b>4.6.</b>	<b>References</b>	<b>154</b>
	<b>Appendix</b>	<b>157</b>

<b>Abstract</b>	<b>159</b>
<b>List of publications and patents</b>	<b>160</b>
<b>List of conferences attended and posters presented</b>	<b>162</b>
<b>Copy of SCI Publications</b>	<b>165</b>
<b>Erratum</b>	<b>185</b>

## Acknowledgements

*First and foremost, I would like to express my profound admiration and deepest gratitude to my guide and research supervisor, **Dr. Shatabdi Porel Mukherjee**, for her invaluable guidance, insightful ideas, and engaging discussions throughout this journey. It is her astute guidance and meticulous evaluation of my research work that has culminated in the successful completion of my thesis under her tutelage. Under her mentorship, I have enjoyed the liberty of working with complete autonomy and at my own pace, which has contributed significantly to the enhancement of my research output. I am also deeply appreciative of her unwavering support during times when I was disheartened and stressed due to personal challenges. I cannot thank her enough for her unconditional support and invaluable contributions not only to my scientific work but also to my future trajectory. Her nurturing, compassionate, and astute personality has always inspired me as a researcher, particularly as a working woman who endeavors to strike a perfect balance between her professional and personal life. Therefore, I am immensely grateful to her for taking me under her wing, and I will always cherish her unwavering support as I continue to learn and progress in life.*

*A big thank you to my Doctoral Advisory Committee, (DAC) chair **Dr. Shubhangi B Umbarkar**, members **Dr. Santhosh Babu Sukumaran** and **Dr. Arup Kumar Rath** for their valuable suggestions and for letting my all DAC presentations be a great learning time for the improvement of my scientific knowledge and experimental work.*

*I would like to thank the present NCL director **Dr. Ashish Lele** and former director **Dr. Ashwin Kumar Nangia**, for providing all the necessary infrastructure for research. I thank to present head of the PMC division, **Dr. Ajith Kumar** and former heads of PMC division **Dr. B. L. V. Prasad** and **Dr. P. A. Joy**, for providing all divisional facilities to carry out research work smoothly. I would also like to thank CMC division for their cooperation in all characterization facilities, which constitutes a significant part of this thesis work.*

*Financial assistance from CSIR, New Delhi, for providing CSIR-SRF fellowship and AcSIR Ph.D. registration are greatly acknowledged.*

*I would like to take this special opportunity to express my sincere respect and thanks to **Dr. Satishchandra B. Ogale** for his crucial scientific mentorship initially during my job as a PA in IISER-Pune and later for extending his guidance during my PhD whenever required. His valuable suggestions in all matters have laid the foundation for my consistency and stability in my personal and professional life. He is my strong mentor who made critical situations easy in my personal and professional life.*

*A special thanks to my lab mates **Jeyavani, Manoj, Supriya and Sahil**, for their support. I also thanks to M.Sc. interns **Reena, Aishwarya, Haritha and Vinayak** and all my NCL friends **Neha, Akash, Himanshu, Swati, Chandan, and Geeta**.*

*I would like to thank **Ms. Neha Dhambare, Dr. Arup Kumar Rath Ms Swati Dilwale and Dr Sreekumar Kurungot, Prof. S. Ogale, Dr. Mallu Chenna Reddy, Dr. Shiv Pal, Mr. Siraj Sidhik, Ms. Tisita Das, Dr. Padmini Pandey, Dr. Sudip Chakraborty, Dr. Aditya D. Mohite and, Dr. Abhijit Biswas** for their help regarding various characterizations.*

*I would like to express my deepest gratitude for my **Father's blessings**. I would like to thank the almighty God for his grace and blessings in the form of my **mother**, **Dr. Jyoti Prasad Kour** and my **sister**, **Dr. Priyanka Kour** for their continuous support and encouragement during the most critical time. Their love, kindness, guidance and support in all personal, professional and financial situations is irreplaceable. Without my mother's support, I would not have reached this stage of my life. Her determination, hard work and strong will power are always a great source of inspiration for me. She has sacrificed a lot to give me this platform.*

*Tons of special thanks to my adorable and loving **husband**, **Mr. Jash Gidwani** for his love, care, understanding, and motivation in all situations when I was about to give up, he pushed and motivated me to not lose hope, to keep going. I got married during 2<sup>nd</sup> year of my PhD with my in-laws house in Gujarat, this journey was very difficult managing both places in different states, however I could reach this point because of my husband who strongly stood by me and fought for*

*me against all odds. Thanks to my very kind, loving and understanding in-laws **Mummy and Papa** for their support which made this journey easier.*

*Last but not the least, I would like to thank all my friends at NCL and, IISER for always lending me a helping hand and for being the sources of joy during my PhD.*


***Prachi Prasad Kour***

<u>Common Abbreviations</u>	
Å	Angstrom
ATR	Attenuated total reflection
BET	Brunauer–Emmett–Teller
COF	Covalent organic frameworks
CB	Conduction band
DRS	Diffuse reflection spectroscopy
0D	Zero-dimensional
1D	One-dimensional
2D	Two-dimensional
3D	Three-dimensional
ESEM	Environmental scanning electron microscope
EDAX	Energy dispersive X-ray spectroscopy
FAPI	Formamidinium lead bromide
FE-SEM	Field emission scanning electron microscopy
FWHM	Full-width half at maximum
FTIR	Fourier transform infrared
HAADF-STEM	High-angle annular electron microscopy
HOIP	Hybrid organic inorganic perovskites
HLHP	Hybrid lead halide perovskite
LFHHP	Lead free hybrid halide perovskite
Low-D	Low dimensional
MOF	Metal–organic frameworks
MAPI	Methylammonium lead bromide
MO	Methyl orange
N <sub>2</sub>	Nitrogen
NPs	Nanoparticles
NMs	Nanomaterials

---

O <sub>2</sub>	Oxygen
PXRD	Powder X-ray diffraction
PbBr <sub>2</sub>	Lead bromide
PL	Photoluminesce
RP	Ruddlesden Popper
SAED	Selected area electron diffraction
SSA	Specific surface area
TEM	Transmission electron microscope
TGA	Thermogravimetric analysis
TEAB	Tetraethylammonium bromide
TBAB	Tetrabutylammonium bromide
UV	Ultra-voilet
VB	Valance band
XPS	X-ray photoelectron spectroscopy
$\chi^2$	chi-square

## Synopsis Report

	<b>Synopsis of the Thesis to be submitted to the Academy of Scientific and Innovative Research for Award of the Degree of Doctor of Philosophy in Sciences</b>
<b>Name of the Candidate</b>	<b>Ms. Prachi Prasad Kour</b>
<b>Degree Enrollment No. &amp; Date</b>	<b>10CC19J26009 &amp; 09/06/2020</b>
<b>Laboratory</b>	<b>CSIR- National Chemical Laboratory</b>
<b>Title of the Thesis</b>	<b>Rational Design and Synthesis of Low-Dimensional Halide Perovskites with Improved Ambient Air Stability for Optoelectronic Applications</b>
<b>Research Supervisor/ Co-supervisor</b>	<b>Dr. Shatabdi Porel Mukherjee</b>

### Introduction

Initially, oxide perovskites were discovered in the 90's with the general formula  $ABO_3$  (where A = monovalent cation, B = divalent cation). However halide perovskites and organic-inorganic perovskites also exist. Hybrid Organic and Inorganic Perovskites (HOIPs),  $ABX_3$  (A =  $Cs^+$ ,  $CH_3NH_3^+$ ,  $C_8H_9NH_3^+$ ,  $CH_5N_2^+$ ; B =  $Pb^{+2}$ ,  $Sn^{+2}$ ,  $Sb^{+2}$ ,  $Cu^{+2}$ ; X =  $I^-$ ,  $Br^-$ ,  $Cl^-$ ,  $BF_4^-$ ) and the halide perovskites (HPs) have an inorganic A site cation such as  $Cs^+$ ,  $Na^+$ , etc.,. These have rapidly emerged as the leading photovoltaic and optoelectronic device materials in the past decade owing to their exceptional properties such as low exciton binding energy, high absorption coefficient, high carrier lifetime, bandgap tunability, dimensionality control, scalability, and low cost of fabrication due to solution processability.<sup>1-3</sup>

These versatile materials are -low-cost and easy to fabricate, thus having the potential to replace many expensive materials for various types of photovoltaic applications such as photocatalytic reactions, oxygen evolution, water splitting, metal ion detection and dye degradation.

### Statement of Problem

The main problem with these fascinating structures is their intrinsic instability to ambient conditions such as air, oxygen, and moisture. This is because they have an ionic lattice and the



intrinsic defects formed on the surface during thin film fabrication and other device applications. Also, another problem that exists till now is that the champion materials for solar cell applications and other practical applications are generally lead-based. Whereas, the limit of lead usage is regulated in most countries.

The conversion of 3D HOIP to 2D HOIP is achieved by increasing the length of the organic cation (two or more carbon atoms), thus pushing the inorganic ( $\text{PbI}_6^-$ ) octahedral layers farther apart and creating a quantum well like structure with sequentially increasing band gaps. 2D HOIPs have gained considerable attention following the work of Mohite and co-workers, wherein they developed a hot casting technique for better charge transport leading to highly efficient perovskite solar cells and light-emitting diodes.<sup>4,5</sup> These 2D systems have already been demonstrated to possess several unique properties such as moisture stability, thermal stability, self-trapping of excitonic features, and long carrier lifetimes. These properties make them highly applicable for LEDs, lasing, and white-light emission applications as well.<sup>6-8</sup> The 2D lead-based HOIPs (tolerance factor,  $t > 1$ ) can form Ruddlesden Popper (RP) type phase (general formula:  $\text{A}_{n+1}\text{B}_n\text{X}_{3n+1}$ ), Dion-Jacobson type perovskite phase (general formula:  $\text{A}'\text{A}_{n-1}\text{P}_n\text{b}_n\text{X}_{3n+1}$ ) or alternating cation type phase (general formula:  $(\text{A}'\text{A})_{n+1}\text{B}_n\text{X}_{3n+1}$ ) by incorporation of long alkyl/aryl organic monovalent or divalent cations, respectively.<sup>9</sup> Although thiol conjugations have been explored, to the best of our knowledge, the incorporation of zwitterionic moieties to form 2D hybrid perovskite has not been studied to date, which sets the goal for the thesis.

The HLHPs (Hybrid lead halide perovskites) suffer from numerous drawbacks due to their fragile crystal structure, which crumbles easily upon attack by water, oxygen, under sunlight and UV rays<sup>10-12</sup>. This raises major concerns about lead pollution by these systems for large-scale environmental applications such as solar cells since they have to withstand all weather conditions. The acceptable level of lead in bare soil given by EPA (Environmental Protection Agency) for play areas is 400 ppm and in non-play areas is 1200 ppm<sup>13</sup>. However, long-term use of lead-based devices can lead to lead accumulation in the soil and water bodies and in turn within our bodies.

Hence, to break off this lead toxicity problem, there is a consequential shift in research towards lead-free hybrid halide perovskites (LFHHPs)<sup>14,15-17</sup>. LFHHPs are a series of compounds with a general chemical formula of  $\text{A}_x\text{B}_y\text{X}_z$  ( $x, y, z$  depends on structural directionality), B represents a mono/divalent metal cation ( $\text{Sn}^{2+}/\text{Sb}^{2+}/\text{Bi}^+/\text{Pd}^{2+}/\text{In}^+/\text{Ti}^+/\text{Pt}^{2+}/\text{Au}^+/\text{Cu}^+/\text{Ag}^+/\text{Mn}^+$ )<sup>18,19-21</sup> The dimensionality of the

perovskite crystal structures mainly depends on the size of the cations which should fulfill the requirement of Goldschmidt tolerance factor ( $t$ )<sup>22</sup>,

$$t = \frac{R_A + R_X}{\sqrt{2}(R_B + R_X)}$$

where,  $R_A$ ,  $R_B$ , and  $R_X$  are the ionic radius of the A-site, B-site, and halide site, respectively. LFHHPs have demonstrated superior properties to their HLHP counterparts.<sup>23, 24-26</sup>

The development of stable copper and manganese-based hybrid halide perovskites is of important since they show a change in oxidation state upon exposure to moisture and oxygen. The tetrahedrally coordinated  $[\text{MnX}_4]^{2-}$  anions, are luminous in the solid state. However, upon interaction with solvents, they lose their structural coordination, making the perovskite non-emissive. The  $\text{Cu}^+$  in cuprous halide perovskites quickly oxidizes in the presence of moisture due to the low hydration energy of  $\text{Cu}^+$  ions, which leads to the formation of  $\text{Cu}^{2+}$  upon loss of an electron.

Another interesting strategy explored in this thesis is the nanocomposite formation. The following section gives a jist of the work carried out with this effect. CLBPs are also known to exist in three-dimensional polymorphs, namely 3D  $\text{CsPbBr}_3$  (cubic) formed by a cubo-octahedral ( $\text{PbX}_6$ ) network in all three directions, 2D  $\text{CsPb}_2\text{Br}_5$  (tetragonal), which possesses octahedral connectivity only in two directions and hence creates a layered structure and 0D  $\text{Cs}_4\text{PbBr}_6$  (hexagonal) which lacks octahedral connectivity in all the directions.<sup>27-29</sup> Therefore, for CLBPs, even in NCs and bulk, it is anticipated that the photoexcited charge carriers in these materials experience strong quantum confinement, and the exciton binding energy for 0D perovskites is much superior to that for 3D perovskites.<sup>30-32</sup> The PL intensity and efficiency of 0D  $\text{Cs}_4\text{PbBr}_6$  found to be much superior to those of 3D  $\text{CsPbBr}_3$ .<sup>33,34</sup> It is also reported that the co-existence of  $\text{CsPbBr}_3$  and  $\text{Cs}_4\text{PbBr}_6$  NCs was hard to suppress,<sup>35</sup> and  $\text{Cs}_4\text{PbBr}_6$  NCs can be easily transformed into  $\text{CsPbBr}_3$  via an insertion reaction with additional  $\text{PbBr}_2$ , physical or chemical extraction of  $\text{CsBr}$ , and ligand-mediated transformation.<sup>36-38</sup> Since,  $\text{CsPbBr}_3$  has superior optical properties and  $\text{Cs}_4\text{PbBr}_6$  has higher moisture stability, their co-existence processed stability as well as outstanding PLQY comparable to  $\text{CsPbBr}_3$  NCs.<sup>39-41</sup> Several strategies have been adopted to form mixed-phase CLBP composites and overcome the abhorrent obstacle of ambient instability, such as using polymer blends and inorganic passivators to solve these issues.<sup>42-44</sup> Metal-organic frameworks (MOFs) are also being used as effective encapsulators due to their framework structure and facile modulation features.<sup>45-47</sup> Covalent Organic Frameworks (COFs) are another sister class of MOFs in which light atoms bond covalently to form an open structure with high porosity.<sup>48,49</sup> These materials

have similar properties to MOFs. Still, they possess a tunable pore size, structural predictability, lower density, and higher stability, making them an exciting class of encapsulators that have not been explored extensively to encapsulate perovskite systems as far as is known currently.<sup>50,51</sup>

Thus there is a need to design and fabricate high-stability structures that can withstand the environmental conditions present in real real-life applications, so that the commercialization of this low- cost versatile photovoltaic materials is easy.

## **Methodology**

The following methodologies have been explored in the thesis in detail:

### **1. Method 1**

With the aim of incorporating the thiol-functional group containing ammonium cation into the organic-inorganic hybrid system, the reaction of  $\text{PbI}_2$  (1 equivalent) with cysteamine (3 equivalent) in HI solution was carried out at  $250^\circ\text{C}$  resulting in the growth of yellow crystals of  $((\text{HSC}_2\text{H}_4\text{NH}_3)_7\text{Pb}_4\text{I}_{15})$  (**1**). The details of the synthesis process are presented in supporting information. The synthesis scheme along with the physical appearance of yellow crystals before and after filtration is shown in Figure 1 (A, B), Scheme 1.  $(\text{HSC}_2\text{H}_4\text{NH}_3)_7\text{Pb}_4\text{I}_{15}$  is green-emitting, as seen under the UV light (Figure 1C) initially and studied later in this work. Figure 1D shows the confocal microscopy images obtained under polarised microscopy indicating well-faceted single crystals for further analysis. Following the appearance of the yellow crystals in the solution, it was allowed to settle for 2-3 hours without any changes in the environmental conditions or additives. An interesting transformation of the yellow crystals into the red crystals was observed in the solution at room temperature after 2-3 hours, as shown in Figure 1, Scheme 2. Our analysis showed that the non-Ruddlesden Popper (RP) 2D perovskitoid gradually got converted into RP-like 2D perovskite ( $n = 1$ )  $(\text{HSC}_2\text{H}_4\text{NH}_3)_2\text{PbI}_4$ . Recently, Kanatzidis and co-workers have reported the transformation of RP ( $n = 1$ ) perovskite to a corrugated structure by using N, N-dimethylethylenediamine (DMEN) cation, wherein both phases maintained the perovskite structure without losing corner-sharing. The important distinction in our case is that along with the structural change, the perovskitoid form (which is a non-perovskite) got transformed into a RP perovskite structure, indicating crystal-to-crystal rearrangements in HOIP systems.

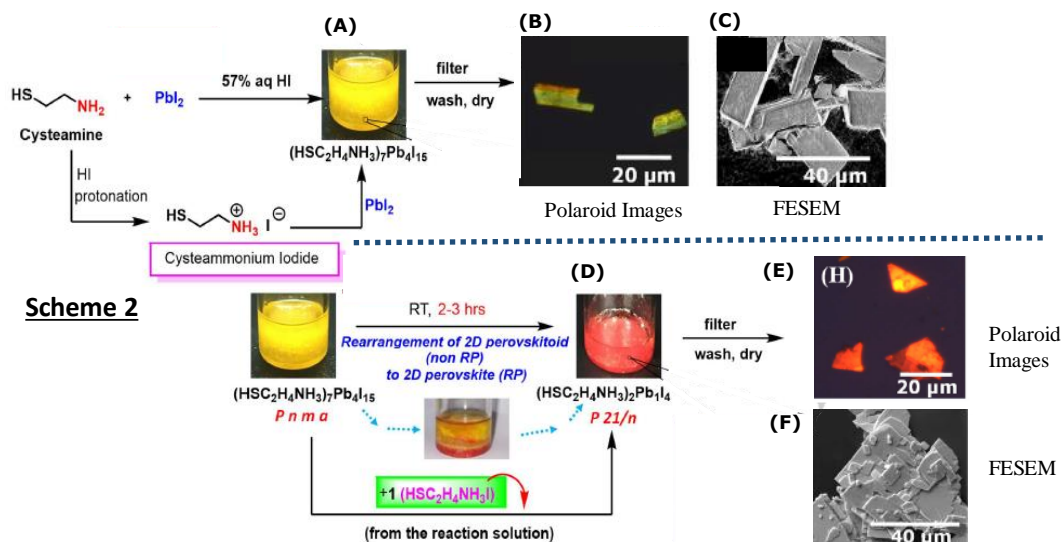


Figure 1: Scheme 1 for reaction and formation of (HSC<sub>2</sub>H<sub>4</sub>NH<sub>3</sub>)<sub>7</sub>Pb<sub>4</sub>I<sub>15</sub> (1); (A) Crystals of **1** formed in the reaction solution; (B) (HSC<sub>2</sub>H<sub>4</sub>NH<sub>3</sub>)<sub>7</sub>Pb<sub>4</sub>I<sub>15</sub> in the ambient, (C) under the 265nm UV lamp showing green emission; (D) polarised microscopy images; (E) FESEM image for **1**; Scheme 2 for conversion of yellow crystals **1** ((HSC<sub>2</sub>H<sub>4</sub>NH<sub>3</sub>)<sub>7</sub>Pb<sub>4</sub>I<sub>15</sub> (2D perovskitoid)) to red crystals **2** ((HSC<sub>2</sub>H<sub>4</sub>NH<sub>3</sub>)<sub>2</sub>PbI<sub>4</sub> (2D perovskite)) in mother solution; (F) RP phase crystals **2** in the solution; (G) (HSC<sub>2</sub>H<sub>4</sub>NH<sub>3</sub>)<sub>2</sub>PbI<sub>4</sub> crystals under ambient light after filtration; (H) polarized microscopy images, (I) FESEM image for (HSC<sub>2</sub>H<sub>4</sub>NH<sub>3</sub>)<sub>2</sub>PbI<sub>4</sub>.

## 2. Method 2

In another strategy, we have synthesized copper and manganese-based halide perovskites using tetramethylammonium bromide and tetraethylammonium bromide as the A site cations to form low-dimensional perovskites. The reason for choosing the quaternary alkyl ammonium salts for our ambient synthesis is that as the size of the organic chain increases, the moisture tolerance is increased. The crystalline samples of compound **1** (TEA)<sub>2</sub>MnBr<sub>4</sub>, compound **2** (TBA)<sub>2</sub>MnBr<sub>4</sub>, compound **3** (TEA)<sub>2</sub>CuBr<sub>4</sub> and compound **4** (TBA)CuBr<sub>2</sub> were prepared by a straightforward and effortless method by using the elementary principle of molar ratio control. The synthesis of HOPIs can be easily tuned by controlling the process of synthesis, molar ratios, alkylamine chain length, and functional groups<sup>52-54</sup>.

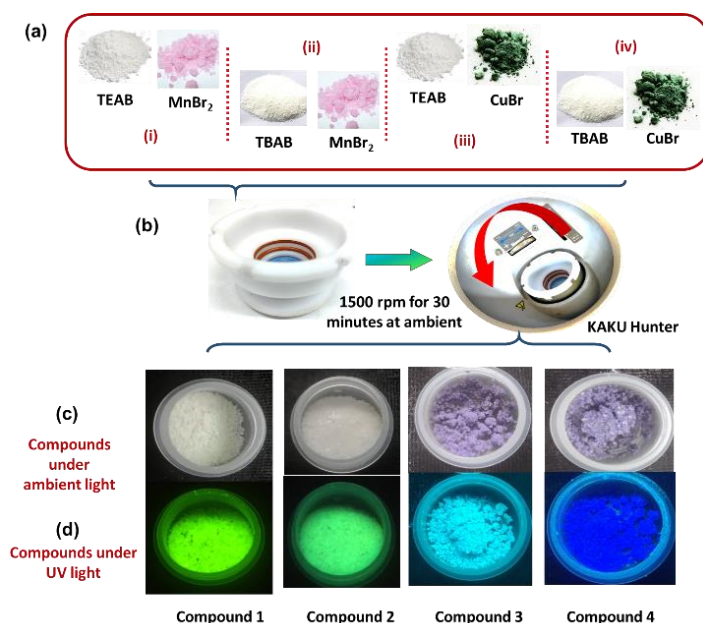


Figure 2: (A) shows the precursor combinations (i, ii, iii and iv) used for the synthesis of (TEA)<sub>2</sub>MnBr<sub>4</sub>, (TBA)<sub>2</sub>MnBr<sub>4</sub>, (TEA)<sub>2</sub>CuBr<sub>4</sub> and (TBA)CuBr<sub>2</sub>, respectively; (B) shows the actual laboratory images of the reaction vessel and its subsequent mounting in the KAKU Hunter instrument; (C) shows the ambient pictures of the compounds; (D) shows the emission on the respective compounds under UV light, images for (HSC<sub>2</sub>H<sub>4</sub>NH<sub>3</sub>)<sub>7</sub>Pb<sub>4</sub>I<sub>15</sub> and (HSC<sub>2</sub>H<sub>4</sub>NH<sub>3</sub>)<sub>2</sub>PbI<sub>4</sub> are recorded under 365 nm light and for (TEA)<sub>2</sub>CuBr<sub>4</sub> and (TBA)CuBr<sub>2</sub> images are recorded under 254 nm.

Hence, we have fixed the molar ratios of the precursors of manganese (II) bromide (MnBr<sub>2</sub>), copper (I) bromide (CuBr), tetraethylammonium bromide (TEAB), and tetrabutylammonium bromide (TBAB) at 1: 3 (metal halide: organic precursor) [Figure 2(A)]. After measuring the appropriate amount of precursors, they are hand shaken in a reaction vessel, followed by mounting the vessel inside KAKU hunter instrument [Figure 2(B)].

The machine is set to rotate at 1500 rpm for 30 minutes, ultimately synthesizing our lead-free bromide compounds [Figure 2 (C)]. The (TEA)<sub>2</sub>MnBr<sub>4</sub> and (TBA)<sub>2</sub>MnBr<sub>4</sub>, when viewed under 365 nm UV light, showed strong green emission [Figure 2 (D)], and (TEA)<sub>2</sub>CuBr<sub>4</sub> and (TBA)CuBr<sub>2</sub> when viewed under 254 nm UV light, showed strong cyan emission, indicating the formation of optically active compounds.

### 3. Method 3

We have specifically selected a cationic COF (EB-COF:Br) having Br-functionalization due to its chemical affinity and non-interference with the PL properties with the bromide containing perovskite, mainly CLBP. Recently, mechanochemical synthesis has become an excellent alternative to the solution based classical synthesis of COFs.<sup>55</sup> Herein, we have used a modified mechanochemical method to synthesize EB-COF:Br avoiding the necessity of using typical inert atmosphere conditions in a Pyrex tube, as reported earlier.<sup>56</sup> In this method, 1,3,5-

triformyl phloroglucinol (TFP) (0.2 mmol) and ethidium bromide (EB) (0.3 mmol) were ground together using a mortar and pestle followed by the addition of 2 mL 1,4-dioxane–mesitylene (v/v, 1 : 1) and 0.2 mL of 6 M aqueous acetic acid solutions at room temperature. The mixing was continued for 2–3 hours by using DI water as the solvent till a dark brown paste was achieved. This paste was then transferred to a vial and heated in an oven at 90 °C for 24 hours. The product was then washed and dried under vacuum for further use (Figure 3).

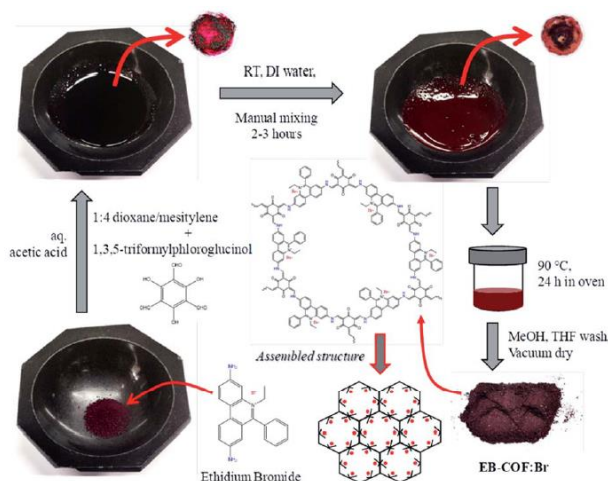


Figure 3: Schematic representation of the modified mechanochemical synthesis of EB-COF:Br through simple Schiff base reactions performed via mechanochemical grinding and mixing using a mortar and pestle, followed by heating.

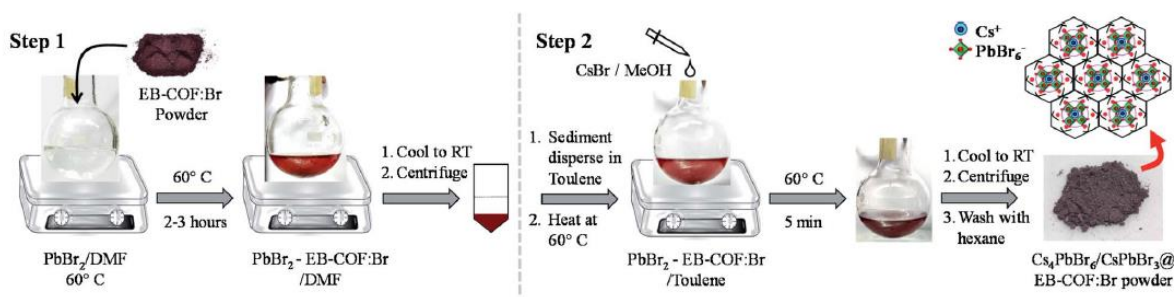


Figure 4: Schematic representation of the two step solution-based synthesis of CsPbBr<sub>3</sub>/Cs<sub>4</sub>PbBr<sub>6</sub>@EB-COF:Br. In the next action, CLBP incorporated EB-COF:Br was synthesized via a two-step precursor addition strategy, wherein first PbBr<sub>2</sub> was added, followed by CsBr addition to achieve the CLBP@EB-COF:Br nanocomposite (Figure 4).

## Results

The resulting materials were then tested for different optoelectronic applications such as metal ion sensing, photodetection and as a photocatalyst, however the applications are material specific.

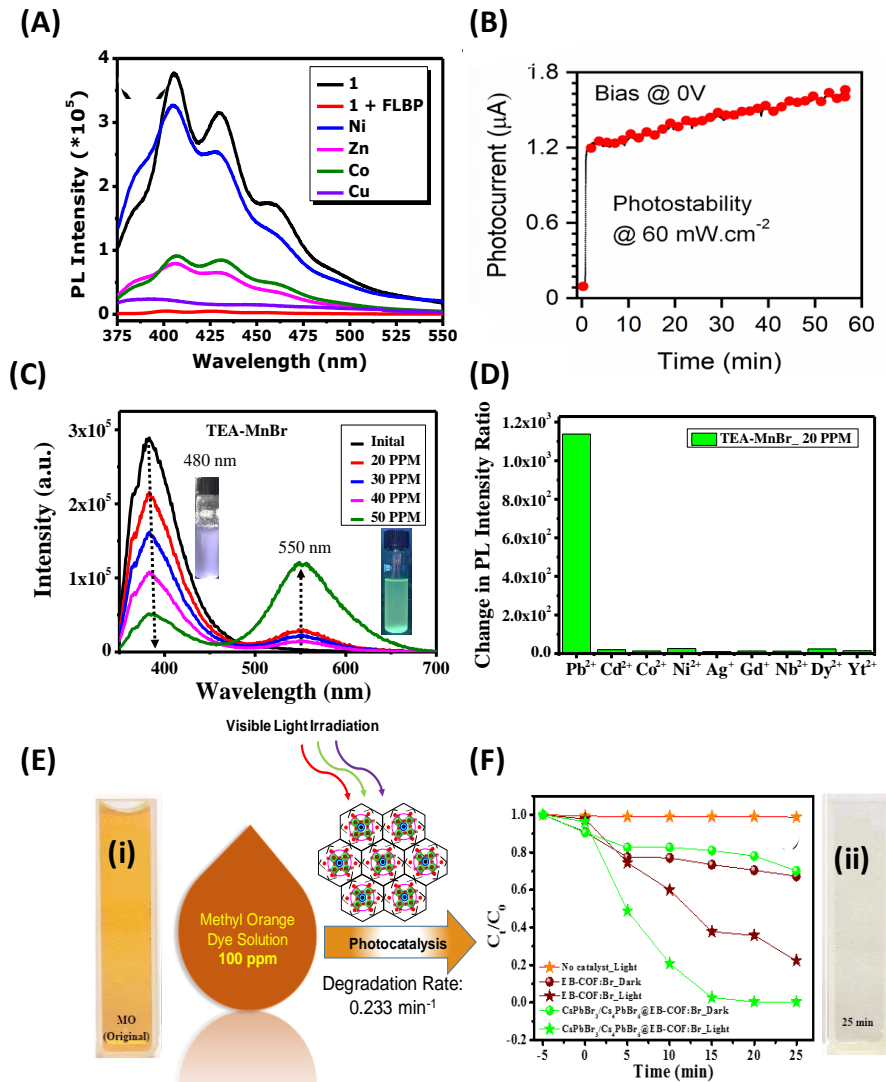


Figure 5: Applications for 2D perovskitoid phase:(A) PL spectra for selective detection of Ni<sup>2+</sup> ions at  $1.79 \times 10^{-2}$  M concentration; (B) Photostability for self-powered photodetector; (C) PL spectra for selective detection of Pb<sup>2+</sup> ions by (TEA)<sub>2</sub>MnBr<sub>4</sub>; (D) Comparative bar graph showing the high selectivity Pb<sup>2+</sup> ions by (TEA)<sub>2</sub>MnBr<sub>4</sub> out of Cd<sup>2+</sup>, Co<sup>2+</sup>, Ni<sup>2+</sup>, Ag<sup>+</sup>, Gd<sup>3+</sup>, Nb<sup>5+</sup>, Dy<sup>3+</sup> and Yt<sup>3+</sup>; (E, F) Process diagram showing the degradation of 100 PPM of methyl orange in water by the photocatalyst CsPbBr<sub>3</sub>/Cs<sub>4</sub>PbBr<sub>6</sub>@EB-COF:Br nanocomposite, the graph shows the reaction kinetics for the photocatalysts EB-COF:Br and CsPbBr<sub>3</sub>/Cs<sub>4</sub>PbBr<sub>6</sub>@EB-COF:Br nanocomposite under light and dark conditions. Photographic images, (i) and (ii) show the change in colour of the MO dye before and after the reactions, respectively.

We further demonstrate that a composite of (HSC<sub>2</sub>H<sub>4</sub>NH<sub>3</sub>)<sub>7</sub>Pb<sub>4</sub>I<sub>15</sub> with few layer black phosphorous (FLBP) is a very effective On-Off-On photoluminescence (PL) probe for selective detection of Ni<sup>2+</sup> (Figure 5A) and it also works as an excellent active layer in a self-powered photodetector when sandwiched between PEDOT:PSS and PCBM (optoelectronic functionality) (Figure 5B).

Mn<sup>-</sup> compounds show ultrafast (fraction of a second) and selective detection of Pb<sup>2+</sup> ions (~103 times enhancement for Pb<sup>2+</sup> @ 550 nm) due to the formation of a new Pb phase, occurring due to the inter-diffusion of Pb<sup>2+</sup> ions into the HOIP framework (Figure 5C, 5D).

The samples water stability, e.g., CsPbBr<sub>3</sub>@EB-COF:Br, CsPbBr<sub>3</sub>/Cs<sub>4</sub>PbBr<sub>6</sub>@-EB-COF:Br, CsPbBr<sub>3</sub>/Cs<sub>4</sub>PbBr<sub>6</sub> without COF encapsulation, was compared, and it was found that the CsPbBr<sub>3</sub>/Cs<sub>4</sub>PbBr<sub>6</sub>@EBCOF: Br nanocomposite has remained reasonably stable in water for 60 minutes. The perovskite@COF nanocomposite shows efficient visible-light-driven photocatalytic performance to degrade Methyl orange (10 mL; 20–100 ppm) (Figure 5E, 5F). The rate of photodegradation was about 0.245 min<sup>-1</sup> with high catalytic activity and recyclability for three to six cycles.

## **Conclusions**

- Demonstrated synthesis of a new low-D hybrid perovskitoid (yellow crystals, P21/n space group) using zwitterion cysteamine (2- aminoethanethiol) linker, and its remarkable molecular diffusion- controlled crystal-to-crystal transformation to Ruddlesden- Popper phase (Red crystals, Pnma space group).
- Demonstrated synthesis of a new low-D hybrid perovskitoid (yellow crystals, P21/n space group) using zwitterion cysteamine (2- aminoethanethiol) linker, and its remarkable molecular diffusion- controlled crystal-to-crystal transformation to Ruddlesden- Popper phase (Red crystals, Pnma space group).
- Demonstrated synthesis of a new low-D hybrid perovskitoid (yellow crystals, P21/n space group) using zwitterion cysteamine (2- aminoethanethiol) linker, and its remarkable molecular diffusion- controlled crystal-to-crystal transformation to Ruddlesden- Popper phase (Red crystals, Pnma space group).
- Applicability of the new perovskitoid yellow phase as selective detection of Ni<sup>2+</sup> based on its composite with few-layer black phosphorous & an excellent active layer in a self-powered photodetector is shown.
- Successfully synthesised hybrid organic and inorganic lead free halide compounds under ambient conditions by a solid state method. The Cu compounds show cyan emission and the Mn compounds are green emissive.
- The compounds thus synthesized are 2D for TEA-CuBr, TEA-MnBr TBA-MnBr is 2D whereas TBA-CuBr is 0D.
- TEA-MnBr shows reasonable PL stability at ~70-80% humidity conditions, out of the four compounds namely, TEA-MnBr, TBA-MnBr, TEA-CuBr and TBA-CuBr.



- Mn- compounds show ultrafast and selective detection of  $\text{Pb}^{2+}$  ions due to the formation of a new Pb phase, occurring due to the inter-diffusion of  $\text{Pb}^{2+}$  ions into the HOIP framework.
- Simple mechanochemical synthetic route to synthesize a cationic covalent organic framework EB-COF:Br with  $\text{Br}^-$  as the counter ion.
- Both single-phase  $\text{CsPbBr}_3@EB\text{-COF:Br}$  and mixed phase  $\text{CsPbBr}_3/\text{Cs}_4\text{PbBr}_6@EB\text{-COF:Br}$  nanocomposites were obtained by slightly tuning the synthesis protocol.
- The samples water stability, e.g.,  $\text{CsPbBr}_3@EB\text{-COF:Br}$ ,  $\text{CsPbBr}_3/\text{Cs}_4\text{PbBr}_6@EB\text{-COF:Br}$ ,  $\text{CsPbBr}_3/\text{Cs}_4\text{PbBr}_6$  without COF encapsulation, was compared, and it was found that the  $\text{CsPbBr}_3/\text{Cs}_4\text{PbBr}_6@EB\text{COF: Br}$  nanocomposite has remained reasonably stable in water for 60 minutes.
- The perovskite@COF nanocomposite shows efficient visible-light-driven photocatalytic performance to degrade Methyl orange (10 mL; 20–100 ppm).
- The rate of photodegradation was about  $0.245 \text{ min}^{-1}$  with high catalytic activity and recyclability for three to six cycles.

## **References**

- [1] D. H. Cao, C. C. Stoumpos, O. K. Farha, J. T. Hupp, M. G. Kanatzidis, *J. Am. Chem. Soc.* 2015, 137, 7843 – 7850.
- [2] Q. Dong, J. Song, Y. Fang, Y. Shao, S. Ducharme, J. Huang, *Adv. Mater.* 2016, 28, 2816 – 2821.
- [3] W. Zhang, X. Yan, W. Gao, J. Dong, R. Ma, L. Liu, M. Zhang, *Org. Electron.* 2019, 65, 56 – 62.
- [4] A. Z. Chen, M. Shiu, J. H. Ma, M. R. Alpert, D. Zhang, B. J. Foley, D. Smilgies, S. Lee, J. J. Choi, *Nat. Commun.* 2018, 9, 1336.
- [5] T. Zuo, X. He, P. Hu, H. Jiang, *ChemNanoMat* 2019, 5, 278 – 289.
- [6] C. C. Stoumpos, D. H. Cao, D. J. Clark, J. Young, J. M. Rondinelli, J. I. Jang, J. T. Hupp, M. G. Kanatzidis, *Chem. Mater.* 2016, 28, 2852 – 2867.
- [7] Y. Yu, D. Zhang, P. Yang, *Nano Lett.* 2017, 17, 5489 – 5494.
- [8] A. Basu, P. Kour, S. Parmar, R. Naphade, S. Ogale, *J. Phys. Chem. C* 2018, 122, 4802 – 4808.
- [9] P. Kour, M. C. Reddy, R. Naphade, S. Ogale, *APL Mater.* 2018, 6, 086107-7.
- [10] R. Naphade, S. Nagane, U. Bansode, M. Tathavadekar, A. Sadhanala, S. Ogale, *ChemSusChem* 2017, 10, 3722 – 3739.
- [11] H. Tsai, W. Nie, J.-C. Blancon, C. C. Stoumpos, R. Asadpour, B. Harutyunyan, A. J. Neukirch, R. Verduzco, J. J. Crochet, S. Tretiak, L. Pedesseau, J. Even, M. A. Alam, G. Gupta, J. Lou, P. M. Ajayan, M. J. Bedzyk, M. G. Kanatzidis, A. D. Mohite, *Nature* 2016, 536, 312 – 316.
- [12] H. Tsai, W. Nie, J. C. Blancon, C. C. Stoumpos, C. M. M. Soe, J. Yoo, J. Crochet, S. Tretiak, J. Even, A. Sadhanala, G. Azzellino, R. Brenes, P. M. Ajayan, V. Bulovic', S. D. Stranks, R. H. Friend, M. G. Kanatzidis, A. D. Mohite, *Adv. Mater.* 2018, 30, 1704217.
- [13] X. Liu, F. Gao, *J. Phys. Chem. Lett.* 2018, 9, 2251 – 2258.
- [14] Z. Yuan, Y. Shu, B. Ma, *Chem. Commun.* 2016, 52, 3887 – 3890.
- [15] R. Guo, Z. Zhu, A. Boulesbaa, F. Hao, A. Puzos, K. Xiao, B. Jiming, Y. Yan, W. Li, *Small Methods* 2017, 1, 1700245.
- [16] "Excitonics in 2D Perovskites": W. K. Chong, D. Giovanni, T. C. Sum, *Halide Perovskites*, pp. 55 – 79, Wiley, Weinheim, 2018.
- [17] D. Yu, B. Cai, F. Cao, X. Li, X. Liu, Y. Zhu, J. Ji, Y. Gu, H. Zeng, *Adv. Mater. Interfaces* 2017, 4, 1700441.

- [18] S. Krishnamurthy, P. Kour, A. Katre, S. Gosavi, S. Chakraborty, S. Ogale, *APL Mater.* 2018, 6, 114204 – 8.
- [19] S. Krishnamurthy, R. Naphade, W. J. Mir, S. Gosavi, S. Chakraborty, R. Vaidhyanathan, S. Ogale, *Adv. Opt. Mater.* 2018, 6, 1800751.
- [20] S. Parmar, S. Pal, A. Biswas, S. Gosavi, S. Chakraborty, M. C. Reddy, S. Ogale, *Chem. Commun.* 2019, 55, 7562 – 7565.
- [21] C. M. M. Soe, C. C. Stoumpos, M. Kepenekian, B. Traor8, H. Tsai, W. Nie, B. Wang, C. Katan, R. Seshadri, A. D. Mohite, J. Even, T. J. Marks, M. G. Kanatzidis, *J. Am. Chem. Soc.* 2017, 139, 16297 – 16309
- [22] L. Mao, Y. Wu, C. C. Stoumpos, M. R. Wasielewski, M. G. Kanatzidis, *J. Am. Chem. Soc.* 2017, 139, 5210 – 5215.
- [23] M. H. Tremblay, F. Thouin, J. Leisen, J. Bacsa, A. R. S. Kandada, J. M. Hoffman, M. G. Kanatzidis, A. D. Mohite, C. Silva, S. Barlow, S. R. Marder, *J. Am. Chem. Soc.* 2019, 141, 4521 – 4525.
- [24] C. C. Stoumpos, L. Mao, C. D. Malliakas, M. G. Kanatzidis, *Inorg. Chem.* 2017, 56, 56 – 73.
- [25] X. Li, Y. He, M. Kepenekian, P. Guo, W. Ke, J. Even, C. Katan, C. C. Stoumpos, R. D. Schaller, M. G. Kanatzidis, *J. Am. Chem. Soc.* 2020, 142, 6625 – 6637.
- [26] Q. Sun, Y. Xu, H. Zhang, B. Xiao, X. Liu, J. Dong, Y. Cheng, B. Zhang, W. Jie, M. G. Kanatzidis, *J. Mater. Chem. A* 2018, 6, 23388 – 23395.
- [27] C. Ma, D. Shen, T. W. Ng, M. F. Lo, C. S. Lee, *Adv. Mater.* 2018, 30, 1800710.
- [28] Y. Xie, H. Yu, J. Duan, L. Xu, B. Hu, *ACS Appl. Mater. Interfaces* 2020, 12, 11190 – 11196.
- [29] Y. Liu, S. Akin, A. Hinderhofer, F. T. Eickemeyer, H. Zhu, J. Y. Seo, J. Zhang, F. Schreiber, H. Zhang, S. M. Zakeeruddin, A. Hagfeldt, M. I. Dar, M. Gr-tzel, *Angew. Chem. Int. Ed.* 2020, 59, 15688 – 15694; *Angew. Chem.* 2020, 132, 15818 – 15824.
- [30] F. Xia, Y. Xu, B. Li, W. Hui, S. Zhang, L. Zhu, Y. Xia, Y. Chen, W. Huang, *ACS Appl. Mater. Interfaces* 2020, 12, 15439 – 15445.
- [31] W. Ke, C. C. Stoumpos, M. Zhu, L. Mao, I. Spanopoulos, J. Liu, O. Y. Kontsevoi, M. Chen, D. Sarma, Y. Zhang, M. R. Wasielewski, M. G. Kanatzidis, *Sci. Adv.* 2017, 3, e1701293.
- [32] I. Spanopoulos, W. Ke, C. C. Stoumpos, E. C. Schueller, O. Y. Kontsevoi, R. Seshadri, M. G. Kanatzidis, *J. Am. Chem. Soc.* 2018, 140, 5728 – 5742.
- [33] T. Rath, J. Handl, S. Weber, B. Friesenbichler, P. Fgrk, L. Troi, T. Dimopoulos, B. Kunert, R. Resel, G. Trimmel, *J. Mater. Chem. A* 2019, 7, 9523 – 9529.
- [34] S. F. Zhang, X. K. Chen, A. M. Ren, H. Li, J. L. Bredas, *ACS Energy Lett.* 2019, 4, 17 – 25.
- [35] M. H. Tremblay, J. Bacsa, S. Barlow, S. R. Marder, *Mater. Chem. Front.* 2020, 4, 2023. [36] T. Kollek, D. Wurmbbrand, S. T. Birkhold, E. Zimmermann, J. Kalb, L. Schmidt-Mende, S. Polarz, *ACS Appl. Mater. Interfaces* 2017, 9, 1077 – 1085.
- [37] J. Cao, J. Yin, S. Yuan, Y. Zhao, J. Li, N. Zheng, *Nanoscale* 2015, 7, 9443 – 9447.
- [38] A. Halder, R. Chulliyil, A. S. Subbiah, T. Khan, S. Chattoraj, A. Chowdhury, S. K. Sarkar, *J. Phys. Chem. Lett.* 2015, 6, 3483 – 3489.
- [39] B. Li, C. Fei, K. Zheng, X. Qu, G. Cao, J. Tian, *J. Mater. Chem. A* 2016, 4, 17018 – 17024. [40] W. A. Saidi, J. J. Choi, *J. Chem. Phys.* 2016, 145, 144702.
- [41] S. Sidhik, A. C. Pasar#n, C. Rosiles P8rez, T. Llpez-Luke, E. De La Rosa, *J. Mater. Chem. C* 2018, 6, 7880 – 7889.
- [42] M. Saliba, T. Matsui, J. Y. Seo, K. Domanski, J. P. Correa-Baena, M. K. Nazeeruddin, S. M. Zakeeruddin, W. Tress, A. Abate, A. Hagfeldt, M. Gr-tzel, *Energy Environ. Sci.* 2016, 9, 1989 – 1997.
- [43] N. Marchal, W. Van Gompel, M. C. G8lvez-Rueda, K. Vandewal, K. Van Hecke, H. G. Boyen, B. Conings, R. Herckens, S. Maheshwari, L. Lutsen, C. Quarti, F. C. Grozema, D. Vanderzande, D. Beljonne, *Chem. Mater.* 2019, 31, 6880 – 6888.
- [44] H. Lin, C. Zhou, J. Neu, Y. Zhou, D. Han, S. Chen, M. Worku, M. Chaaban, S. Lee, E. Berkwits, T. Siegrist, M. H. Du, B. Ma, *Adv. Opt. Mater.* 2019, 7, 1801474
- [45] B. Saparov, D. B. Mitzi, *Chem. Rev.* 2016, 116, 4558 – 4596.
- [46] M. E. Kamminga, G. A. De Wijs, R. W. A. Havenith, G. R. Blake, T. T. M. Palstra, *Inorg. Chem.* 2017, 56, 8408 – 8414.
- [47] Y. Xue, J. Yuan, J. Liu, S. Li, *Nanomaterials* 2018, 8, 591.
- [48] P. Chen, Y. Bai, S. Wang, M. Lyu, J. H. Yun, L. Wang, *Adv. Funct. Mater.* 2018, 28, 1706923.

- [49] Y. Li, P. Li, Z. H. Lu, AIP Adv. 2018, 8, 035218.
- [50] Z. Zheng, X. Zhang, C. Neumann, D. Emmrich, A. Winter, H. Vieker, W. Liu, M. Lensen, A. Gölzh-user, A. Turchanin, Nanoscale 2015, 7, 13393 – 13397.
- [51] S. Chen, T. W. Goh, D. Sabba, J. Chua, N. Mathews, C. H. A. Huan, T. C. Sum, APL Mater. 2014, 2, 081512 – 7.
- [52] A. Dualeh, P. Gao, S. Il Seok, M. K. Nazeeruddin, M. Gr-tzel, Chem. Mater. 2014, 26, 6160 – 6164.
- [53] T. Chen, W. L. Chen, B. J. Foley, J. Lee, J. P. C. Ruff, J. Y. P. Ko, C. M. Brown, L. W. Harriger, D. Zhang, C. Park, M. Yoon, Y. M. Chang, J. J. Choi, S. H. Lee, Proc. Natl. Acad. Sci. USA 2017, 114, 7519 – 7524.
- [54] Y. Chen, H. T. Yi, X. Wu, R. Haroldson, Y. N. Gartstein, Y. I. Rodionov, K. S. Tikhonov, A. Zakhidov, X. Y. Zhu, V. Podzorov, Nat. Commun. 2016, 7, 12253.
- [55] C. H. Chu, C. W. Leung, Integr. Equations Oper. Theory 2001, 40, 391 – 402.
- [56] Y. Wang, T. Zhang, P. Zhang, D. Liu, L. Ji, H. Chen, Z. D. Chen, J. Wu, S. Li, Org. Electron. 2018, 57, 263 – 268.

## **Publications**

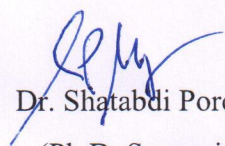
### **Thesis Work:**

1. **P. Kour**, M. C. Reddy, S. Pal, S. Sidhik, T. Das, P. Pandey, S. P. Mukherjee\*, S. Chakraborty\*, A. D. Mohite\*, and S. Ogale\*, An Organic-Inorganic Perovskitoid with Zwitterion Cysteamine Linker and Its Crystal-Crystal Transformation to Ruddlesden-Popper Phase, **Angew. Chem. Int. Ed.**, **60**, **18750**, **2021**.
2. **P. Kour** and S. P. Mukherjee\*, CsPbBr<sub>3</sub>/Cs<sub>4</sub>PbBr<sub>6</sub>Perovskite@COF Nanocomposites for Visible-Light-Driven Photocatalytic Application in Water, **J. Mater. Chem. A**, **9**, **6819**, **2021**.
3. **P. Kour** and S. P. Mukherjee\*, Low-Dimensional Mn- and Cu- based Organic-Inorganic Perovskites for Metal Ion Detection. {*Manuscript under preparation*}
4. **P. Kour** and S. P. Mukherjee\*, Invention Disclosure 2021-INV-057 dated 12-14-2022, CSIR no 2022-NF-0038, entitled "CsPbBr<sub>3</sub>/Cs<sub>4</sub>PbBr<sub>6</sub> Perovskite@COF Nanocomposites for Visible-Light-Driven Photocatalytic Applications", Provisional patent filing application no 202211009056 dated 18-02-2022. {**Patent**}

### **Out of thesis:**

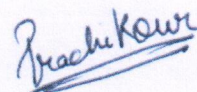
1. A. Biswas, A. Swarnkar, P. Pandey, **P. Kour**, S. Parmar, and S. Ogale\*, Dynamics of Photo-Generated Carriers across the Interface between CsPbBr<sub>3</sub> Nanocrystals and Au–

2. Ag Nanostructured Film, and Its Control via Ultrathin MgO Interface Layer, ACS Omega, 21, 11915, 2020.



Dr. Shatabdi Porel Mukherjee  
(Ph.D. Supervisor)

11/11/22



Ms. Prachi Kour  
(Student)

# Chapter 1

## Classification, Properties and Applications of Perovskites: A Brief Overview

This chapter highlights perovskite structures which have received significant attention in the field of materials science due to their unique properties and potential applications. There are various types of perovskite structures, including Oxide perovskites and Halide Perovskites (HPs) which are broadly divided into Inorganic Halide Perovskites (IHPs) and Hybrid organic-inorganic Perovskites (HOIPs). HOIPs have emerged as a promising class of materials for various applications such as metal ion detection, photocatalytic and photodetector applications. However, the structure of HOIPs poses several challenges, including environmental instability, lead toxicity, and solvent effects, limiting their applicability. Strategies such as low-dimensional HOIP structures, lead-free HOIPs, and nanocomposite formation have been proposed to enhance the applicability of HOIP systems. Further studies are required to overcome the challenges posed by the HOIP structure and maximize their potential applications.

Also this chapter includes, various characterization techniques that are used to study the properties of HOIPs, including X-ray Diffraction (XRD), Single Crystal XRD, UV-visible absorption spectroscopy, Photoluminescence (PL) spectroscopy, Transmission electron microscopy (TEM), Scanning electron microscopy (FESEM), X-Ray Photoelectron Spectroscopy (XPS), and Ultraviolet photoelectron spectroscopy (UPS). These techniques offer insights into the structural and electronic properties of materials at different length scales, providing valuable information for materials design and optimization. XRD and single crystal XRD are used to study the crystal structure of materials, while UV-visible absorption spectroscopy and PL spectroscopy are used to investigate their optical properties. TEM and FESEM provide information on the microstructure and morphology, while XPS and UPS offer insights into the surface properties of materials.

## 1.1. Introduction

The emergent need for the next generation of sustainable, clean, and renewable energy sources has attracted critical attention due to the exceptionally increasing power consumption in daily use. To overcome the growing demand for energy requirements, more powerful energy sources with excellent efficiency are needed <sup>1</sup>. Currently, around 80% of world energy requirements are generally fulfilled by non-renewable energy sources, like fossil fuels, natural gases, and coal which cause profound climate impact, i.e., emission of greenhouse gases, resulting in global warming, and several health-related issues <sup>2</sup>. The 21<sup>st</sup> century is the era of science and technology, where everything depends on energy while natural energy sources are limited and can't be reused. The demand for more efficient, powerful, and renewable energy sources are increasing day by day. The combustion of fuel cells, coal, and minerals produces a large amount of toxic and harmful CO<sub>2</sub>, CO, SO<sub>2</sub>, and NO<sub>2</sub> gasses, causing global warming and other considerable environmental problems <sup>3</sup>.

The name “perovskite” was given in honor of the Russian nobleman Count Lev Alexander Von Perovski (1792–1856), a passionate geologist during Tsar Nicolas's 1st era. In 1829, Gustav Rose discovered the first CaTiO<sub>3</sub> perovskite in the Ural Mountains (western Russia). Examples of insulating, FESEMiconducting, and superconducting perovskite structured materials are known. These materials are the archetypal systems for phase transitions with accessible cubic, tetragonal, orthorhombic, trigonal, and monoclinic polymorphs depending on the tilting and rotation of the BX<sub>3</sub> polyhedra in the lattice <sup>4,5</sup>. Reversible phase changes can be induced by various external stimuli, including temperature, pressure, and magnetic or electric fields. The HOIP solar cells have shown a promising improvement in Power Conversion Efficiency (PCE) from 3% to over 25.6% in a short time period, which reveals PSC as the most efficient emerging PV device technology <sup>6</sup>. Also, the PSC technology is considered one of the top 10 emerging technologies by the World Economic Forum because of their low production cost, lightweight, and, above all reason, the swift rise in PCE demonstrated for this technology. All these promising facts have made perovskite solar cell devices one of the potential competitors to other well-established PV technologies.

Perovskite is a family of minerals known for its simple arrangement and wide variety of cations. Inorganic perovskite-type oxides have many uses in fuel cells, catalysis, and electrochemical sensing <sup>7</sup>. Nanoperovskites have shown high electrocatalytic activity, low activation energy,

and high electron transfer kinetics in oxygen reduction and hydrogen evolution processes, with some perovskites having the potential as effective anodic catalysts for direct fuel cells<sup>8</sup>. Organometallic halide perovskites are also promising for photovoltaic (PV) solar cells with high efficiency and stability<sup>9</sup>. Perovskite-structured materials exhibit properties such as ferroelectricity, ferromagnetism, and enormous magnetoresistance, with a wide range of design possibilities for improving or controlling these properties<sup>10</sup>. This chapter provides an overview of perovskite materials and their structure-property connections, focusing on the recent interest in halide HOIP materials.

## 1.2. Perovskite Systems

Perovskite systems are broadly divided into the categories depicted in Figure 1.1. Since the beginning of the 20<sup>th</sup> century, this  $ABO_3$  system's intriguing physical characteristics and significant applications have been the subject of extensive research. The mineral perovskite  $CaTiO_3$  belongs to a broad family of compounds known as the structural family of perovskites<sup>11</sup>. The A cation occupies the 12-fold coordination site that is generated in the midst of the cube formed by eight of these  $BX_6^-$  octahedra in the ideal form of the cubic  $ABX_3$  perovskite crystal structure.

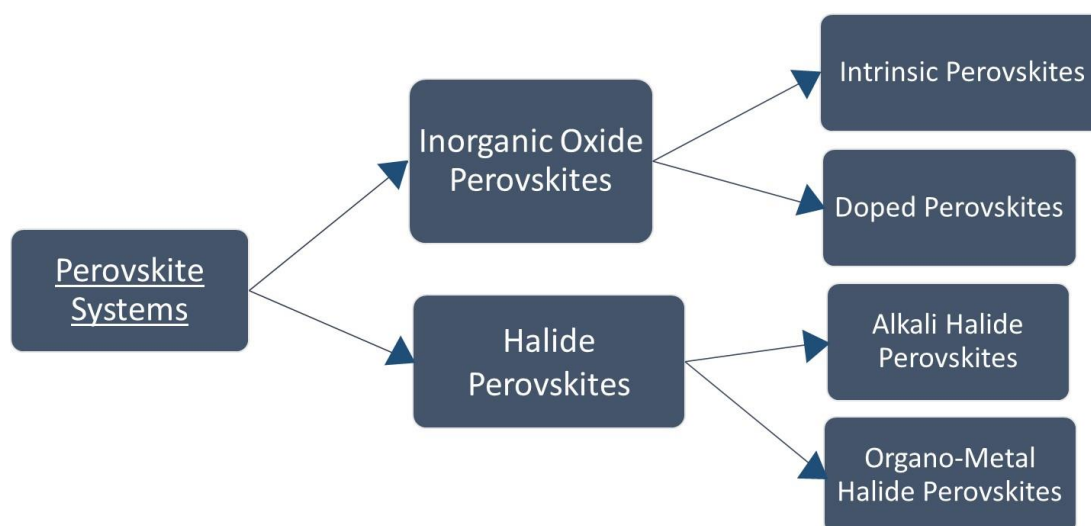


Figure 1.1: Broad categories of perovskite systems.

Perovskite itself is slightly deformed and does not frequently have the ideal cubic structure. The family of oxides known as perovskites has perhaps garnered far more attention from researchers. The wide range of characteristics demonstrated by compounds with this family of

crystal structures, as well as their adaptability to accommodate almost all of the periodic system's elements, are something that sparks curiosity in these <sup>12</sup>. Goldschmidt et al. carried out ground-breaking structural research on perovskites in the 1920s, which served as the foundation for future studies of the perovskite family of compounds <sup>13</sup>. Reduced symmetry in distorted perovskites is crucial for the magnetic and electric characteristics of these materials. Perovskites, especially the ferroelectric tetragonal form of BaTiO<sub>3</sub>, have significant industrial significance because of these characteristics <sup>14</sup>.

BaTiO<sub>3</sub> is the first perovskite to show photocurrent back in 1956 <sup>15</sup>. Later, LiNbO<sub>3</sub> was also reported to show such similar phenomenon. These materials are robust ferroelectric in nature<sup>12</sup>. It was found that the internal crystal field in these perovskites has something to do with the generation of photocurrent. Separation of photo-generated carriers is done by polarization-induced strong internal field. This mechanism can produce a voltage higher than the band gap, leading to high photo conversion efficiency (PCE), surpassing the theoretical limit of p-n junction solar cells. Several different oxide perovskites were researched for solar uses as a result of this groundbreaking discovery. But the outcome was not what was expected. The maximum PCE was less than 1%. Thus sooner it was understood that oxide perovskites are not a favorable option for PV applications. However, these oxide perovskites have been investigated for other device applications like electro-catalysis, and photocatalysis.

Even though the terms perovskite and perovskite structure are sometimes used interchangeably, real perovskite (the mineral) is composed of calcium, titanium, and oxygen in the form CaTiO<sub>3</sub>. In contrast, a perovskite structure is any material with the general form ABX<sub>3</sub> and the same crystallinity as perovskite (the mineral) <sup>16</sup>. A cubic unit cell with titanium atoms at the corners (orange), oxygen atoms at the midpoints of the edges (green and red), and a calcium atom in the middle (purple) is the simplest way to describe a perovskite structure as depicted in Figure 1.2. Halide perovskites, have halide anions in place of oxide ions and are represented by the chemical structure ABX<sub>3</sub>, are a different family of perovskites <sup>17</sup>. The A-site cations are often larger than the B-site cations and comparable in atomic size to the X-site anions in ideal perovskites, which have the general formula ABX<sub>3</sub>. Figure 1.3, provides a schematic picture of the ideal perovskite structure. The B-site cations are surrounded by six anions in octahedral coordination (BX<sub>6</sub>), in contrast to the twelve anions that surround the A-site cations. Four A-site cations and two B-site cations work together to coordinate the X-site anions.



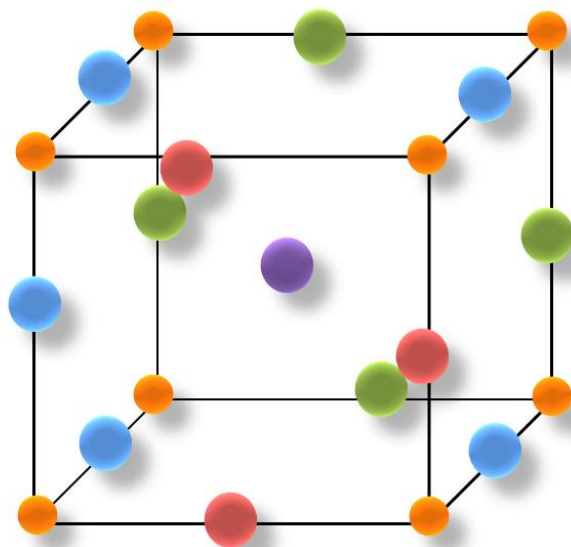


Figure 1.2: Cubic unit cell structure of perovskite (CaTiO<sub>3</sub>).

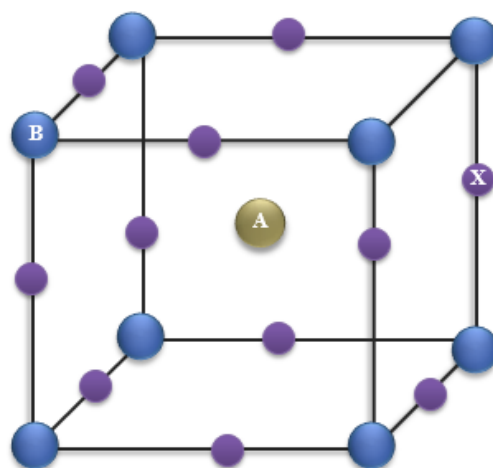


Figure 1.3: The ideal ABX<sub>3</sub> perovskite structure.

The A-site cation occupies the body center position, and the B-site cations are at the eight corners of the lattice (Figure 1.3). The B-site cation has 6-fold coordination with the X anions, thus forming a  $BX_6^-$  octahedron. In this way, the A-site cation is in 12-fold coordination with the X-site anions. A notable feature of the perovskites is that all the constituent ions (A, B, or X) can be replaced with other alternatives, and thus, a new compound can be formed as long as it satisfies the condition set by Goldschmidt tolerance factor as quantified below,

$$t = \frac{R_A + R_X}{\sqrt{2}(R_B + R_X)}$$

Where  $R_A$ ,  $R_B$ , and  $R_X$  are the ionic radius of the A-site cation, B-site cation, and X-site anion. A perfectly packed perovskite structure has  $t = 1$ . However, if  $t$  value lies anywhere between 0.7 to 1.1, the compound will have a fair chance of building a perovskite structure. Another parameter, the octahedral factor  $\left(m = R_B/R_X\right)$  measures deformation in the perovskite structure. Therefore, the ionic radius should be in order to form a structurally stable compound in Figure 1.4.

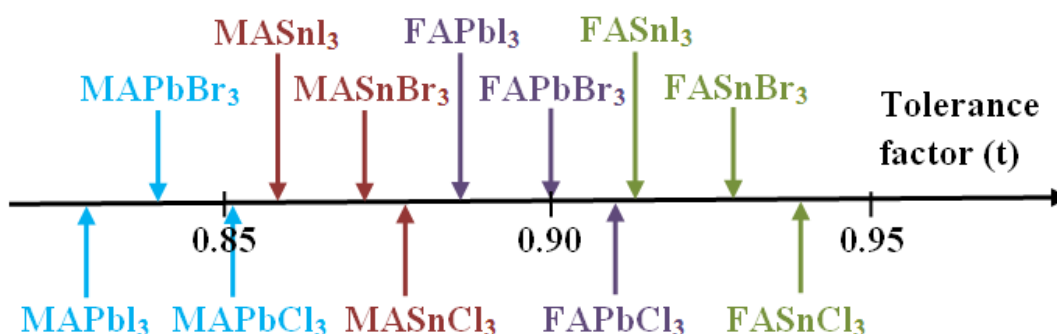


Figure 1.4: Tolerance factor of different perovskite materials.

### 1.3. Types of Perovskite Systems

#### 1.3.1 Oxide Perovskites

Around 90% of the elements in the periodic table can be doped in the perovskite structure by partial substitution at anionic or cationic sites, taking advantage of compositional and structural flexibility<sup>18</sup>. Perovskite oxides can easily be produced in a wide range of morphologies and particle sizes depending on the synthesis technique and operational conditions. Due to their adaptability in terms of composition, structure, and shape, perovskites exhibit extraordinary physicochemical capabilities due to their changeable electronic structure.

Oxide perovskites exhibit physical properties such as ferroelectric, dielectric, pyroelectric, and piezoelectric behaviors due to their anions and cations<sup>19</sup>. They have been extensively studied for novel capabilities like multi-ferroelectricity and superconductivity and their potential in electrocatalysis, photocatalysis, and PVs<sup>20, 21</sup> However, their low electrical conductivity

restricts their electronic applicability. The idealized oxide perovskite  $ABO_3$  has a cubic structure at high temperatures (100K), but undergoes octahedral rotations and transitions along  $([100], [010], [001])$  symmetry axes to lower-symmetry phases when the temperature drops. Glazer created a way to explain the octahedral tilting in perovskites in the 1970s<sup>5</sup>.

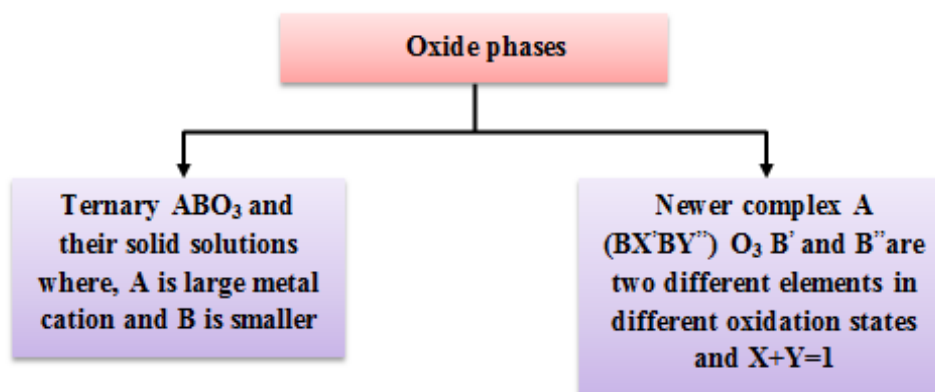


Figure 1.5: Flowchart of oxide perovskite structure types.

Double perovskites have two different types of cations occupying the A or B-site, as indicated by the formulas  $A'A''B_2O_6$  (double A-site) or  $A_2B'B''O_6$  (double B-site)<sup>22</sup> (Figure 1.5). B-site cations are primarily responsible for the physical characteristics of  $ABO_3$  perovskites while A-site cations typically serve as the electron donor to the  $[BO_6]^-$  framework, double perovskites often denote double B-site perovskites. By adjusting the composition, oxide-based perovskite materials can exhibit a wide range of electronic properties, including capacitive, ferroelectric, piezoelectric, metallic, superconductive, catalytic, and magnetic ones, under ambient settings. Ferroelectric and thermoelectric applications account for the majority of uses for perovskite minerals like  $BaTiO_3$  and  $SrSnO_3$ . Recently, rare earth ions were introduced to these materials as dopants to produce an entirely novel type of phosphor material, as shown in Table 1.1.

**Table 1.1:** For single- and double-oxide perovskites, there are four typical phases.<sup>5</sup>

Glazer notation	Single perovskite		Double perovskite	
	Space group	Frequency	Space group	Frequency
$a^-a^-b^-$	$Pnma$	119	$P2_1/n$	168
$a^0a^0a^0$	$Pm\bar{3}a$	21	$Fm\bar{3}a$	94

$a^0 a^0 c^-$	$14/mcm$	9	$14/m$	27
$a^- a^- a^-$	$R\bar{3}c$	24	$R\bar{3}$	15

Oxide perovskites can be broadly divided into two categories as follows:

- a) **Intrinsic:** The catalytic property of perovskite oxides is said to be intrinsically modulated through inductive alteration of oxygen with the method of non-stoichiometric for the purpose of generating oxygen deficient structures<sup>23</sup>. Oxygen vacancies in complex metal oxides, specifically in perovskites, are demonstrated to significantly enhance the electrocatalytic activities due to facilitating a degree of control in the material's intrinsic properties.
- b) **Doped:** The A/B/O sites in these materials can all be doped with different elements without changing the lattice's fundamental makeup, allowing for the creation of a variety of materials with adjustable and unique properties. Using the properties of dopants, we can modify the conductivity of a FESEMiconductor. FESEMiconductor conductivity may be significantly boosted by adding a small number of suitable alternative elements.<sup>24</sup> It is necessary to understand the dopant integration process, dopant diffusivity, and activation limitations in order to assess a certain dopant's suitability for a particular application.

### 1.3.2. Halide Perovskites

Inorganic Halide Perovskites (IHPs) and HOIPs are the two primary forms of this new generation of FESEMiconductor materials<sup>25</sup>. HPs are becoming a more stable alternative to HOIPs due to their inherent/thermal stability, even though HOIPs have received a lot of attention in applications to various optoelectronics, such as solar cells, light-emitting devices, radiation/photodetectors, scintillators, transistors, and memristors<sup>26</sup>. Halide-based perovskite has the same chemical formula as oxide-based perovskite,  $ABX_3$ , where  $X = I^-$ ,  $Cl^-$ , and  $Br^-$  stands for divalent (inorganic) cation on the fundamentals of A cation of  $ABX_3$  structure (Figure 1.6).

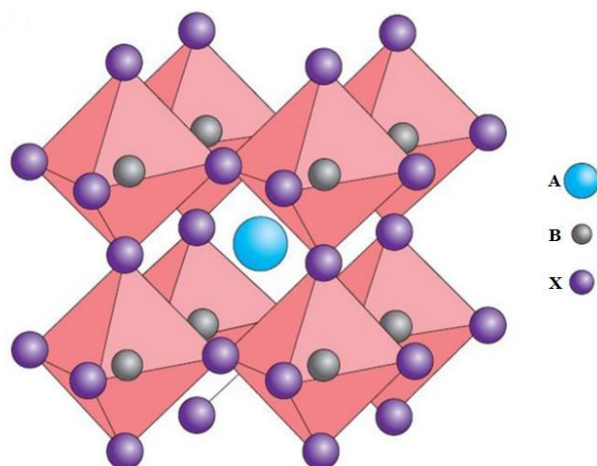


Figure 1.6: Structure of HPs showing the position of the A, B site cations and the X halide.

With recent advancements in a new class of materials known as HOIPs, the development of optoelectronic devices has entered a new age. Due to their unique features, such as high carrier mobility, tuneable bandgap (BG), and extended diffusion length, these materials have emerged as market-competitive optoelectronic materials for PV device applications <sup>27</sup>.

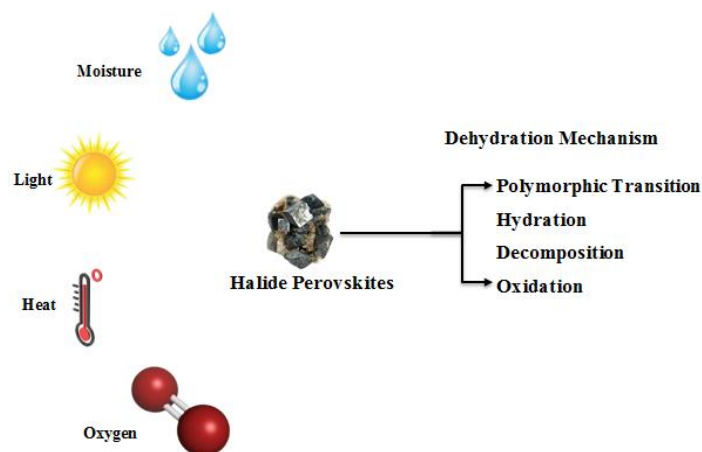


Figure 1.7: Illustration of the mechanisms by which halide perovskites degrade under critical environmental conditions (moisture, light, heat, and oxygen).

Furthermore, simple and low-cost device manufacturing processes with high PCE make HOIPs extremely attractive materials for various PV applications. The first application of HOIP in a PV device was in 2006 when Miyasaka and colleagues utilized  $\text{CH}_3\text{NH}_3\text{PbBr}_3$  as a sensitizer in dye-sensitized solar cells <sup>28</sup>. Following that, HOIPs have been widely investigated as a layer of PV absorber material in PV cells with PCE that have quickly grown over the years by exceeding 24% <sup>29</sup>.

The breakdown processes for all varieties of halide perovskites, which comprise polymorphic transition, hydration, decomposition, and oxidation, have been succinctly outlined (Figure 1.7)<sup>24</sup>. IHPs are devoid of hygroscopic organic cations, in contrast to HOIPs, hence their hydration may not take place regularly. By changing the choice of the B-site cation (usually Pb and/or Sn), which presents thousands of different candidate material options since we are theoretically able to modify the choices of A, B, and X, three choices for the A-site, cation – methyl ammonium (MA), cesium (Cs), formamidinium (FA), and three options of the anion [chloride (Cl), bromide (Br), and iodide (I)]<sup>31</sup>.

### (a) Inorganic halide perovskites

In this kind of perovskite material, A belongs to the 1<sup>st</sup> group of the periodic table (alkaline metals), such as Cs<sup>+</sup>, Rb<sup>+</sup>, K<sup>+</sup>, Li<sup>+</sup>, etc. Inorganic halide perovskites have similar properties as like organic-inorganic perovskite materials. Still, the thermal stability of inorganic perovskite is higher than the organic-inorganic perovskite e.g. CsPI<sub>3</sub>, CsPbBr<sub>3</sub>, CsSnI<sub>3</sub>, and CsPbI<sub>3-x</sub>Br<sub>x</sub>, which have well known inorganic perovskite materials for perovskite quantum dot fabrication<sup>32</sup>. Among these, the stability of CsPbI<sub>3</sub> perovskite materials in ambient conditions has been challenging. The size of Cs<sup>+</sup> is smaller than MA<sup>+</sup>, which induces octahedral tilting and subsequently a lower symmetry<sup>33</sup>. This is the prime factor for CsPbI<sub>3</sub> to possess a higher BG (1.73 eV) over the CH<sub>3</sub>NH<sub>3</sub>PbI<sub>3</sub> (1.57 eV) or, popularly MAPbI<sub>3</sub>.

Regardless of the outstanding optoelectronic qualities of halide perovskites, their poor stability is a significant barrier to their industrialization. To increase the thermal stability of the perovskite layers, there is a significant push to switch from organic A-site cations like methylammonium and formamidinium to Cs<sup>34</sup>. Although having very strong optoelectronic characteristics and device performance, all-inorganic lead-halide perovskites based on Cs still need to catch up to those of perovskites that use organic cations. Optoelectronics in inorganic halide perovskites has recently been given a lot of attention. The prevalent HOIPs, which are frequently employed in optoelectronic devices, including solar cells and light-emitting devices, are projected to outperform HPs in terms of chemical stability<sup>35</sup>.

Due to their exceptional photophysical characteristics and simple solution production procedures, all-inorganic metal halide perovskites have attracted enormous interest as long-term stable materials for highly efficient solar applications<sup>36</sup>. Inorganic perovskite solar cells

are receiving more attention. They are being developed quickly thanks to the recent creation of high-quality inorganic perovskite films and the stabilization of the three-dimensional perovskite phase<sup>37</sup>. The use of in-situ phase transition events characterization and visualization to link significant (photo)physical characteristics to phase diagrams is a primary research subject. For instance, *in-situ* optical techniques have revealed the underlying dynamics and mechanisms of anion exchange processes, and *in-situ* synchrotron-based XRD has helped us understand the microstructural variations of strain-stabilized thin films. As a result, it is demonstrated that it is possible to precisely control the perovskite phase and composition in nanocrystals as well as key optoelectronic properties. The small inorganic cations can be adopted at the A site to stabilize the perovskite lattice. It opens the avenue for achieving the inorganic halide perovskites with good stabilities because they are compatible with the smaller sizes of Bi<sup>3+</sup>/Sb<sup>3+</sup> than Pb<sup>2+</sup>.

#### (b) Hybrid Organic-Inorganic Halide Perovskites

Crystals with the structural formula ABX<sub>3</sub>, where A, B, and X are organic and inorganic ions respectively, are known as HOIPs. Although they have been around for a while, HOIPs have only recently become recognized as highly promising FESEMiconducting materials for solar energy applications<sup>38</sup>. For instance, after just over six years of PV research, the power conversion efficiency of HOIP-based solar cells has crossed the 20% threshold, which is an exceptional accomplishment for a material that can be processed in a solution. Therefore, it is crucial to identify the physical and chemical processes that support or constrains these astounding PV efficiencies. The fast-rising performance of methylammonium lead halide perovskite solar cells, mostly attributable to advancements in film morphology, continues to excite the scientific community<sup>39</sup>. Control of the crystal morphology is the following stage in this development, which necessitates a deeper conceptual comprehension of crystal growth. In 1978, Weber and Naturforsch employed the organic cation methylammonium (CH<sub>3</sub>NH<sub>3</sub><sup>+</sup> or MA<sup>+</sup>) for the first time in halide perovskites. For low-cost and high-performance solar cells, HOIPs, like methylammonium lead iodide, have received a lot of interest. A fundamental comprehension of the relationship between solution chemistry and crystallization pathways is necessary to control HOIP thin-film quality and morphology, which is crucial to achieving constant solar-cell efficiencies<sup>40</sup>.

In the structure of HOIPs, an inorganic halide  $X^-$  (i.e.,  $I^-$ ,  $Br^-$ , and  $Cl^-$ ) is combined with an organic cation  $A^+$  ( $MA^+$ ,  $EA^+$  or  $CH_3CH_2NH_3^+$ ,  $FA^+$  or  $CH_5N_2^+$ , etc.) and a divalent metal cation  $B_2^+$  (i.e.  $Pb^{2+}$ ,  $Sn^{2+}$ , and  $Ge^{2+}$ ) as the term halide indicates. The XRD study of the crystal structure of these HOIPs revealed cubic, tetragonal, and orthorhombic symmetry (Figure 1.8) with corresponding space groups  $pm\bar{3}m$ ,  $I4/mcm$ , and  $Pnam$ <sup>41</sup>.

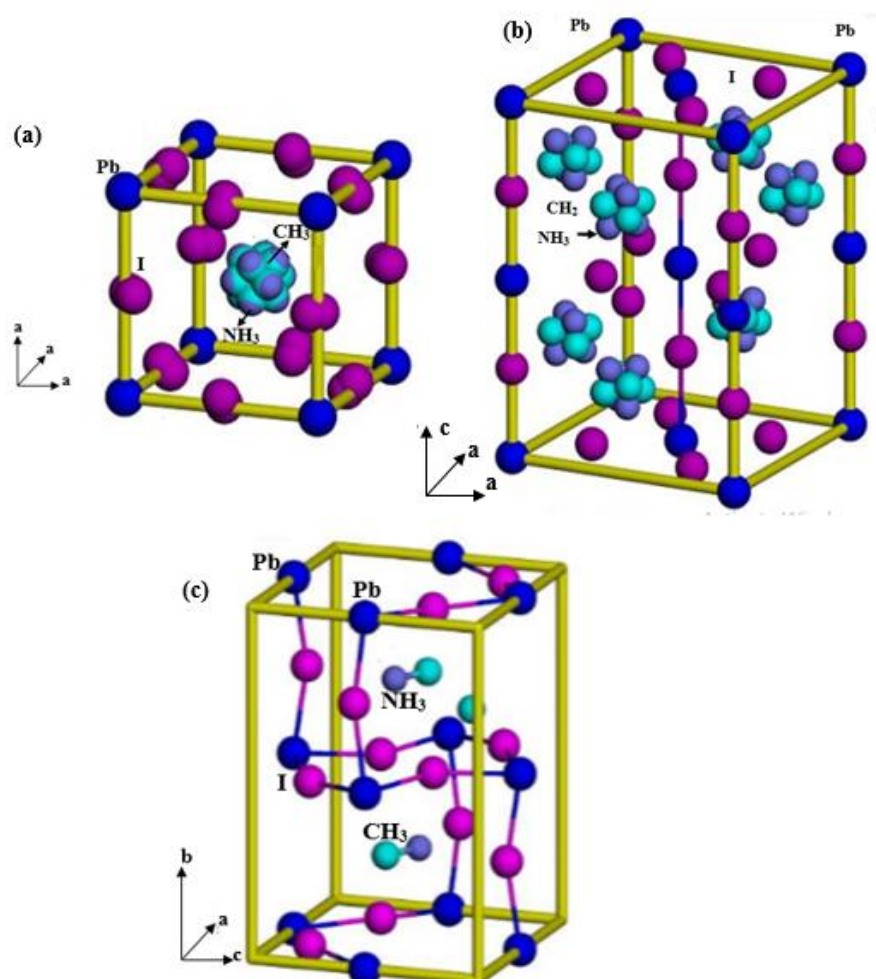


Figure 1.8: (a) Cubic, (b) tetragonal, and (c) orthorhombic structural model of perovskite  $MAPbI_3$ .

Ideally, the HOIPS are expected to be crystallized in cubic symmetry having  $pm\bar{3}m$  space group, and 12-fold and 6-fold coordination of the  $A^+$  and  $B^{2+}$ , respectively. A material must have cubic symmetry to be used in PV devices with the best electrical characteristics<sup>42</sup>. Deviations from cubic symmetry are caused by several variables, including ion size and heat or oxidation of a material in the surroundings, which are listed as following:

- **Effect of Lattice site: A**



The metal-halide bond (B-X bond) affects the electronic properties of HOIPs. Numerous investigations have shown that the organic cation (A-site) has no direct impact on the electronic properties of HOIPs. However, its size affects crystal symmetry due to a distortion in the B-X bond, which alters the material's electronic properties<sup>43</sup>. Three-dimensional crystal symmetry can be obtained for a monovalent cation at lattice site A by keeping the radius  $R_A$  small enough, so that  $t$  is less than unity. As long as it is less than unity, increasing the value of  $R_A$  by placing an appropriate ion at site A increases tolerance factor  $t$  and decreases in BG due to enhanced packing symmetry.

Initially, researchers explored Caesium ion  $\text{Cs}^+$  at lattice site A for PV applications. Because of the octahedral tilting and poorer symmetry produced by the smaller size of  $\text{Cs}^+$ , a larger BG of 1.73 eV has been reported for the material  $\text{CsPbI}_3$ <sup>44</sup>. Following that, the methylammonium ion ( $\text{MA}^+$ ) with an ionic radius of 0.18 nm has been intensively investigated at lattice site A in HOIPs, and devices based on this cation have attained PCE more than 23%. However, due to the tiny size of  $\text{MA}^+$ , the material  $\text{MAPbI}_3$  was discovered to be crystallized with tetragonal symmetry rather than cubic, producing a BG in the 1.51- 1.55 eV range. In this respect, larger Formamidinium ( $\text{FA}^+$ ) ion in  $\text{FAPbI}_3$  material produces a BG in the range of 1.43 eV to 1.48 eV, which is better suited for PV applications<sup>45</sup>. Even though  $\text{FAPbI}_3$  has a nearly cubic crystal structure, a trigonal structure has been found due to the off-center location of the  $\text{FA}^+$  ion within the octahedron produced by distorted FA-I ion interaction. Pellet and colleagues were the first to obtain a PCE of 14.9% by changing  $x$  in a mixed A-cation  $(\text{MA})_x(\text{FA})_{1-x}\text{PbI}_3$ -based devices<sup>45</sup>.

Thus, substituting  $\text{MA}^+$  with a bigger cation is expected to result in a narrower BG due to increased symmetry, allowing for better light harvesting across the spectrum<sup>1</sup>. As a result, we must search for large alternative cations at site A such that the  $t$ -value remains close to unity.

#### ▪ **Effect of Lattice site: B**

The cation dictates the electronic characteristics of HOIPS at site B, which is usually occupied by metal ions in the  $2^+$  oxidation state from the group IVA metals ( $\text{Pb}^{2+}$ ,  $\text{Sn}^{2+}$ , and  $\text{Ge}^{2+}$ ). Lead ( $\text{Pb}^{2+}$ ) has been widely used in PV devices due to its superior performance and stability<sup>46</sup>. As the cation at site B is occupied by metal from the group IVA metals ranging from Pb to Ge, the stability and BG of the produced perovskite material diminish. This may be attributed to

reducing inert electron pair effects and enhanced electronegativity or covalent character<sup>47</sup>. As a result,  $\text{MASnX}_3$  has a narrower BG in the 1.2 eV to 1.4 eV range than  $\text{MAPbX}_3$  in the 1.6 eV to 1.8 eV range. Thus, while  $\text{MASnX}_3$  is expected to produce significantly more photocurrent than  $\text{MAPbX}_3$ , the former's stability is a significant barrier to its uses in PV devices.

- **Effect of Lattice site: X**

The most efficient way to modify the optoelectronic characteristics of  $\text{ABX}_3$  type HOIPs is to change the halide anion at lattice position X. As one replaces the halide anion at site X in the material from F to I, the BG of the produced material structure reduces<sup>46</sup>. This can be attributed to an increase in the covalent nature of the B-X bond caused by a reduction in the electronegativity of the halide anion, which has a better match with the B cation.

#### 1.4. Properties of HOIPs

The distinctive chemical changes caused perovskite materials to exhibit various intriguing characteristics, including non-stoichiometry of the anions and/or cations, the mixed electronic structure, distortion of the cation configuration, and mixed valency. The various properties of HOIPs are listed in Figure 1.9.

The ability of perovskite to synthesize multicomponent materials by partially substituting cations in positions A and B results in a variety of complex types with peculiar properties, including dielectric, optical, ferroelectric, superconducting, piezoelectric, multiferroitic, and catalytic properties<sup>16</sup>. Strong optical absorption, BG tuning, long diffusion length, high charge carrier mobility, ambipolar charge transport, and high defect tolerance are all characteristics of organic-inorganic perovskite materials<sup>48</sup>. The substance's potent light-absorbing qualities make it perfect for solar cell technology. On the other hand, light-emitting devices are appropriate due to band tuning features and a broad spectrum of visible light emissions with small emission bandwidth (FWHM)<sup>49</sup>. The direct BG and minimally disordered materials are indicated by the sharp optical band edge of organic-inorganic perovskite materials<sup>50</sup>. Notably, dielectric materials show linear polarisation behavior as a function of the applied field,. HOIPs have demonstrated applicability as pyroelectric materials display spontaneous polarisation. Still, when an electric field is used, the polarisation cannot be reversed, and when mechanically

pressured, piezoelectric materials either produce an electrical charge or deform mechanically when an electric field is applied <sup>51</sup>.

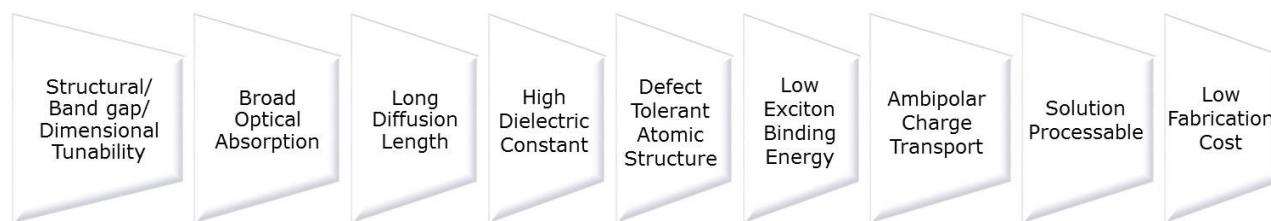


Figure 1.9: Key distinguishing properties of HOIPs <sup>52</sup>.

These HOIPs band gaps range from 1.48 eV (FAPbI<sub>3</sub>), 1.55 eV (MAPbI<sub>3</sub>), 2.23 eV (FAPbBr<sub>3</sub>), 2.35 eV (MAPbBr<sub>3</sub>), and more than 3 eV (MAPbCl<sub>3</sub>). The band gaps of the iodide perovskites are close to the shockley-queisser limit of 1.1–1.5 eV, which is ideal for single-junction solar systems. Due to the halide p orbitals' significant contribution to the optical transition, the inorganic framework predominately controls the BG of HOIPs <sup>53</sup>. Yet, when the A-site cations are considered, neither the hydrogen 1s orbitals nor the carbon and nitrogen 2p orbitals have a significant impact on the density of states close to the Fermi level.

### 1.5. Applications of HOIPs

Optoelectronic innovations, including display, solar, computing, sensor, and memory technologies, are revolutionizing human society. Such technologies have been identified as essential need for a better future. Scientists are working to create new concepts, materials, and technologies that facilitate daily convenience using renewable energy sources to various FESEMIconductor materials to satisfy this demand. For numerous optoelectronic applications, including LEDs, solar cells, photodetectors, field-effective transistors, memory devices, water splitting, switching devices, gas detectors, etc., lead halide perovskites have lately come to light as a potential luminous hybrid material <sup>54</sup>.

The astounding improvement in the performance of perovskite-based solar cells has significantly rekindled interest in HOIPs. These materials, which exhibit outstanding qualities, could transform the renewable energy sector by producing inexpensive, effective solar cells that can compete with silicon PV technology <sup>55</sup>. As reported by KRICT/UNIST in November 2016, organic-inorganic metal halide perovskites have lately demonstrated considerable potential for use in solar cells with excitingly high performances and a current NREL-certified

record efficiency of 22.1%<sup>56</sup>. Due to their inexpensive composition, affordable fabrication processes, and capacity to serve as an effective light-absorbing layer for both organic and inorganic PV applications, perovskite materials are now being studied.

The recent creation of the HOIPs heralds the start of a new era in optoelectronic technologies. Materials containing CsPbX<sub>3</sub> are well suited for optoelectronic applications because they have various benefits, such as a higher melting point (>500 °C), greater thermal stability, and more excellent stability against photobleaching<sup>57</sup>. The remarkable optoelectronic features of HOIPs, including their high absorption coefficient, long carrier lifetimes, and extremely high defect tolerance that enables simple and affordable thin-layer production, have attracted attention in the last ten years. A complex perovskite structure based on a molecular scale composite of organic and inorganic cations opens new avenues for scientific investigation and technical application. Organic molecules interact through weaker bondings than inorganic perovskites, such as hydrogen and van der Waals interaction, which results in more structural diversity, a high degree of polarizability, and reduced weight, and many other intriguing optical properties<sup>58</sup>.

### 1.5.1. Metal Ion Detection Applications

HOIPs has emerged as a promising class of materials for metal ion detection applications due to their unique optical and electronic properties.

The metal ion detection of HOIPs stem from the fact that they are susceptible to changes in their local electronic and crystal structure, in response to the presence of metal ions. Specifically, when metal ions are introduced into the perovskite lattice, they can alter the perovskite's charge distribution and lattice parameters, leading to changes in its optical and electronic properties<sup>59</sup>. These changes can be exploited for metal ion detection by using various sensing techniques, such as fluorescence, absorption, an electrical conductivity measurements.

One of the most commonly used sensing techniques for metal ion detection using HOIPs is fluorescence spectroscopy. Fluorescence occurs when a molecule or material absorbs light at a specific wavelength and emits longer wavelength. In the case of HOIPs, the metal ions can quench or enhance the fluorescence emission, depending on their concentration and the specific perovskite composition<sup>60</sup>. This change in fluorescence intensity can be used as a quantitative measure of the metal ion concentration. Another sensing technique that has been used with

HOIPs is absorption spectroscopy. Absorption spectroscopy measures the amount of light absorbed by a material at a specific wavelength. For detections, the metal ions can cause a shift in the absorption spectra of the perovskite, which can be used as a qualitative or quantitative measure of the metal ion concentration.

HOIPs have also been used for metal ion detection through their electrical conductivity properties. When metal ions are introduced into the perovskite lattice, they can alter the charge carrier concentration and mobility, leading to changes in the material's electrical conductivity<sup>61</sup>. This change in conductivity can be used as a quantitative measure of the metal ion concentration.

Thus, HOIPs have shown great potential for metal ion detection applications due to their unique optical and These materials' metal ion detection properties low cost. The metal ion detection properties of these materials can be exploited through various sensing techniques, such as fluorescence, absorption, and conductivity measurements<sup>62</sup>. With further research and development, HOIPs have the potential to be used for a wide range of metal ion sensing applications, including environmental monitoring, biomedical diagnostics, and industrial process control.

▪ **Related factors and parameters:**

Metal ion detection involves identifying and quantifying various metal ions in a given sample. Detecting metal ions is an essential process in several fields, including environmental monitoring, clinical diagnostics, and industrial analysis. Here are some of the factors and parameters related to metal ion detection along with their relevant formulas<sup>63</sup>:

1. Concentration of the metal ion: The concentration of the metal ion is one of the most critical factors in metal ion detection. The formula to calculate the concentration of a metal ion in a solution is:

$$\text{Concentration (C)} = \text{Mass of solute (m)} / \text{Volume of solution (V)}$$

2. Sensitivity: The sensitivity of a metal ion detector refers to its ability to detect low concentrations of metal ions. Sensitivity is calculated as the limit of detection (LOD) or the limit of quantification (LOQ), which are the minimum concentrations of the metal ion that can be detected and quantified, respectively.

3. **Selectivity:** Selectivity refers to the ability of a detector to distinguish between different metal ions. The selectivity of a metal ion detector can be calculated using the selectivity coefficient (K), which is defined as the ratio of the equilibrium constants for the metal ion of interest and an interfering ion:

$$\text{Selectivity coefficient (K)} = K(\text{Metal ion of interest}) / K(\text{Interfering ion})$$

4. **Response time:** The response time of a detector is the time it takes to produce a measurable signal after exposure to a metal ion. The response time is an important factor in real-time monitoring applications, and it can be calculated by measuring the time required for the signal to reach a certain percentage of its maximum value.
5. **Stability:** Stability refers to the ability of a detector to maintain its performance over time. The stability of a metal ion detector can be evaluated by measuring its response over a period of time or by performing calibration checks at regular intervals.
6. **Detection limit:** The detection limit is the minimum concentration of a metal ion that detector detector can detect. It is usually defined as the concentration that produces a signal equal to three times the standard deviation of the blank signal.
7. **Signal-to-noise ratio:** The signal-to-noise ratio (SNR) measures the quality of the signal produced by a detector. It is calculated as the signal's ratio to the noise's standard deviation. A high SNR indicates a robust and reliable signal.

Some commonly used metal ion detection methods include colorimetry, spectroscopy, electrochemistry, and mass spectrometry. The specific factors and parameters relevant to each method may vary.

### 1.5.2. Photocatalytic Applications

IHPs and HOIPs have emerged as promising photocatalytic materials due to their unique properties, such as intense light absorption, high charge carrier mobility, and long carrier lifetimes. One of the most significant applications of these materials is in the field of solar-driven water splitting to produce clean and renewable hydrogen fuel. HPs have been reported to show efficient photocatalytic water-splitting activity under visible light, with hydrogen evolution being the primary reaction product <sup>64</sup>.

In addition to the water splitting, halide perovskites have also been effective in other photocatalytic applications such as oxygen evolution and organic pollutant degradation. 0D and 2D halide perovskites have been studied for these applications and have shown promising results due to their unique electronic and structural properties<sup>65</sup>. The photocatalytic activity of HOIPs arises from their ability to generate electron-hole pairs when exposed to light. These electron-hole pairs can then react with organic pollutants and degrade them into harmless products.

The mechanism of photocatalytic activity is complex and involves several processes, including charge separation, adsorption, and reaction. Charge separation occurs when the perovskite absorbs a photon, and an electron is excited from the valence band to the conduction band, leaving a hole behind in the valence band<sup>66</sup>. The electron and hole can then migrate to the surface of the perovskite, where they can participate in reactions with adsorbed organic pollutants. Adsorption of organic pollutants onto the surface of the perovskite is critical for photocatalytic activity<sup>67</sup>. HOIPs produce electron-hole pairs when exposed to sunlight or other light sources. These electron-hole pairs can then interact with the attached complex organic moieties to cause their breakdown or conversion into less dangerous chemicals. The perovskite surface serves as a catalyst for this reaction, which is referred to as photocatalysis.

The type of organic pollutant, its concentration and the perovskite composition can all affect the adsorption process. The reaction between the photocatalytically generated electron-hole pairs and the organic pollutants can occur via several mechanisms, such as oxidative degradation, reduction, or hydrolysis etc.<sup>68</sup>. The specific mechanism depends on the type of organic pollutant and the composition of the perovskite<sup>69</sup>.

For example, it has been reported that HOIPs with lead (Pb) can effectively degrade dyes and antibiotics, while perovskites with tin (Sn) have been shown to degrade pesticides and phenols<sup>70</sup>. The degradation products of organic pollutants are typically less toxic and more biodegradable than the parent compounds. Therefore, HOIPs can be an effective tool for removing organic contaminants from water.

A recent study reported that  $\text{Cs}_4\text{PbBr}_6$ , a 0D halide perovskite, exhibited high photocatalytic activity for hydrogen evolution under visible light, with a hydrogen evolution rate of 13.5  $\mu\text{mol/h}$ , which is among the highest reported for halide perovskites<sup>71</sup>. Meanwhile, 2D halide

perovskites such as CsPbBr<sub>3</sub> have been used for organic pollutant degradation and have shown efficient photocatalytic activity for the degradation of rhodamine B and methylene blue under visible light <sup>72</sup>.

Overall, the unique properties of HOIPs make them promising for various photocatalytic applications, including water splitting, hydrogen evolution, oxygen evolution, and organic pollutant degradation. With continued research and development, these materials have the potential to revolutionize the field of renewable energy and environmental remediation.

Here are some of the factors and parameters related to photocatalytic properties <sup>73</sup>:

1. Catalyst Material: The choice of catalyst material is critical for photocatalysis. The most commonly used catalysts are FESEMiconductors such as titanium dioxide (TiO<sub>2</sub>), zinc oxide (ZnO), and tungsten oxide (WO<sub>3</sub>). Other materials such as carbon nitride (C<sub>3</sub>N<sub>4</sub>), iron oxide (Fe<sub>3</sub>O<sub>4</sub>), and tantalum oxide have also been studied.
2. Light Source: Photocatalysis relies on the energy provided by light to drive chemical reactions. Therefore, the type, intensity, and wavelength of the light source can significantly affect the efficiency of photocatalysis. The most commonly used light sources are UV lamps, but visible light sources, such as light-emitting diodes (LEDs), have gained attention due to their energy efficiency and lower cost.
3. pH: The pH of the solution can affect the surface charge of the catalyst, which, in turn, affects the reaction rate. Depending on the catalyst, a slightly acidic or neutral pH is usually preferred for photocatalysis.
4. Temperature: Temperature can affect the reaction rate in photocatalysis, with higher temperatures generally leading to higher reaction rates. However, excessively high temperatures can cause catalyst degradation.
5. Catalyst Loading: The amount of catalyst used in photocatalysis can affect the reaction rate. A higher catalyst loading can result in higher reaction rates, but increasing the amount of catalyst may not improve the reaction rate at a certain point.
6. Binding affinity: In some cases, dyes are used as indicators of a specific biomolecule or chemical species. In these cases, the binding affinity of the dye to the target molecule or



species is an important factor. The binding affinity can be described using equilibrium constants such as dissociation constants ( $K_d$ ).

7. **Rate of reaction:** The rate of reaction is the change in concentration of a reactant or product per unit of time. It can be expressed as:

Rate =  $\Delta C/\Delta t$ , where  $\Delta C$  is the change in concentration of a reactant or product and  $\Delta t$  is the time interval over which the change occurs.

8. **Quantum Yield:** Quantum yield is a measure of the efficiency of photocatalysis, indicating the number of reactant molecules converted to products per photon absorbed by the catalyst. It can be expressed as:

$\Phi = (\text{Number of molecules of reactant converted to product})/(\text{Number of photons absorbed by catalyst})$

9. **Langmuir-Hinshelwood model:** The Langmuir-Hinshelwood model is a widely used kinetic model in photocatalysis, which relates the rate of reaction to the concentration of reactants and catalysts. It can be expressed as:

$r = k [A] [B]/(1 + kK [A])$ , where  $r$  is the rate of reaction,  $k$  is the rate constant,  $[A]$  and  $[B]$  are the concentrations of reactants, and  $K$  is the adsorption constant.

### 1.5.3. Photodetector Application

HOIPs have emerged as a promising material for photodetector applications due to their excellent optoelectronic properties, including higher light absorption coefficient, long carrier lifetime, high carrier mobility, and tunable BG. These properties make them suitable for high-performance optoelectronic devices, such as photodetectors, solar cells, and light-emitting diodes <sup>74</sup>.

Photodetectors are devices that convert light energy into electrical signals. The working mechanism of a photodetector involves the absorption of light, which generates electron-hole pairs, followed by the separation of these charge carriers by an electric field, leading to a measurable electrical signal <sup>75</sup>. HOIPs have shown significant potential in photodetector applications due to their high charge carrier mobility, high photoresponsivity, and low noise, as discussed previously in section 1.3.

The photoresponse of HOIPs-based photodetectors can be improved by optimizing their device architecture and using suitable electron and hole transport layers. Various strategies have been employed to enhance the performance of HOIP-based photodetectors, such as surface passivation, interface engineering, and the incorporation of nanostructures. For example, using an organic interlayer between the perovskite and the metal electrode can improve the photodetector's performance, by reducing the charge recombination rate and enhancing the charge extraction efficiency <sup>76</sup>.

Furthermore, the performance of HOIP-based photodetectors can also be improved by optimizing the fabrication process, such as controlling the film thickness, grain size, and thermal annealing. These optimizations can improve the crystallinity and reduce the defect density in the perovskite layer, resulting in higher device performance. Recent studies have reported the use of HOIPs in various photodetector applications, including visible and near-infrared photodetection, ultrafast photodetection, and photodetection with high sensitivity and stability. For example, Huang et al. reported a hybrid perovskite-based photodetector with a high responsivity of  $5.5 \times 10^4$  A/W and a detectivity of  $1.1 \times 10^{13}$  Jones in the near-infrared region <sup>77</sup>. Zhang et al. demonstrated a hybrid perovskite photodetector with an ultrafast response time of 41 ps and a high on/off ratio of  $1.9 \times 10^5$  <sup>78</sup>.

Several studies have also reported the use of HOIPS in flexible and wearable photodetector applications. For example, Lee et al. reported a flexible perovskite-based photodetector with a high photoresponsivity of 2.47 A/W, and Liu et al. demonstrated a wearable photodetector with a high sensitivity of 0.43 A/W <sup>79,80</sup>.

Thus, HOIPs have shown great potential in photodetector applications due to their high charge carrier mobility, high photoresponsivity, and low noise. With further optimization of the device architecture and fabrication process, HOIPs could be used to develop high-performance photodetectors with various applications, including ultrafast, flexible, wearable, high-sensitivity and stability photodetection.

Here are some of the factors and parameters related to photodetection <sup>81</sup>:

1. **Responsivity (R):** Responsivity measures the conversion efficiency of incident photons into electric current. It is defined as the ratio of the generated photocurrent ( $I_{ph}$ ) to the incident optical power ( $P_{in}$ ) and is given by  $R = I_{ph}/P_{in}$ .

2. Quantum Efficiency (QE): QE is a measure of the probability of generating an electron-hole pair per incident photon. It is defined as the ratio of the number of charge carriers generated by the detector to the number of incident photons. It is given by  $QE = (\text{number of electron-hole pairs generated per incident photon}) / (\text{number of incident photons})$ .
3. Noise Equivalent Power (NEP): NEP measures the minimum detectable signal of a detector. It is defined as the input optical power that generates a signal-to-noise ratio of 1 and is given by  $NEP = (\text{noise power spectral density}) / (\text{responsivity})$ .
4. Dark Current ( $I_d$ ): Dark current is the current generated without incident light. It is caused by thermally generated carriers and can be reduced by cooling the device. The dark current is given by  $I_d = A \cdot (I_0/q) \cdot (\exp(qV/kT) - 1)$ , where  $A$  is the junction area,  $I_0$  is the reverse saturation current,  $V$  is the applied bias voltage,  $q$  is the elementary charge,  $k$  is the Boltzmann constant, and  $T$  is the temperature.
5. Noise Equivalent Irradiance (NEI): NEI measures the minimum detectable irradiance of a detector. It is defined as the input optical power that generates a signal-to-noise ratio of 1 and is given by  $NEI = NEP / (\text{responsivity} \cdot \text{bandwidth})$ .
6. Bandwidth (B): Bandwidth is the range of frequencies the detector can respond to. It is typically limited by the RC time constant of the detector and is given by  $B = 1 / (2\pi RC)$ .
7. Rise Time ( $t_r$ ): Rise time is required for the detector to respond to a change in incident light. It is given by  $t_r = 0.35 / B$ .
8. Fall Time ( $t_f$ ): Fall time is required for the detector to recover from a change in incident light. It is given by  $t_f = 0.35 / B$ .
9. Detectivity ( $D^*$ ): Detectivity is a measure of the sensitivity of a detector and is defined as  $D^* = [\text{responsivity} \cdot \sqrt{(A \times B)}] / NEP$ , where  $A$  is the detector area.
10. Fill Factor (FF): FF measures device's efficiency in collecting charge carriers. It is defined as the ratio of the maximum power that can be generated by the device to the theoretical maximum power and is given by  $FF = (I_{max} \cdot V_{max}) / (I_{sc} \cdot V_{oc})$ , where  $I_{max}$  is current at the maximum power point,  $V_{max}$  is the voltage at the maximum power point,  $I_{sc}$  is the short-circuit current, and  $V_{oc}$  is the open-circuit voltage.

## 1.6. Problems With HOIPs Structure

The methylammonium cations inhabit the "interstices" (the A sites) within the  $ABX_3$  perovskite lattice, which are sufficiently large to allow tiny organic cations, in the structure of the  $MAPbI_3$  HOIPs material, which has an octahedral coordination around the Pb atoms. The mobilities of most HOIP materials are actually small, especially when compared to inorganic FESEMiconductors employed as absorbers in high-efficiency PV cells, despite their highly advantageous FESEMiconducting characteristics<sup>82</sup>. Due to their use in solar cells that provide high efficiencies comparable to that of traditional silicon-based solar cells, HOIPs have garnered a great deal of attention.

### 1.6.1. Environmental Instability in HOIPs

Environmental sustainability refers to the obligation to safeguard global ecosystems and conserve natural resources to support current and future health and well-being. The tremendous success of HOIPs as PV materials producing extremely high-efficiency solar cells has been shown. Within a few years, they set a record for power conversion efficiency that is more than 25%. HOIP materials with properties including simplicity of fabrication, panchromatic sunlight absorption, high carrier mobility, superior carrier diffusion length, long carrier lifetimes, etc. are primarily responsible for the high efficiency of PSCs<sup>74</sup>.

Both IHPs and HOIPs have several issues, such as phase instability and environmental stability. HOIP solar cells are highly efficient, however there is a great desire to increase their environmental stability. Epi-layers of a wide band gap 1D lead iodide perovskitoid structure, based on a short organic cation, can be used to fix the issue. For instance, the environmental stability was significantly increased in copper-doped  $NiO_x$ -based PSCs, and the PCE was impressively increased to 15.40%<sup>83</sup>.

#### (a) Effect of water

In essence, water molecules easily enter the perovskite structure, forming a transitional monohydrate and dihydrate perovskite. According to XRD, the hydrate structures can completely revert back to the original perovskite within 48 hours in dry air<sup>84</sup>. Strong hydrogen bonds that form between water molecules and organic cations in perovskite crystals weaken the link between the cation and the  $PbI_6^-$ , enabling the organic cation to deprotonate more

quickly and external stressors like heat or an electric field to degrade the perovskite. According to theory, organic-inorganic perovskite materials degrade under humidity by reacting with water to form intermediate molecules that eventually break down into  $\text{PbI}_2$  <sup>85</sup>.

For instance,  $\text{MAPbI}_3$  readily interacts with water to produce the hydrates  $\text{MAPbI}_3 \cdot \text{H}_2\text{O}$  and  $(\text{MA})_4\text{PbI}_6 \cdot \text{H}_2\text{O}$ , which later decomposes into  $\text{MAPbI}_3$  and  $\text{PbI}_2$ . The performance and stability of HOIP PSCs can be impacted by the presence of moisture and water in an ambient environment. A sufficient amount of water has been found to facilitate the nucleation and crystallization of perovskite materials, enhancing the quality of perovskite films and the PSC performance <sup>2</sup>. The impact of water on  $\text{MAPbI}_{3-x}\text{Cl}_x$ 's electrical structure prior to any apparent structural damage. In fact, after extended exposure to rising RH,  $\text{MAPbI}_3$  perovskites structurally change into monohydrates and then into  $\text{PbI}_2$  <sup>84</sup>.

### (b) Effect of Oxygen

The third most plentiful element in the universe, oxygen, makes up around 21% of the atmosphere on earth. An effective and convenient method to reduce non-radiative recombination and enhance the PV performance of HOIPs has been reported as defect passivation utilizing oxygen <sup>86</sup>. Yet, superoxide's reactivity with protonated organic cations like  $\text{MA}^+$  and  $\text{FA}^+$  can substantially impact the chemical stability of HOIPs, making it difficult to grasp how oxygen influences their defect features fully. The performance of  $\text{MAPbI}_3$ -based solar cells is significantly improved by this effective oxygen passivation, which can increase the PL intensity of  $\text{MAPbI}_3$  by over three orders of magnitude and extend the PL lifetime from a few nanoseconds to hundreds of nanoseconds <sup>87</sup>. Unfortunately, oxygen has a double-edged effect on HOIPs, as it can both hasten their decomposition and impair the efficiency of solar cells. Because of the strong hydrogen bonds between oxygen and organic cations, oxygen can deprotonate the organic moiety in HOIPs, such as  $\text{MA}^+$  or  $\text{FA}^+$ , creating  $\text{MA}$  (or  $\text{FA}$ ),  $\text{PbI}_2$ ,  $\text{H}_2\text{O}$ , and  $\text{I}_2$ . Worse, this oxygen-induced deterioration severely restricts the knowledge of how oxygen affects perovskites through passivation. Due to the fact that inorganic cations lack acid protons, HOIPs, which switch out the organic cation for an inorganic cation like  $\text{Cs}^+$ , might innately boost the beneficial effects of oxygen while suppressing its detrimental consequences. HOIPs may therefore be the best option to study the passivation effects of oxygen for perovskites.

**(c) Effect of Atmospheric gases**

99% of the air comprises these gases, predominantly oxygen, and nitrogen. In comparison, the remaining 1% comprises of greenhouse gases, including carbon dioxide, methane, nitrous oxide, water vapour, and ozone. The optoelectronic properties of perovskite materials and, consequently, the performance loss of the devices is significantly influenced by the environment. The fundamental principles behind the atmosphere-induced photo-physics of perovskites are still completely unknown<sup>88</sup>. Consequently, it is essential for fundamental study and technological uses of perovskite to examine how HOIPs interact with various air conditions, particularly when ambient and inert environments are exchanged.

The research on the intrinsic properties of the perovskite materials is best done on individual perovskite crystals, which can range in size from a few nanometers to a submicrometer level and provide precise information beyond the enFESEME averaging picture acquired from bulk and film. There is no denying that various macroscopic operating circumstances, in particular a variable ambient, can significantly affect the materials' microscopic behaviour. When atmospheric conditions vary, PL from perovskites at the single-particle level frequently exhibits substantial changes.

In order to quantify the impact of atmospheric factors on radiative decay or deterioration in perovskites and to provide insights into their microscopic origins, which are otherwise muddled in enFESEME averaging, examination of the evolution of PL characteristics can be a powerful technique. The fundamental mechanism governing the long-term stability of perovskite materials can be revealed by understanding the impact of atmospheric conditions on the photophysical characteristics of specific perovskite crystals. This knowledge also offers recommendations for the creation of perovskite-based devices. While trap state filling by photogenerated carriers is probably responsible for the activation of the perovskite PL, the effect of the surrounding atmosphere is crucial, pointing to oxygen as being a determinant<sup>89</sup>. The effect of the atmosphere is discovered by placing the samples under controlled ambient conditions.

**(d) Effect of Solvents**

A solute can be dissolved by a solvent, which creates a solution. In addition to being a liquid, a supercritical fluid, a solid, or a gas can also be solvent. Unfortunately, several issues still

prevent the widespread use of HOIP-based technology. Poor control of solution-mediated crystallisation of HOIP materials is a significant issue among these difficulties. It has been demonstrated that the production of solution-based intermediates affects both the crystallisation of HOIPs and the functionality of devices made up of the ensuing HOIP active layers. Although it is generally acknowledged that the choice of the solvent determines the production of such intermediates, it needs to be clarified how solvent-precursor coordination influences crystallization. Although solvent-solute coordination is crucial for the crystallization of HOIP, it is unclear how the choice of solvent affects these interactions. For instance, solvents were added to the precursor to interact with  $\text{Pb}^{2+}$  and create intermediates, such as dimethyl sulfoxide (DMSO) and dimethylacetamide (DMAC). Moreover, the presence of intermediates may reduce the crystallization rate by slowing the rate at which  $\text{Pb}^{2+}$  is released during the crystallization process <sup>90</sup>.

These discrepancies lead to an ambiguous picture of how solvent selection influences the generation of intermediates or how it might be used to regulate HOIP crystallization. Focused research on each type of contact and its impact on the synthesis of HOIPs is relevant for device applications. Thus it is required to study the complex phase space of solution chemistry in HOIP precursor solutions, including electrostatics, ionic, and sterics interactions. The preparation of perovskite precursor solution typically involves combining N, N-dimethylformamide (DMF) and dimethyl sulfoxide (DMSO), where DMF serves as the host solvent because of its outstanding dissolving capacity and DMSO serves as the ligand solvent owing to its strong coordination. Superior solvents interact with the  $\text{Pb}_2^+$  core more strongly, preventing iodide coordination and delaying perovskite crystallization to synthesize oriented and highly ordered HOIP structures <sup>91</sup>. It is possible to finely control the crystallisation and the subsequent morphology of HOIP active layers by varying the concentration of high additives in precursor solutions.

### 1.6.2. Lead toxicity

Adult's and children's health may suffer severely from lead exposure. Excessive exposure results in brain and central nervous system attacks that can cause unconsciousness, convulsions, and even death. It is a significant environmental illness with devastating repercussions. Cost and energy usage are minimal for perovskite solar cells. Due to their quick energy payback times compared to other solar cell technologies, perovskite solar modules have

promise for reducing CO<sub>2</sub> emissions, as shown by the thorough life-cycle inventory analysis. All of the ingredients necessary to make lead halide perovskite are plentiful on Earth. Pb, for instance, is frequently utilized in the automotive industry, and a paper even suggests that lead halide PSCs might be made using lead waste recycled from lead-acid batteries<sup>92</sup>. Iodine production is naturally lower than lead production, which could provide a problem for large-scale production. The efficiency and payback time of perovskite are promising, and finding the elements for lead halide perovskite may be too difficult. Hence we must look for appropriate alternatives to lead in the HIP and HOIP systems.

Halide perovskites are composed of organic and inorganic lead salts that are very soluble in water, making them potentially bioavailable, or available to plants and, subsequently other living things. However, due to the toxicity of its Pb concentration, the commercialization or application of lead halide PSCs has been questioned. The World Health Organization (WHO) states that less than 5 mg kg<sup>-1</sup> of body weight is required for lead to be 50% deadly [LD50(Pb)]. It is challenging for Pb-based perovskites to meet environmental regulations for PV systems since the WHO has established that the maximum blood lead level for children is 5 mg L<sup>-1</sup>. As a result of the potential for lead to leaking into the environment, the toxicity of lead-based perovskites has become another clear issue<sup>93</sup>.

It should be emphasized that the development process has been delayed by the organic-inorganic perovskites' susceptibility to moisture, air, heat, prolonged exposure to sunshine, and toxicity problems. Since lead halide is extremely water-sensitive, dissolving it in water can cause it to be discharged into the environment. Further requiring the search for alternatives to MAPbI<sub>3</sub> is the toxicity of lead-based chemicals. Consequently, it is highly important to find suitable elements for perovskite to increase stability and obtain perfect photo-electronic properties without harming the environment. As a result, viable solutions must be put forth to address lead poisoning, the environmental risks associated with lead-containing items, as well as chemical instability in ambient environments.

### **1.7. Strategies to Enhance the Applicability of HOIPs**

HOIP nanostructures have recently come into the spotlight as incredibly promising systems for applications like optoelectronic devices, adding a whole new level to the field of nanotechnology. The ability to blend various inorganic and organic component qualities into a



single molecular substance is a significant benefit of these hybrid systems. A restricted structure with different chemical and physical characteristics from 3D perovskite might be produced by regulating the number of perovskite layers. Perovskite PVs can perform better by improving the structure, decreasing flaws, and growing the grain size. The materials utilized in the synthesis process and the choice of manufacturing techniques for the devices have unquestionably impacted these endeavors. This creates a whole more extensive set of remarkable selections of materials, all of which have great potential for use in optoelectronic devices.

### 1.7.1. Low-Dimensional HOIPs

The 2D HOIP's ability to self-assemble has received a lot of attention over the years. It is difficult to readily create a perfect 2D structure from an artificial quantum well when utilizing conventional semiconductor materials<sup>94</sup>. Strongly confined exciton energy and third-order optical nonlinearity are two distinctive optical and physical properties of the HOIPs. Low-dimensional HOIPs have generated interest due to their abilities to exhibit magnetic spin selectivity, broad band emission, and exciton dynamics. Nevertheless, there is no quantitative model that can be used to anticipate how the structure of these low-dimensional perovskites will be affected by the organic cations. The fluctuation in electrical potential between layers, which raises the exciton binding energy, is a crucial characteristic of low-dimensional layered materials like HOIPs<sup>95</sup>.

This dissertation will concentrate on low-dimensional materials because of their intriguing optoelectronic capabilities, even though the phrase "quantum material" encompasses various issues and objectives<sup>96</sup>. The term "low-dimensional materials" refers to those systems, having at least one of the three dimensions shown in Figure 1.10, in which the size effect constrains the electronic wave function. The confinement effect often manifests in the 1 to 100 nm range.


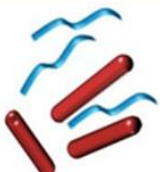
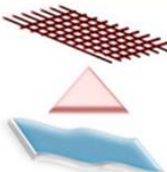

Isotropic Nanomaterials	Anisotropic Nanomaterials		
			
<b>0D</b>	<b>1D</b>	<b>2D</b>	<b>3D</b>
Spheres, Clusters	Nanorods, Wires	Nanofilms, Plates	Nanoparticles

Figure 1.10: Overview of Structures of 0D, 1D, 2D, and 3D Materials

Due to their excellent photoelectric conversion efficiency, high absorption coefficient, variable BG, long carrier diffusion lengths, and comparatively low material costs, HOIPs are receiving a lot of attention for use in perovskite solar cells (PSCs) <sup>97</sup>. Notably, the use of halide perovskites in energy conversion, light emitting diodes (LEDs), low-power transistors, and very effective photo detectors is investigated. HOIPs PCE is comparable to that of traditional crystalline silicon solar cells. A resurgence of interest in molecular-level low-dimensional perovskites, including two-dimensional (2D), one-dimensional (1D), and zero-dimensional (0D) materials, has resulted from advances in three-dimensional (3D) HOIPs used in PVs <sup>98</sup>. Bulk asFESEMblies of perovskite quantum-wells, quantum-wires, and molecular species or clusters comprise the molecular level 2D, 1D, and 0D perovskites, respectively, in which metal halide anions are divided by sizable organic cations <sup>99</sup>.

In comparison to the impressive advancements made in 3D and 2D perovskites, the 1D perovskites have received far less attention till now. Low dimensional metal halide perovskites, such as 0D perovskite quantum dots, 1D perovskite nanowires, and 2D perovskite nanoplatelets, have been created to display different properties from their bulk counterparts due to quantum size effects <sup>100</sup>. Charge carriers are concentrated within ordered metal halide sheets, rods, or clusters separated by cationic lattices in low-dimensional-networked (low-DN) perovskite derivatives. This class of FESEMiconductors had been dormant for 20 years before resurfacing in the last two years, partly due to the demand for more reliable absorbers than MAPbI<sub>3</sub>-type perovskites in PVs.

Low-dimensional perovskites differ from their three-dimensional counterparts in that they contain at least one large organic cation that cannot match the cubic core. It's interesting to note that octahedral [BX<sub>6</sub>]<sup>4-</sup> may be bonded in a variety of ways to generate 3D, 2D, 1D, and 0D perovskites <sup>101</sup>. The 3D structure will not be stable if the size of A<sup>+</sup> is too great. Instead, [BX<sub>6</sub>]<sup>4-</sup> octahedral 2-dimensional layers are favoured, with organic cations residing between the layers. A<sup>+</sup>, B<sup>2+</sup>, and X<sup>-</sup> have the same interpretations as they do in 3D perovskite in the empirical formula for (100) 2D perovskite, which is A'A<sub>n-1</sub>B<sub>n</sub>X<sub>3n+1</sub>.

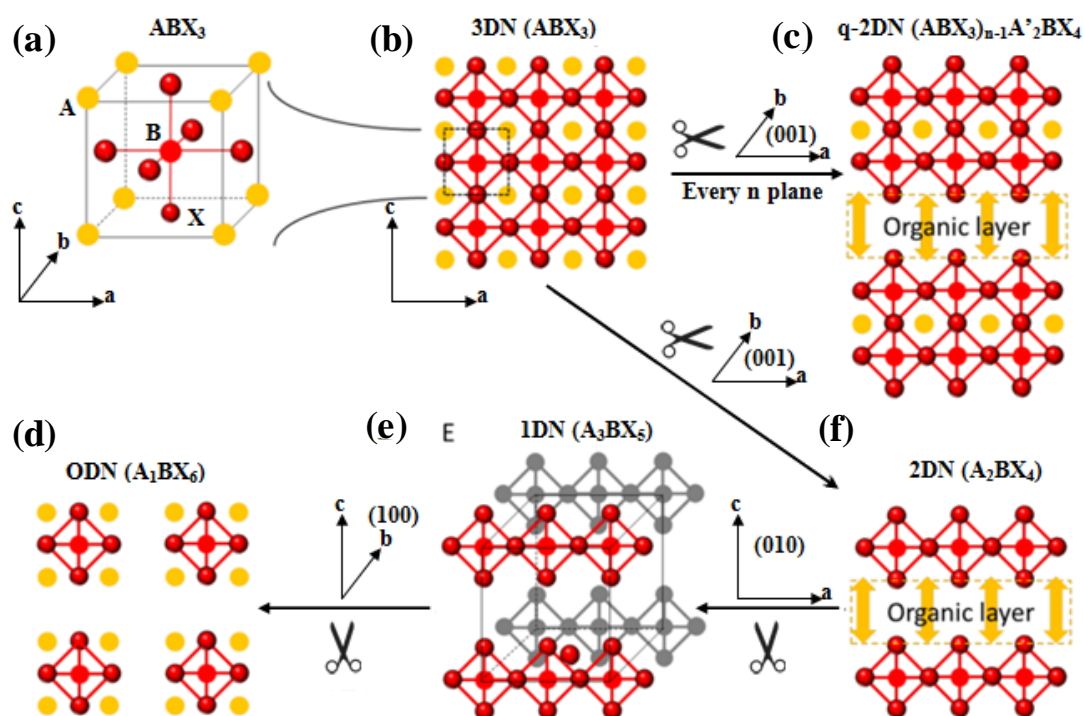


Figure 1.11: Graphic illustrations illustrating the creation of three-dimensional network (3DN) by slicing along crystallographic planes and the connection of  $BX_6$  octahedra in low-DN perovskites; (a) The 3DN perovskite unit cell; (b) The 3DN perovskite structure projected in the (010) plane, showing three-axes-networked octahedra; (c) 3DN is cut along  $n(100)$  planes to create quasi-2DN perovskite; (d) 3DN is cut along the (100) plane to create 2DN perovskite, which displays octahedra connectivity along two axes. To create 1DN perovskite; (e) 2DN is cut along the (010) plane, with octahedra networking along one axis. In (f), 1DN is cut along the (001) plane to create 0D perovskite, displaying isolated (non-connected) octahedra.

Here, the 3D lattice divides into layers made of various thicknesses of  $[BX_4]_{2n-n}$ , indicated by  $n$ , along the (100) plane. If  $A'$  only possesses one positive charge as  $A'^+$ , then the stoichiometry of  $A'^+$  is 2, which can be calculated using the formula  $A'_2A_{n-1}B_nX_{3n+1}$ . Cations  $A^+$  and  $A'^{2+}$  are found in and between the layers, respectively. In lead iodide perovskites, Figure 1.11 compares 3D perovskite with (100) 2D perovskites with  $n=1, 2$ , and 3.  $A^+$  is commonly referred to as a stabilizer because it prevents each layer from separating, while  $A'^{2+}$  is typically referred to as a separator because it divides up to 100 layers<sup>102</sup>. Perovskite-type structures can be divided into different dimensionalities, as shown in Figure 1.11, based on the connectivity characteristics of metal halide octahedra.

Perovskites that have the empirical formula,  $ABX_3$  (e.g.  $MAPbX_3$ ) are categorised as 3DN perovskites because they include  $BX_6$  octahedra that are corner-shared along all three 4-fold octahedral axes [Figure 1.11 (a), (b)]. By slicing along particular crystallographic planes, it is possible to create 2DN perovskites from the 3DN with a layered structure made of octahedra joined along two octahedral axes [Figure 1.11 (d)]. Octahedra remain connected only along one axis when 2DN perovskites are further divided perpendicular to the inorganic sheets, resulting in 1DN perovskites [Figure 1.11 (e)]. The most extreme case is 0DN perovskites, which are created by further slicing 1DN to create isolated or nonconnected octahedra [Figure 1.11 (f)]. Perovskites can also be created by superimposing two or more types; for example, quasi-2DN perovskites are created by superimposing 3DN and 2DN [Figure 1.11 (c)]<sup>102</sup>. It is important to note that a cationic organic or inorganic sub-lattice stabilises the ordered metal halide framework in perovskites of all dimensions.

#### (a) Types of 0D, 1D, 2D and 3D structure

Methylammonium lead halides perovskite is the perovskite that has received the most attention. The six closest iodine atoms encircle Pb at the corners of the lattice, forming a  $PbX_6$  octahedron, with MA occupying the centre. The organic perovskites promise optical and PV features, including highly intense luminescence and great optical absorption, which gives them an advantage over ordinary all inorganic perovskites<sup>103</sup>. Additionally, the adaptability of organic cations A provides more scope for adjusting the optical and quantum properties of organic-inorganic halide perovskites, as well as altering the crystal structure. There is an exponential growth in quantum conversion efficiency over the previous decades, from 3.8% to 22.1%, to a world record of 25.2% in 2019<sup>104</sup>. In addition to having a lower production cost than silicon, organic perovskite heralds a revolutionary development in solar energy technology.

Low-dimensional perovskites are characterized by the presence of at least one large organic cation that cannot fit the cubic framework of traditional perovskites as shown in Figure 1.12. These structures have a layered or quasi-layered morphology, with the inorganic components forming the layers and the organic cations located between the layers<sup>105, 106</sup>.

- 2D: The Dion-Jacobson perovskite structure has a layered morphology consisting of two-dimensional (2D) sheets of corner-sharing  $[BX_6]$  octahedra separated by organic

cations. The octahedra are connected through edge-sharing to form infinite chains that extend in one direction.

- **Pillared 1D Perovskite Structure:** The pillared 1D perovskite structure consists of alternating layers of inorganic  $[BX_6]$  octahedra and organic cations. The organic cations bridge the inorganic layers to form pillars that extend in one direction, resulting in a one-dimensional (1D) morphology.
- **0D Perovskite Structure:** In 0D perovskites, the  $[BX_6]$  octahedra are completely isolated from each other and surrounded by organic cations. The absence of any connectivity between the octahedra results in a zero-dimensional (0D) morphology.

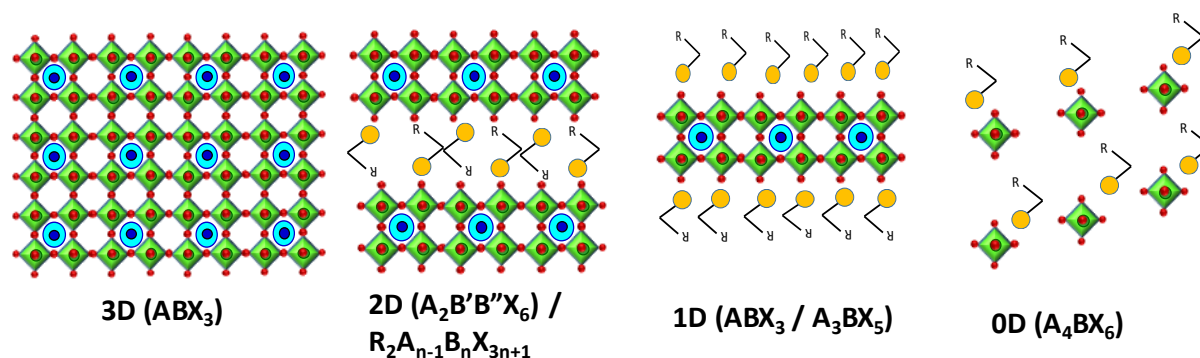


Figure 1.12: Schematic crystal structures of the broad family of hybrid perovskites 0D, 1D, 2D, and 3D.

The general formula for the most common 2D perovskites is  $(RNH_3)_2MA_nM_nX_{3n+1}$ , where  $n$  is the number of metal (like Pb or Sn) halide (like I, Br, or Cl) octahedrons sandwiched between adjacent insulating organic cation layers.  $RNH_3^+$  is a large organic cation, like butyl ammonium ( $C_4H_9-NH_3^+$ , BA) and phenyl ethyl ammonium ( $C_6H_5-CH_2CH_2-NH_3^+$  PEA). The band gap and exciton binding energy of 2D perovskites significantly rely on the degree of quantum confinement, which is mostly determined by the thickness of the inorganic layers (i.e., the value of  $n$ )<sup>107</sup>.

Except for 3D and 2D, perovskites can also crystallize in quasi-1D nanoribbons. Last, 0D quantum dots with nanometer dimensions, such as  $CsPbBr_3$  and  $CdPbBr_3$ , can also be produced by solution-based methods. By filtering different sizes of nanoparticles, the PL can be tuned within a wide range, allowing the mass production of LEDs in different colors. The quantum dots perform an appealing quantum photoemission effect. They have been widely favored due

to their low cost and energy consumption compared to the commercial organic light-emitting diodes and their high color purity. Due to the interconnectedness of their  $[MX_6]^{4-}$  octahedron networks, this perovskite system has a multi-dimensional crystal structure system that ranges from 3D to 0D<sup>108</sup>.

▪ **Tunability in structure: Effect of Organic chain length, Effect of center metal**

The structural tunability of organic-inorganic perovskites is a significant characteristic. Several structural variations are seen if the counter ions of the inorganic components are mono- or di-protonated amines. By selecting the proper organic cations, the perovskite sheets' thickness and crystallographic orientation can be changed. The HOIPs physical characteristics are significantly influenced by the extended inorganic anion's effective dimensionality. Given the HOIPs flexible structure, it is intriguing to investigate the relationship between structures and properties within a single structural family by using various organic ammonium cations to support different orientations or dimension perovskite sheets.

To put it another way, inorganic units can self-organize into low-dimensional crystals, where they create networks in 0D, 1D, 2D, and 3D spaces depending on the organic cations. The physical characteristics of the HOIPs are significantly influenced by the effective dimensionality of the extended inorganic anion<sup>109</sup>. Owing to the HOIPs structural adaptability, it is intriguing to investigate the relationship between structures and properties within a single structure family by using various organic ammonium cations to support different orientations or dimensions perovskite sheets<sup>110</sup>.

The long organic ligands of the Ruddlesden-Popper and Dion-Jacobson phases (derived from the perovskite structure) act as barriers against moisture ingress or as passivating agents, enabling PVs stable for 1000 h and up to 10000 h. This has been addressed by tuning the dimensionality of halide perovskites<sup>111</sup>. Due to their divalent cation's twofold hydrogen bonding to the inorganic lattice, Dion-Jacobson perovskites are more durable than Ruddlesden-Popper perovskites. Wider band gaps and lessened band dispersion, which result in lower mobilities, are drawbacks of reduced dimensionality, which is achieved by producing 2D, quasi-2D phases, or nanocrystals. Nonetheless, this process has proven crucial in enabling enhanced LED performance. Multi-dimensional perovskites, which cover a bulk 3D perovskite (low band gap, high mobility) with a surface layer of a 2D perovskite to improve stability and

passivate surface flaws, have been used to overcome this in PVs. LED applications, in which perovskites with dimensionality varying from 3D to 2D are combined onto one thin film, have also benefited from multi-dimensional perovskites<sup>112</sup>. The 3D perovskite phase has the lowest band gap, and injected carriers are subsequently directed. Here, electrons and holes are tightly contained, resulting in larger EQEs.

The capacity to readily alter the characteristics of the HOIP system is another key benefit. This can be done by substituting cations (organic components) or anions (halide components) in the precursor solutions.

### (b) Change in Properties upon changing dimensionality

Due to its flexible structural design and potentially valuable magnetic, electrical, and optical capabilities, HOIPs with organic-inorganic layer alternating topologies have received extensive research. The study of the HOIPs' physical characteristics and electrical composition has advanced quickly. High-quality HOIP thin film devices' scalable solution-based processing techniques enable flexible electronics as one of its possible applications, in addition to PVs. The mechanical robustness of HOIP-based devices as well as their electrical properties can be considerably impacted by the mechanical stress state of HOIPs in various applications. There have been several theoretical and experimental examinations of the materials' mechanical properties about 3D HOIPs.

#### 1.7.2. Lead-free HOIP systems

The design of lead-free materials, which are chosen by "inspiration" from the defect tolerance of the lead-halide perovskites, has focused on the development of lead-free and low-toxicity oxide, sulfide, and selenide perovskites (i.e., perovskite inspired materials or PIMs). Dimensionality is a crucial factor in selecting and optimizing these lead-free materials.

Lead-halide perovskites challenge common wisdom in that they can produce solar devices with minimal open-circuit voltage losses and non-radioactive recombination rates despite having large defect densities of  $10^{14}$ – $10^{16}$  cm<sup>-3</sup><sup>113</sup>. In contrast, GaAs and silicon, which are both utilized in electronics, have defect concentrations between  $10^7$  and  $10^8$  cm<sup>-3</sup>. This has raised the question of whether or not alternative classes of lead-free materials or "perovskite-inspired" materials could also exhibit such fault tolerance. In addition to producing defect-tolerant

FESEMiconductors that are non-toxic and stable without encapsulation, the quest for such materials may also lead to new insights into defect tolerance. This would help to solve two of the major problems with lead-halide perovskites. Three general approaches can be used to find lead-free materials inspired by perovskites:

- Finding analogous materials that are similar to lead-halide perovskites in terms of structure and chemistry (such as tin-based perovskites or bismuth-based defect-ordered perovskites),
- Finding lead-free halides with a perovskite structure (such as double cation perovskites and vacancy-ordered perovskites), and
- Finding materials that mimic the defect tolerance factor of lead-halide perovskites are all possible (e.g., bismuth oxyiodide or BiOI).

It has been discovered that certain lead-free  $ns^2$  compounds, such as InI, BiI<sub>3</sub>, BiSI, BiOI, and SbSI, also have an anti-bonding to anti-bonding state transition in addition to having high dielectric constants. BiOI has recently undergone calculations and experimental work demonstrating its tolerance for vacancy and anti-site faults. Nonetheless, it has been discovered that deep traps can be found in BiI<sub>3</sub>, SbI<sub>3</sub>, Cs<sub>2</sub>AgBiBr<sub>6</sub> double perovskites, BiSI, BiSeI, and Sb<sub>2</sub>Se<sub>3</sub>. When compared to orbitals from other species (like directional d orbitals), such as in the case of Cs<sub>2</sub>AgBiBr<sub>6</sub>, the contribution of the  $ns^2$  cation valence s orbital to the valence band density of states can be minimal. As a result, these other orbitals predominate the electronic structure at the band edges <sup>114</sup>.

The recently discovered low-cost and solution-processable lead-free organic-inorganic halide perovskite solar cells have received remarkable interest. A class of materials known as lead-free organic-inorganic halide perovskites share the chemical formula ABX<sub>3</sub><sup>115</sup>. The tiny B<sup>+</sup> (lead-free) cation is amid the octahedral sites generated by the anions in an ideal lead-free organic-inorganic halide perovskite. The X anion is in the middle of each face. A is an organic cation (such as ammonium, [NH<sub>4</sub>]<sup>+</sup>, hydroxyl-ammonium, [CH<sub>3</sub>OH]<sup>+</sup>, MA<sup>+</sup>, EA<sup>+</sup>, FA<sup>+</sup>, etc.) and B is an inorganic cation, like group 14 element (e.g., Sn<sup>2+</sup>, and Ge<sup>2+</sup>), alkaline earth metals (e.g. Mg<sup>2+</sup>, and Ca<sup>2+</sup>), transition divalent metals (such as Cu<sup>2+</sup>, Zn<sup>2+</sup>, etc.), and lanthanide (e.g., Eu<sup>2+</sup>, and Yb<sup>2+</sup>). Each B<sup>+</sup> cation mentioned above can be an alternative to replace the divalent lead cation (Pb<sup>2+</sup>). Perovskite absorber layers consisting of germanium, silicon, tin, or a mixture



of the two cations are most adequate for overall PV performance to replace lead based materials<sup>116</sup>.

The most excellent replacements to lead are germanium and silicon<sup>117</sup>.  $\text{Si}^{2+}$ ,  $\text{Sn}^{2+}$ , and  $\text{Ge}^{2+}$  are alternate elements that become unstable when exposed to oxygen. In the formula, X is an anion that can be either a halogen (F, Cl, Br, and I) or a non-halogen ( $[\text{HCOO}]$ ,  $[\text{CN}]$ ,  $[\text{BH}_4]$ , or  $\text{SCN}$ ). Stability and structural ordering are the primary responsibilities of the inorganic sites. At the same time, mechanical flexibility and cost-effective processing are provided by the organic component, and charge neutrality between cations and anions is maintained by the X anions. The criteria of the Goldschmidt Tolerance Factor determine the stability of organic-inorganic halide perovskite. Table 1.2 displays the predicted effective ionic radii of several A-cations, B-cations, and X-anion.

**Table 1.2:** Calculated effective ionic radii of A-organic cations, metal cations, and halide anions<sup>118</sup>.

<b>A-Cation</b>	$r_{A,eff} / pm$	<b>B-Cation</b>	$r_{B,eff} / pm$	<b>X-Anion</b>	$r_{X,eff} / pm$
<b>Ammonium</b> $[\text{NH}_4]^+$	146	$\text{Be}^{2+}$	45	$\text{I}^-$	220
<b>Hydroxylammonium</b> $[\text{NH}_3\text{OH}]^+$	216	$\text{Mg}^{2+}$	72	$\text{Br}^-$	196
<b>Methylammonium</b> $[\text{MA}]^+$	217	$\text{Ca}^{2+}$	100	$\text{Cl}^-$	181
<b>Hydrazinium</b> $[\text{NH}_3\text{NH}_2]^+$	217	$\text{Ti}^{2+}$	86	$\text{F}^-$	133
<b>Azetidinium</b> $[(\text{CH}_2)_2\text{NH}_3]^+$	250	$\text{V}^{2+}$	79		
<b>Formadinium</b> $[\text{FA}]^+$	253	$\text{Cr}^{2+}$	80		
<b>Imidazoline</b> $[\text{C}_3\text{N}_2\text{H}_5]^+$	258	$\text{Mn}^{2+}$	83		

<b>Ethylammonium</b> [EA] <sup>+</sup>	274	Fe <sup>2+</sup>	78		
<b>Guanidinium</b> [(NH <sub>2</sub> ) <sub>3</sub> C] <sup>+</sup>	278	Ni <sup>2+</sup>	69		
<b>Tetramethylammonium</b> [(CH <sub>3</sub> ) <sub>4</sub> N] <sup>+</sup>	292	Cu <sup>1+</sup>	77		
<b>Thiazolium</b> [C <sub>3</sub> H <sub>4</sub> N <sub>5</sub> ] <sup>+</sup>	320	Cu <sup>2+</sup>	73		
<b>3-pyrrolinium</b> [NC <sub>4</sub> H <sub>8</sub> ] <sup>+</sup>	272	Zn <sup>2+</sup>	74		
<b>Tropylium</b> [C <sub>7</sub> H <sub>7</sub> ] <sup>+</sup>	333	Ge <sup>2+</sup>	73		
<b>Cesium</b> [Cs] <sup>+</sup>	167	Si <sup>2+</sup>	118		
<b>Potassium</b> [K] <sup>+</sup>	138	Ag <sup>2+</sup>	94		
		Ag <sup>1+</sup>	115		
		Cd <sup>2+</sup>	95		
		Ba <sup>2+</sup>	135		
		Eu <sup>2+</sup>	117		
		Tm <sup>2+</sup>	103		
		Yb <sup>2+</sup>	102		
		Pt <sup>2+</sup>	80		
		Hg <sup>2+</sup>	102		
		Np <sup>2+</sup>	110		
		Ni <sup>2+</sup>	69		

---

		Sn <sup>2+</sup>	115		
		Sb <sup>3+</sup>	76		

### 1.7.3. Nanocomposite Formation

The term "nano-composite material" has significantly broadened to include a wide range of systems, including one-dimensional, two-dimensional, and three-dimensional materials, made of distinctly different components that are mixed at the nanometer scale, whether they are either amorphous or crystalline <sup>119</sup>. An organic polymer, metal, or ceramic matrix material embeds nano- or molecular domain-sized particles in nanocomposite materials, a special type of composite material. Metal-matrix, ceramic-matrix, and polymer-matrix nanocomposites fall into these categories. To create nanocomposite films utilized in nanoelectronic systems, polymer-matrix nanocomposites can be manufactured as an electrically conductive nanocomposites.

It is believed that the close integration of these nanoparticles in these matrices can completely alter the properties. The physical characteristics of these base materials can be altered by using the nanoparticles as matrix reinforcement. These nanocomposites now contain a significant quantity of interfacial phase material due to the tiny inclusions, which allows the material's chemical, mechanical, and morphological domain structures to change completely. Nowadays, much research is being done on polymer-based HOIP- based nanocomposites with mechanical and electrical properties that are better than those of their individual parts.

New intercalation chemistry has been developed due to the increased interest in new nanocomposite functional hybrid materials for fundamental and device-oriented research. Due to their wide range of applications in the fields of optics, electronics, mechanics, and photoconductors, inorganic-organic nanocomposites have garnered a lot of attention. A group of materials known as nanocomposites are made up of two or more phases containing particles smaller than a nanometer. It can be regarded as a solid structure with nanoscale dimensions comprising many phases <sup>120</sup>. These materials can either be composed of two or more inorganic/organic phases in some combinational form with the restriction that at least one of the phases or features can be in the nanosize, or they can be composed of an inorganic (host) solid containing an organic component (or vice versa). These materials include gels, copolymers, porous media, and colloids.

In addition to the individual component qualities in a nanocomposite, the interfaces between those components also significantly influence the overall properties. This might be because nanocomposites, which are present at the interfaces between constituent intermixed phases, have significant surface areas<sup>121</sup>. The interaction of their phases at the interfaces is a common source of the unique features of nanocomposite materials. As macromolecules move from the melt into a small gap and experience the confinement effect of the walls, modifier molecules gain more conformational freedom when the layers split during the development of nanocomposite materials. As the silicate-modifier-polymer system's overall entropy change is negative, the energetic interactions must overcome the entropic barrier for a thermodynamically stable nanocomposite to develop. In the absence of phase separation, components will combine to form a common micro composite. Hence, the polymer's polarity is what determines the polymer's capacity to intercalate into layered silicates and conform macromolecules in 2D space. Figure 1.13 depicts a general strategy of HP encapsulation in which the encapsulation can be polymer, metal oxide, or a covalent organic framework<sup>120, 121</sup>.

If one of the structural components, organic or inorganic, falls within the specified size range of 1-100 nm, the term "nanocomposite" is employed. Because more giant molecular building blocks for hybrid materials, including large inorganic clusters, can already be of the nanoscale length scale, a progressive shift exists between hybrid materials and nanocomposites<sup>122</sup>. When discrete structural units in the appropriate size regime are employed to design the materials, the term "nanocomposite" is frequently used. However, if molecular precursors create the inorganic units *in situ*, the term "hybrid materials" is more frequently employed.

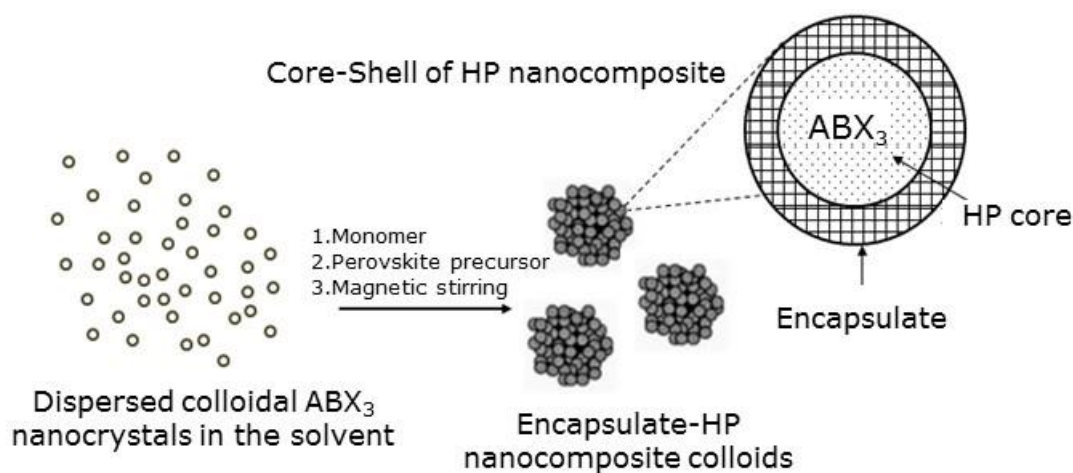


Figure 1.13: General Structure of encapsulate-HP nanocomposite formation.

## 1.8. Characterization Techniques

### 1.8.1. X-ray diffraction (XRD)

XRD is a beneficial technique to assure the composition and the crystalline structure of the as-synthesized materials. A crystalline solid has a continuous structure with the periodic and repeated arrangement of the unit cell. X-rays are electromagnetic waves with a wavelength of a few Å that fall between ultraviolet and gamma rays in general. One of the most significant characterizing methods in material science, XRD is capable of examining the crystalline structures of produced nanostructures. The study of chemical composition, crystal structures and phases, size, unit cell symmetry, lattice constants of nanoparticles, and physical properties of any material may all be done using this non-destructive method<sup>123</sup>. More than 90% of solid materials in nature are crystalline, and each crystalline solid has a distinctive XRD pattern that may be used to identify the substance, much like a "fingerprint." A diffraction pattern that identifies the substance and associated phase was produced due to the X-ray beam's interaction with the crystal. The diffraction pattern provides a wealth of data, including crystallite size, the unit cell's symmetry, stress, strain, growth orientation, etc. X-rays interact with the atoms arrayed in all planes when they pass through a substance.

As a result of this interaction, X-ray is diffracted. If the incident beam forms an angle  $\theta$  with a set of planes, then the beam will be diffracted at the same angle  $\theta$  depending upon the crystal structure and orientation of the materials, and different diffraction patterns arise. The information about the structure and grains of the powder sample can be obtained by using Bragg's law<sup>124</sup>,

$$n\lambda = 2d \sin \theta$$

Where,  $d$  is the inter planner distance,  $\lambda$  is the wavelength of the incident X-ray, and  $\theta$  is the diffraction angle. From the application point of view, it is important to get the values of  $\theta$  and the intensity of the diffracted rays, which are characteristic of the individual crystal lattice. It is possible to identify the different compounds and phases from this diffraction pattern. A photograph of the instrument is shown in Figure 1.14.

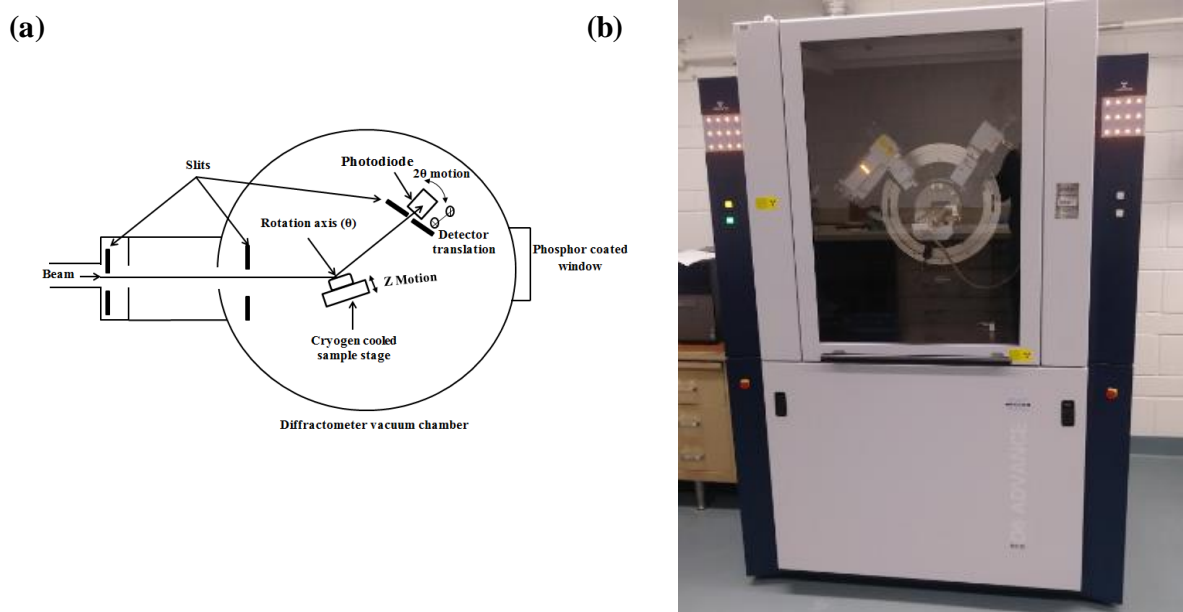


Figure 1.14: (a) Schematic representation of diffraction method within XRD; (b) Photograph of XRD instrument

### 1.8.2. Single Crystal XRD (SC-XRD)



Figure 1.15: Photograph of SC-XRD instrument.

X-ray crystallography, often known as SC-XRD, is an analytical technique that uses X-ray technologies to accurately pinpoint the precise arrangement of atoms inside a crystalline specimen. When Laue discovered that crystals diffracted X-rays in 1912, the field of X-ray crystallography was born. Since then, SC-XRD has grown into the most potent technique for determining the arrangement of atoms in solids<sup>125</sup>. Atomic-level X-ray A non-destructive

analytical method called diffraction can provide specifics about the internal lattice of crystalline materials, such as the size of unit cells, bond lengths, bond angles, and information regarding site order. Single-crystal refinement, in which the data produced by the X-ray analysis is interpreted and refined to yield the crystal structure, is closely linked. Figure 1.15 shows a typical SC-XRD instrument.

### 1.8.3. UV-visible (UV-Vis) absorption spectroscopy

Monochromators are responsible for creating the light that emanates from a source or group of sources. For the purpose of calculating the transmission as a function of wavelength, the sample is positioned between the monochromatic source and detector (after calibration to take into account variation in source intensity as a function of wavelength). When a specific transmission spectrum is applied, the optical band gap of a material can be found. This thesis uses two techniques to determine the optical band gap from a transmission spectrum. The first approach is the Tauc method, which calls for the absorption coefficient and a plot of  $(h\nu)^n$  with  $n = 2, 1/2$  depending on whether the band gap is direct or indirect<sup>126</sup>. The linear section of the curve is extrapolated to the x-axis (the photon energy or wavelength axis) after transmission data processing into a Tauc plot to provide a precise numerical value for the material's band gap. The second technique uses the derivative of the transmission spectrum; the gradient will be sharpest near the absorption edge, resulting in a peak in the derivative; this peak's location (on the energy/wavelength axis) corresponds to the optical band gap in Figure 1.16.

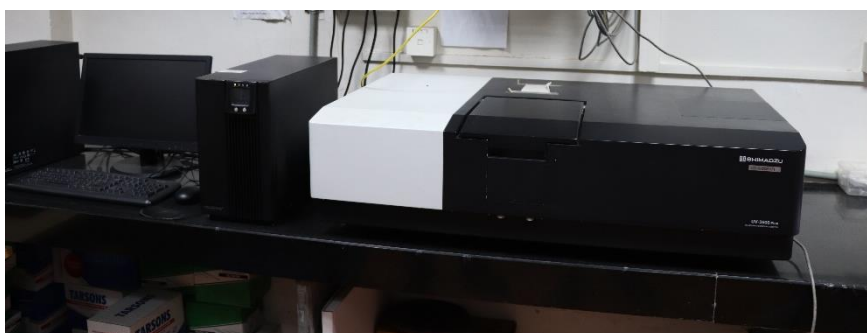


Figure 1.16: Photograph of UV-Vis spectrophotometer

### 1.8.4. Photoluminescence (PL) spectroscopy

PL is a non-destructive optical technique used to characterise, investigate, and discover point defects or to gauge the band gaps of materials PL. In order to characterise a crystal, it must be

exposed to photons that have an energy higher than the material's BG. The incident photons in the case of a crystal scintillator produce electron-hole pairs. The energy of electrons and holes recombining changes into non-radiative and radiative emission in different proportions. In order to cause PL, relatively high frequency light must impinge on material and excite atomic electrons. Upon relaxing, photons that are distinctive to the crystal or defect site that is the source of the light may be created. Band-to-band recombination, inherent crystallographic defects (growth defects), dopant impurities (added during growth or ion implantation), or other extrinsic defect levels could all contribute to the luminous signals observed (as a result of radiation or thermal effects) <sup>127</sup>.



Figure 1.17: Photograph of PL spectrometer

The resulting PL spectra can be used to identify the specific type of FESEMIconductor defect because the photons, which have an energy greater than the band gap of the material when bombarded with an impurity energy level, may emit characteristic photons via a variety of radiative recombination events. The native and extrinsic impurity levels present in the material band gap seen in Figure 1.17 can be measured qualitatively and with extreme sensitivity using this interaction.

### 1.8.5. Transmission electron microscopy (TEM)

TEM is a technique to study the atomic structure of any material. It uses an electron beam for analyzing the sample. The four main parts of a TEM are,

- (i) Electron gun to produce a monochromatic polarized electron beam,
- (ii) Set of condenser lenses provides to focus electron beam onto the sample,
- (iii) Objective lens to form the image of the sample on the image plane,



(iv) Set of magnification lenses to produce a final sample image.

Electron gun uses tungsten or LaB<sub>6</sub> filament to generate electrons by thermionic emission and field emission. By field emission (non-heating source) also, we can generate electrons, it uses a high potential gradient across fine tip single crystal of tungsten and LaB<sub>6</sub>. This beam is then passed through a condenser lens to produce a monochromatic, highly coherent, and focused beam. A condenser lens uses a magnetic focusing phenomenon for focusing the electron beam on the condenser aperture. This aperture restricts the high-angle electron to pass through. This beam is then transmitted through The objective lens then focuses transmitted electronsObjective aperture also blocks the high-angle scattered electron and increases the contrast of the image. This transmitted beam falls on a phosphor screen place where fewer electrons are transmitted and look darker on screen and the place from where large numbers of electrons are transmitted looks brighter on screen <sup>128</sup>.



Figure 1.18: Digital photograph of HRTEM

Mainly, there are three types of electrons obtained after the beam strike: transmitted electrons that do not get interacted with by the sample, elastically scattered electrons, and third are inelastically scattered electrons. The intensity of transmitted electrons that do not get interacted depends upon the thickness of the sample so it mainly gives the morphological information about the sample. Elastically scattered electron follows Bragg's law and gives information about the crystal structure after being collected by the magnetic lens. This mode of operation

is called selected area electron diffraction (SEAD) <sup>129</sup>. Inelastically scattered electrons lose their energy due to collision with elements and the amount of energy loss depends upon the atomic no. of elements, thus we get the information about the composition of the sample in Figure 1.18.

### 1.8.6. Scanning electron microscopy (FESEM)

FESEM is a versatile, cutting-edge tool that is frequently used to examine materials surface morphology. High-energy electrons are used to shoot the sample, and the emitted electrons and X-rays are then examined. These emitted electrons and X-rays provide details on a material's topography, morphology, composition, grain orientation, crystallographic information, etc. The morphology of the material has been examined using the scanning electron microscopy (FESEM) technique. High-energy electron beams are employed in FESEM to provide a high-resolution image of the sample's surface. The resolving power of a microscope, the minimum separation that can be resolved by a microscope, can be obtained by using the formula <sup>130</sup>,

$$d = \lambda / 2n \sin \theta$$

Here,  $\lambda$  is the wavelength and  $n$  is the refractive index of the medium;  $\theta$  is the half angle of the cone of light from the objects. Thus, the smaller the wavelength, the greater the resolving power. For an optical microscope, the resolution is about 0.2  $\mu\text{m}$  or 200 nm, whereas most of the FESEM can go down to 10 nm.

The schematic diagram of FESEM is shown in Figure 1.19. FESEM has a column shape and an electron gun that is being used as a cathode; for its high melting point, it is placed at the top. The cathode has the ability to produce electrons with an energy of 0.1-30 keV. There is a series of electromagnetic apertures and lenses to optimize the diameter of the beam and focus on the sample. To prevent the scattering of the electron by air, a vacuum is created inside the chamber. When the beam impinges on the sample, it produces a variety of signals, such as backscattered electrons, secondary electrons, Auger electrons, characteristic X-rays, visible light, etc. Out of them, backscattered and secondary electrons are collected by the detectors and the high-resolution images of the sample surface are made after several internal processes. The sample preparation for FESEM is easier than other characteristics techniques <sup>130</sup>. Usually, a smooth and thin film of sample is made on glass, metal sheet, or Si substrate. A very thin (~5 nm)

conducting film of gold or platinum is being made on the sample to improve the conductivity, which effectively removes the electrons as well as reduces the effect of space charge.

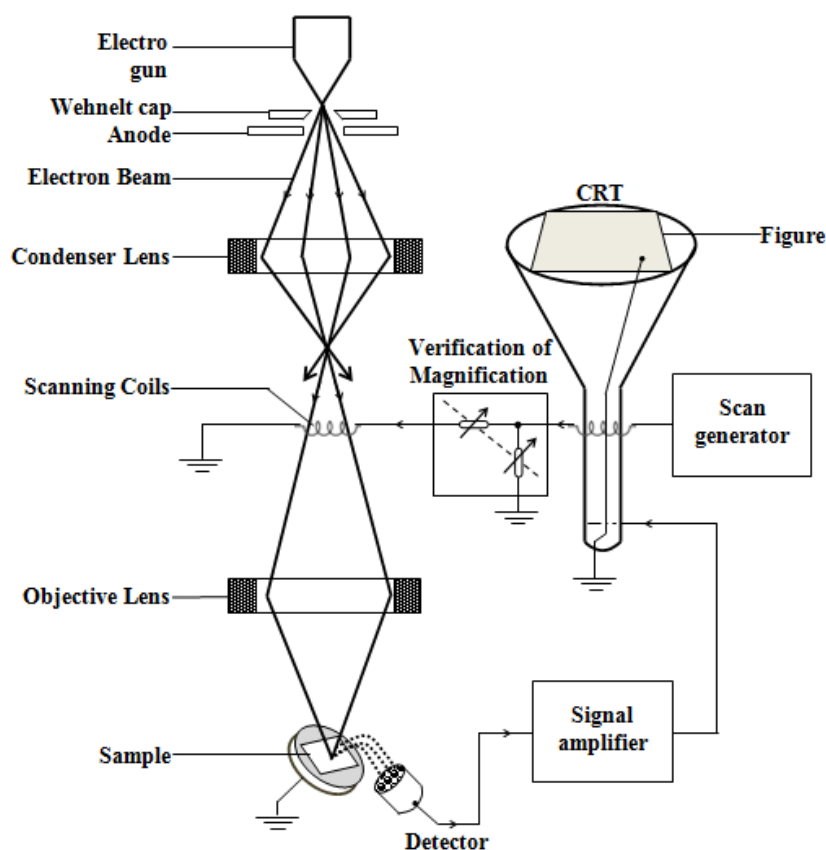


Figure 1.19: Scheme showing the working principle of a FESEM

FESEM has the ability to offer the specimen's topography, morphology, composition, and crystallographic details, among other qualitative data. In other words, it offers details about the texture, shape, size, and organisation of the particles that are present on the sample's surface. It is also possible to offer information on the kinds of elements and compounds the sample contains, their proportions, the arrangement of atoms inside single crystal particles, and the degree of order in those arrangements.

### 1.8.7. X- ray Photoelectron Spectroscopy (XPS) and Ultraviolet photoelectron spectroscopy (UPS)

#### ▪ XPS

XPS is a quantitative analysis technique. This technique is useful in determining empirical formulas, electronic states, chemical states, etc. When a sample is irradiated with X-ray under

an ultra-high vacuum, its inner core electron gets ejected <sup>131</sup>. Measuring the kinetic energy and number of an electron ejected gives the XPS spectra. Generally, electrons having energy in the range of 10 to 2000 eV are detected.

The main parts of the spectrometer are:

1. X-ray source: There are two types of X-ray sources. They are the dual anode x-ray source and the single anode X-ray source. The Main X-ray radiations are Mg K $\alpha$  ( $h=1253.6\text{eV}$ ) and Al K $\alpha$  ( $h= 1486.6\text{eV}$ ). For accurate working of X-rays, some conditions are a must, such as stable vacuum, stable coolant flow, stable filament current, and accelerating voltage.
2. X-ray monochromator: The main types of X-ray monochromators are the Czerny turner (plane multilayer) and the Rowland type (curved multilayer). These two are grating based monochromators. There is some instrument in which Quartz single crystal is used as a monochromator with Al K $\alpha$  radiation. These monochromators are used to obtain monochromatic X-rays.
3. Energy analyzer: Hemispherical analyzers (HA) and cylindrical analyzers (CA) are the two main types of energy analyzers. These energy analyzers transfer XPS-generated electrons from the sample to XPS detectors. So, its efficiency must be high for better performance, which is determined by the transmission function.
4. Detectors: Generally solid-state detectors.

Electrons that are by X-ray radiation after traveling through an energy analyzer strike on the screen. According to their energy, they get distributed along the radius of HA. Detectors detect the intensity and radius, which can be used for further analysis of data. XPS is used to determine the element and amount of that element, the thickness of different layers within the range of 10nm, compositional uniformity, impurity elements, etc. The only limitation of XPS is that it cannot detect hydrogen and Helium. This electron emission mechanism is schematically depicted in the illustration of Figure 1.20.

- **UPS**

It is a simple method to obtain information about the band gap of the material. It uses a UV source of radiation mostly a deuterium lamp and a tungsten lamp for visible light. In place of two lamps, the Xenon lamp is used to irradiate the material with both UV and visible light. Then, by comparing the intensity of incident and transmitted light, we obtain the spectra of absorbance or transmittance as a function of wavelength. Detectors used are mostly CCD cameras, photodiodes, or PMT. The absorbance of light depends upon the band gap of the material as a high band gap absorbance of a lower wavelength is greater and with low band gap absorbance of a higher wavelength is greater.



Figure 1.20: Digital photograph of XPS instrument

There are two types of modes of working, one is single beam and the other one is double beam. In single-beam, mode intensity of the reference beam is measured by removing the sample from the cell; in double beam, there is no need of removing the sample. To determine the band gap of the material from the data, Tauc's plot is used. This is a plot between the incident energy  $h\nu$  and absorbed energy  $(\alpha h\nu)^2$ , where  $\nu$  has different values corresponding to the mode of transmission,  $\alpha$  is the absorption coefficient of the material. There are some linear regions in Tauc's plot extrapolating them to abscissa leads to the onset of absorption of radiation<sup>132</sup>.

This technique is used in different monitoring processes, as with the change in particle size, the amount of light scattered and absorbed by the sample also varies. In the study of

photocatalytic degradation, this is used to determine the decay of dye (degrading material). In some other catalytic processes also it is used to monitor the progress of the process. In both the above processes, the UV-Visible of sample to be under monitoring is taken at some regular interval of time, which tell the decay of material present in the sample with time. A digital photograph of ultraviolet photoelectron spectroscopy.

#### **1.8.8. Thermogravimetric Analysis and Differential Scanning Calorimetry (TGA-DSC)**

TGA-DSC instrumentation combines two techniques, thermogravimetric analysis (TGA) and differential scanning calorimetry (DSC), to provide simultaneous measurements of sample mass and heat flow during heating or cooling. The TGA measures the changes in the mass of a sample as it is heated or cooled, while the DSC measures the heat flow associated with thermal events that occur during the heating or cooling process. The TGA consists of a balance, a furnace, and a temperature controller. The sample is placed on the balance and heated at a constant rate while the balance continuously measures the sample's mass. As the sample undergoes thermal changes, such as decomposition or evaporation, its mass changes, and the TGA records these changes. The TGA can provide information on the thermal stability, decomposition temperatures, and mass loss of a sample.

The DSC measures the heat flow associated with thermal events that occur during the heating or cooling of the sample. The DSC consists of two thermocouples, one placed in the sample and the other in a reference material, both of which are heated or cooled at the same rate. The difference in temperature between the sample and the reference material generates a signal that is proportional to the heat flow. The DSC can provide information on the heat capacity, enthalpy, and melting behavior of a sample.

Combining the TGA and DSC measurements allows for a more comprehensive analysis of the thermal properties and behavior of a sample. The information obtained from TGA-DSC analysis can be used to determine the thermal stability, decomposition temperatures, and heat capacity of a wide range of materials, including polymers, pharmaceuticals, and biomaterials. TGA-DSC can also be used to study the thermal stability of fuels and the kinetics of chemical reactions. In summary, TGA-DSC instrumentation provides a powerful tool for the study of thermal properties and behavior of materials. Its ability to provide simultaneous measurements of mass and heat flow makes it a valuable technique in a wide range of fields.

## 1.9. References

1. N. F. Atta, A. Galal, and E. H. El-Ads, *Prop. Appl.*, 2016.
2. B. Aïssa, A. Ali and F. El-Mellouhi, *Catalysts*, 2021, 11, 9.
3. S. Sarkar & A. K. Singh, *J. of Environ. Chem. Eng.*, 2022, 10(1), 108260.
4. P. M. Woodward, 1997, 142, 1, 1-20.
5. A. M. Glazer, 1972, 28(11), 3384-3392.
6. T. Wu et al., *Nano-Micro Lett.*, 13, 1, 1–18, 2021.
7. Z. Lian, C. Yan and H. Huang, *JMCA*, 2022, 10, 759-779.
8. Y. Chen, J. Wei and Y. Yan, *Journal of Energy Chemistry*, 2021, 60, 55-70.
9. Y. Li & Y. Hu, *Energy & Environmental Science*, 2022, 15, 10-37.
10. X. Wang, Q. Liu and R. Xiong, *Materials Today Physics*, 2021, 19, 100423.
11. W. E. Pickett, 1989, 45, 373-380.
12. A. Kojima, K. Teshima, Y. Shirai and T. Miyasaka, *Journal of the American Chemical Society*, 2019, 131, 6050-6051.
13. V. Goldschmidt, *Zeitschrift für Kristallographie*, 1926, 63, 349-356.
14. A. F. Demirors and A. Imhof, *Chem. Mater.*, 2009, 21, 13, 3002–3007.
15. K. C. Smith & M. J. Weber, *Physical Review*, 1956, 104, 504.
16. M. Cai, D. Cao and C. Ma, 2018, 19, 243-258.
17. Q. A. Akkerman and L. Manna, *ACS Energy Lett.*, 2, 604–610, 2020.
18. J. Ma, X. Wang and H. Xu, *Nature Reviews Materials*, 2021, 6(9), 702-719.
19. A. Kumar, & K. Sreenivas, *Journal of Materials Chemistry C*, 2020, 8(26), 8809-8839.
20. J. Liu, Y. Guo and J. Zhou, *Journal of Materials Chemistry A*, 2021, 9(28), 16232-16256.
21. X. Lu, L. Wang, H. Kim and A. Selloni, *Chemical Reviews*, 2021, 121(7), 4124-4160
22. M. Kumar, B. Kaur and A. Kumar, *Journal: Journal of Materials Chemistry C*, 2022
23. M. Tyunina, *Materials (Basel)*, 13, 1–11, 2020.
24. R. Ranjith Kumar, K. Arumugam, M. Thambidurai and V. Thangadurai, *Materials Research Bulletin*, vol. 102, 2018, pp. 248-254.
25. F. Zhang, Y. Wu, and Z. Shen, *Journal of Materials Chemistry C*, 2022, 10(5), 1265-1291.
26. X. Wang, F. Gao, H. Xie, Y. Li and Y. Li, *Advanced Materials*, 2021, 33(2), 2004151.
27. Z. Wang, J. Zhang, W. Guo, W. Xiang and A. Hagfeldt, *Matter*, 2021, 4, 2, 528–551.
28. T. Miyasaka, M. Ikegami, T. Kondo and A. U. Rahman Md, *Journal of the American Chemical Society*, 2006, 128 (51), 16676-16677.
29. K. Zhu, & Y. Yang, Springer, Cham. 2019, 6, 1
30. J. A. Steele et al., *Accounts Mater. Res.*, 2020, 1, 1, 3–15.
31. B. Saparov & D. B. Mitzi, In *Chemical reviews*, 2016, 116, 7, 4558-4596.
32. D. T. Moore et al., *J. Am. Chem. Soc.*, 2015, 137, 6, 2350–2358, 2015.
33. A. Chilvery, S. Palwai, P. Guggilla, K. Wren, and D. Edinburgh, *Perovskite Mater. Devices Integr.*, 2020, 1–16. doi: 10.5772/intechopen.88500.
34. Y. T. Huang, S. R. Kavanagh, D. O. Scanlon, A. Walsh, and R. L. Z. Hoye, *Nanotechnology*, 2021, 32, 13.
35. J. S. Manser, J. A. Christians, and P. V. Kamat, *Chem. Rev.*, 2016, 116, 21, 12956–13008.
36. X. Yang and D. Wang, *ACS Appl. Energy Mater.*, 2018, 1, 12, 6657–6693.
37. C. J. Yu, *J Phys Energy*, 2019, 1, 2.
38. Z. Zheng, S. Wang, Y. Hu, Y. Rong, A. Mei, and H. Han, *Chem. Sci.*, 2022, 13, 8, 2167–2183.
39. J. Shamsi, A. S. Urban, M. Imran, L. De Trizio, and L. Manna, *Chem. Rev.*, 2019, 119, 5, 3296–3348.
40. N. G. Park, *Mater. Today*, 2015, 18, 2, 65–72.
41. C. Motta, et al. *The Journal of Physical Chemistry Letters* 2017, 8.13, 2999-3007.
42. T. Nakamura, et al. *Journal of Materials Chemistry A* 2018, 6.23, 10883-10888.
43. C. Motta, et al. *Nature Reviews Materials* 2018, 3.9, 18047.
44. H. Wang, Y. A. Rahaq, P. Sharma, Y. Zhou, & J. He, *Journal of Materials Chemistry A*, 2019,

- 7(18), 11276-11284.
45. H. Tsai, W. Nie, J. C. Blancon, C. C. Stoumpos, R. Asadpour, B. Harutyunyan, and J. Even, *Nature*, 2016, 536 (7616), 312-316.
  46. M. I. Dar, M. Arora, O. F. Mohammed, A. G. Kumar, R. S. Gupta, M. S. Seikh, R. H. Bari, and S. A. Shivashankar, *Chemical Society Reviews*, 2016, 45, 23, 6592-6629.
  47. X. Li, D. Bi, C. Yi and T. C. Sum, *Advanced Materials*, 2018, 30(45), 1804779.
  48. A. Biewald, N. Giesbrecht, T. Bein, P. Docampo, A. Hartschuh, and R. Ciesielski, *ACS Appl. Mater. Interfaces*, 2019, 11, 23, 20838–20844.
  49. R. Singh, P. Singh, and G. Balasubramanian, *Comput. Mater. Sci.*, 2022, 213, 111649.
  50. L. Protesescu, S. Yakunin, M. L. Bodnarchuk, F. Krieg, R. Caputo, C. H. Hendon, M. V. Kovalenko, *Nano Letters*, 2015, 15(6), 3692–3696.
  51. Q. Zhang, J. Wang, J. Xu, Y. Zhang, J. Zheng, and R. Xiong, *Advanced Materials Interfaces*, 2019, 6(2), 1801565.
  52. L. M. Herz, *ACS Energy Lett.*, 2017, 2, 7, 1539–1548.
  53. S. D. Stranks, & H. J. Snaith, *Nature nanotechnology*, 2015, 10(5), 391-402.
  54. X. Liu et al., *Nanotechnology Rev.* 2022, 11, 3063–3094,
  55. F. J. Iftikhar et al., *Org. Electron.*, 2021, 91, 106077.
  56. National Renewable Energy Laboratory (NREL), (2020). [Online]. Available: <https://www.nrel.gov/news/program/2020/nrel-charts-pathway-to-slashing-cost-of-iii-v-solar-cells.html>.
  57. X. Li et al., *Adv. Func. Mater.* 2016, 26, 15, 2435.
  58. R. Mukherjee, *Eur. J. Mol. Clin. Med.*, 2020, 07, 07, 3927–3931.
  59. W. Wu, Q. Dai, H. Chen, Z. Wei, J. Zhou, Y. Liu and M. Zhou, *Small*, 2021, DOI: 10.1002/sml.202005228
  60. Y. Wang, X. Yang, L. Sun, X. Jiang, M. Yu, Z. Xie and L. Gao, *Journal of Materials Chemistry C*, 2021, 9(9), 2884-2904.
  61. D. Sun, Y. Zhou, S. Liu, J. Huang, Y. Wang, Z. Yang and X. Sun, *Chemical Society Reviews*, 2019, 48(7), 2160-2187.
  62. J. Fang et al., *Advanced Materials Interfaces*, 2018.
  63. Q. A. Han, M. L. Li, and H. B. Liang, *Sensors (Basel)*. 2019, 19(7): 1618.
  64. T. Miyasaka, & K. Sugiura, *ACS Energy Letters*, 2018, 3(9), 2144-2152.
  65. Y. Li, X. Li, Li Li, X. Ren, and X. Wang, *Chemical Engineering Journal*, 2021, 405, 2021, 126785.
  66. J. Liu, M. Leng, X. Zhang, J. Luo, and H. Zhong, *Advanced Energy Materials*, 2021, 11(14), 2100275.
  67. L. Zhou, Y. Tian, J. Wang, L. Pan, H. Liu, and H. Fu, *Chemical Communications*, 2020, 56(28), 3977-3980.
  68. Y. Zhang, B. Liu, Y. Shi, T. Zhang, L. Guo, and F. Cao, *Journal of Materials Chemistry A*, 2019, 7(7), 3471-3479.
  69. P. Wang, Z. Lu, and H. Zhou, *Journal of Materials Chemistry A*, 2019, 7(22), 13169-13186.
  70. S. Kumar & R. Suriyaprabha, *ACS Sustainable Chemistry & Engineering* (2020).
  71. J. Jiang, et al. *J. Mater. Chem. A* 9, 2021, 10573-10578.
  72. J. Feng, et al. *RSC Adv.* 2018, 8, 3050-3055.
  73. A. Kudo & Y. Miseki, *Chemical Society Reviews*, 2009, 38(1), 253-278.
  74. Y. Yuan, L. Han, L. Zhang, W. Huang, and Y. Yang, *Journal of Materials Chemistry C*, 2017,.
  75. J. Park, I. Kang, M. Kim, & B. Lee, *Advanced Materials*, 2019, 31(47), 1904306.
  76. Y. Liu, Y. Zhang, Y. Wang, Y. Lin, Q. Jiang, W. Zhang and M. Wei, *Journal of Materials Chemistry C*, 2021, 9(5), 1555-1574.
  77. H. Huang, Q. Lin, J. Xing, F. Xie, F. Yan and W. Huang, *Advanced Materials*, 2018, 30(1), 1703580.
  78. X. Zhang, Y. Liu, X. Li, Y. Li, Z. Li, Y. Wei and H. Zhu, *Advanced Optical Materials*, 2019, 7(7), 1801179.
  79. D. Lee, J. Kim, H. Cho, K. Cho, and T. W. Lee, *Advanced Materials*, 2019, 31(12), 1806329.



80. Y. Liu, C. Li, Y. Ji, X. Li, X. Li, and H. Li, *ACS Nano*, 2020, 14(4), 4683-4693.
81. A. K. Gautam & R. K. Sharma, *Journal of Materials Science: Materials in Electronics*, 2017, 28(17), 12663-12680.
82. J. Berry et al., *Adv. Mater.*, 2015, 27, 35, 5102–5112.
83. F. Hao, C. C. Stoumpos, D. H. Cao, R. P. H Chang, and M. G. Kanatzidis, *Nature Photonics*, 2014, 8(6), 489-494.
84. C. C. Boyd, R. Cheacharoen, T. Leijtens, and M. D. McGehee, *Chem. Rev.*, 2019, 119, 5, 3418–3451.
85. W. Zhang, J. Xiong, J. Li, and W. A. Daoud, *ACS Appl. Mater. Interfaces*, 2019, 11, 13, 12699–12708.
86. S. C. Liu et al., *J. Am. Chem. Soc.*, 2019, 141, 45, 18075–18082.
87. J. He, W. H. Fang, R. Long, and O. V. Prezhdo, *J. Am. Chem. Soc.*, 2020, 142, 34, 14664–14673.
88. R. Chen et al., *Nanoscale Adv.*, 2022, 4, 22, 4838–4846.
89. J. F. Galisteo-López, M. Anaya, M. E. Calvo, and H. Míguez, *J. Phys. Chem. Lett.*, 2020, 6, 12, 2200–2205.
90. N. Li et al., *iScience*, 2022, 25, 2, 103753.
91. K. Wang, X. Xu, Z. Li, and X. Li, *Journal of Materials Chemistry C*, 2020, 8(15), 4831-4849.
92. K. Wang, Z. Li, X. Xu, and X. Li, *Energy & Environmental Science*, 2019, 12(10), 2934-2977.
93. A. Babayigit, H.-G. Boyen, and B. Conings, *MRS Energy Sustain.*, 2018, 5, 1, 1–15.
94. R. K. Misra, B. El Cohen, L. Iagher, and L. Etgar, *ChemSusChem*, 2017, 10, 19, 3712–3721.
95. M. R. Filip, D. Y. Qiu, M. Del Ben, and J. B. Neaton, *Nano Lett.*, 2022, 22, 12, 4870–4878.
96. N. Samarth, *Nat. Mater.*, 2017, 16, 11, 1068–1076.
97. Z. Shi and A. H. Jayatissa, *Materials (Basel)*, 2018, 11, 5.
98. C. Ma et al., *J. Mater. Chem. A*, 2019, 7, 15, 8811–8817.
99. C. Zhou et al., *Mater. Sci. Eng. R Reports*, 2019, 137, 38–65.
100. J. Zhang et al., *Nano-Micro Lett.*, 2017, 9, 3, 1–26.
101. X. Liu, Z. Zhang, F. Lin, and Y. Cheng, *InfoMat*, 2021, 3, 11, 1218–1250.
102. C. R. Kagan, D.B. Mitzi, C. D. Dimitrakopoulos, *Science* 2000, 286, 945-947.
103. A. Kojima, K. Teshima, Y. Shirai, and T. Miyasaka, *Journal of the American Chemical Society*, 2009, 131(17), 6050-6051.
104. W. S. Yang, B. Park, E. H. Jung, et al., *NATURE*, 2017, 542, 7641.
105. W. Zhang, G. E. Eperon, H. J. Snaith, and L. M. Herz, *Nature Energy*, 2019, 4(11), 408-418.
106. C. C. Stoumpos, & M. G. Kanatzidis, *Advanced Materials*, 2016, 28(28), 5778-5793.
107. A. Kojima, K. Teshima, Y. Shirai, and T. Miyasaka *JACS*, 2009, 131(17), 6050-6051.
108. Z. Wang, D. Wang, Q. Zhang, X. Sun, and Y. Li, *Nature nanotechnology*, 2017, 12(9), 861-866.
109. C. C. Vidyasagar, B. M. Muñoz Flores, and V. M. Jiménez Pérez, 2018, 10, 4.
110. P. Gao, A. R. Bin Mohd Yusoff, and M. K. Nazeeruddin, *Nat. Commun.*, 2018, 9, 1, 1–14.
111. P. Fu et al., *Nano Energy*, 2021, 88, 106249.
112. F. Cao, P. Zhang, and L. Li, *Fundam. Res.*, 2022, 2, 2, 237–253.
113. T. Kirchartz, *Philos. Trans. R. Soc. A Math. Phys. Eng. Sci.*, 2019, 377, 2152.
114. Z. Li, D. Yang, X. Yang, Y. Ren, X. Wu, J. Xing, and Q. Zhang, *ACS applied materials & interfaces*, 2020, 12(10), 11548-11553.
115. F. Sani, S. Shafie, H. N. Lim, and A. O. Musa, *Materials (Basel)*, 2018, 11, 6,–17.
116. M. A. William, A. W. Azhari, N. S. B. N. Hassan, N. Hasan, D. S. C. Halin, and A. K. Thottoli, *IOP Conf. Ser. Earth Environ. Sci.*, 2021, 920, 1.
117. Q. Zhang, F. Hao, J. Li, Y. Zhou, Y. Wei, and H. Lin, *Sci. Technol. Adv. Mater.*, 2018, 19, 1, 425–442.
118. I. Y. Jeon and J. B. Baek, *Materials (Basel)*, 2010. 3, 6, 3654–3674.
119. X. Ren, Y. Liu, and Y. Yang, *Solar RRL*, 2019, 3(1), 1800189.
120. P. Dwivedi, S. S. Narvi, and R. P. Tewari, *J. Appl. Biomater. Funct. Mater.*, 2013, 11, 3, 129–142.
121. C. I. Idumah and C. M. Obele, *Surfaces and Interfaces*, 2021, 22, 100879.

122. S. Faruk, S. Shafie, L. Hong Ngee and M. Abubakar Ohinoyi, *Materials*, 2018, 11., 6, 1-17.
123. B. D. Cullity, & S. R. Stock, (2001). *Elements of X-ray Diffraction* (3rd ed.). Prentice Hall. ISBN: 978-0201610918.
124. W. L. Bragg, *The Diffraction of Short Electromagnetic Waves by a Crystal*. Proceedings of the Cambridge Philosophical Society, 1913, 17(1), 43-57.
125. A. Popa, R. R. Piticescu, and E. Andronescu, X-ray diffraction techniques for the characterization of nanomaterials. In N. N. Thadhani, Z. G. Moussa, & Y. K. Vohra (Eds.), *Nanomaterials: A Guide to Fabrication and Applications* (pp. 147-180). Springer. 2014, DOI: 10.1007/978-1-4939-0428-3\_7.
126. S. Adachi, *Journal of Applied Physics*, 2006, 100(7), 74104.
127. N. C. Greenham, *Handbook of Conducting Polymers*, edited by T. A. Skotheim (CRC Press, 1998), pp. 95-137.
128. D.B. Williams, C.B. Carter, *Transmission Electron Microscopy: A Textbook for Materials Science*, Springer, 2009.
129. J. M. Zuo and J. C. H. Spence, Springer, 2003.
130. Bentley, Peter M. *Journal of Materials Science: Materials in Electronics* 1991, 2, 1, 3-11.
131. *X-ray photoelectron spectroscopy: An introduction to principles and practices*, Paul van der Heide, Publisher: Wiley-VCH, Year: 2011
132. M. Oshima and A. Nagashima. *Ultraviolet photoelectron spectroscopy: From an experimental tool to a surface science tool*. *Surface Science Reports*, 2005, 56 (6-8), 231-322.

## Chapter 2

### Zwitterionic Cysteamine linker based 2D Organic-Inorganic Perovskitoid for Metal Ion Detection and Photodetector Applications

In this chapter we demonstrate synthesis of a new low-D hybrid perovskitoid (a perovskite-like hybrid halide structure, yellow crystals, P21/n space group) using zwitterion cysteamine (2- aminoethanethiol) linker, and its remarkable molecular diffusion- controlled crystal-to-crystal transformation to Ruddlesden-Popper phase (Red crystals, Pnma space group). Our stable intermediate perovskitoid distinctly differs from all previous reports by way of a unique staggered arrangement of holes in the puckered 2D configuration with a face-sharing connection between the corrugated-1D double chains. The PL intensity for the yellow phase is 5 orders higher as compared to the red phase and the corresponding average lifetime is also fairly long (143 ns). First principles DFT calculations conform very well with the experimental band gap data. We demonstrate applicability of the new perovskitoid yellow phase as an excellent active layer in a self-powered photodetector and for selective detection of Ni<sup>2+</sup> via On-Off-On PL based on its composite with few-layer black phosphorous.

Ref: This chapter is based on the thesis author's own publication, Prachi Kour, Mallu Chenna Reddy, Shiv Pal, Siraj Sidhik, Tisita Das, Padmini Pandey, Shatabdi Porel Mukherjee, Sudip Chakraborty, Aditya D. Mohite, and Satishchandra Ogale, **Angew. Chem. Int. Ed.** **2021**, **60**, **18750–18760**.

## 2.1. Introduction

Hybrid Organic and Inorganic Perovskites (HOIPs),  $ABX_3$  (where,  $A = CH_3NH_3^+$ ,  $C_8H_9NH_3^+$ ,  $CH_5N_2^+$ , ;  $B = Pb^{+2}$ ,  $Sn^{+2}$ ,  $Sb^{+2}$ ,  $Cu^{+2}$ ;  $X = I^-$ ,  $Br^-$ ,  $Cl^-$ ,  $BF_4^-$ ) have rapidly emerged as the leading photovoltaic and optoelectronic device materials in the past decade owing to their exceptional properties such as low exciton binding energy, high absorption coefficient, high carrier lifetime, bandgap tunability, dimensionality control, scalability, and low cost of fabrication due to solution processability.<sup>1-10</sup> The conversion of 3D HOIP to 2D HOIP is achieved by increasing the length of the organic cation (two or more carbon atoms), thus pushing the inorganic ( $PbI_6^-$ ) octahedral layers farther apart and creating a quantum well-like structure with sequentially increasing band gaps. 2D HOIPs have gained considerable attention following the work of Mohite and co-workers, wherein they developed a hot casting technique for better charge transport leading to highly efficient perovskite solar cells and light-emitting diodes.<sup>11,12</sup> Indeed, these 2D systems have already been demonstrated to possess several unique properties such as moisture stability, thermal stability, self-trapping of excitonic features, and long carrier lifetimes. These properties make them highly applicable for LEDs, lasing, and white-light emission applications as well.<sup>13-20</sup> The 2D lead-based HOIPs (tolerance factor,  $t > 1$ ) can form Ruddlesden Popper (RP) type phase (general formula:  $A_{n+1}B_nX_{3n+1}$ ), Dion-Jacobson type perovskite phase (general formula:  $A'A_{n-1}Pb_nX_{3n+1}$ ) or alternating cation type phase (general formula:  $(A'A)_{n+1}B_nX_{3n+1}$ ) by incorporation of long alkyl/aryl-organic monovalent or divalent cations, respectively.<sup>21</sup>

Also, in some cases some degree of strain is imparted to the  $MX_6^-$  octahedra from the organic cations, which leads to distorted octahedra, giving rise to some uniquely interesting electronic density of states and properties. Mao et al. have reported a corrugated 2D hybrid perovskite (DMEN) $PbBr_4$  (2-Dimethylaminoethylamine lead bromide), which exhibited broadband white light emission with an impressive color rendering index (CRI) value of 73.<sup>22</sup> Recently, Tremblay et al. have demonstrated successful incorporation of a mono-cation to form  $(4NPEA)_2PbI_4$  (4-nitrophenyl ethyl ammonium lead iodide) as a  $3 \times 3$  corrugated 2D HOIP, containing regular as well as distorted  $PbI_6^-$  octahedra rendering optical properties similar to the systems containing distorted octahedra.<sup>23</sup> Other than the 2D corrugated systems, recently C. C. Stoumpus et al. have described the existence of the hexagonal perovskite polytypes in tin iodide hybrid perovskites by incorporation of various cations / mixed cation by interesting synthetic strategies of halo acid

reaction of the precursor tin iodide ( $\text{SnI}_2$ ) with varied organic linkers of primary, secondary, tertiary, and quaternary amines.<sup>24</sup>

Kanatzidis and co-workers have also reported some other interesting perovskite-like hybrid halide structure with combinations of the corner, face, or edge sharing octahedral chains, termed as perovskitoids recently.<sup>25,26</sup> The organic molecules, which minimize the octahedral distortion and maximize the interlayer charge transport in 2D HOIPs are generally preferred for their favourable optoelectronic applications.<sup>27</sup> Several reports on the incorporation of organic cations containing a few carbon atoms such as methylammonium (MA), formamidinium (FA), phenyl-ethyl ammonium (PEA), ethylenediamine (en), and 2-aminoethanethiol (AET) highlight the importance of such small molecules in this context.<sup>28-30</sup> Recently, W. Ke et al. enhanced the air stability of the formamidinium tin iodide ( $\text{FASnI}_3$ ) perovskite by the introduction of ethylenediammonium {en} in its 3D  $\text{FASnI}_3$  structure and were able to tune the bandgap of the new system by the incorporation of several defects within the 3D framework, thereby retaining its dimensionality. They also showed the champion solar cell efficiency of {en} $\text{FASnI}_3$  to be 7.14%.<sup>31</sup> Spanopoulos et al. showed a similar {en}-concentration dependent bandgap tuning in MAPI ( $\text{CH}_3\text{NH}_3\text{PbI}_3$ ) while retaining the 3D framework of  $\text{MAPbI}_3$ .<sup>32</sup> Rath et al. showed a 5.0% efficiency of  $\text{MA}_{0.75}\text{FA}_{0.15}\text{PEA}_{0.1}\text{SnI}_3$  perovskite system retaining this efficiency for 5000 h under glove-box conditions and an impressive 87% initial PCE retention.<sup>33</sup> The long chain organic cations have drawbacks such as they act as barriers to electron transport due to the absence of  $\pi$ -electron conjugations and also they are liable to moisture attack when incorporated in the HOIP framework.<sup>34,35</sup> Several benefits of thiol incorporation in HOIP have also been highlighted.<sup>36</sup>

Recently, Cao et al. showed an efficiency of 14.1% under ambient conditions in a mesoporous configuration, with  $\text{HOOC-Ph-SH}$  modifications at the mesoporous- $\text{TiO}_2$ /MAPI and MAPI/spiro-OMeTAD interfaces.<sup>37</sup> They showed that the Pb-S coordination post-thiol-treatment of the HOIP leads to the formation of a hydrophobic barrier, which prevents the infusion of water molecules, thereby preventing degradation. Halder et al. examined the incorporation of thiocyanate anion ( $\text{SCN}^-$ ) in MAPI<sup>38</sup> and found that these  $\text{MAPbI}_{3(1-x)}(\text{SCN})_x$  films show an enhancement in emission quantum yield suggesting a reduction in the non-radiative channels. Li et al. showed the incorporation of 2-AET in  $\text{MAPbI}_3$  as a bridging ligand to facilitate the formation of highly uniform and water stable (> 10 minutes)  $\text{MAPbI}_{3x}\text{-2-AET}$  thin films.<sup>39</sup> Although thiol conjugations

have been explored, to the best of our knowledge, the incorporation of zwitterionic moieties to form 2D hybrid perovskite has not been studied to date, which sets the goal for the present work.

The molecule used in this study for synthesizing structurally and optoelectronically interesting HOIP single crystals is cysteamine (2-aminoethanethiol). This hetero-bifunctional cation (or zwitterion) contains an ammonium group at one end and thiol functional group at the other end of an ethyl chain. The ammonium group derived from amine of cysteamine can be incorporated into HOIP to make cysteamine ammonium cation based hybrids. In addition, thiol is a versatile and selective functional group that can involve in several functionalization reactions with different organic, inorganic reagents, bio, nanosystems which makes a huge difference vis a vis the traditional mostly amino group-containing molecules. The selective functionalization of the free thiol group of the zwitterion cysteamine could be utilized for connecting or conjugating the perovskite systems with other materials (Au, Ag) to form new material systems with interesting features.

Herein, we study the incorporation of zwitterion cysteamine or 2-AET  $\{NH_3-CH_2-CH_2-SH\}$  to form a robust perovskitoid and 2D RP phase of HOIP. We have successfully isolated the intermediate single crystals referred to as the yellow phase  $((HSC_2H_4NH_3)_7Pb_4I_{15})$ , compound **1**, which further converts to the red phase  $((HSC_2H_4NH_3)_2PbI_4)$ , compound **2** when left undisturbed in the mother solution for 2-3 hours. We further propose a mechanism for this phase transformation (yellow to red), as limited by the in-diffusion of the organic cation. The compound **1** perovskitoid structure (layered 2D crystal structure with structural units of perovskite structure) has a unique puckered  $PbI_6^-$  framework comprising of both corner and face-sharing octahedra. Interestingly, under visible excitation of 470 nm, compound **1** is highly luminescent with a large Stokes shift of 47 nm (FWHM 45 nm), while compound **2** is weakly luminescent with a Stokes shift of 38 nm (FWHM 55 nm). The PL intensity of compound **1** is 5 orders of magnitude higher than that of compound **2**, and compound **1** also has an impressively long carrier lifetime component, as revealed by time-resolved photoluminescence (TRPL). First principles DFT calculations match very well with the experimental band gap data. We further demonstrate that compound **1** (perovskitoid) works as an excellent active layer in a self-powered photodetector when sandwiched between PEDOT:PSS and PCBM (optoelectronic functionality) and a composite of compound **1**

with few layer black phosphorous (FLBP) is a very effective On-Off-On photoluminescence (PL) probe for selective detection of  $\text{Ni}^{2+}$ .

## **2.2. Experimental Section**

### **2.2.1. Synthesis of (cysteammonium)<sub>7</sub>Pb<sub>4</sub>I<sub>15</sub> (compound 1)**

The compound 1 was prepared by adding solutions A and B as described as followed. The solution A was prepared by adding an amount of 230.5 mg (1equiv, 0.5 mmol) of  $\text{PbI}_2$  in 3 ml of 57% aqueous HI under constant stirring and heating at 150° C till  $\text{PbI}_2$  dissolved completely. Solution B was prepared to make cysteammonium iodide by adding 116 mg (3 equivalent, 1.5 mmol) of cysteamine to 2 ml of HI and stirred for a few minutes to make it a clear solution. This solution B was added slowly dropwise drop to solution A under constant stirring and heating. The reaction mixture was kept for 30 min under the same conditions. Then the mixture was slowly allowed to room temperature (3-4 °C / h) and kept undisturbed for good quality crystal growth. After half an hour, nice yellow colored crystals were seen to nucleate. After 3-4 hours the crystal growth was completed, good quality of yellow crystals were observed as shown in Figure 2.1(a). The crystals were collected after filtering and washing with ethyl acetate to remove the surface impurities, the resulting compound was vacuum dried before further characterizations.

### **2.2.2. Synthesis of (cysteammonium)<sub>2</sub>PbI<sub>4</sub> (compound 2)**

For the synthesis of compound 2, the same above mentioned method was followed. Further, the solution containing yellow colored crystals of compound 1 was kept undisturbed for 2-3 hours instead of filtering. It was observed that the yellow crystals gradually turned to red colored crystals, apparently via nucleation and growth mechanism. All the crystals turned to red color indicating the formation of compound 2. The red crystals were collected after filtering and washing with ethyl acetate to remove the surface impurities followed by vacuum drying before further characterizations.

### **2.2.3. Preparation of compound 1 and FLBP (Few Layer Black Phosphorous) nanocomposite**

Few layer black phosphorus from black phosphorus crystal is prepared by previous reported method by using probesonication in NMP solvent<sup>40</sup>. The as prepared FLBP were redispersed in

toluene. The nanocomposite was synthesised in two steps firstly, 2 mg of compound 1 was dispersed in toluene by sonication for 2 minutes. Secondly, 0.8 mg of the as prepared FLBP is added to compound 1 dispersion followed by bath sonication at room temperature.

#### **2.2.4. Metal-oleate synthesis**

The Nickel oleate and other metal oleate's were prepared by previously reported protocol <sup>[41]</sup>.

#### **2.2.5. Photo-detector fabrication**

We used an inverted planar architecture ITO/PEDOT:PSS/perovskite-film/PCBM/Cu for the fabrication of self-powered photodetector. First, we prepared the top part of our solar cells consisting of the patterned indium doped tin oxide (ITO, Thin Film Device Inc.) substrates and the hole transporting layer (HTL). The ITO substrates were washed in water, acetone, acetone/ethanol (50:50) and isopropyl alcohol by ultrasonication for 15 min, respectively. The substrates were further dried under argon airflow and treated with UV for 30 min. Then, a PEDOT: PSS was spin-coated on the clean ITO substrates at 5000 revolutions per minute (r.p.m.) for 30 s (layer thickness was about 30 nm). The ITO/PEDOT:PSS substrates were subsequently transferred to an argon-filled glovebox for the rest of the solar cell fabrication process. In the glovebox, the 2D perovskite thin films of about 250 nm thickness was fabricated onto the ITO/PEDOT: PSS substrates by the hot casting approach. The substrates were heated to 120°C, and immediately transferred on the spin coater where 60 µl of the 0.25 M solution was immediately dropped on the rotating substrate at 5000 rpm for 20 sec, followed by deposition of the electron transport layer, PCBM. The PCBM solution was prepared by dissolving 25 mg PCBM in 1 ml of chlorobenzene, followed by overnight stirring at 60°C. A 50µl of the PCBM solution was dropped on the ITO/PEDOT/2D-Perovskite samples and spin-coated at 1000 r.p.m. for 45s to form a thin layer of ~30 nm. The solar cell devices were completed by evaporating a 100 nm layer of aluminum using a shadow mask yielding eight cells of 31.4 mm<sup>2</sup> per 1'x1' area of the sample device.

### **2.3. Results and Discussion**

With the aim of incorporating the thiol-functional group containing ammonium cation into the organic-inorganic hybrid system, the reaction of PbI<sub>2</sub> (1 equivalent) with cysteamine (3 equivalent) in HI solution was carried out at 250°C resulting in the growth of yellow crystals of



$(\text{HSC}_2\text{H}_4\text{NH}_3)_7\text{Pb}_4\text{I}_{15}$  (**1**). The synthesis Scheme along with the physical appearance of yellow crystals before and after filtration is shown in Figure 2.1(a, b), Scheme 1.

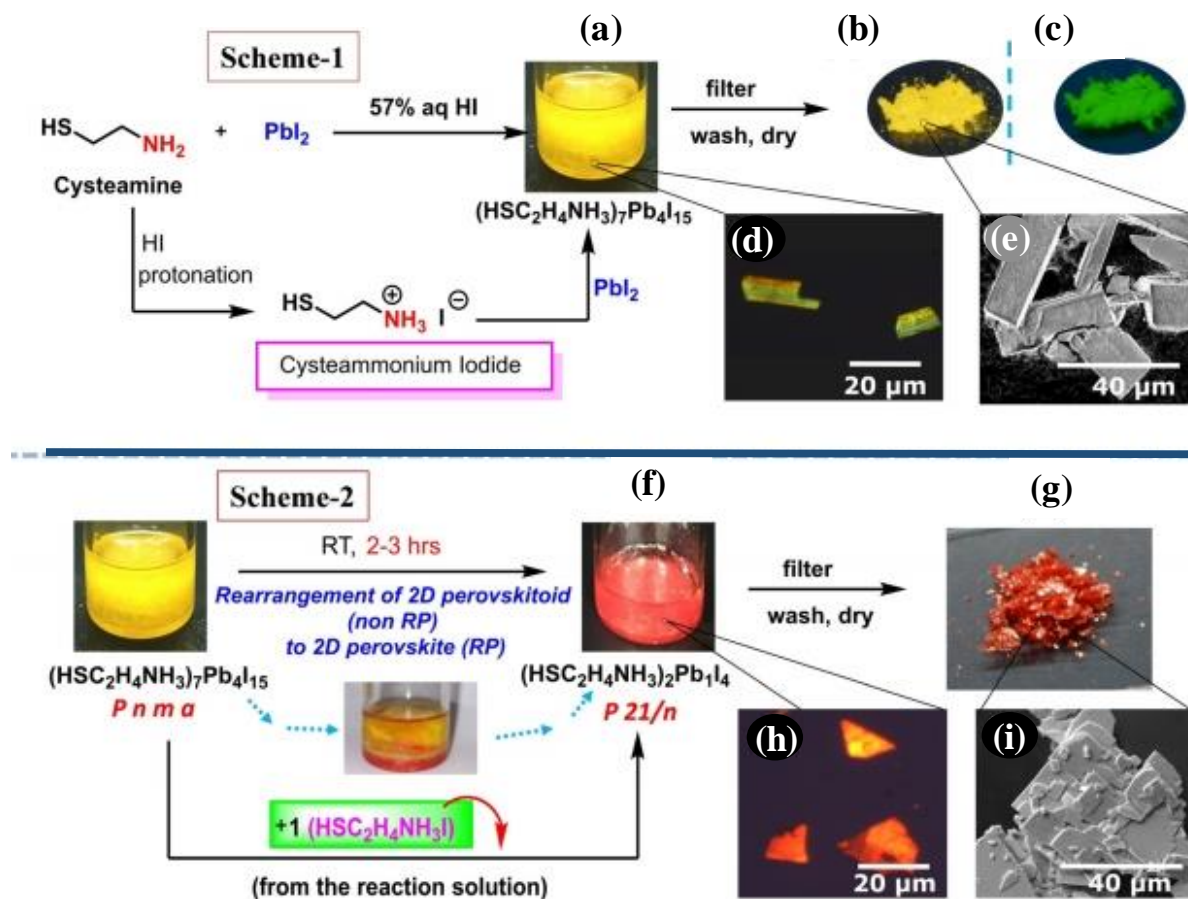


Figure 2.1: Scheme 1: the reaction and formation of  $(\text{HSC}_2\text{H}_4\text{NH}_3)_7\text{Pb}_4\text{I}_{15}$  (**1**); (a) Crystals of **1** formed in the reaction solution, (b) compound **1** in the ambient, (c) under the 265 nm UV lamp showing green emission; (d) polarised microscopy images; (e) FESEM image for **1**; Scheme 2: the conversion of yellow crystals **1** ( $(\text{HSC}_2\text{H}_4\text{NH}_3)_7\text{Pb}_4\text{I}_{15}$  (2D perovskitoid)) into red crystals **2** ( $(\text{HSC}_2\text{H}_4\text{NH}_3)_2\text{Pb}_1\text{I}_4$  (2D perovskite)) in the mother solution; (f) RP phase crystals **2** in solution; (g) Compound **2** crystals under ambient light after filtration; (h) polarized microscopy images, (i) FESEM image for **2**.

Compound **1** is green-emitting, as seen under the UV light [Figure 2.1(c)] initially and studied later in this work. Figure 2.1(d) shows the confocal microscopy images obtained under polarised microscopy indicating well-faceted single crystals for further analysis. Following the appearance of the yellow crystals in the solution, it was allowed to settle for 2–3 hours without any changes in the environmental conditions or additives. An interesting transformation of the yellow crystals into

the red crystals was observed in the solution at room temperature after 2–3 hours, as shown in Figure 2.1, Scheme 2. Our analysis showed that the non-Ruddlesden Popper (RP) 2D perovskitoid gradually got converted into RP-like 2D perovskite ( $n = 1$ )  $(\text{HSC}_2\text{H}_4\text{NH}_3)_2\text{PbI}_4$ . Recently, Kanatzidis and co-workers have reported the transformation of RP ( $n = 1$ ) perovskite to a corrugated structure by using *N,N*-dimethylethylenediamine (DMEN) cation, wherein both phases maintained the perovskite structure without losing corner-sharing. The important distinction in our case is that along with the structural change, the perovskitoid form (which is a non-perovskite) got transformed into a RP perovskite structure indicating crystal-to-crystal rearrangements in HOIP systems.

Moreover, in the work of Kanatzidis and co-workers, the molecular formula of the two phases b-(DMEN) $\text{PbBr}_4$  and a-(DMEN) $\text{PbBr}_4$  before and after conversion is the same.<sup>22</sup> Such phase changes ( $\alpha$ ,  $\beta$ ,  $\gamma$ ,  $\delta$ ) have been reported in the colloidal state by varying the temperature.<sup>36</sup> However, quite surprisingly, as explained below, in our case the molecular formula is also changed upon conversion, which indicates that this is an incorporative transformation via molecular in-diffusion, which is distinctly different from a stoichiometry-preserving phase change, as previously reported.<sup>22, 40–42</sup> We further solved the crystal structure to obtain the molecular formula of **1**,  $(\text{HSC}_2\text{H}_4\text{NH}_3)_7\text{Pb}_4\text{I}_{15}$  [CCDC No. 1951646] which is short by one cysteammonium iodide vis a vis the four formula units of the red crystallites of compound **2**,  $(\text{HSC}_2\text{H}_4\text{NH}_3)_2\text{PbI}_4$  [CCDC No. 1951645]. This suggests that the cysteammonium iodide diffusing slowly from the solution into the (intermediate) yellow crystal renders the crystal-to-crystal rearrangement leading to the transformation of compound **1** to compound **2**. The physical appearance of red crystals before and after filtration, and the confocal microscopy images obtained under polarised microscopy are illustrated in Figure 2.1 (f, g, h). FESEM images show thin rectangular platelet-like and sheet-like morphology for compounds **1** and **2** [Figure 2.1 (e, i)]. The experimental and simulated X-ray diffraction patterns of **1** and **2** were matched to check the purity of the dried compounds [Figure 2.2 (a, b)]. The PXRD patterns matched well with the simulated pattern with no detectable impurity peaks. Thus, the crushed crystalline powder faithfully retains its original crystal structure.

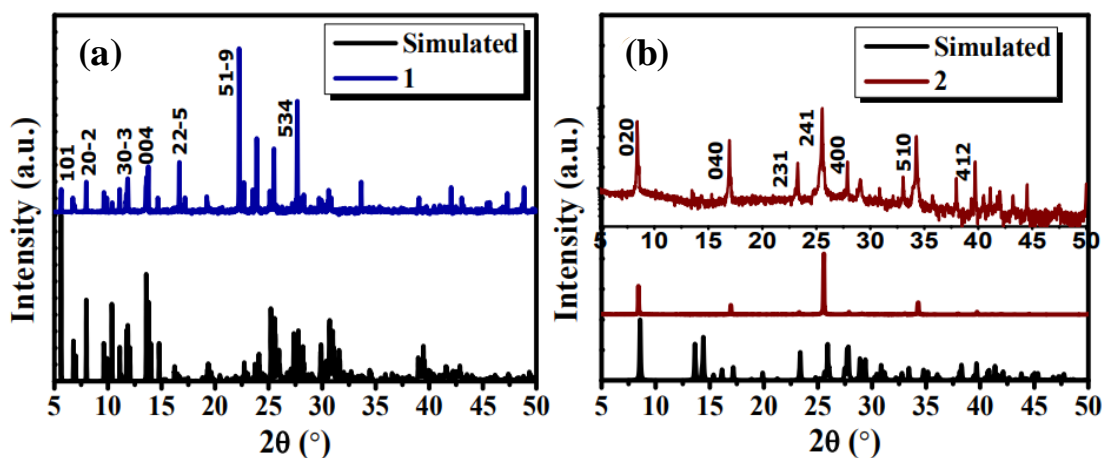


Figure 2.2: Powder X-Ray Diffraction and simulated XRD patterns for (a) **1**, (b) **2**. Top graph in (b) is log scale intensity pXRD pattern

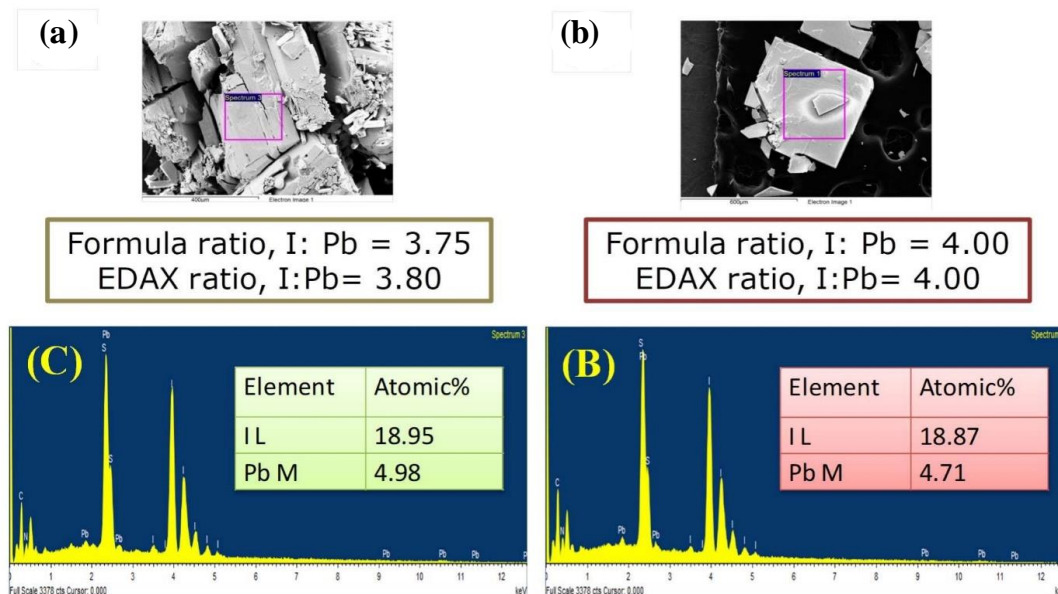


Figure 2.3: Top view of FESEM image of as-synthesized crystals morphology and I to Pb ratio from formula (obtained from SXRD) (a) **1**, (b) **2**, Showing EDAX image of crystals with atomic % of Pb M and I L of **1**, **2** (c, d).

The I: Pb stoichiometric ratio of crystals of **1** from SEM (EDAX) data is 3.75 [Figure 2.3(a)] and that for **2** it is 4.00 [Figure 2.3(b)] which approximately matches with the corresponding single crystal composition.

In general, the reaction of metal (II) halide ( $\text{MX}_2$ ) with cysteamine leads to the formation of organometallic complexes, which are involved in the formation of the thiolate in the presence of base NaOH and this is followed by halide replacement and coordination of  $\text{NH}_2$  to the metal as shown in Figure 2.4(a). This is a competitive reaction for the growth of the organic-inorganic hybrid structure with cysteamine incorporation. The reactive behaviour of cysteamine is very interesting and varies from basic to acidic medium. In the acidic medium (in HI solution), it generates cysteammonium iodide (cysteaminehydroiodide) salt from zwitterion by protonation of thiolate group or neutral molecule by the neutralization of the amine group. The mechanism showing the formation of cysteammonium ion from the zwitterion and neutral molecule of cysteamine is shown in Figure 2.4(b). In the following step, the in situ formed cysteammonium iodide in the reaction mixture reacts with  $\text{PbI}_2$  to form a new cysteamine incorporated HOIP, the compound **2** ( $\text{HSC}_2\text{H}_4\text{NH}_3^+$ ) $_7\text{Pb}_4\text{I}_{15}$ . This schematic of the diffusion of cysteammonium is presented in Figure 2.4(b).

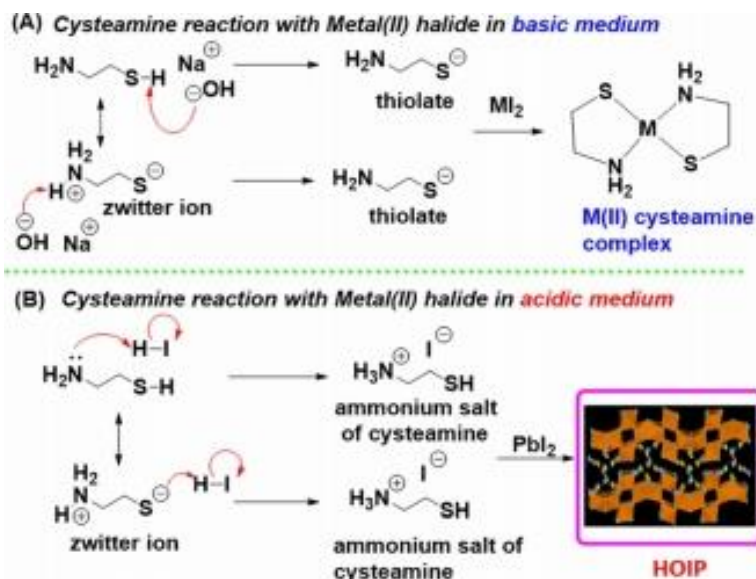


Figure 2.4: The variation between cysteamine reaction with metal(II) halide in (a) basic medium and (b) acidic medium with the possible mechanism; (a) cysteamine with base (NaOH) generates thiolate

intermediate which forms  $M^{II}$  cysteamine complex with  $MI_2$ ; (b) cysteamine with acid (HI) generates cysteammonium iodide salt, which forms HOIP with  $PbI_2$ .

### 2.3.1. Crystallographic Analysis

The structural features obtained from single crystal data of **1** are illustrated in Figure 2.7(a). The complete crystallographic data for compound **1** is given in Table 2.1.

Compound name	(HS-C <sub>2</sub> H <sub>4</sub> -NH <sub>3</sub> ) <sub>7</sub> Pb <sub>4</sub> I <sub>15</sub> <b>1</b>	(HS-C <sub>2</sub> H <sub>4</sub> -NH <sub>3</sub> ) <sub>2</sub> PbI <sub>4</sub> <b>2</b>
CCDC number	1951646	1951645
Identification code	aaa_a	PK16_a
Empirical formula	C <sub>14</sub> H <sub>56</sub> I <sub>15</sub> N <sub>7</sub> Pb <sub>4</sub> S <sub>7</sub>	C <sub>4</sub> H <sub>16</sub> I <sub>4</sub> N <sub>2</sub> PbS <sub>2</sub>
Formula weight	3274.29	871.10
Temperature	150(2) K	150(2) K
Wavelength	0.71073 Å	0.71073 Å
Crystal system	monoclinic	Orthorhombic
Space group	'P 21/n'	'P n m a'
<i>a</i>	26.768(9) Å	12.9729(5) Å
<i>b</i>	9.238(3) Å	20.6291(9) Å
<i>c</i>	27.595(11) Å	6.4366(3) Å
<i>α, β, γ</i>	90°, 109.164(9)°, 90°	90°, 90°, 90°
Volume	6445(4) Å <sup>3</sup>	1722.56(13) Å <sup>3</sup>
<i>Z</i>	4	4
Crystal size	170x110x56 mm	210x138x30mm
Density (calculated)	3.374 Mg/m <sup>3</sup>	3.359 Mg/m <sup>3</sup>
Absorption coefficient	17.849 mm <sup>-1</sup>	17.179 mm <sup>-1</sup>
F(000)	5676	1520
Theta range for data collection	0.920 to 28.464°	3.141 to 28.318°

<b>Index ranges</b>	-34<=h<=35 -12<=k<=12 -37<=l<=36	-17<=h<=14 -26<=k<=27 -8<=l<=8
<b>Reflections collected</b>	113404	36702
<b>Independent reflections</b>	16182 [R(int) = 0.1034]	2201 [R(int) = 0.0553]
<b>Completeness to theta = 25.242°</b>	99.4 %	99.6%
<b>Refinement method</b>	Full-matrix least-squares on F <sup>2</sup>	Full-matrix least-squares on F <sup>2</sup>
<b>Data / restraints / parameters</b>	16182 / 244 / 514	2201 / 0 / 66
<b>Goodness-of-fit on F<sup>2</sup></b>	1.056	1.081
<b>Final R indices [I&gt;2sigma(I)]</b>	R1 = 0.0493, wR2 = 0.1132	R1 = 0.0259, wR2 = 0.0647
<b>Final R indices (all data)</b>	R1 = 0.0733, wR2 = 0.1316	R1 = 0.0321, wR2 = 0.0681
<b>Largest diff. peak and hole</b>	3.050 and -4.127 e.Å <sup>-3</sup>	1.612 and -2.045 e.Å <sup>-3</sup>

Table 2.1: Crystal data and structure refinement for (HS-C<sub>2</sub>H<sub>4</sub>-NH<sub>3</sub>)<sub>7</sub>Pb<sub>4</sub>I<sub>15</sub> (**1**), (HS-C<sub>2</sub>H<sub>4</sub>-NH<sub>3</sub>)<sub>2</sub>PbI<sub>4</sub> (**2**)

Analysis reveals that compound **1** crystallizes with a centrosymmetric monoclinic P system in the *P21/n* space group with lattice parameters  $a = 26.768(9) \text{ \AA}$ ,  $b = 9.238(3) \text{ \AA}$ , and  $c = 27.595(11) \text{ \AA}$ , respectively. The asymmetric unit consists of seven cysteammonium cations along with one Pb<sub>4</sub>I<sub>15</sub> inorganic moiety (Figure 2.5), and it shows a clear charge balancing framework, where Pb<sub>4</sub>I<sub>15</sub> contributes +7 charge and 7 cysteammonium cations contribute -7 charge. Our newly synthesized hybrid structure **1** features PbI<sub>6</sub><sup>-</sup> octahedra that are uniquely connected in both face and corner sharing moieties. This configuration is different from the perovskites that configure only corner sharing PbI<sub>6</sub><sup>-</sup> octahedra. Hence the nomenclature used to describe our structure is perovskitoid, as indicated in some recent papers.<sup>24, 43</sup> Interestingly, our structure has an additional peculiar feature that separates it from all the previous reports on perovskitoids. We have a peculiar staggered

arrangement of holes in the puckered 2D configuration as shown in Figure 2.6(a), 7(a, b). The 2D net like puckered structure is thus uniquely formed with the face sharing connection between corrugated-1D double chains, as shown in Figure 2.7(d).

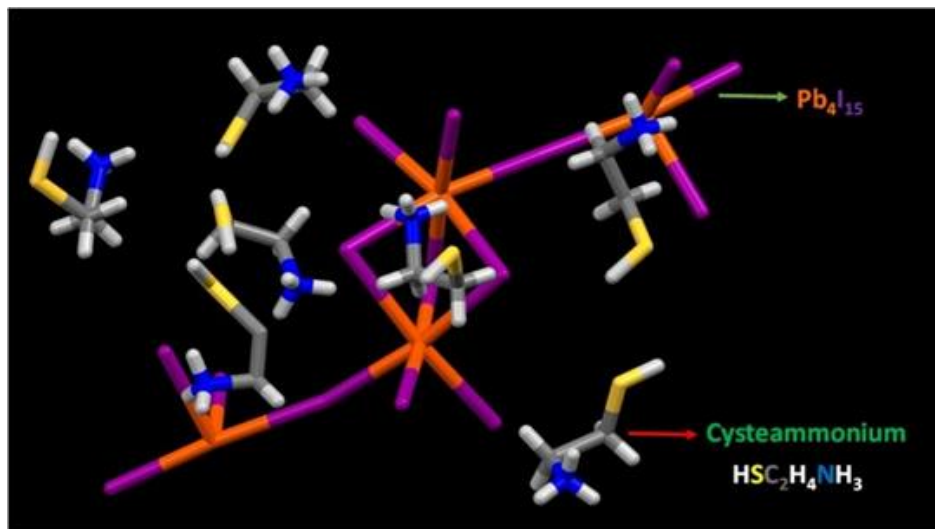


Figure 2.5: The asymmetric unit of **1** from X-ray crystal data showing with 7 cysteammonium cations and one  $\text{Pb}_4\text{I}_{15}$  inorganic part.

The  $\text{PbI}_6^-$  octahedra connected with two adjacent octahedra through corner-sharing are seen to form a 1D zigzag chain. This is further connected [chain 1 in Figure 2.7(d)] to another 1D zigzag chain [chain 2 in Figure 2.7(d)] to form a nanowire, which can be considered as a corrugated-1D double chain structure.<sup>24, 44</sup>

The alternate octahedra of the two zigzag chains participate in face sharing connectivity, while the other alternating free octahedra lead to the formation of a unique inorganic network with small cave/cup type of arrangement, with the caves alternating in opposite directions to each other throughout the 2D net [Figure 2.7(a)]. All the other alternate octahedra stand free without connection; bringing a uniquely interesting look to the total framework [Figure 2.7(d)]. The adjacent nanowires are twisted with a twisting angle of  $64.92^\circ$  at face sharing. To give a clear view and understanding of the inorganic layer, a model was made and is presented in Figure 2.8. The inorganic puckered layer with cups directed in and out alternately as in the present 2D perovskitoid structure mimics a model reflected by a typical egg box with rows arranged alternatively opposite to each other, as shown in Figure 2.8.

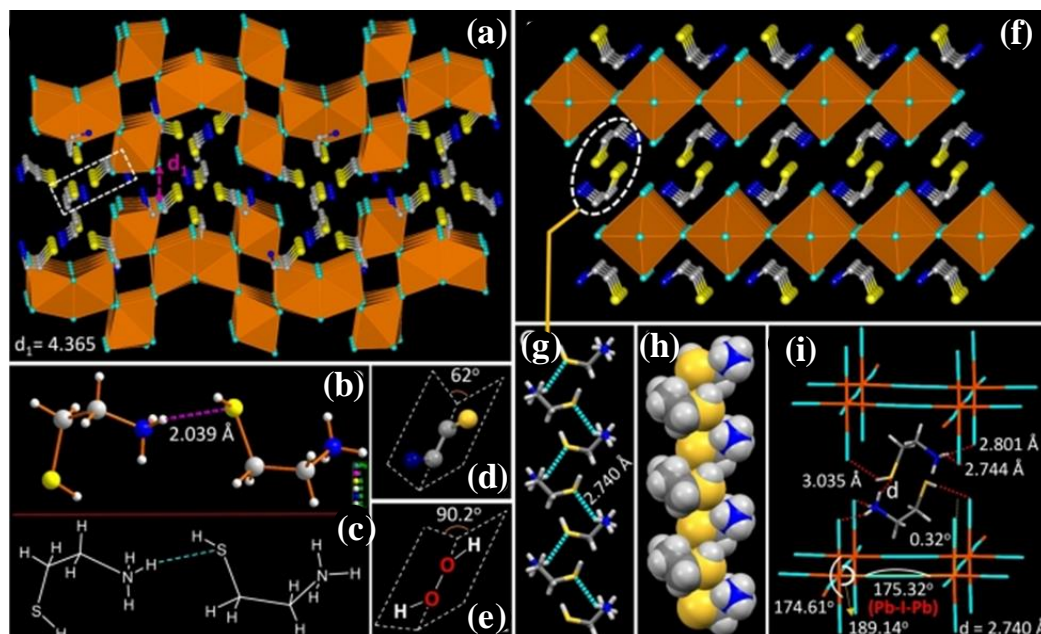


Figure 2.6: The crystal structure of **1**, (a)  $(\text{HSC}_2\text{H}_4\text{NH}_3)_7\text{Pb}_4\text{I}_{15}$  featuring with  $\text{PbI}_6^-$  octahedra are uniquely connected in both face and corner sharing moieties to form 2D perovskitoid HOIP with 4.365 Å of a minimum distance between two inorganic layers; (b) the dimeric cysteamine unit present between  $\text{Pb}_4\text{I}_{15}^{7-}$  puckered layers with hydrogen bonding distance of 2.039 Å; (c) chemical structure representation of dimeric cysteamine unit; (d) open book structure of  $\text{H}_2\text{O}_2$ ; (e) slightly open book structure of  $\text{N}_1\text{C}_2\text{C}_1\text{S}_1$  skeleton of cysteamine; (f) The crystal structure of **2**,  $(\text{HSC}_2\text{H}_4\text{NH}_3)_2\text{PbI}_4$  featuring the  $\text{PbI}_4^{2-}$  plat inorganic sheets are separated by two consecutive organic cysteammonium layers; (g) The unique helical-type of polymeric organic network with hydrogen bonds of cysteamine in capped sticks model and (h) space fill model; (i) H-bonding interactions between organic and inorganic layers, I-Pb-I angles and out of plane distortion ( $0.32^\circ$ ).

The other organic part formed between two inorganic puckered layers consists of two types of cysteammoniums, that is, dimeric units of cysteammonium through hydrogen bonding with hydrogen bonding distance of 2.039 Å, and isolated cysteammonium units as shown in Figure 2.6(b, c). Moreover, the cation size, length of alkyl groups, and shape of the cation skeleton structure, all play an important role in rendering a new type structure of HOIPs with interesting structural and optoelectronic properties.<sup>24, 45, 46</sup>



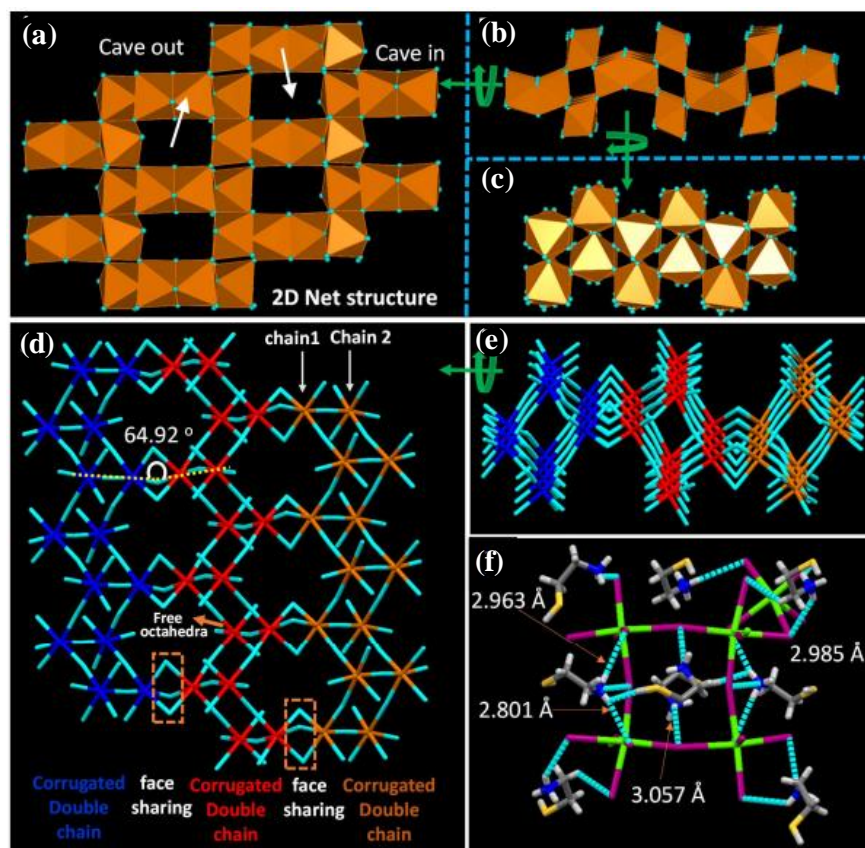


Figure 2.7: (a) Showing the crystal structural features of compound **1**, 2D net structure with caves out and in type of arrangement viewing from the top side of the inorganic layer; (b) Front view of the inorganic layer; (c) Side view of the inorganic layer; (d) Showing chain 1 and chain 2 to form 1D Corrugated double, the corrugated double chains connecting through face sharing, twisting angle between two Corrugated double chains, the free octahedron; (e) capped sticks model of the front view of the inorganic layer; (f) The capped stick model showing with all electrostatic forces and Van der Waals interactions between organic-inorganic and organic-organic moieties of a yellow crystal.

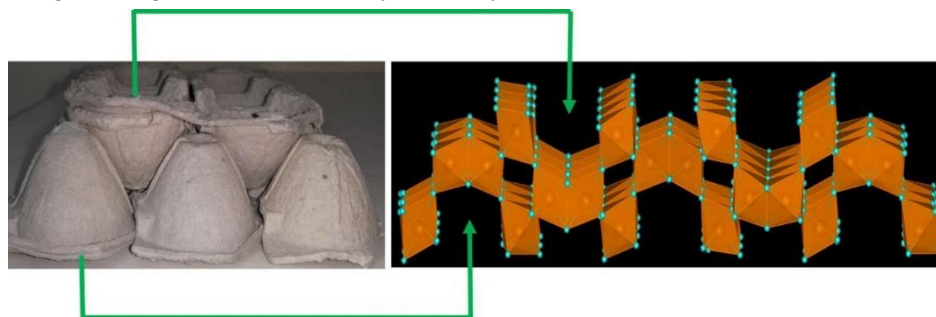


Figure 2.8: The inorganic pucker layer of **1** (right) mimicking with a 2D sheet model made by a typical egg box rows arranged in oppositely to each other in alternatively (right).

The interesting feature of cysteammonium ion is that it has a peculiar structural shape that is, like an open book type structure of  $N_1C_2C_1S_1$  skeleton with  $\approx 65^\circ$  angle between two covers containing  $N_1$  and  $S_1$  on each side, connected with  $C_1C_2$  bond on the spine [Figure 2.6(d)]. So far this special structural shape is limited to only a few molecules; one well known example being  $H_2O_2$  which exhibits open book structure with  $90.2^\circ$  between covers in the crystal [Figure 2.6(e)]. The structural features extracted from the single crystal data for compound **2** are presented in Figure 2.6(f). Table 2.1 gives complete crystallographic data for compound **2**. The phase transformation changes the crystal system from a monoclinic P system in the  $P21/n$  space group to an orthorhombic P system in the  $Pnma$  space group with lattice parameters  $a = 12.9729(5) \text{ \AA}$ ,  $b = 20.6291(9) \text{ \AA}$  and  $c = 6.4366(3) \text{ \AA}$ , respectively. Most interestingly, the yellow to red (perovskitoid to RP) solid state crystal-crystal transformation changes all the structural features of inorganic as well as organic part. The puckered inorganic layer with corner- and face-shared connectivity gets changed into a planar layered structure.

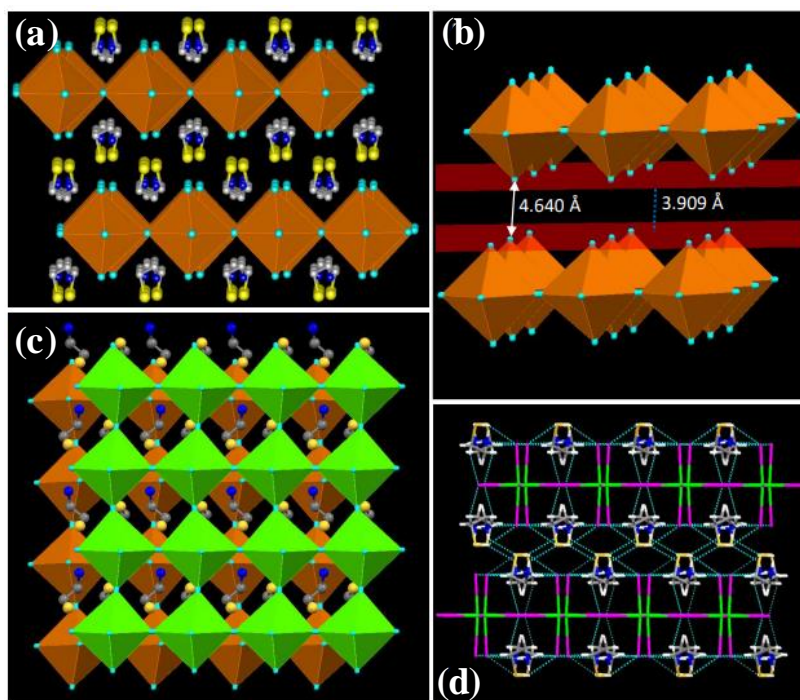


Figure 2.9: (a) Showing crystal structure features of **2**; (b) The side view of the 2D layered crystal structure of  $(HSC_2H_4NH_3)_2PbI_4$  (staggered arrangement); (c) The top view showing inorganic plat layers are in a staggered arrangement; (d) Interlayer distance between the 2D inorganic sheets (It is the distance between two planes with terminal Iodines of two inorganic sheets) ( $3.909 \text{ \AA}$ ) and closest  $I \cdots I$  distance ( $4.640 \text{ \AA}$ ). The

stick model showing with all electrostatic forces and Van der Waals interactions between organic-inorganic and organic-organic moieties of the Ruddlesden-Popper phase of red crystal.

Compound **2** adopts a structure where the layer is formed with corner-shared octahedra and the cysteammonium acts as a spacer between the two layers, stabilizing the total framework by electrostatic forces (between negatively charged head, namely the terminal iodide, and the positively charged head, namely  $\text{NH}_3$ ) and van der Waals interactions between the organic molecules (Figure 2.9). Upon diffusion of the cysteammonium iodide into the crystallites of **1**, the cysteammonium dimers and isolated cysteammonium units of **2** get nicely rearranged into a unique helical-type of polymeric organic network which is formed through the intermolecular interactions between S and H of  $\text{NH}_3$  groups @ 2.740 Å (weak hydrogen bonding), as shown in Figure 2.6(g, h). In the 2-(dimethylamino)ethylamine (DMEN) case, RP 2D perovskite with flat inorganic sheets is a kinetically favoured product.<sup>22</sup> On the other hand, the use of cysteammonium cation changes the phenomenon drastically and the RP 2D perovskite containing planar inorganic sheets acts as a thermodynamically stable product. Interestingly, the yellow crystals after filtration do not get converted into red crystals, due to the absence of reaction solution (excess molecules to impart required small but important stoichiometry change). Thus, it is a stable material for utilization in any viable application. This is an additional benefit of the present work, where two different and interesting materials are synthesized, starting with one set of precursor materials and using a single method with time domain control (Figure 2.10).

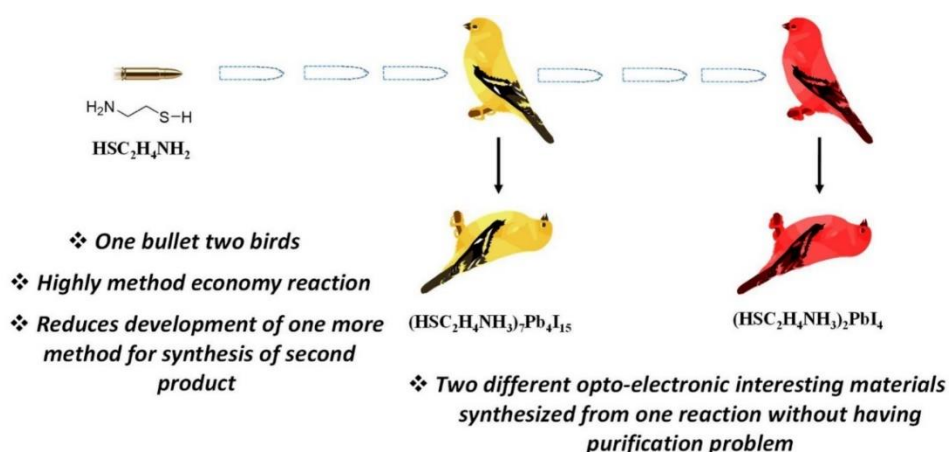


Figure 2.10: The economic benefit of this scheme of synthesis

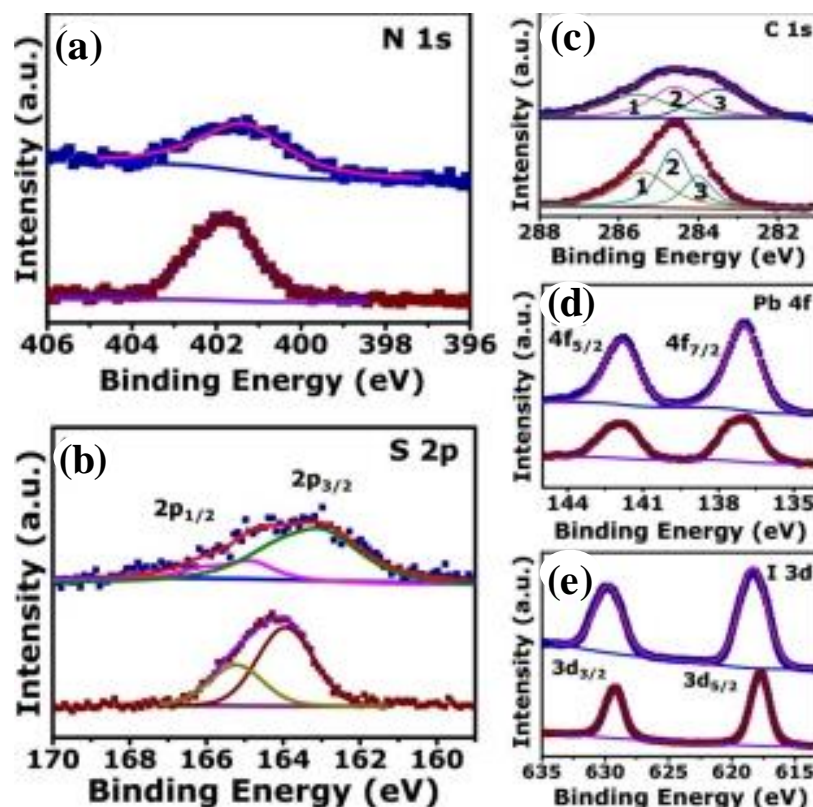


Figure 2.11: XPS core level spectra for compound **1** and compound **2** the Carbon correction C1s=284.6 eV for all spectra, (a) N 1s; (b) S2p; (c) C 1s; (d) Pb 4f and (e) I 3d.

The XPS spectra for both the compounds **1** and **2** were recorded to identify the subtle changes in the chemical environments of cysteamine molecules. In N1s spectra, we can observe only a single peak assigned to  $\text{NH}^{3+}$  for both the crystal systems [Figure 2.11(a)].<sup>47, 48</sup> There is a shift of the peak at 401.44 eV noted for compound **1** to 401.86 eV in the case of compound **2** resulting from the change in the state of  $\text{NH}^{3+}$  moiety from being relaxed in **1** to more ordered state in **2**.<sup>49</sup> The S2p spectra, for compound **2** have the standard thiol binding energies (BE) [Figure 2.11(b)]. But the S2p spectra for compound **1** has slight shifting for these peaks to lower B.E. due to the more distorted bonds in this crystal system. Surface oxidation is more likely to occur in **1** since out of the two types of -SH bonds one is attracted to N by weak van der Waals attraction, whereas the other type of thiol is free to undergo oxidation during the course of the experiment which can be pointed out by the appearance of **2** peaks in the spectra.<sup>50</sup> The C1s spectra for compound **1** can be deconvoluted into 3 peaks, at 285.56 eV (C-N) (1) 284.6 eV (C-C) (2) and 283.48 eV (C-S) (3) [Figure 2.11(c)]. The corresponding spectra for compound **2** show a 0.5 eV shift to higher B.E. for

C-S bond indicating a lower bond electronegativity resulting from the vander Waals interaction with its more electronegative neighbouring N {N.S atomic distance 3.39 Å }. The C-N bond shows a shift to lower B.E. by 0.18 eV due to its electrostatic attraction with adjacent  $\text{PbI}_6^-$  octahedron. Out of the Pb4f [Figure 2.11(d)] and I3d [Figure 2.11(e)] spectra, it can be seen that the I3d spectrum concurs with a higher order of shifting due to the more protected environment of  $\text{Pb}^{+2}$  cation in the octahedron.<sup>51</sup>

The corrugated arrangement of  $\text{PbI}_6^-$  octahedron in compound **1** implies a weaker Pb-I interaction therein. The inclusion of cysteamine molecules in both the crystal systems was further examined by ATR-IR spectroscopy (Figure 2.12). The cysteamine peaks are present in both the spectra as reflected by the vibrations for the N-H stretching at  $3735.42\text{ cm}^{-1}$ , C-H stretching at  $2999.13\text{ cm}^{-1}$ , S-H stretching at  $2329.31\text{ cm}^{-1}$ , and N-H bending at  $1698.21\text{ cm}^{-1}$ . Surprisingly only the C-H stretching peak showed a major difference due to changes in the dipole moment of the bonds attributed to their differential interactions with the neighbouring  $\text{PbI}_6^-$  octahedra as reflected in the XPS discussion.

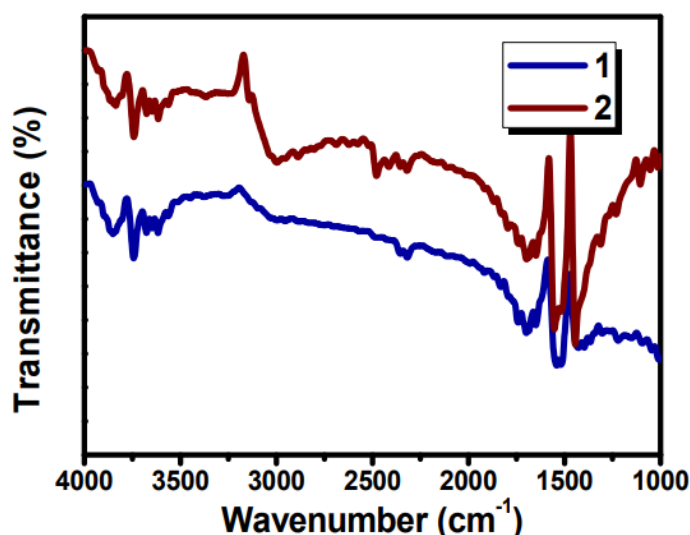


Figure 2.12: FTIR spectra for **1** and **2** crystal systems

### 2.3.2. TGA & DSC

To examine the thermal stability properties of the newly synthesized crystals **1** and **2**, thermogravimetric analysis (TGA) was performed from room temperature (RT) up to  $600\text{ }^\circ\text{C}$  under nitrogen flow and the results are shown in Figure 2.13.<sup>52</sup> The decomposition temperatures of

compound **1** and **2** are almost same because it is directly related to the acidity of the organic cation, which is same in both compounds; they being stable up to 252°C. However, interestingly, despite the organic cation being the same in both the compounds, the decomposition of cysteammonium iodide in **1** occurred from 252°C to 330°C, while that of **2** occurred from 252°C to 415 °C; a huge difference of around 85°C. This can be attributed to the polymeric helical structural arrangement of the cation in **2** which requires a higher temperature range to decompose; while the cation arrangement in **1** is in the form of dimeric and monomeric units.

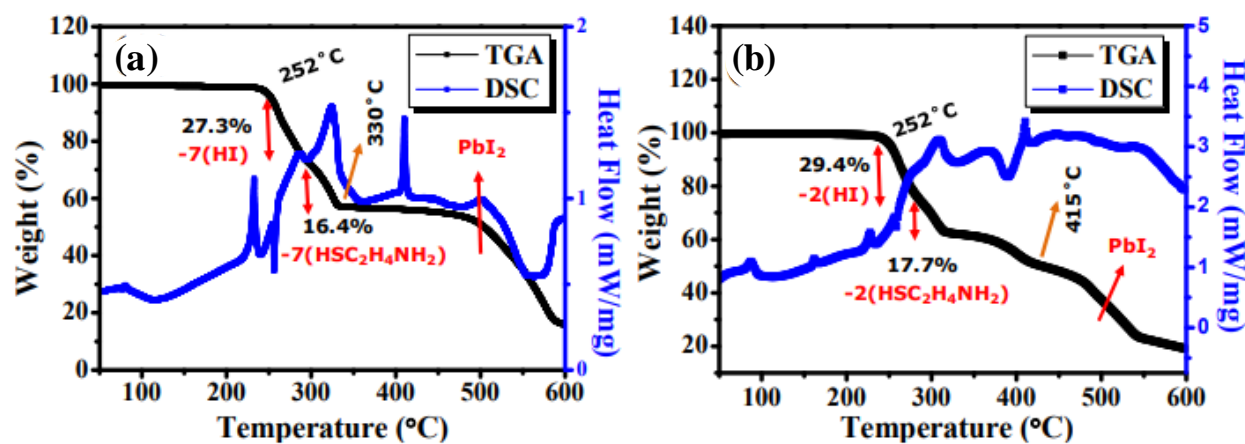


Figure 2.13: TGA and DSC data of (a) compound **1**; (b) and **2** showing with mass loss steps corresponding to HI, Cysteamine and PbI<sub>2</sub>

(TGA) The thermal decomposition of **1** involves with loss of organic salt (cysteammonium iodide) and PbI<sub>2</sub>. The decomposition of cysteammonium iodide which gets incorporated into the perovskite structure should be the sequential loss of HI followed by the organic part.<sup>3,4</sup> The first step of rapid mass change from 252 °C to 275 °C is due to the loss of HI which is around 27.3% (7 HI molecules) of the weight of (HSC<sub>2</sub>H<sub>4</sub>NH<sub>3</sub>)<sub>7</sub>Pb<sub>4</sub>I<sub>15</sub>, as shown in Figure 2.13(a). The following step of rapid mass change from 275 °C to 330 °C is due to the loss of organic ammonium (cysteamine) which is around 16.4% (7 HSC<sub>2</sub>H<sub>4</sub>NH<sub>3</sub> molecules) weight of (HSC<sub>2</sub>H<sub>4</sub>NH<sub>3</sub>)<sub>7</sub>Pb<sub>4</sub>I<sub>15</sub>. Finally, the last step starts rapidly at around 490 °C which is attributed to the thermal decomposition of the lead iodide which is completed at 600 °C.

The identical thermal behavior corresponding to the loss of HI, cysteamine, and PbI<sub>2</sub> is also reflected in the data of differential scanning calorimetry (DSC) shown in Figure 2.13(a). The TGA results of **2** are shown in Figure 2.13(b). The first step of rapid mass change from 252 °C to 296

°C is due to the loss of HI which is around 29.4% (2 HI molecules) of the weight of  $(\text{HSC}_2\text{H}_4\text{NH}_3)_2\text{PbI}_4$ , as shown in Figure 2.13(b). The following step of rapid mass change from 296 °C to 415 °C is due to the loss of organic ammonium (cysteamine) which is around 17.7% (2  $\text{HSC}_2\text{H}_4\text{NH}_3$  molecules) weight of  $(\text{HSC}_2\text{H}_4\text{NH}_3)_2\text{PbI}_4$ . Finally, the last step starts rapidly at around 476 °C which is attributed to the thermal decomposition of the lead iodide which is completed at 600 °C. The identical thermal behavior corresponding to the loss of HI, cysteamine, and  $\text{PbI}_2$  is also reflected in the data of differential scanning calorimetry (DSC) shown in Figure 2.13(b).

### 2.3.3. Optical Spectroscopy

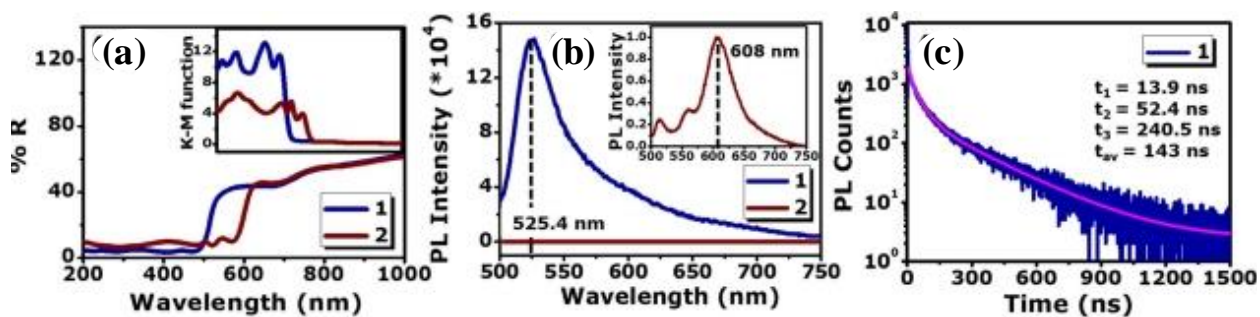


Figure 2.14: (a) DRS (%R) data with K-M function shown as an inset for the compounds **1** and **2**; (b) Comparative PL spectra for compounds **1** and **2**, inset shows the PL for compound **2** at 470 nm excitation; (c) TRPL data for compounds **1**. Note: All optical measurements are performed on compound **1** and compound **2** powders.

Figure 2.14(a) compares the diffuse reflectance spectroscopy (DRS) data for compounds **1** and **2** and the inset shows the Kubelka - Munk (K-M) function values. It can be seen that there is a significant change in the band gap (Figure 2.15) from about 2.27 eV for **1** to about 2.02 eV for **2**. The reason for significant difference in the band gaps of **1** and **2** lies in the structural orientation of the cysteamine cation within the crystal, depicted in Figure 2.16. The orientation of the bifunctional organo-ammonium cations with respect to the  $\text{PbX}_6^-$  ( $X = \text{I}, \text{Br}, \text{Cl}$ ) octahedral layers controls the type of hydrogen bonding and X-Pb-X (in and out of plane) distortions, finally influencing the band gap for the 2D perovskite systems. Generally, for the case of  $\text{Y}(\text{CH}_2)_2\text{NH}_3^+$  ( $\text{Y} = \text{OH}, \text{Cl}, \text{Br}, \text{I}, \text{CN}, \text{SH}$ ) cation in the  $(\text{Y}(\text{CH}_2)_2\text{NH}_3^+)_2\text{PbI}_4$  perovskite, as the size of the Y cation increases, the I-Pb-I bond distortion increases for halide 2D systems.<sup>45</sup> In 2D Chloro and

Bromo 2D halide cases, the ammonium cation heads are located out of the inorganic chain giving lower H-bonding. For the 2D Iodo systems, the amino heads are inside leading to higher H-bonding and consequently, the band gap is higher.<sup>45</sup>

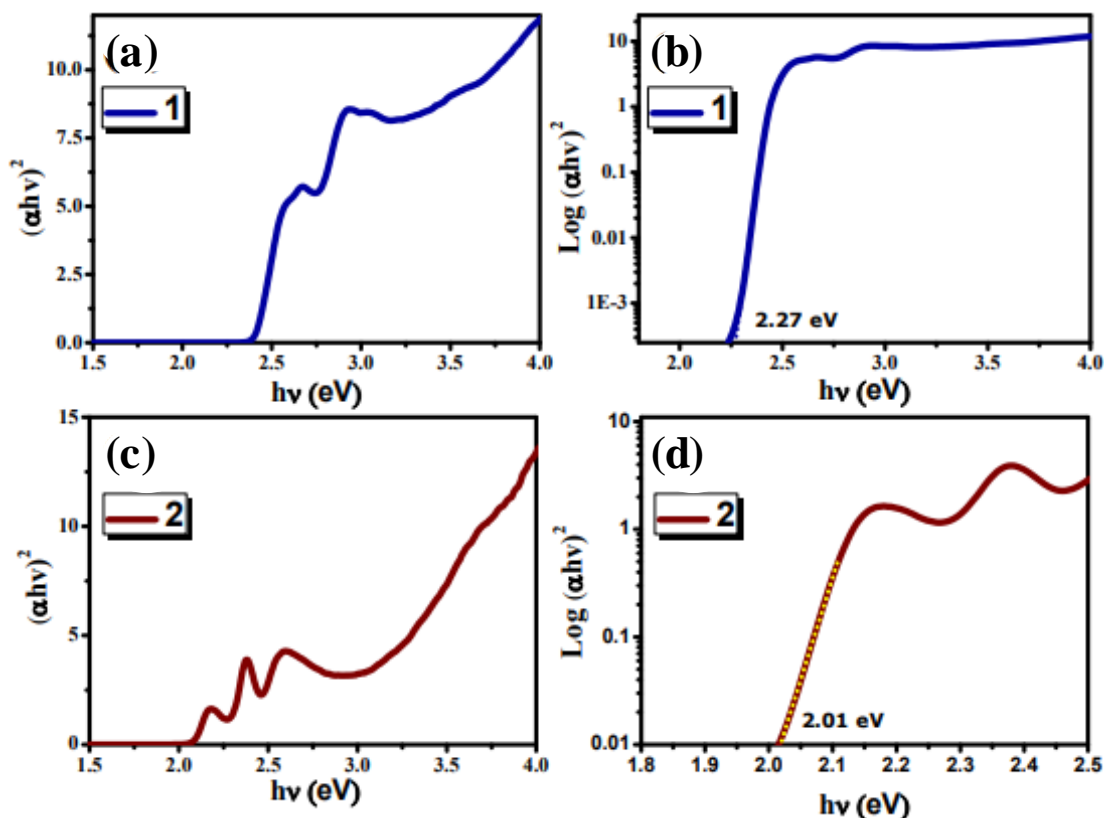


Figure 2.15: Tauc's Plot (a) and (c); magnified band edge (b) and (d).

However, for **2** crystallites the ammonium cation head lies out of the perovskite layer whereas ethyl parts are located in the inorganic framework [Figure 2.16(a, b)], leading to weaker hydrogen bonding interaction and weaker distortions in the I-Pb-I layers. This explains the band gap reduction for our **2** crystallites RP perovskite.

The PL data for both compounds are shown in Figure 2.14(b), respectively, for excitation @ 470 nm. Interestingly, **1** is highly luminescent (peak @ 525 nm) while **2** crystallites exhibit only a feeble PL intensity (with peak @ 608 nm) for the 470 nm excitation condition. We briefly address this intensity aspect below, following the discussion of the results of DFT calculations. We have also done excitation wavelength dependent PL experiment and it was observed that PL intensity



for both compounds is realized under UV excitation (near 350 nm). Even then the intensity for the compound **2** is orders of magnitude lower than that for the compound **1** (Figure 2.17).

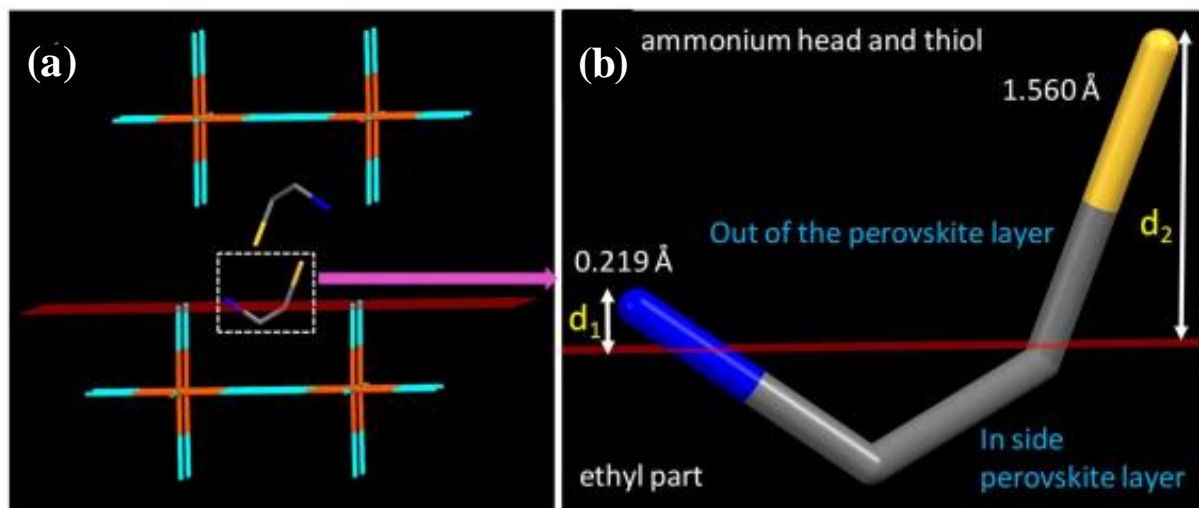


Figure 2.16: (a) The undistorted inorganic layers of compound **1** due to the ammonium functional groups lie outside and ethyl parts are located in the inorganic sheets; (b) The distance ( $0.219 \text{ \AA}$ ) between N and the plane with terminal iodides of the inorganic sheet, (left) the distance ( $1.560 \text{ \AA}$ ) between S and the plane with terminal iodides of the inorganic sheet (right).

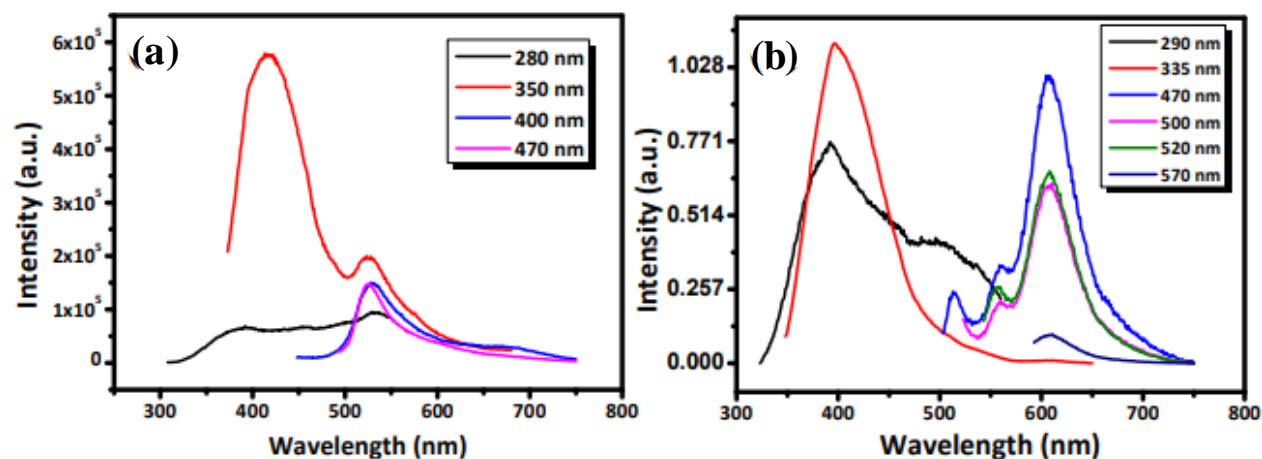


Figure 2.17: Excitation wavelength dependent solid state PL spectra (a) compound **1**; (b) compound **2**. (excitation  $\lambda = 470 \text{ nm}$ , please note this experiment is performed on the crystal powders.)

The Stokes shift is also found to be small in both compounds **1** and **2**. The PL intensity being feeble in compound **2** case, the time resolved PL (TRPL) data for this case was noisy and hence is not analysed. Finally, we also looked at the time resolved PL for the yellow crystal for which

significant PL intensity was observed and the same is shown in Figure 2.14(c). The same was fitted into three relaxation time components with short (13.9 ns), medium (52.4 ns), and very long (240.5 ns) time scales (Table 2.2). Further detailed studies will be required to pinpoint the mechanisms of the relaxations rendering these time domains. Possible mechanisms may include polaronic effects and strong screening as discussed in some reports.<sup>53, 54</sup>

Sample	$\tau_1$ (ns)	$\alpha_1$ (ns)	$\tau_2$ (ns)	$\alpha_2$ (ns)	$\tau_3$ (ns)	$\alpha_3$ (ns)	$\tau_{avg}$ (ns)
Compound 1	13.87	0.468	52.44	0.421	240.55	0.119	143

Table 2.2: Tri-exponential peak fitting parameters for powdered compound **1**, lifetime values with their individual contributions.

### 2.3.4. Density Functional Theory

In order to validate the experimental outcome, we have rigorously performed electronic structure calculations based on Density Functional Theory (DFT) formalism<sup>55</sup> for the newly synthesized crystal structures of compound **1** and compound **2** respectively.

Figure 2.18 (a, b) shows the results for the total and projected density of states (DOS) for compound **1** and compound **2** crystals based on the first principles electronic structure calculations within the framework of density functional theory (DFT) formalism. We note that the continuum of valence band states for both compounds starts below about -1 eV with a few localized sharp density of states separated out from the continuum and located just below the Fermi energy. The continuum of states belonging to the conduction band for both the compounds, on the other hand, starts just above 1 eV. Thus, the band gap values for both compounds that would be reflected in optical measurements are expected to be over 2 eV, as is indeed confirmed experimentally [Figure 2.14(a)], while the sharp states below the Fermi energy would contribute to the band tailing effects in the absorbance. Therefore, considering the continuum states into account, the DFT-calculated values turn out to be about 2.46 eV (2.276 eV) for compound **1** and 2.27 eV (2.085 eV) for compound **2**, if we consider the mid-points of the leading edges (edges) of the valence and conduction bands. The agreement with the experimental values for **1** (**2**) of 2.27 eV (2.02 eV) is thus quite good. We have also determined the projected density of states in order to find the elemental contributions of the constituents towards the total DOS of compounds **1** and **2**, while having a profound understanding of the hybridization. In case of compound **1**, we can observe Pb-

6p contributions in the valence band regime of DOS, similar to I-5p contribution with comparatively larger intensity.

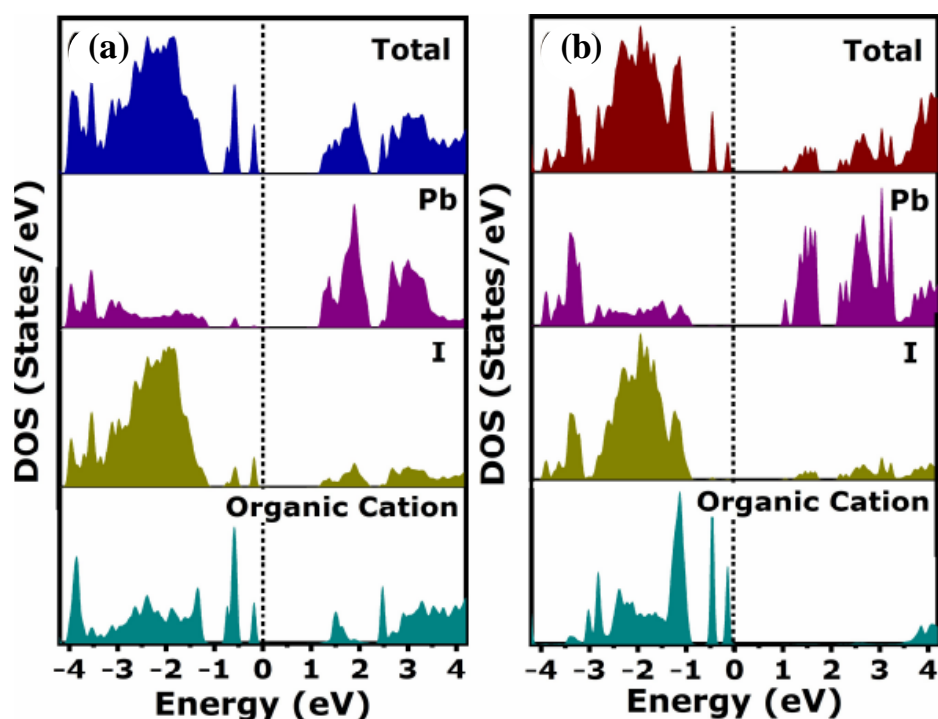


Figure 2.18: Density of states calculation for (a) **1** and (b) **2** by DFT.

This leads to the hybridization between Pb-6p and I-5p, which provides the inherent stability of the  $\text{PbI}_6^-$  octahedra in the structure. Similar observations have been found in case of compound **2**, while the contributions from I-5p are negligible near the fermi vicinity of valence band maxima (VBM) as compared to compound **1**. It is also worth to mention the different contribution of Pb-6p orbitals in valence band regime corresponding to the two compounds, in compound **1**, there is finite density of states around -0.5 eV, which can act as defect states, which is not present in the compound **2**. This particular defect-like state is certainly unique to the perovskitoid structure as compared to compound **2**.

The difference in the Pb-6p contributions in both the compounds is also visible in the conduction band regime, where the density of states corresponding to Pb-6p appear below 1 eV in case of compound **2**, while the same appeared above 1 eV in compound **1**. The density of states corresponding to I-6p orbitals is having more intensity as it prevailed in the conduction band regime in case of perovskitoid structure as compared to the compound **2**. The electronic

contribution corresponding to the organic cation also bears the difference of less intensity in case of RP system, as compared to the perovskitoid one. Additionally, the organic contribution in the conduction band regime has been prevailed more in perovskitoid as compared to compound **2**.

Thus, based on the combined analysis of the experimental results on absorbance and PL and the total DOS calculated from DFT calculations one can understand as to why the luminescence is bright for the **1** and weak for **2**, along with the corresponding energy maxima. Moreover, from the projected density of states analysis, we have observed the states in the Fermi vicinity, while this exciting signature can be envisaged further from the perspective of band edge alignment and non-linear optical features, having a direct implication in the electronic transport phenomena. This would certainly pave the way to a series of investigations for probing the combination of Wannier and Frenkel excitons.

## **2.4. Applications of the Perovskitoid Phase**

With the impressive optical properties of the new perovskitoid phase as discussed above, we further endeavored to explore its efficacy for optoelectronic and sensing applications. In the first application, we could demonstrate its applicability for an interesting design of a self-powered photodetector with the perovskitoid layer sandwiched between PEDOT:PSS and PCBM. In another application we integrated the perovskitoid with few layer black phosphorous (FLBP) in a functional composite and demonstrated the ability of the composite for selective detection of Ni<sup>2+</sup> ion via on-off-on PL probe.

### **2.4.1. Self-powered photodetector using (HSC<sub>2</sub>H<sub>4</sub>NH<sub>3</sub>)<sub>7</sub>Pb<sub>4</sub>I<sub>15</sub> crystals**

We explored the optoelectronic functionality of the new perovskitoid (HSC<sub>2</sub>H<sub>4</sub>NH<sub>3</sub>)<sub>7</sub>Pb<sub>4</sub>I<sub>15</sub> crystals, the thin films of the same were deposited by hot casting method.<sup>11</sup> Figure 2.19(a) shows the absorbance of the thin films of (HSC<sub>2</sub>H<sub>4</sub>NH<sub>3</sub>)<sub>7</sub>Pb<sub>4</sub>I<sub>15</sub> which establishes that its band gap lies in optically interesting region.

The X-ray diffraction pattern of the film confirms that the perovskitoid phase seen in the crystal is retained in the film grown by the hot casting method [Figure 2.19(b)]. Figure 2.19(c) shows the band diagram upon which the design of our selfpowered photodetector was based. The I-V curves of the device in the dark and under illumination with light intensity of 1.5 mWcm<sup>-2</sup> using

a broadband

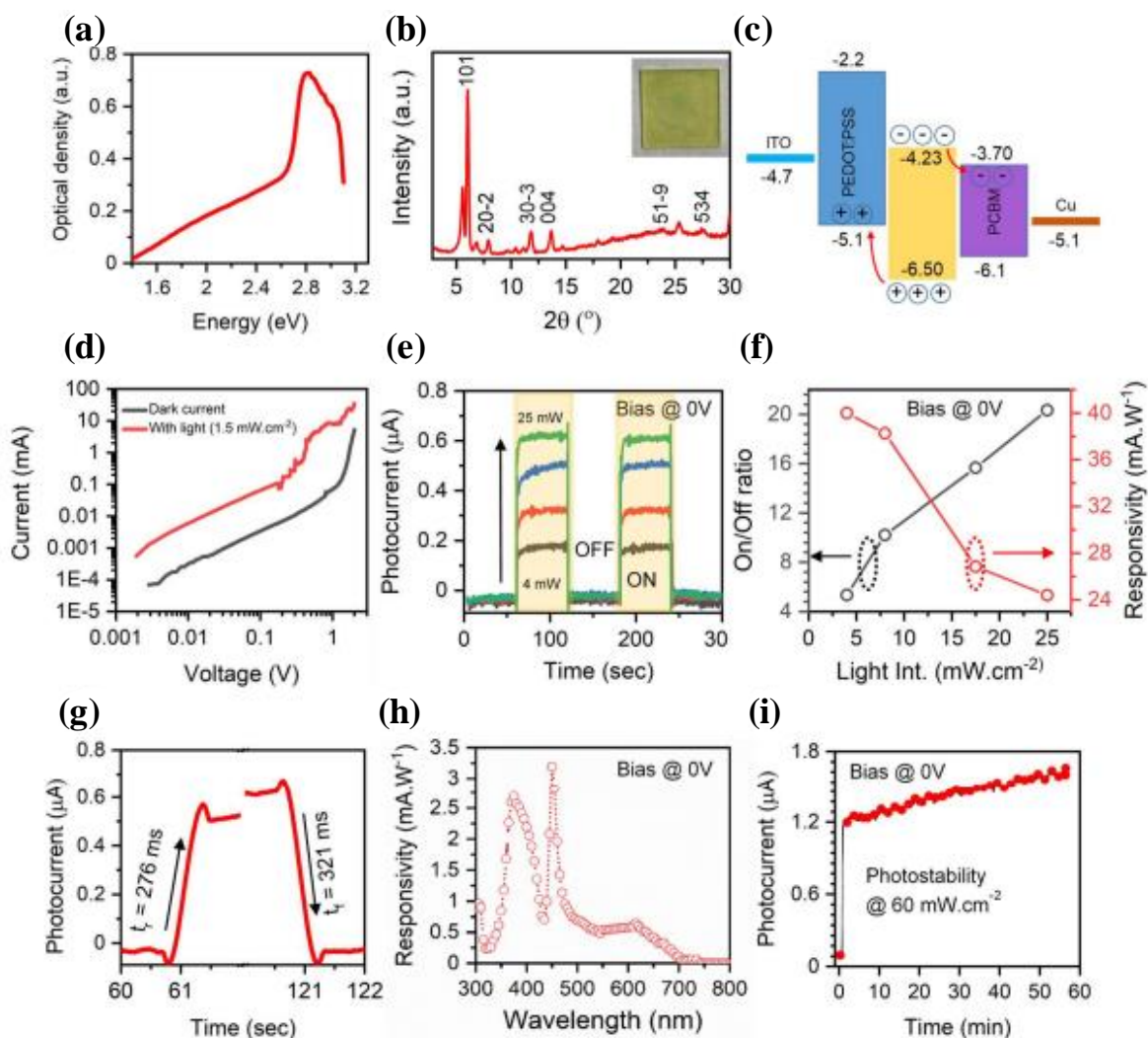


Figure 2.19: (a) Absorbance of the thin films of compound **1** fabricated by hot-casting technique; (b) X-ray diffraction of the thin films of compound **1** fabricated by hot-casting technique; (c) Band diagram showing the self-powered photodetector with the synthesized crystals; (d) I–V curves of the device in the dark and under illumination with light intensity of  $1.5 \text{ mWcm}^{-2}$  using a broadband source at  $0 \text{ V}$ ; (e) current versus time curves of the PD under bias voltage of  $0 \text{ V}$  using a broad band light source; (f) Variation in the ON/OFF ratio and responsivity with the intensity of light at  $0 \text{ V}$  bias; (g) Plot showing the response time of the self-powered photodetector at  $25 \text{ mWcm}^{-2}$  light intensity under  $0$  bias; (h) Responsivity spectra of the fabricated photodetector at  $0 \text{ V}$  bias; (i) Photostability of the self-powered photodetector at high light intensity of  $60 \text{ mWcm}^{-2}$ .

source are shown in Figure 2.19(d) (Note the log scale on both axes). Clearly, over the full voltage range, more than a factor of 10 change is seen in the current upon illumination. Figure 2.19(e) shows the current vs. time curves for the photodetector under bias voltage of 0 V using a broad band light source. An impressive power dependence is noted with fast rise and fall times. The on-off ratio and responsivity values measured at 0 V bias, plotted in Figure 2.19(f) as a function of the incident light intensity, show the expected trends with fairly impressive numbers. The plot showing the response time of the selfpowered photodetector at  $25 \text{ mWcm}^{-2}$  light intensity under 0 bias is shown in Figure 2.19(g). The observed rise and fall times are commensurate with the regime reflected in other reports.<sup>56,57</sup>

Figure 2.19(h) shows the responsivity spectra of the fabricated photodetector at 0 V bias; the sharp peak at about 450 nm corresponds to photon energy of 2.755 eV which is near the absorbance peak in Figure 2.19(a). We also examined the photostability of the photodetector at a rather high light intensity of  $60 \text{ mWcm}^{-2}$  and the data are shown in Figure 2.19(i). The photostability of the self-powered photodetector clearly appears to be good for the duration of time it is tested.

#### 2.4.2. Perovskitoid/FLBP interfacing and metal ion detection

With the impressive optical properties of the new perovskitoid (compound **1**) as discussed above, we further endeavor its integration with few layers of black phosphorous (FLBP) to investigate the electronic coupling and charge transfer between the duo, and possible heavy metal ion sensing application. This was achieved by mixing compound **1** (2 mg) with FLBP (0.8 mg) in 2 mL anhydrous toluene and sonicating together to achieve the integration. The XRD pattern of compound **1** + FLBP shown in Figure 2.20 confirms the coexistence of both perovskitoid and FLBP, without the formation of any other phase.

The high-resolution transmission electron microscopy (HRTEM) image [Figure 2.21(a)] reveals the surface decoration of compound **1** on FLBP. It shows the lattice spacing of  $d = 3.3 \text{ \AA}$  corresponding to the (534) plane of compound **1**. The absorption spectra of compound **1** and compound **1** + FLBP as-prepared composite in toluene are shown in Figure 2.22. With the addition of FLBP, the absorption spectral nature of compound **1** is maintained, although with a slight shift, and the absorption above the band edge of compound **1** ( $>$  about 410 nm) represents the contribution of FLBP. Figure 2.21(b) represents the PL of compound **1** and its quenching upon

FLBP addition. The multi-peak structure of PL of the perovskitoid quantum dots (with the peaks separated roughly equally on the energy scale) is quite intriguing and will be addressed and pursued in future work. The PL quenching observed for **1** + FLBP case can be assigned to the charge transfer from compound **1** to FLBP. This electron transfers from compound **1** to FLBP can be understood from the band alignment shown in Figure 2.21(c).

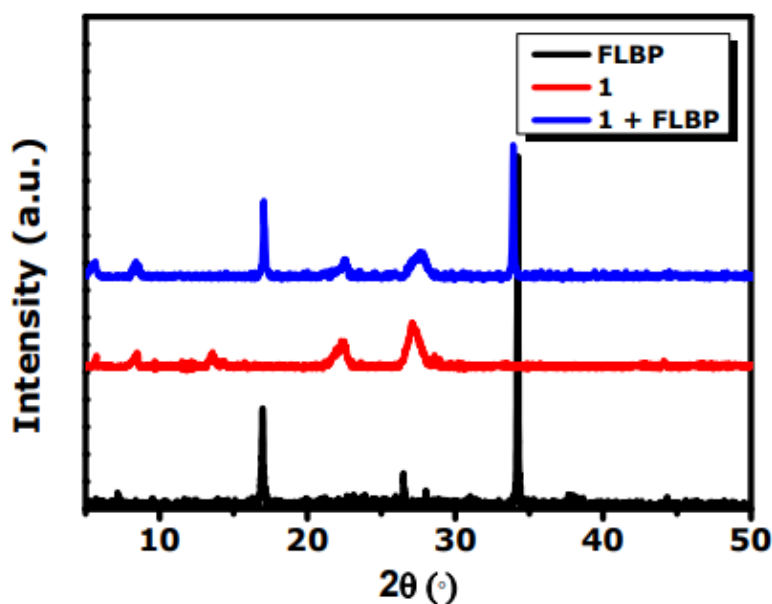


Figure 2.20: Powder XRD patterns for the composite and the pure materials from toluene solutions.

The locations of the conduction and valence bands of FLBP have been reported.<sup>58</sup> In order to obtain the same for the case of compound **1**, we first recorded the ultraviolet photoelectron spectrum (UPS) for **1** (Figure 2.23) and the work function was calculated using the relationship between the incident photon energy ( $h\nu$ ) and the secondary edge position (cut off), as described in eq  $\{\Phi = h\nu - \text{cutoff}\}$ <sup>59</sup> which yields the work function 5.02 eV for compound **1**.

From this the location of valence band maximum was found to be -6.5 eV which is indicated in Figure 2.21(c). The location of the conduction band was then found from the optically determined band gap. When a photon of energy 3.2 eV ( $\lambda = 350$  nm) is incident on the composite system, the photogenerated electrons from the perovskitoid can be easily transferred to FLBP as shown and therefore the PL is dramatically quenched. The time resolved PL (TRPL) data shown in Figure 2.21(d) is consistent with this observation, as expected. The corresponding fitted data for relaxation times are provided in Table 2.3.

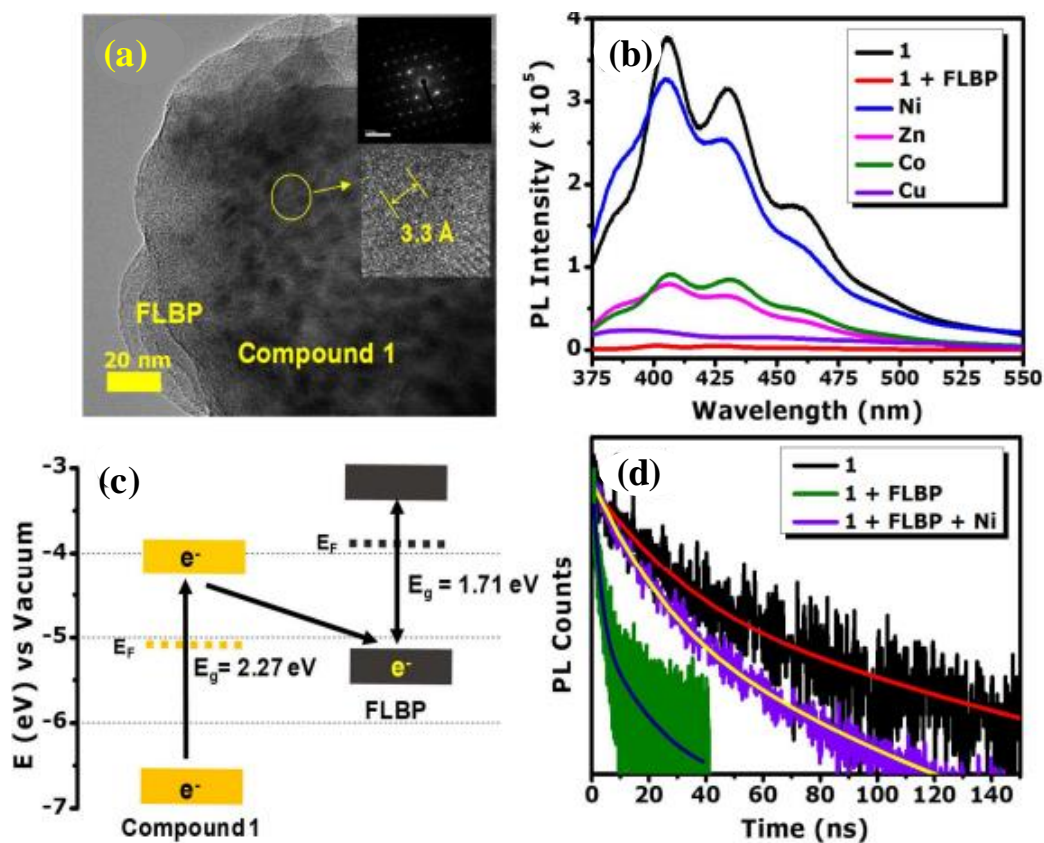


Figure 2.21: (a) HRTEM image depicting the formation of nanocomposite of compound **1** and FLBP, inset depicts SAED pattern (top) and d-spacing (bottom); (b) PL spectra at 350 nm excitation for perovskitoid/FLBP composite with  $1.79 \times 10^{-2}$  M concentration of various metal ions in toluene; (c) Energy-band diagram showing excitonic charge transfer between compound **1** and FLBP; (d) TRPL data depicting subsequent recovery of lifetime after addition of  $1.79 \times 10^{-3}$  M  $\text{Ni}^{2+}$  ions in solution.

It may be seen from Table 2.3 that the average life time of compound **1** reduced from 37.84 ns to 12.34 ns with the addition of FLBP [Figure 2.21(d)]. The exceptional properties and versatility of such hybrid systems can facilitate their applicability as a PL On-Off-On probe for heavy metal ion detection.<sup>60–63</sup>

Herein we therefore examined the use of perovskitoid/ FLBP composite as a PL On-Off-On probe for 3d transition element ion detection. The preparation procedure of metal-oleates for this study was adopted from the reported literature.<sup>62</sup> The PL modification by the addition of different metal-oleate compounds of  $\text{Ni}^{2+}$ ,  $\text{Zn}^{2+}$ ,  $\text{Co}^{2+}$  and  $\text{Cu}^{2+}$  to the solution containing compound **1** + FLBP composite was then studied.



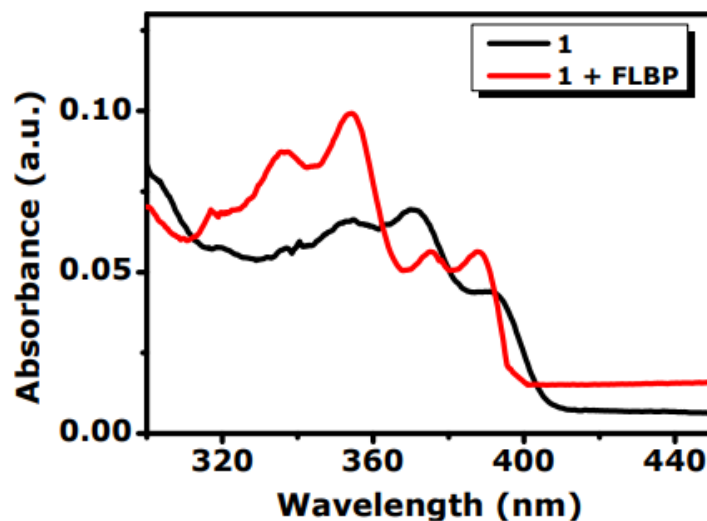


Figure 2.22: UV-Visible spectra for Compound **1** and perovskitoid/FLBP composite in toluene.

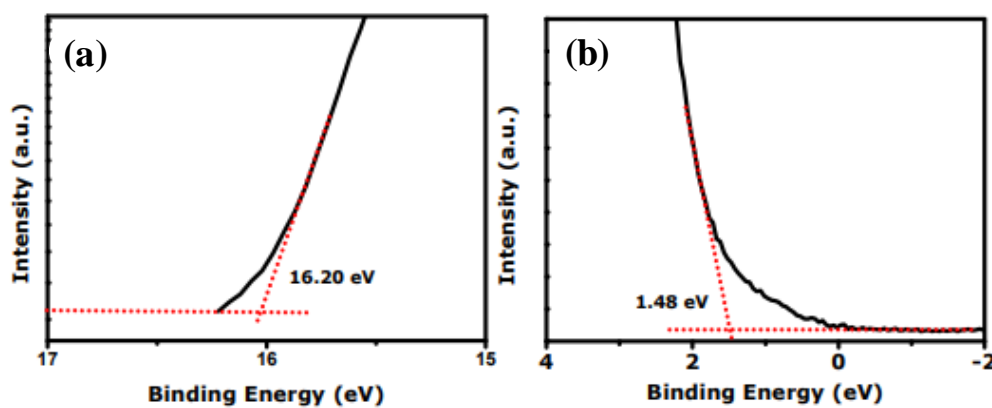


Figure 2.23: (a) Ultraviolet photoelectron spectroscopy (UPS) measurements for compound **1** Work function [Formula:  $\Phi = h\nu - \text{cutoff} = 21.22\text{eV} - 16.20\text{eV} = 5.02\text{eV}$ ] and (b) VB edge [Formula =  $\Phi + \text{edge position} = 5.02 + 1.48 = 6.5\text{eV}$ ].

Sample	$\tau_1$ (ns)	$\alpha_1$ (ns)	$\tau_2$ (ns)	$\alpha_2$ (ns)	$\tau_{\text{avg}}$ (ns)
<b>1</b>	1.55409	0.471	39.11228	0.528	37.84
<b>1 + FLBP</b>	1.93392	0.79	16.80488	0.210	12.34
<b>1 + FLBP + Ni</b>	6.37631	0.377	32.70981	0.622	29.97

Table 2.3: Tri-exponential peak fitting parameters for compound **1** in toluene, Compound **1 + FLBP** composite and composite after addition of Ni ions lifetime values with their individual contributions

The corresponding PL spectra are shown in Figure 2.21(b) for various cases of interest. It was noted that  $\text{Ni}^{2+}$  renders a remarkable (almost full) recovery of PL, while the recovery is either negligible ( $\text{Cu}^{2+}$ ) or small ( $\text{Zn}^{2+}$  and  $\text{Co}^{2+}$ ) for other transition elements.

Since for all the cases the nature of PL is similar to that of the parent compound **1**, the transition element interaction with the perovskitoid is of primary importance for PL changes. Also, the average life time [Figure 2.21(d)] of compound **1** which was reduced from 37.84 ns to 12.34 ns with the addition of FLBP showed a significant recovery back to 29.97 ns (Table 2.3) upon addition of  $1.79 \times 10^{-3} \text{ M}$  concentration of  $\text{Ni}^{2+}$ . The biexponentially fitted slow component (for radiative recombination)<sup>64</sup> of compound **1** reduced from 39.11 ns (52.8%) to 16.80 ns (21.0%) upon compositing with FLBP, which upon addition of  $\text{Ni}^{2+}$  ions is seen to recover to 32.70 ns (62.2%). These findings corroborate well with the PL quenching and recovery discussed above. Highly selective  $\text{Ni}^{2+}$  detection is an important result because humans exposed to nickel inhalation or Ni internalization via oral, and dermal routes can cause several severe health problems if nickel exposure exceeds certain limit.<sup>65-67</sup>

#### (a) $\text{Ni}^{2+}$ ion concentration dependence of PL intensity

Figure 2.24(a) presents the PL spectra of Compound **1** + FLBP composite as modified with a systematic increase in  $\text{Ni}^{2+}$  ion concentrations from  $0.36 \times 10^{-3} \text{ M}$  to  $3.22 \times 10^{-3} \text{ M}$ , under 350 nm excitation. A significant enhancement of PL intensity from 6% (**1** + FLBP) to 87% (**1** + FLBP + Ni) can be noted. The increase in relative PL intensity with  $\text{Ni}^{2+}$  concentration is shown in Figure 2.24(b). The change appears to be small below a concentration of about 1 mM, but above this concentration, the change is quite significant and linear. This suggests the influence of  $\text{Ni}^{2+}$  ion cooperative effects that would require further work to elucidate.

This suggests the influence of  $\text{Ni}^{2+}$  ion cooperative effects that would require further work to elucidate. Such concentration dependence of PL systematic have been reported in some systems.<sup>12-14</sup> Our data establishes that the composite of compound **1** with FLBP can indeed serve as an effective On-Off-On PL probe for  $\text{Ni}^{2+}$  ion detection, and even more importantly that the probe is also highly selective.

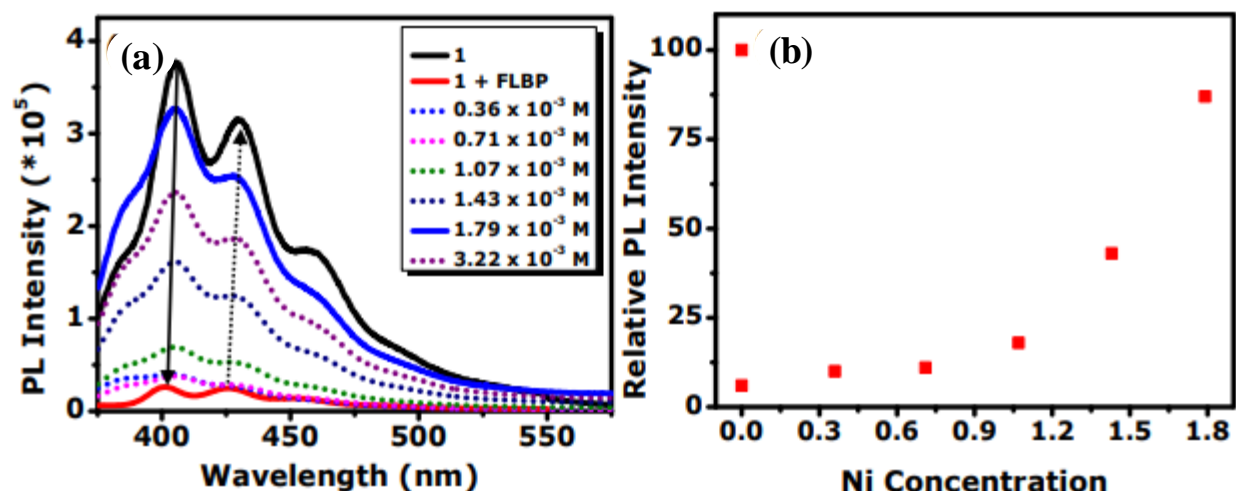


Figure 2.24: (a) Systematic recovery of PL intensity after sequential addition of increasing concentrations of Ni ions to nanocomposite in toluene solution, excitation at 350 nm and (b) Comparison of PL intensity enhancement in percentage with respect to PL intensity of compound **1**.

### (b) Mechanism of Selective $\text{Ni}^{2+}$ ion sensing

To understand the nature of the attachment of  $\text{Ni}^{2+}$  ion with Perovskitoid/FLBP composite and gain insight into the PL recovery of this system, we conducted XPS measurements. Figure 2.25(a, b) depict the core level spectra of I 3d and Pb 4f for compound **1**, the composite of compound **1** with FLBP and the composite dressed with  $\text{Ni}^{2+}$  ions. The binding energy (BE) peaks of I 3d for compound **1** located at 619.1 eV and 630.6 eV [Figure 2.25(a)] corresponds to I 3d<sub>5/2</sub> and I 3d<sub>3/2</sub> level contributions<sup>7</sup>. The Pb 4f spectrum of compound **1** [Figure 2.25(b)] exhibits two peaks at 138.1 eV and 143.0 eV corresponding to Pb 4f<sub>7/2</sub> and Pb 4f<sub>5/2</sub> levels, respectively<sup>8,9</sup>. Also we observe a very small signature for PbO<sub>2</sub> at 137.2 eV and 142.5 eV due to surface oxidation<sup>10</sup>. It is observed that due to interface formation between compound **1** and FLBP, a shift of 0.3 eV results towards higher BE, signifying a small shift in the Fermi level of the perovskite<sup>9</sup>, along with broadening of the peaks. The latter could be attributed to the dual contributions from the Pb of the PbI<sub>6</sub><sup>-</sup> octahedra at the interface with FLBP and those progressively away from it.

However, in the case of I 3d contribution, only a smaller shift is observed along with peak broadening. We also compared the P2p core level spectrum of FLBP with that for compound **1**+FLBP [Figure 2.25(c)]. The peak located at approx. 129.6 eV corresponds to the P 2p<sub>1/2</sub> level in

FLBP<sup>11</sup> which is shifted towards lower BE value of 129.0 eV for the composite case, further establishing the coupling between perovskitoid and FLBP.

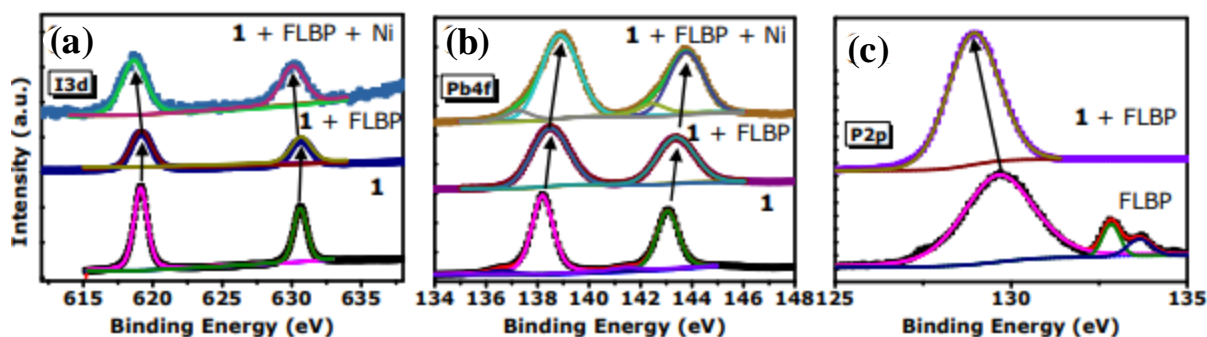


Figure 2.25: XPS core level for compound **1**, compound **1** + FLBP and Compound **1** + FLBP + Ni Carbon correction C1s = 284.6 eV for all spectra, (a) I3d, (b) Pb4f and of (c) P2p, the peaks above 132.5 are due to oxidation of phosphorous.

Upon Ni<sup>2+</sup> ion interaction with the perovskitoid/FLBP composite, it is observed that the BE values of I 3d peaks [Figure 2.25 (a)] shift towards the lower values 618.8 eV (I 3d<sub>5/2</sub>) and 630.1 eV (I 3d<sub>3/2</sub>), which implies enhanced electron density on the iodide ions. Concurrently, the shift in the BE of Pb 4f [Figure 2.25(b)] contributions is towards higher values, implying the electron cloud moving away from the Pb<sup>2+</sup> ion. Thus, it appears that the Ni<sup>2+</sup> ion has a strong bonding with the PbI<sub>6</sub><sup>-</sup> octahedron, polarising it strongly. Such a Ni<sup>2+</sup>-PbI<sub>6</sub><sup>-</sup> complex would redistribute the electronic states of the perovskitoid, thereby creating states that could siphon the photogenerated electron to a site and recombine within the perovskitoid itself, without getting transferred to FLBP from compound **1**. This would regenerate the PL emission that is quenched by FLBP.

## 2.5. Conclusions

A zwitterion cysteamine linker is used for the first time to synthesize unique organic-inorganic single crystal perovskitoid structure with face sharing and corner sharing octahedra. It is further shown that if left in the reaction medium, this yellow phase gradually (kinetically) transforms into a red-coloured compound with Ruddlesden-Popper structure via incorporative crystal-to-crystal transformation. This involves a change in the overall formula of the HOIP compound from the initial phase (HSC<sub>2</sub>H<sub>4</sub>NH<sub>3</sub>)<sub>7</sub>Pb<sub>4</sub>I<sub>15</sub> (**1**) to the final phase (HSC<sub>2</sub>H<sub>4</sub>NH<sub>3</sub>)<sub>2</sub>PbI<sub>4</sub> (**2**). Photo-physical properties are also examined and analysed via comparison with the results of DFT calculations.

Two appealing applications of the opto-electronically interesting compound **1** are demonstrated which include a self-powered photodetector exhibiting impressive performance features and selective detection of Ni<sup>2+</sup> ion via on-off-on PL probe measurements.

## 2.6. References

1. D. H. Cao, C. C. Stoumpos, O. K. Farha, J. T. Hupp and M. G. Kanatzidis, *J. Am. Chem. Soc.*, 2015, 137, 7843–7850.
2. Q. Dong, J. Song, Y. Fang, Y. Shao, S. Ducharme and J. Huang, *Adv. Mater.*, 2016, 28, 2816–2821.
3. W. Zhang, X. Yan, W. Gao, J. Dong, R. Ma, L. Liu and M. Zhang, *Org. Electron.*, 2019, 65, 56–62.
4. A. Z. Chen, M. Shiu, J. H. Ma, M. R. Alpert, D. Zhang, B. J. Foley, D. Smilgies, S. Lee and J. J. Choi, *Nat. Commun.*, 2018, 9, 1336.
5. T. Zuo, X. He, P. Hu and H. Jiang, *ChemNanoMat.*, 2019, 5, 278–289.
6. C. C. Stoumpos, D. H. Cao, D. J. Clark, J. Young, J. M. Rondinelli, J. I. Jang, J. T. Hupp and M. G. Kanatzidis, *Chem.Mater.*, 2016, 28, 2852–2867.
7. Y. Yu, D. Zhang and P. Yang, *Nano Lett.*, 2017, 17, 5489–5494.
8. A. Basu, P. Kour, S. Parmar, R. Naphade and S. Ogale, *J.Phys.Chem C*, 2018, 122, 4802–4808.
9. P. Kour, M. C. Reddy, R. Naphade and S. Ogale, *APL Mater.*, 2018, 6, 086107–7.
10. R. Naphade, S. Nagane, U. Bansode, M. Tathavadekar, A. Sadhanala and S. Ogale, *ChemSusChem*, 2017, 10, 3722–3739.
11. H. Tsai, W. Nie, J.-C. Blancon, C. C. Stoumpos, R. Asadpour, B. Harutyunyan, A. J. Neukirch, R. Verduzco, J. J. Crochet, S. Tretiak, L. Pedesseau, J. Even, M. A. Alam, G. Gupta, J. Lou, P. M. Ajayan, M. J. Bedzyk, M. G. Kanatzidis and A. D. Mohite, *Nature*, 2016, 536, 312–316.
12. H. Tsai, W. Nie, J. C. Blancon, C. C. Stoumpos, C. M. M. Soe, J. Yoo, J. Crochet, S. Tretiak, J. Even, A. Sadhanala, G. Azzellino, R. Brenes, P. M. Ajayan, V. Bulović, S. D. Stranks, R. H. Friend, M. G. Kanatzidis and A. D. Mohite, *Adv. Mater.*, 2018, 30, 1704217.
13. X. Liu and F. Gao, *J. Phys. Chem. Lett.*, 2018, 9, 2251–2258.
14. Z. Yuan, Y. Shu and B. Ma, *Chem. Commun.*, 2016, 52, 3887–3890.
15. R. Guo, Z. Zhu, A. Boulesbaa, F. Hao, A. Poretzky, K. Xiao, B. Jiming, Y. Yan and W. Li, *Small Methods*, 2017, 1, 1–6.
16. W. K. Chong, D. Giovanni and T. Sum, Wiley, 2018, 55–79.
17. X. Zhang, E. Zheng, M. R. Esopi, C. Chai and Q. Yu. *Appl. Mater. Interfaces.*, 2018, 10, 28, 24064–24074

18. S. Krishnamurthy, P. Kour, A. Katre, S. Gosavi, S. Chakraborty and S. Ogale, *APL Mater.*, 2018, 6, 114204–8.
19. S. Krishnamurthy, R. Naphade, W. J. Mir, S. Gosavi, S. Chakraborty, R. Vaidhyanathan and S. Ogale, *Adv. Opt. Mater.*, 2018, 6, 1800751.
20. S. Parmar, S. Pal, A. Biswas, S. Gosavi, S. Chakraborty, M. C. Reddy and S. Ogale, *Chem. Commun.*, 2019, 55, 7562–7565.
21. C. M. M. Soe, C. C. Stoumpos, M. Kepenekian, B. Traoré, H. Tsai, W. Nie, B. Wang, C. Katan, R. Seshadri, A. D. Mohite, J. Even, T. J. Marks and M. G. Kanatzidis, *J. Am. Chem. Soc.*, 2017, 139, 16297–16309.
22. L. Mao, Y. Wu, C. C. Stoumpos, M. R. Wasielewski, M. G. Kanatzidis and *J. Am. Chem. Soc.*, 2017, 139, 5210–5215.
23. M. H. Tremblay, F. Thouin, J. Leisen, J. Bacsá, A. R. S. Kandada, J. M. Hoffman, M. G. Kanatzidis, A. D. Mohite, C. Silva, S. Barlow and S. R. Marder, *J. Am. Chem. Soc.*, 2019, 141, 4521–4525.
24. C. C. Stoumpos, L. Mao, C. D. Malliakas and M. G. Kanatzidis, *Inorg. Chem.*, 2017, 56, 56–73.
25. X. Li, Y. He, M. Kepenekian, P. Guo, W. Ke, J. Even, C. Katan, C. C. Stoumpos, R. D. Schaller and M. G. Kanatzidis, *J. Am. Chem. Soc.*, 2020, 142, 6625–6637.
26. Q. Sun, Y. Xu, H. Zhang, B. Xiao, X. Liu, J. Dong, Y. Cheng, B. Zhang, W. Jie and M. G. Kanatzidis, *J. Mater. Chem. A*, 2018, 6, 23388–23395.
27. C. Ma, D. Shen, T. W. Ng, M. F. Lo and C. S. Lee, *Adv. Mater.*, 2018, 30, 1800710.
28. Y. Xie, H. Yu, J. Duan, L. Xu and B. Hu, *ACS Appl. Mater. Interfaces*, 2020, 12, 11190–11196.
29. Y. Liu, S. Akin, A. Hinderhofer, F. T. Eickemeyer, H. Zhu, J. Y. Seo, J. Zhang, F. Schreiber, H. Zhang, S. M. Zakeeruddin, A. Hagfeldt, M. I. Dar and M. Grätzel, *Angew. Chem. Int. Ed. Int. Ed.*, 2020, 59, 15688 – 15694.
30. F. Xia, Y. Xu, B. Li, W. Hui, S. Zhang, L. Zhu, Y. Xia, Y. Chen and W. Huang, *ACS Appl. Mater. Interfaces*, 2020, 12, 15439–15445.
31. W. Ke, C. C. Stoumpos, M. Zhu, L. Mao, I. Spanopoulos, J. Liu, O. Y. Kontsevoi, M. Chen, D. Sarma, Y. Zhang, M. R. Wasielewski and M. G. Kanatzidis, *Sci. Adv.*, 2017, 3, e1701293.
32. I. Spanopoulos, W. Ke, C. C. Stoumpos, E. C. Schueller, O. Y. Kontsevoi, R. Seshadri and M. G. Kanatzidis, *J. Am. Chem. Soc.*, 2018, 140, 5728–5742.
33. T. Rath, J. Handl, S. Weber, L. Troi, T. Dimopoulos, B. Friesenbichler, B. Kunert and T. Resel, Roland, Gregor, *J. Mater. Chem. A*, 2019, 7, 9523–9529.
34. S. F. Zhang, X. K. Chen, A. M. Ren, H. Li and J. L. Bredas, *ACS Energy Lett.*, 2019, 4, 17–25.
35. M. H. Tremblay, J. Bacsá, S. Barlow and S. R. Marder, *Mater. Chem. Front.*, 2020, 4, 2023.

36. T. Kollek, D. Wurmbrand, S. T. Birkhold, E. Zimmermann, J. Kalb, L. Schmidt-Mende and S. Polarz, *ACS Appl. Mater. Interfaces*, 2017, 9, 1077–1085.
37. J. Cao, J. Yin, S. Yuan, Y. Zhao, J. Li and N. Zheng, *Nanoscale*, 2015, 7, 9443–9447.
38. S. Halder, Ansuman, Chulliyil, Ramya, Subbiah, S Anand, Khan, Tuhin, Chattoraj, A. Chowdhury and S. K. Sarkar, *J. Phys. Chem. Lett.*, 2015, 6, 3483–3489.
39. B. Li, C. Fei, K. Zheng, X. Qu, G. Cao and J. Tian, *J. Mater. Chem. A*, 2016, 4, 17018–17024.
40. W. A. Saidi and J. J. Choi, *J. Chem. Phys.*, 2016, 145, 144702.
41. S. Sidhik, A. C. Pasarán, C. Rosiles Pérez, T. López-Luke and E. De La Rosa, *J. Mater. Chem. C*, 2018, 6, 7880–7889.
42. M. Saliba, T. Matsui, J. Y. Seo, K. Domanski, J. P. Correa-Baena, M. K. Nazeeruddin, S. M. Zakeeruddin, W. Tress, A. Abate, A. Hagfeldt and M. Grätzel, *Energy Environ. Sci.*, 2016, 9, 1989–1997.
43. N. Marchal, W. Van Gompel, M. C. Gélvez-Rueda, K. Vandewal, K. Van Hecke, H. G. Boyen, B. Conings, R. Herckens, S. Maheshwari, L. Lutsen, C. Quarti, F. C. Grozema, D. Vanderzande and D. Beljonne, *Chem. Mater.*, 2019, 31, 6880–6888.
44. H. Lin, C. Zhou, J. Neu, Y. Zhou, D. Han, S. Chen, M. Worku, M. Chaaban, S. Lee, E. Berkwits, T. Siegrist, M. H. Du and B. Ma, *Adv. Opt. Mater.*, 2019, 7, 1801474.
45. B. Saparov and D. B. Mitzi, *Chem. Rev.*, 2016, 116, 4558–4596.
46. M. E. Kamminga, G. A. De Wijs, R. W. A. Havenith, G. R. Blake and T. T. M. Palstra, *Inorg. Chem*, 2017, 56, 8408–8414.
47. Y. Xue, J. Yuan, J. Liu and S. Li, *Nanomaterials*, 2018, 8, 591.
48. P. Chen, Y. Bai, S. Wang, M. Lyu, J. H. Yun and L. Wang, *Adv. Funct. Mater.*, 2018, 28, 1706923.
49. Y. Li, P. Li and Z. H. Lu, *AIP Adv.*, 2018, 8, 1–7.
50. Z. Zheng, X. Zhang, C. Neumann, D. Emmrich, A. Winter, H. Vieker, W. Liu, M. Lensen, A. Götzhäuser and A. Turchanin, *Nanoscale*, 2015, 7, 13393–13397.
51. S. Chen, T. W. Goh, D. Sabba, J. Chua, N. Mathews, C. H. A. Huan and T. C. Sum, *APL Mater.*, 2014, 2, 081512–7.
52. A. Dualeh, P. Gao, S. Il Seok, M. K. Nazeeruddin and M. Grätzel, *Chem. Mater.*, 2014, 26, 6160–6164.
53. T. Chen, W. L. Chen, B. J. Foley, J. Lee, J. P. C. Ruff, J. Y. P. Ko, C. M. Brown, L. W. Harriger, D. Zhang, C. Park, M. Yoon, Y. M. Chang, J. J. Choi and S. H. Lee, *Proc. Natl. Acad. Sci. U. S. A.*, 2017, 114, 7519–7524.
54. Y. Chen, H. T. Yi, X. Wu, R. Haroldson, Y. N. Gartstein, Y. I. Rodionov, K. S. Tikhonov, A.

- Zakhidov, X. Y. Zhu and V. Podzorov, *Nat. Commun.*, 2016, 7, 12253.
55. C. H. Chu and C. W. Leung, *Integr. Equations Oper. Theory*, 2001, 40, 391–402.
56. Y. Wang, T. Zhang, P. Zhang, D. Liu, L. Ji, H. Chen, Z. D. Chen, J. Wu and S. Li, *Org. Electron.*, 2018, 57, 263–268.
57. Y. Li, Z. F. Shi, X. J. Li and C. X. Shan, *Chinese Phys. B*, 2019, 28, 017803.
58. S. K. Muduli, E. Varrla, Y. Xu, S. A. Kulkarni, A. Katre, S. Chakraborty, S. Chen, T. C. Sum, R. Xu and N. Mathews, *J. Mater. Chem. A*, 2017, 24874–24879.
59. N. Cheng, J. Tian, Q. Liu, C. Ge, A. H. Qusti, A. M. Asiri, A. O. Al-Youbi and X. Sun, *ACS Appl. Mater. Interfaces*, 2013, 5, 6815–6819.
60. D. Zhang, Y. Xu, Q. Liu and Z. Xia, *Inorg. Chem.*, 2018, 57, 4613–4619.
61. Y. Liu, X. Tang, T. Zhu, M. Deng, I. P. Ikechukwu, W. Huang, G. Yin, Y. Bai, D. Qu, X. Huang and F. Qiu, *J. Mater. Chem. C*, 2018, 6, 4793–4799.
62. P. Pandey, A. Sengupta, S. Parmar, U. Bansode, S. Gosavi, A. Swarnkar, S. Muduli, A. D. Mohite and S. Ogale, *ACS Appl. Nano Mater.*, 2020, 3, 3305–3314.
63. C. H. N. H. Pb, I. O, M. Zhu, L. Zhang, J. Yin, J. Chen and L. Bie, *Inorg. Chem. Commun.*, 2019, 109, 107562.
64. A. Biswas, A. Swarnkar, P. Pandey, P. Kour, S. Parmar and S. Ogale, *ACS Omega*, 2020, 5, 11915–11922.
65. G. Genchi, A. Carocci, G. Lauria and M. S. Sinicropi, *Int. J. Environ. Res. Public Heal.*, 2020, 17, 679.
66. <https://apps.who.int/iris/handle/10665/107335>, World Heal. Organ. Reg. Off. Eur. (2000). Air Qual. Guidel. Eur. Second Ed. World Heal. Organ. Reg. Off. Eur., 2000, 11–23.
67. K. K. Das, R. C. Reddy, I. B. Bagoji, S. Das, S. Bagali, L. Mullur, J. P. Khodnapur and M. S. Biradar, 2019, 30, 141–152.



## Appendix

### Materials

Lead (II) iodide, PbI <sub>2</sub>	Sigma-Aldrich, 99%
Cysteamine (cyst)	Sigma-Aldrich, ~ 95%
N, N dimethylformamide, DMF	Sigma-Aldrich, anhydrous, 99.99%
Toulene	Sigma-Aldrich, 99.9%
Nickel Sulfate	Sigma-Aldrich, 99.8%
Copper Sulphate	Sigma Aldrich, 99.8%
Zinc Sulphate	Sigma Aldrich, 99.8%
Cobalt Sulphate	Sigma Aldrich, 99.8%
6,6-Phenyl C61 butyric acid methyl ester, PC61BM	Sigma Aldrich, 99.8%
Hydriodic acid, HI	55-58 wt. % in H <sub>2</sub> O, Avra
Clevios TM poly(3,4-ethylenedioxythiophene) polystyrene sulfonate (PEDOT: PSS)	Heraeus Epurio

### Characterizations

*powder X-ray diffraction (pXRD):* The structural measurements were performed on a Bruker D8-Advance X-ray diffractometer (Germany) with Cu K $\alpha$  radiation ( $\lambda = 1.5418 \text{ \AA}$ ).

*Ultraviolet-visible (UV-vis) spectrophotometer:* The LAMBDA 950, Perkin Elmer, instrument was used to collect the absorption spectra.

*Photoluminescence (PL) Spectroscopy:* A Horiba Scientific FluoroMax-4 spectrofluorometer was used to record the PL spectra at various wavelengths.

*Time correlated single photon counting (TCSPC):* Fluorescence lifetimes were measured by time correlated single photon counting (TCSPC), using a spectrofluorometer (Horiba Scientific), and LED excitation source is used. We used UV light (365nm) for recording the images in the dark.

*Field Emission Scanning Electron Microscopy (FESEM):* The surface morphologies and energy dispersive X-ray spectroscopy (EDX) were recorded using field emission scanning electron microscope (FESEM) JEM-2100F, JEOL, Japan.

*Fourier Transform Infrared Spectroscopy (FTIR):* FTIR was performed using the Bruker Alpha-E instrument.

*Thermo-gravimetric analysis (TGA):* was carried out using the NETSZCH TGA-DSC system. TGAs were performed under 20 ml/min N<sub>2</sub> gas flow (purge + protective) and the heating rate was maintained 5 K/min from 25°C to 600°C.

*X-ray photoelectron spectroscopy (XPS) and Ultraviolet photoelectron spectroscopy (UPS):* XPS is performed with monochromatic Al K $\alpha$  radiation ( $h\nu = 1486.7$  eV). UPS is performed with a helium discharge lamp (He I,  $h\nu = 21.2$  eV) in the same instrumentation setup.

### **Single Crystal XRD**

Crystal was coated with Paratone-N oil, attached to a Kapton loop, and transferred to a Bruker D8 Venture Diffractometer equipped with a Photon 100CMOS detector. Frames were collected using  $\phi$  and  $\omega$  scans and the unit-cell parameters were refined against all data. The crystals did not show significant decay during data collection. Data were integrated and corrected for Lorentz and polarization effects using SAINT 8.27b and were corrected for absorption effects using SADABS V2012. The structures were solved by direct methods and expanded through successive difference Fourier maps using the SHELXTL-2013 software package. Hydrogen atoms were inserted at idealized positions and refined using a riding model with an isotropic thermal parameter 1.2 times that of the attached carbon atom or 1.5 times that of the attached nitrogen.

### **DFT: Methodology**

Throughout the first principles calculations, we have used Vienna Ab-initio Simulation Package (VASP).<sup>5</sup> The Perdew-Burke-Ernzerhof (PBE) type exchange correlation functional is used, which is in the framework of generalized gradient approximation (GGA)<sup>6</sup>. The lattice parameters and the space group of compounds **1** and **2** are consistent with the experimental values of the synthesized structure. In order to achieve a minimum energy configuration of the considered system, we have

undertaken a full ionic relaxation until the corresponding Hellman-Feynman forces are getting smaller than 0.001 eV/Ao.

We have used  $5 \times 5 \times 5$  Monkhorst-Pack k-points while performing the ionic relaxation of the system. After getting the optimized structure with the minimum most energy, we determine the projected density of states (PDOS) to know the elemental contribution towards the total DOS of compounds **1** and **2**.

## Chapter 3

### Lead-Free Low Dimensional Mn- and Cu- based Hybrid Organic and Inorganic Perovskites for Pb<sup>2+</sup> Metal Ion Detection

For the first time, we have synthesized lead (Pb)-free manganese (Mn)- and copper (Cu)-based hybrid organic-Inorganic perovskites (HOIPs) compounds, compound **1** (TEA)<sub>2</sub>MnBr<sub>4</sub>, compound **2** (TBA)<sub>2</sub>MnBr<sub>4</sub>, compound **3** (TEA)<sub>2</sub>CuBr<sub>4</sub> and compound **4** (TBA)CuBr<sub>2</sub>, (where TEA is tetraethylammonium and TBA is tetrabutylammonium) under ambient conditions via mechanochemical synthesis methodology using KaKuHunter made planetary mixer. The compounds are characterized as 2D except for (TBA)CuBr<sub>2</sub>, which has crystallized in the 0D lattice. The synthesized compounds are phase pure and show stable solid-state emission at room temperature. The Mn-based perovskite compounds **1** showed excellent environmental photo stability for more than a month and reasonable stability under a relative humidity of 70% - 80%. Compounds **1** and **2** were used further for fluorescence titration studies using various heavy metal cations, including transition metals and lanthanides (e.g., Y<sup>3+</sup>, Nb<sup>3+</sup>, Co<sup>2+</sup>, Ni<sup>2+</sup>, Ag<sup>+</sup>, Zn<sup>2+</sup>, Cd<sup>2+</sup>, Pb<sup>2+</sup>, Gd<sup>3+</sup>, and Dy<sup>3+</sup>), where they showed good fluorescence quenching by Pb<sup>2+</sup> ion. Compound **1** demonstrated excellent fluorescence quenching performance with Pb<sup>2+</sup> titration with a Pb<sup>2+</sup> detection limit of (LOD)  $2.43 \times 10^{-8}$  M, and hence can be used to fabricate a Pb<sup>2+</sup> calorimetric sensor. A very in-situ ion exchange based, mechanism for the sensitivity of compound **1** is noted. A preliminary visual sensor for the change in emission was fabricated to test the result correlation in the film for blue to green emission change for compound **1**. This study reveals the ability of Pb-free TEA and TBA-based Mn bromide HOIPs to detect oxidizing metal cation, Pb<sup>2+</sup>, efficiently and quantitatively.

### 3.1. Introduction

Hybrid organic-inorganic lead (Pb) halide perovskites (HLHPs) have been reported to perform exceptionally well in optoelectronic applications such as solar cells<sup>1-7</sup>, LEDs<sup>8</sup>, transistors<sup>9-13</sup>, optical sensors<sup>14-19</sup>, etc. The general formula for HLHPs is APbX<sub>3</sub> where A is an organic or inorganic monovalent cation [Methylammonium (CH<sub>3</sub>NH<sub>3</sub><sup>+</sup>), Formamidinium (HC(NH<sub>2</sub>)<sub>2</sub><sup>+</sup>), Cysteammonium (C<sub>2</sub>H<sub>8</sub>N<sup>+</sup>S), Cystammonium (C<sub>4</sub>H<sub>13</sub>N<sub>2</sub><sup>+</sup>S<sub>2</sub>), CH<sub>3</sub>(CH<sub>2</sub>)<sub>3</sub>NH<sub>3</sub><sup>+</sup> (BA), and C<sub>6</sub>H<sub>5</sub>(CH<sub>2</sub>)<sub>2</sub>NH<sub>3</sub><sup>+</sup> (PEA), Cs<sup>+</sup>, Rb<sup>+</sup>] and X represents halide anion (Cl<sup>-</sup>/Br<sup>-</sup>/I<sup>-</sup>) at micro- and nano-scales<sup>2,4,16,20-31</sup>. They have been shown to perform at par with the other metallic systems in thin film, single crystal and nanocrystalline forms. These HLHPs possess several interesting properties due to the presence of a wide gamut of A, B and X site atoms, such as tunable band gap, high carrier mobilities, defect tolerance, large electron diffusion lengths, easy solution processing and so on.<sup>1,32-36</sup>

However, despite the advantages, HLHPs suffer from numerous drawbacks due to their fragile crystal structure, which crumbles easily upon oxygen and moisture penetration sunlight and UV exposure<sup>37-42</sup>. The destruction of chemical structure tends to cause Pb leakage with severe human health issues and environmental hazards hindering the commercialization of HLHPs in optoelectronic devices. The acceptable level of Pb in bare soil given by the EPA (Environmental Protection Agency) for play areas is 400 ppm and in non-play areas is 1200 ppm<sup>43</sup>. However, long-term use of Pb-based devices can lead to Pb accumulation in the soil and water bodies and in turn within our bodies.

Hence to overcome the issue of Pb toxicity there is a significant advancement in research towards Pb-free hybrid halide perovskites (LFHHPs)<sup>9,44-46</sup>. LFHHPs cover a wide range of compounds with a general chemical formula of A<sub>x</sub>B<sub>y</sub>X<sub>z</sub> (x, y, z depends on structural directionality), B represents a mono/ divalent cation (Sn<sup>2+</sup>/Sb<sup>2+</sup>/Bi<sup>+</sup>/Pd<sup>2+</sup>/In<sup>+</sup>/Ti<sup>+</sup>/Pt<sup>2+</sup>/Au<sup>+</sup>/Cu<sup>+</sup>/Ag<sup>+</sup>/Mn<sup>+</sup>).<sup>9,47-50</sup> The dimensionality of perovskite mainly depends on the size of cations which should fulfill the requirement of Goldschmidt tolerance factor (t)<sup>51</sup>,

$$t = \frac{R_A + R_X}{\sqrt{2}(R_B + R_X)}$$

where,  $R_A$ ,  $R_B$ , and  $R_X$  are the ionic radius of the A-site, B-site, and halide (X) site, respectively. LFHHPs have demonstrated superior properties than their HLHP counterparts.<sup>47,52-58</sup>

The development of stable manganese (Mn) and copper (Cu) -based hybrid halide perovskites is important since they show a change in oxidation state upon exposure to moisture and oxygen. The tetrahedrally coordinated  $[\text{MnX}_4]^{2-}$  anions, are luminous in the solid state; however, upon interaction with solvents lose their structural coordination and hence making the perovskite non-emissive<sup>59</sup>. The  $\text{Cu}^+$  in cuprous halide perovskites easily oxidizes in the presence of moisture due to low hydration energy of  $\text{Cu}^+$  ions which leads to the formation of  $\text{Cu}^{2+}$  upon loss of an electron<sup>60</sup>.

LFHHPs have demonstrated superior performance when compared to HLHPs in areas of photovoltaics, as light emitting diodes, photocatalysis, sensing and data storage<sup>44,61–63</sup>. Tin (Sn)-based perovskites have been studied extensively as efficient solar cell and gas sensing materials, owing to their good optoelectronic properties, high selectivity and sensitivity towards various gases<sup>14,64</sup>. Bismuth (Bi)-, Cu- and Mn-based perovskites have been studied for their photocatalysis and data storage applications<sup>57,58,65</sup>. Another interesting application for LFHHPs and HLHPs for which only limited studies are there is the metal ion detection application<sup>66–69</sup>. Metal ions play a significant role in the functioning of various biological and chemical processes. Thus, the easy detection and monitoring of metal ions have become crucial in diverse applications such as environmental monitoring, food safety, and medical diagnosis. Hybrid organic-inorganic perovskites have emerged as a promising candidate for metal ion detection due to their unique structure and physicochemical properties<sup>17,18,70–76</sup>. The structure of low dimensional LFHHPs consists of organic cations and metal halide layers, providing a large surface area for interaction with metal ions. Moreover, the presence of metal ions can affect the electronic and optical properties of perovskites, leading to changes in their luminescence and conductivity<sup>17,70–72</sup>. This property can be exploited for metal ion sensing applications. Compared to existing materials for metal ion detection, such as organic dyes and metal-organic frameworks, hybrid organic-inorganic perovskites offer several advantages. Firstly, they exhibit high sensitivity and selectivity towards metal ions, owing to their unique surface chemistry and crystal structure. Secondly, they have a tunable bandgap and photoelectric properties, allowing for the development of high-performance optical sensors. Finally, the synthesis of perovskites<sup>45</sup> is relatively simple and cost-effective<sup>45</sup>.

The main advantage of Pb-free perovskites is their reduced toxicity and environmental impact, making them a more sustainable alternative to Pb-based perovskites. However, Pb-free perovskites face some challenges such as lower stability and lower efficiency compared to Pb-

based perovskites. Nonetheless, significant progress has been made in addressing these challenges, and Pb-free perovskites are expected to play an increasingly important role in various applications in the future.

In this work, we have synthesized Mn- and Cu- based halide perovskites using tetramethylammonium bromide and tetraethylammonium bromide as A site cations to form low dimensional perovskites. The reason for choosing the quaternary alkyl ammonium salts for our ambient synthesis is that as the size of the organic chain increases the moisture tolerance of the perovskite increases<sup>52,58,77,78</sup>. A solid-state methodology using KaKuHunter made planetary mixer is chosen to synthesize compound **1** (TEA)<sub>2</sub>MnBr<sub>4</sub>, compound **2** (TBA)<sub>2</sub>MnBr<sub>4</sub>, compound **3** (TEA)<sub>2</sub>CuBr<sub>4</sub> and compound **4** (TBA)CuBr<sub>2</sub> under ambient conditions. The compounds, are then characterized by XRD, PL, UV-visible, IR spectroscopy and TGA-DSC analysis. Metal compounds **1** and **2** showed reasonable stability under high humidity, and were used for fluorescence titration studies with heavy metal cations. The compounds, stability was tested under 70-80% humidity conditions. Finally, metal ion detection applications were carried out on these to find out high selectivity of compound **1** for Pb<sup>2+</sup> ion detection.

## 3.2. Experimental Section

### 3.2.1. Synthesis of (TEA)<sub>2</sub>CuBr<sub>4</sub> and (TEA)<sub>2</sub>MnBr<sub>4</sub>

We have carried out solid state synthesis, wherein 3 mmol of tetraethylammonium bromide (TEAB) and 1 mmol of manganese (II) bromide (MnBr<sub>2</sub>) or copper (I) bromide (CuBr), is added to the reaction vessel, separately with the organic linker. Further this vessel is mounted in KaKuHunter made planetary mixer instrument, at 1500 rpm for 30 minutes, under mixing and degassing mode as reported earlier from our group<sup>79</sup>. The temperature of the reaction vessel reached during the synthesis is 30°C. Followed by characterizations.

### 3.2.2. Synthesis of (TBA)CuBr<sub>2</sub> and (TBA)<sub>2</sub>MnBr<sub>4</sub>

The synthesis procedure was similar as above using tetraethylammonium bromide and tetrabutylammonium bromide (TBAB). To give a brief overview, 3 mmol of tetraethylammonium bromide (TEAB) and 1 mmol of manganese (II) bromide (MnBr<sub>2</sub>) or copper (I) bromide (CuBr), is added to the reaction vessel, separately with the organic linker. Further this vessel is mounted in KaKuHunter made planetary mixer instrument, at 1500 rpm for 30 minutes, under mixing and degassing mode. Temperature of the reaction vessel reached during the synthesis is 30°C. Followed by characterizations.

### 3.2.3. Nanoparticle (NP) solutions synthesis:

0.25mg/mL of each sample is dispersed in toluene to make the respective NP solutions followed by ultra-sonication for 15 minutes to make a well dispersed NP solution.

### 3.2.4. Synthesis of Metal Oleate Solution:

Metal oleate (M-oleate) was prepared by the method reported by Y. Liu et al., for preparing metal ion<sup>80</sup>. In the typical synthesis of metal-oleate, 0.1 mmole of metal sulfate / nitrate was added with 0.5 mL water followed by the ultrasonication for 10 min until it becomes transparent. In another 10 mL vial 0.25 m mole sodium oleate (procured from Sigma Aldrich) was added with water: ethanol (1:1 by volume) solution and kept for ultra-sonication for 10 to 15 min until a homogeneous solution appears. The above metal sulfate solution was further mixed with the sodium oleate solution and sonicate for 15 min. The as-prepared mixture was further centrifuged and washed several times with ethanol and vacuum dried overnight.

### 3.2.5. Metal Ion Detection Application:

(a) In Solution:

We carried out the fluorescence quenching studies were carried out in the presence of various other metal cations (such as, Y<sup>3+</sup>, Nb<sup>3+</sup>, Co<sup>2+</sup>, Ni<sup>2+</sup>, Pb<sup>2+</sup>, Ag<sup>+</sup>, Zn<sup>2+</sup>, Cd<sup>2+</sup>, Gd<sup>3+</sup>, and Dy<sup>3+</sup>) at a concentration ranging from  $0.25 \times 10^{-7}$  M –  $2.0 \times 10^{-7}$  M. Nanoparticle dispersions of compound **1** and **2** were prepared as above mentioned and sequentially toluene metal- oleate solutions for each of the metal ions was added to it in a fixed ratio followed by sonication for about 2-5 minutes.

(b) In thin film:

Compound **1** was solubilized at a concentration of 1 mg/ml in DMF solvent. The solution was spin coated using HOLMARK spin coater (Model No. H0-TH-05). A two-step programme at 1000 RPM for 60 seconds and second step at 4000 RPM for 30 seconds was pre-set for film casting. This was followed by annealing at 80°C for 20 minutes to prepare the films.



(c) Sensory sensitivity test:

A calorimetric sensitivity test was performed by dipping the spin coated films of compound **1** were dipped in toluene solution of  $2.0 \times 10^{-7}$  M Pb-oleate for 2-4 seconds and the emission change was observed under a UV-lamp at  $\lambda = 253$  nm.

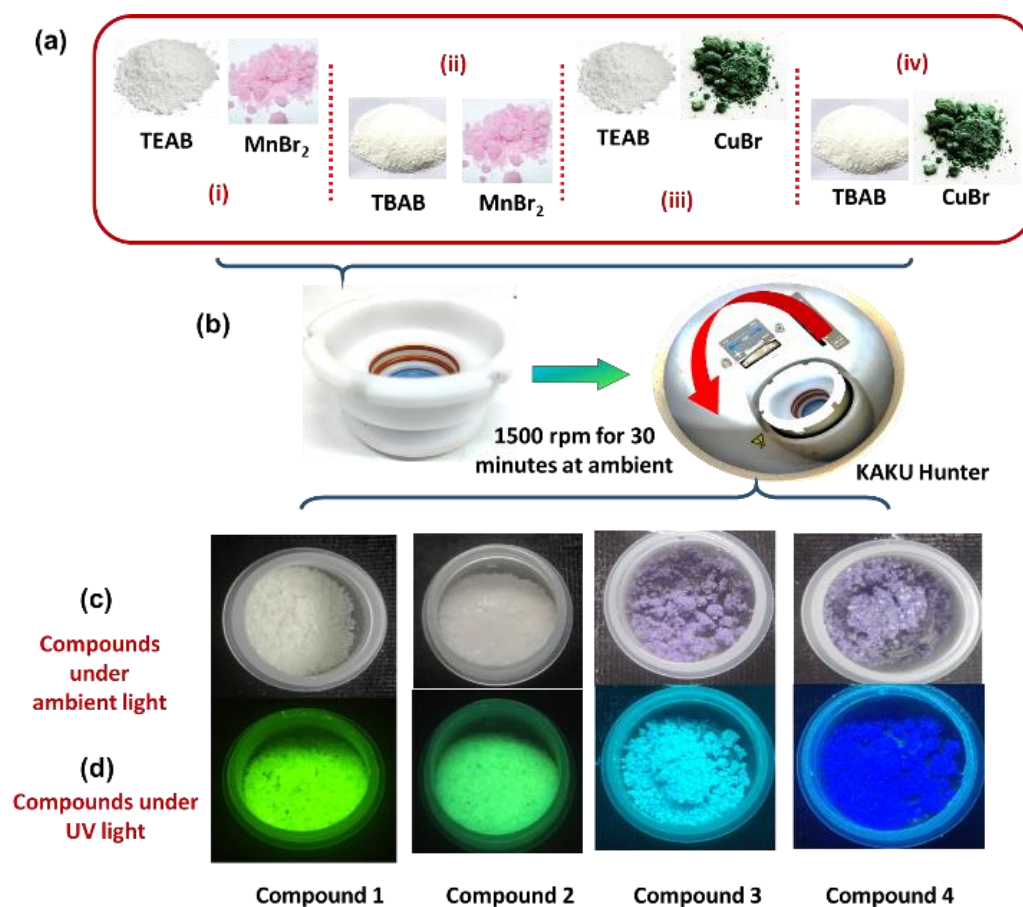
### 3.3. Results and Discussion

We have used a novel one step solid state method to synthesize following compounds, compound **1** (TEA)<sub>2</sub>MnBr<sub>4</sub>, compound **2** (TBA)<sub>2</sub>MnBr<sub>4</sub>, compound **3** (TEA)<sub>2</sub>CuBr<sub>4</sub> and compound **4** (TBA)CuBr<sub>2</sub>. Previously solid state synthesis method was reported for the synthesis of other Pb/ Pb-free halide perovskites<sup>81-84</sup>. Herein, the novel solid state synthesis was carried out in a using KaKuHunter made planetary mixer at 1500 rpm for 30 minutes, under mixing and degassing mode using only the precursors in the optimum ratios under ambient conditions. The fundamental principle of planetary mixture depends on the centrifugal force, similar to the one created by mortar and pestle<sup>79</sup>. The concentration of each compound was precisely calculated to obtain phase pure compounds and hence remove the washing step completely. It was found that, out of all the compounds, compound **1**, (TEA)<sub>2</sub>MnBr<sub>4</sub> shows maximum environmental photostability for up to 45 days followed by compound **2**, (TBA)<sub>2</sub>MnBr<sub>4</sub>. Upon metal ion detection experiments it was found that compounds **1** and **2** show highest sensitivity towards Pb<sup>+2</sup> followed by compounds **3** and **4** in the given order.

The crystalline compounds of compound **1** (TEA)<sub>2</sub>MnBr<sub>4</sub>, compound **2** (TBA)<sub>2</sub>MnBr<sub>4</sub>, compound **3** (TEA)<sub>2</sub>CuBr<sub>4</sub> and compound **4** (TBA)CuBr<sub>2</sub> were prepared by a straightforward and effortless method by using the elementary principle of molar ratio control. The synthesis of HOPIs can be tuned easily by controlling the method of synthesis, molar ratios, alkyamine chain length and functional groups<sup>85-87</sup>. Hence we have fixed the molar ratios of the precursors of manganese (II) bromide (MnBr<sub>2</sub>), copper (I) bromide (CuBr), tetraethylammonium bromide (TEAB) and tetrabutylammonium bromide (TBAB) at 1: 3 (metal halide: organic precursor) [Scheme 3.1 (a)]. Table 3.1 enlists the concentration of precursors powders (in mmol) used to form the respective compounds in a tabular form for more clarity.

After measuring the appropriate amount of precursors they are hand shaken for few second in a reaction vessel followed by mounting of the vessel inside using KaKuHunter made planetary

mixer [Scheme 3.1(b)]. After this the machine is set to rotate at 1500 rpm for 30 minutes ultimately leading to the synthesis of our Pb-free bromide compounds [Scheme 3.1 (c)].



Scheme 3.1: (a) shows the precursor combinations (i, ii, iii and iv) used for the synthesis of compounds 1, 2, 3 and 4 respectively; (b) shows the actual laboratory images of reaction vessel and its subsequent mounting in the using KaKuHunter made planetary mixer instrument; (c) shows the ambient pictures of the compounds; (d) shows the emission on the respective compounds under UV light, images for compounds 1 and 2 are recorded under 365 nm light and for compounds 3 and 4 images are recorded under 254 nm.

Table 3.1: Molar ratios of the precursors used for reactions enlisted in tabular form for ease of understanding.

Compound	TEA	TBA	MnBr	CuBr
Compound 1	3 mmol		1 mmol	
Compound 2		3 mmol	1 mmol	
Compound 3	3 mmol			1 mmol

Compound 4		3mmol		1 mmol
------------	--	-------	--	--------

The compounds **1** and **2** when viewed under 365 nm UV light show strong green emission [Scheme 3.1 (d)], and compounds **3** and **4** when viewed under 254 nm UV light showed strong cyan emission indicating the formation of optically active compounds.

### 3.3.1. Structural Characterizations

Thereafter we proceeded with structural characterizations using XRD analysis. Upon matching the XRD patterns of the as obtained products with the simulated SCXRD patterns of  $(\text{TEA})_2\text{MnBr}_4$  compound reported by S. Chen et. al,<sup>58</sup> we found that the compounds **1**, **2** and **3** crystallized as 2D perovskites (Figure 3.1 a). We also compared the XRD patterns of compound **4** with the reported SCXRD for 0D structure of  $(\text{TBA})\text{CuBr}_2$  by H. Peng et al.<sup>52</sup> As reported, the ionic radii for  $(\text{TEA})^+$  and  $(\text{TBA})^+$  is 0.337 and 0.413 nm, respectively.<sup>88</sup> This causes formation of low dimensional perovskite systems as the size of the cation exceeds the size of the A site cavity hence pushing the  $[\text{MX}_4]^{2-}$  octahedrons away from each other and leading to creation of an electronic quantum well like structure<sup>89</sup>. We also noticed that the crystal structure of compounds **2** shows orientated growth on the (110) plane compound **1** is due to change in organic cations from TEABr to TBABr.

The importance and different strategies used for achieving *in situ* orientation control during the synthesis of 2D hybrid perovskites for improving the photovoltaic performance of are highlighted in a recent review by J. Du et al.<sup>90</sup>

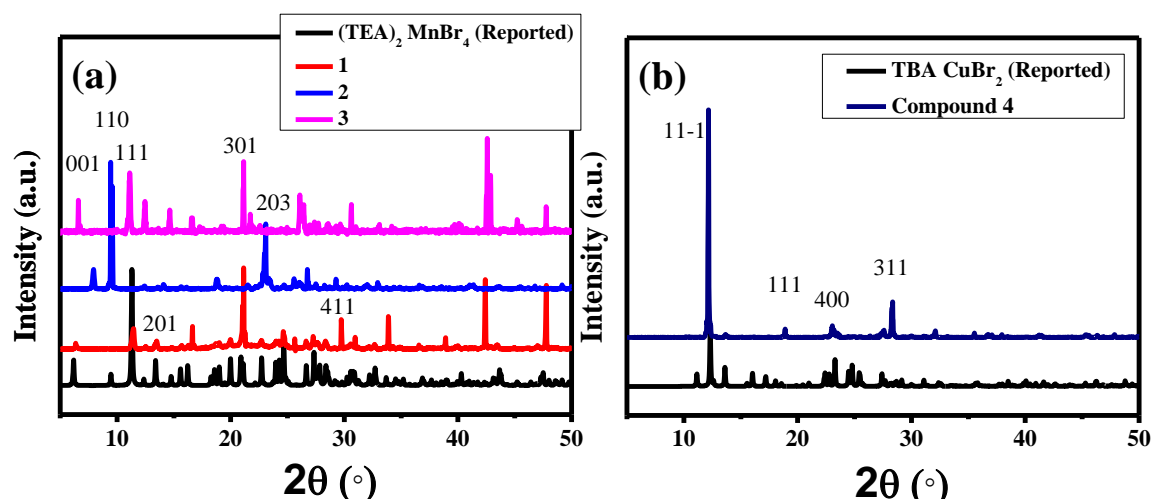


Figure 3.1: pXRD patterns of as synthesized compounds compared with the simulated single crystal pXRD patterns of the reported compounds,<sup>52,58</sup> (a) XRD pattern for compounds **1**, **2** and **3**; (b) XRD pattern for compound **4**.

From our literature survey this is the first report for controlling the molecular orientation in hybrid perovskite crystals simply by changing the organic cations without any change in the ambient synthesis protocol to form highly emissive compounds.

### 3.3.2. IR Spectroscopy

No presence of unreacted precursors was noted as seen in the pXRD pattern and also confirmed by the FTIR data, Figure 3.2. It can be seen from Figure 3.2(a) that the final products, i.e. compounds **1** and **3**, resulting from reactions between metal halides and TEABr salt possess all the characteristic precursor salt peaks.

The main peaks in the spectra were assigned to N-H stretching at  $3411.48\text{ cm}^{-1}$ , C-H stretching at  $2875.82\text{ cm}^{-1}$ , C-H<sub>2</sub> wagging & twisting vibrations at  $1459.86\text{ cm}^{-1}$ , C-H<sub>3</sub> out of plane vibrations at  $1389.38\text{ cm}^{-1}$ , C-N<sup>+</sup> stretch aliphatic amine stretching at  $1005.97\text{ cm}^{-1}$  and  $793.82\text{ cm}^{-1}$ .<sup>91</sup> Presence of a very sharp peak at  $3411.48\text{ cm}^{-1}$  shows the characteristic N-H stretching, which can occur due to partial hydrogen bonding with the atmospheric humidity but the absence of any precursor peaks in XRD shows this bond is only on the surface and does not affect the perovskite structure and its properties.<sup>92-94</sup>

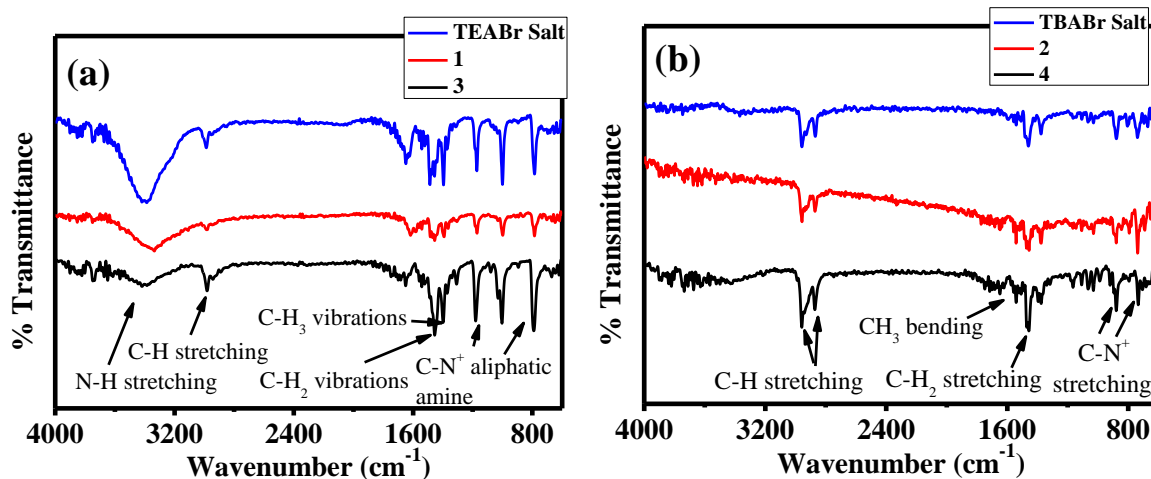


Figure 3.2: FTIR spectra for (a) compounds **1** and **3** matched with the precursor salt of tetraethylammonium bromide; (b) compounds **2** and **4** matched with the precursor salt of tetrabutylammonium bromide.

Also interestingly the intensity of the N-H stretching vibrations has reduced drastically from the TEABr salt as the compounds **1** and **3** are synthesized indicating increased interactions of

the free  $N^+$  species with the  $[MnBr_4]^{2-}$  and  $[CuBr_4]^{2-}$  octahedrons and less availability of free  $N^+$  for moisture attack. Figure 3.2(b) shows the IR spectra for compounds **2** and **4**, all the characteristic peaks are similar to the aforementioned peak positions due to similarity in the TEABr and TBABr salts. However slight changes in the wavenumbers are noticed and are as follows, C-H stretching vibrations are noted at  $2963.93\text{ cm}^{-1}$  and  $2875.82\text{ cm}^{-1}$ , C-H<sub>3</sub> out-of-plane bending vibrations are at  $1459.86\text{ cm}^{-1}$ , C-H<sub>2</sub> wagging & twisting vibrations at  $1389.38\text{ cm}^{-1}$ , C-N<sup>+</sup> stretch aliphatic amine stretching at  $1364.28\text{ cm}^{-1}$  and  $734.61\text{ cm}^{-1}$ <sup>91,95</sup>. The spectra shows successful formation of the perovskite structure using our method of synthesis.

### 3.3.3. XPS

To further validate the authenticity of our ambient one step synthesis methodology for formulating luminous Pb-free halide perovskites we carried out XPS analysis and it was found that no oxidation of the  $Mn^{2+} / Cu^+$  species occurred during the ambient synthesis (Figure 3.3 and 3.4). The XPS peak maxima for Mn 2p<sub>3/2</sub> is at 645.64 eV for compound **1** [Figure 3.3(a)] and 645.51 eV for compound **2** [Figure 3.3(b)]<sup>96</sup>. Also the Cu 2p spectra shows characteristic peaks at 952.98 eV and 933.07 eV corresponds to Cu 2p<sub>1/2</sub> and Cu 2p<sub>3/2</sub> core levels, respectively for compound **3** [Figure 3.4 (a)]. Similarly, the peak positions for Cu 2p<sub>1/2</sub> and Cu 2p<sub>3/2</sub> core levels for compound **4** are 953.47 eV and 933.92 eV, respectively<sup>52</sup> (Figure 3.4 (b)). The bromine XPS peak positions for Br 3d spectra are also recorded for all the compounds and are shown in Figure 3.5 (a-d). The slight changes in the XPS peak binding energy values is related to the change in the crystal structure and orientation of the inorganic layer with respect to the organic layers, as previously reported by our group<sup>16</sup>.

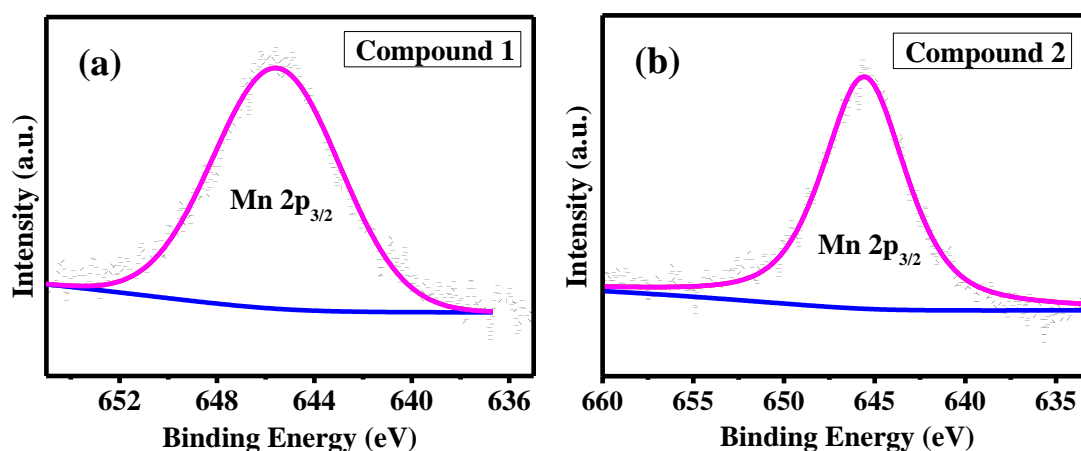


Figure 3.3: High-resolution deconvoluted XPS spectra for Mn 2p core levels for compounds (a) **1** and (b) **2** powders, toluene dispersions are drop casted on a Si substrate.

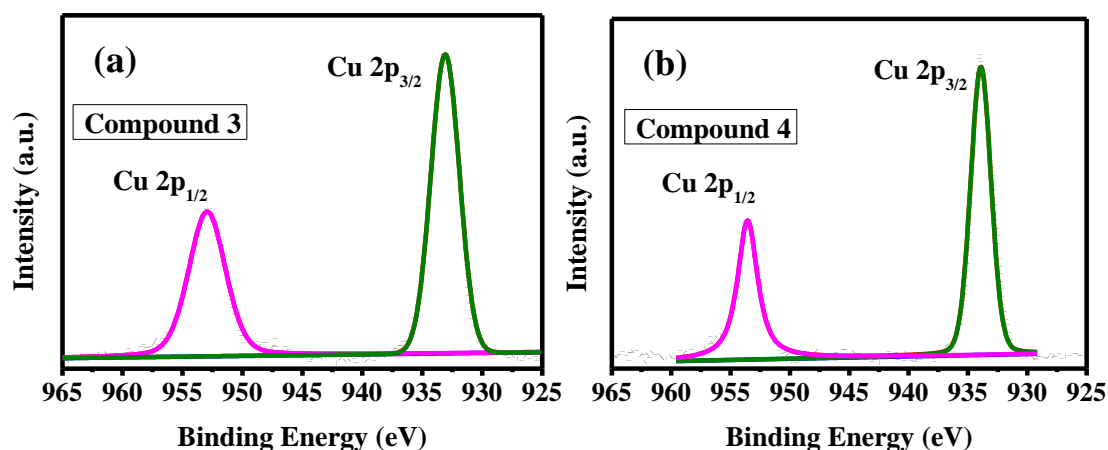


Figure 3.4: High-resolution deconvoluted XPS spectra for Cu 2p core levels for compounds (a) 1 and (b) 2 powders, toluene dispersions are drop casted on a Si substrate.

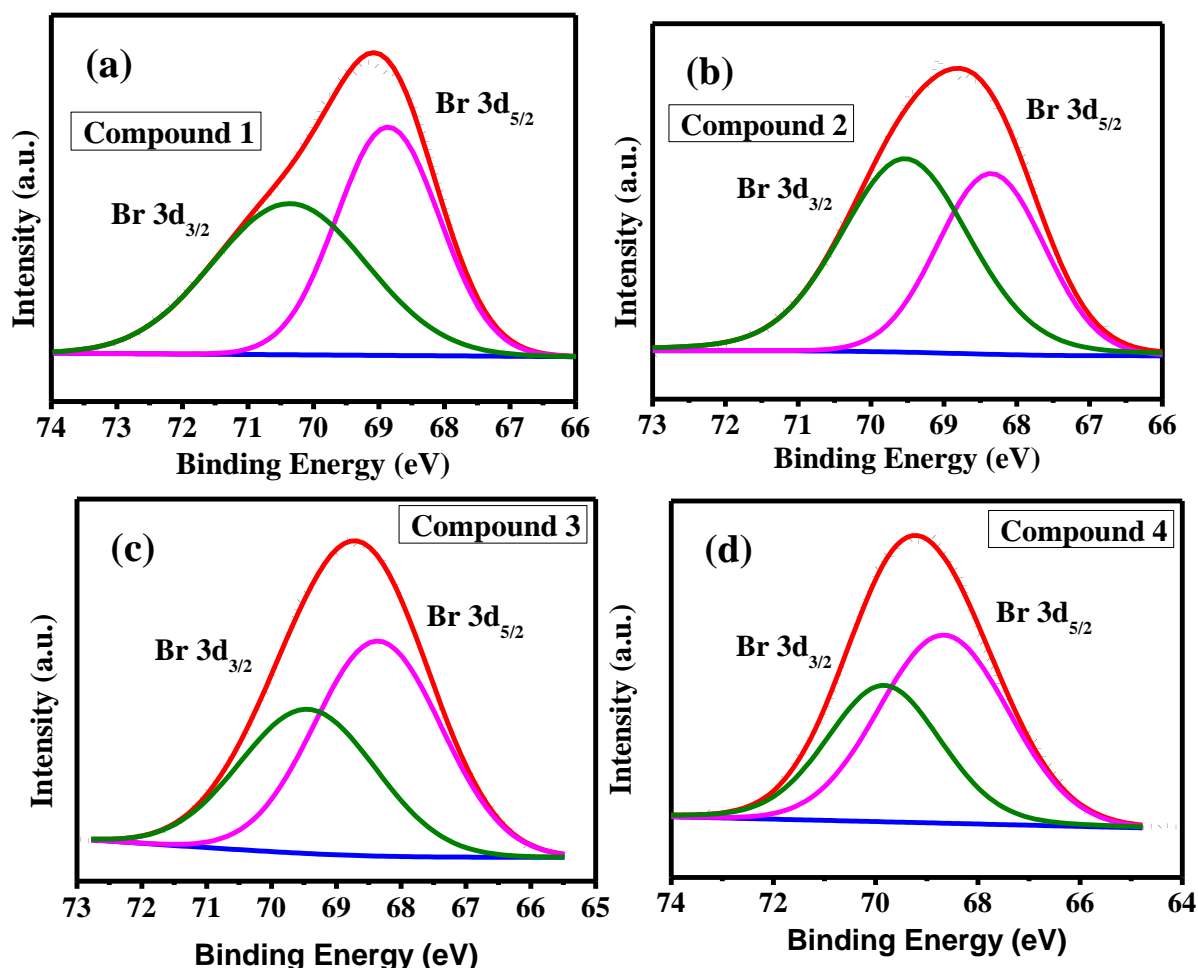


Figure 3.5: High-resolution deconvoluted XPS spectra for Br 3d core levels for compounds (a) 1 and (b) 2 powders, toluene dispersions are drop casted on a Si substrate.

### 3.3.4. Nanoscale Microscopic Imaging

After complete compositional and elemental analysis of the as synthesized Pb-free HOIP compounds we proceeded with the structural analysis. Figure 3.6 shows the FESEM images for the compounds. It can be seen that compound **1** has a comparatively smooth and compact surface structure, thereby the number of grain boundary and the defect arising thereafter would be less. Compounds **2**, **3** and **4** have a comparatively rough surface morphology. We also carried out FESEM-EDAX and elemental mapping for all the samples to confirm the presence of all elements in the equitable abundance. The ratios for Mn: Br for compounds **1** and **3** as realized from their structural formula should be 1:4 which is reflected from the atomic% ratio as obtained from the FESEM elemental ratios [Figures 3.7 (a) and 3.8 (a)] and verified by the elemental mapping [Figures 3.7 (b) and 3.8 (b)].

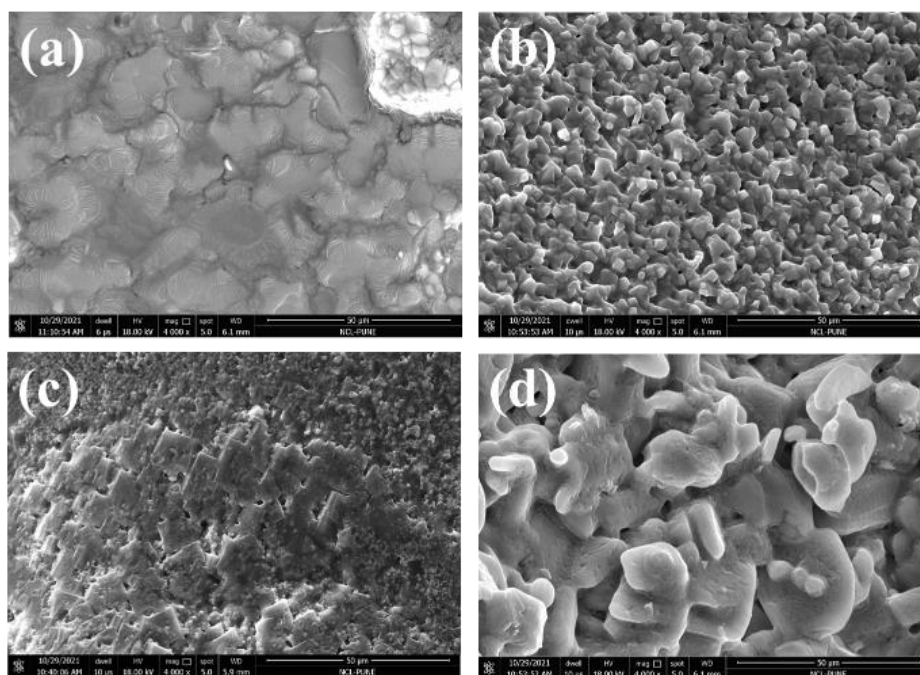


Figure 3.6: FESEM images of the powder samples for (a) compound **1**, (b) compound **2**, (c) compound **3** and (d) compound **4** (Scale bar = 50 µm).

Also, the Cu: Br ratios from the structural formula for compound **2** is 1: 4 and for compound **4** should be 1: 2 match with the FESEM-EDAX atomic % ratios [Figures 3.9 (a) and 3.10 (a)] also reflected from the elemental mapping micrographs [Figures 3.9 (a) and 3.10 (b)].

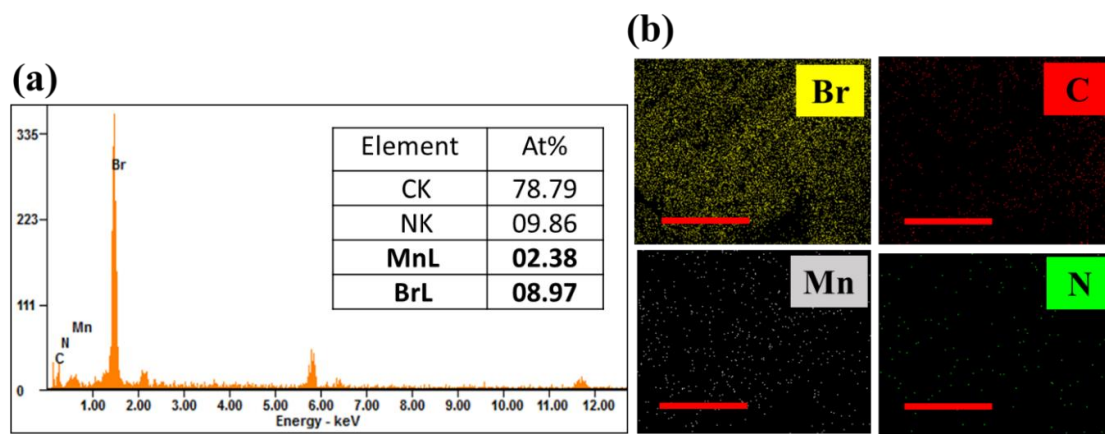


Figure 3.7: FESEM analysis for compound **1** powder samples (a) EDAX spectra, (b) Elemental ratio the bold numbers are indicative of the Mn: Br ratio, and (c) The elemental mapping, the colour codes used are, yellow for Br, red for C, gray for Mn and green for N elements.

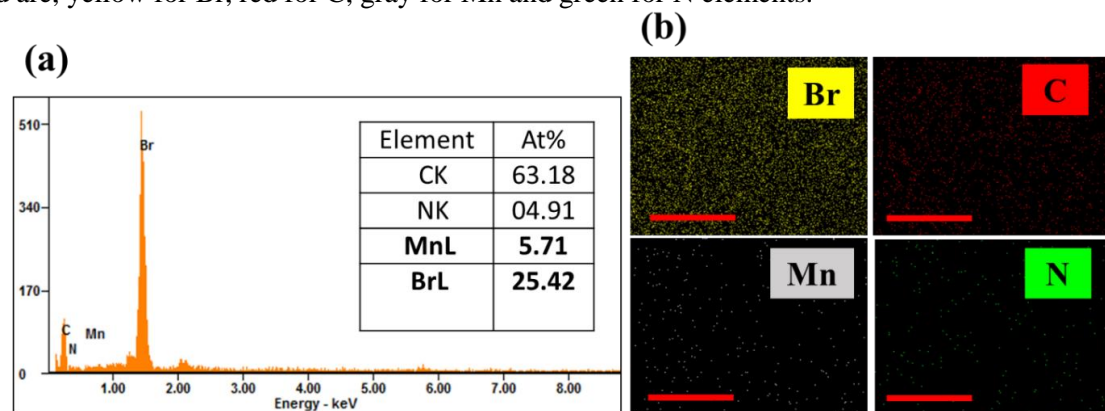


Figure 3.8: FESEM analysis for compound **2** powder samples (a) EDAX spectra, (b) Elemental ratio the bold numbers are indicative of the Mn: Br ratio, and (c) The elemental mapping, the colour codes used are, yellow for Br, red for C, gray for Mn and green for N elements.

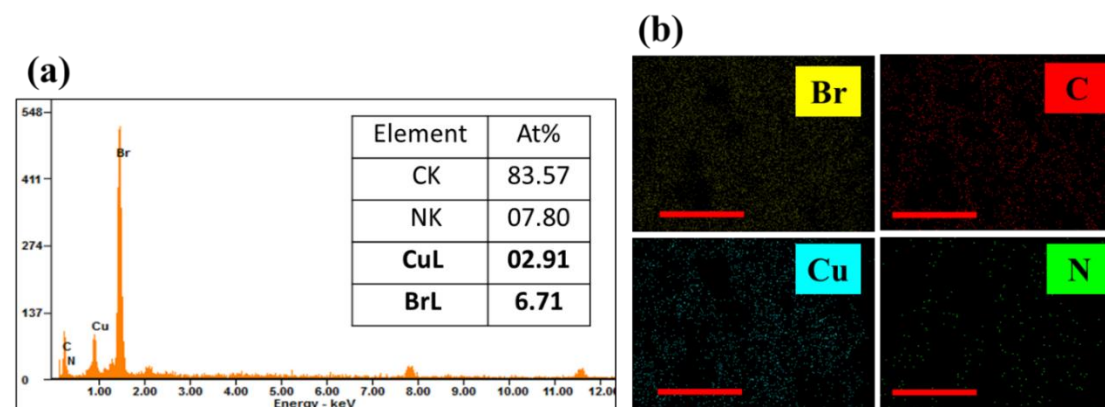


Figure 3.9: FESEM analysis for compound **3** powder samples (a) EDAX spectra, (b) Elemental ratio the bold numbers are indicative of the Cu: Br ratio, and (c) The elemental mapping, the colour codes used are, yellow for Br, red for C, blue for Cu and green for N elements.



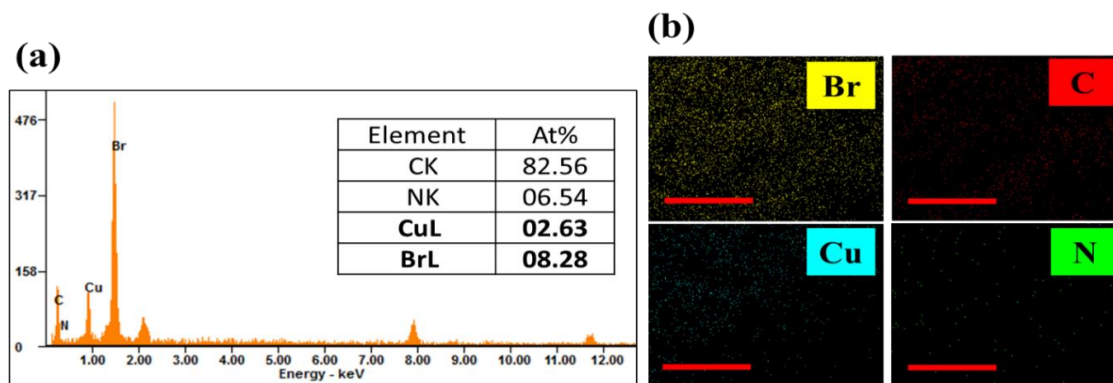


Figure 3.10: FESEM analysis for compound **4** powder samples (a) EDAX spectra, (b) Elemental ratio the bold numbers are indicative of the Cu: Br ratio, and (c) The elemental mapping, the colour codes used are, yellow for Br, red for C, blue for Cu and green for N elements.

To elucidate the thermal stability of the compounds we carried out thermo-gravimetric (TGA-DSC) analysis. All the compounds are stable upto  $\sim 220$  °C. we can see a slope from 220 °C to 700 °C which can be concurred with the loss or melting of the organic moiety.

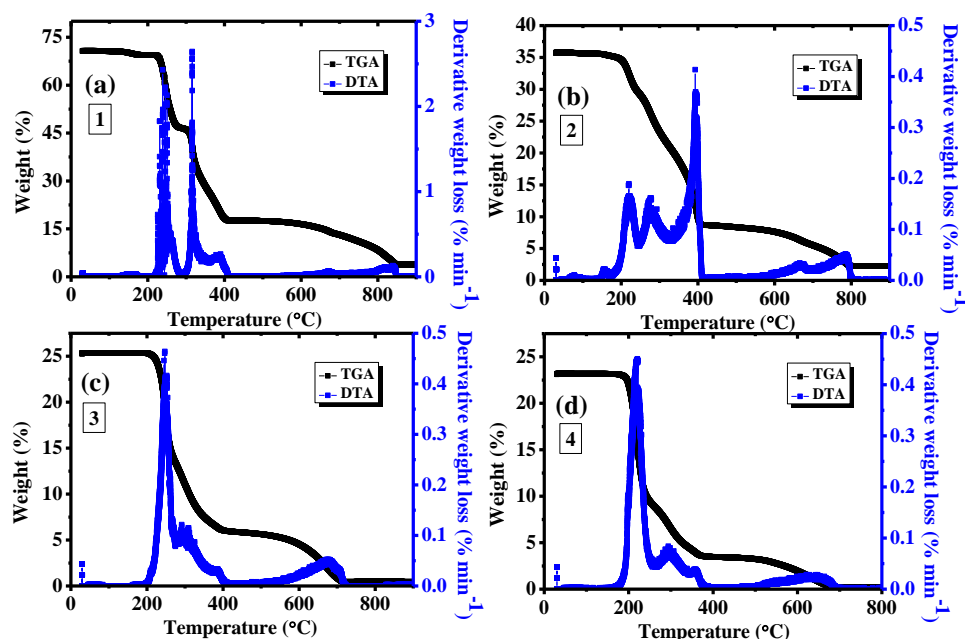


Figure 3.11: TGA and DSC spectra for compounds (a) **1**, (b) **2** (c) **3** and (d) **4**. Recorded in the range of 0-1000 °C, using a ramp rate of 5 °C min<sup>-1</sup>.

The weight loss for compounds **1** and **2** are shown in Figure 3.11(a, b), it starts around 200 °C with the evaporation of surface water molecules. Both **1** and **2** show a similar weight loss characteristic, with 70.81% weight loss up to 400 °C the TEAB melting peak is observed at  $\sim 286$  °C as indicated in figure 3.11(a). The organic moiety TBAB has a melting point of 133 °C as shown.

The single phase change slope for both the compounds indicate the  $[\text{MnBr}_4]^{2-}$  octahedral bond breaking within the perovskite framework<sup>97</sup>. This is followed by the final melting of  $\text{MnBr}_2$  at 698 °C for both **1** and **2** which marks the complete dissociation of the structure<sup>97</sup>. Figure 3.11(c,d) shows the TGA spectra for compounds **3** and **4**.

The first step in the TGA graphs for HOIPs mark the breaking of ionic bonds within the framework and the second step is generally assigned to the breaking of covalent bonds forming the octahedrons<sup>98</sup>. The first step shows phase change for compound **3** wherein, 44.39% degradation occurs up to 450 °C indicating slow evaporation of the organic moiety however the second phase change starts after the complete melting of TEA Br at 286 °C causing a weight loss of 31.22% [Figure 3.11(c)]. Compound **4** shows first change up to 250°C and a weight loss of 57.59%. The second change causes a weight loss of 25.58%. Finally, the structure crumbles at 504 °C which indicates onset for CuBr melting<sup>47,56,57</sup> [Figure 3.11(d)].

### 3.3.5. Optical Spectroscopy

The Diffuse Reflectance Spectra (DRS) spectra was recorded for each of the compounds as shown in Figure 3.12(a). We observed a strong absorption edge at around 290 nm for all the compounds. This is the characteristic peak for formation of the 2D perovskite structure. It can be noted that the Mn-compounds (**1**, **2**) display several absorption bands at 377.56 nm (i), 416.47 nm (ii), 528.92 nm (iii) and, 619.60 (iv) nm<sup>58</sup>. These absorption peaks are associated with electronic transition (from the  ${}^6\text{A}_1$  ground state to different excited states) of  $\text{Mn}^{2+}$  ions in the tetrahedral  $[\text{MnBr}_4]^{2-}$  crystal-field<sup>58</sup>. The Cu-compounds (**3**, **4**) show a single edge sharp absorption at about 290 nm with weak tail states below 500 nm.

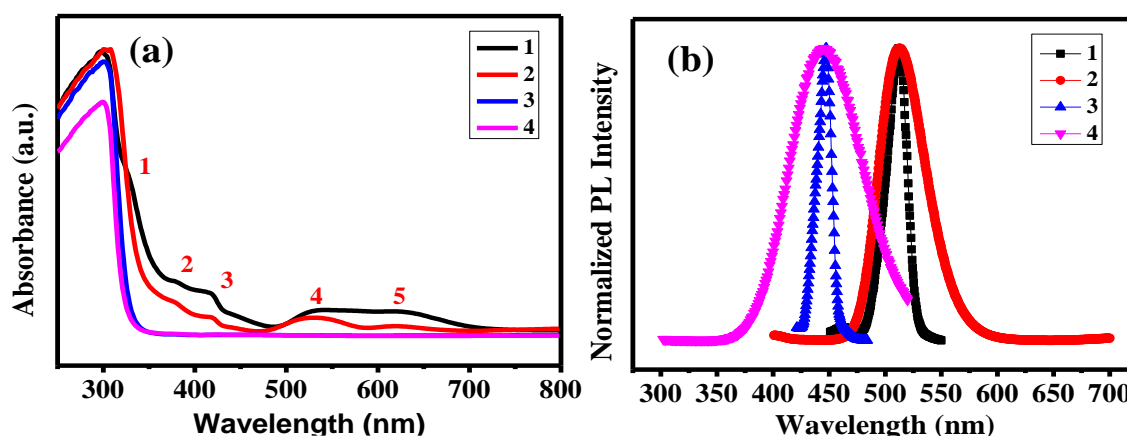


Figure 3.12: (a) DRS spectra, and (b) PL spectra for all the compounds (Excitation wavelength = 350 nm).

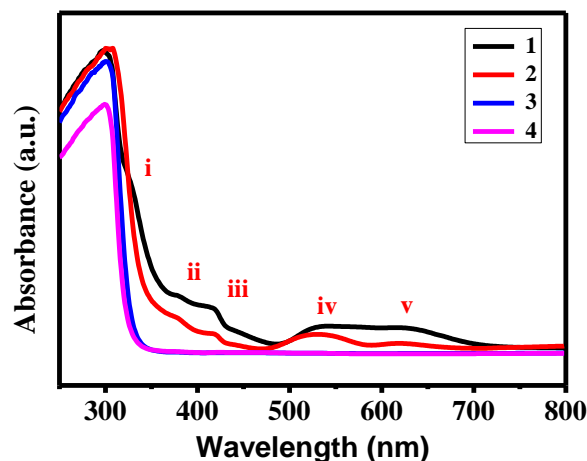


Figure 3.13: Tauc's plot calculated from the DRS spectra, at the maximum intensity edge state.

All the materials show luminescence under 365 nm UV lamp as shown in scheme 1. The normalized PL spectra shown in Figure 3.12(b) demonstrates that the PL emissions are in order with the visible emissions of the compounds from scheme 1. The compounds **1** and **2** show emission peak at centered at 514.21 nm and compounds **3** and **4** show peaks centered at 446.06 nm. The emission of peaks for compounds **1** and **2** can be assigned to the  $4T_1 \rightarrow 6A_1$  transition of the  $Mn^{2+}$  ion<sup>58</sup>.

The Tauc's plot for all the compounds is shown in Figure 3.13. The band gap energy of a nanomaterial can be determined from the Tauc's plot by extrapolating the linear portion of the plot to the x-axis (i.e., the photon energy axis). The point at which the extrapolated line intersects the x-axis is known as the Tauc intercept, which corresponds to the band gap energy. The values of  $(\alpha h\nu)^2$  vs  $h\nu$  for direct band gap & for indirect band gap  $(\alpha h\nu)^{1/2}$  vs  $h\nu$ , HOIP materials are direct band gap materials<sup>99</sup>. The as calculated band gaps are shown in Table 3.2. To elucidate the stability of the compounds we have carried out PL measurements at 70-80% humidity, Figure 3.14. We have noticed a drastic change in PL for compound **3** indicating a complete loss of the perovskite structure. However, comparatively very low material degradation is noted for compound **1**.

Manganese has a larger ionic radius than copper, which means that it can form stronger bonds with the surrounding ligands in the perovskite structure<sup>100</sup>. This results in a more stable crystal lattice, making the manganese-based 2D perovskites less prone to degradation in the presence of water. Furthermore, the stable electronic configuration for  $Mn^{+2}$ , electronic configuration  $[Ar]4s^0,3d^5$ , configuration where d-block is half filled making the centre more stable as

compared to compound **3**. These stronger metal-ligand bonds help to stabilize the crystal lattice and prevent water from attacking the perovskite<sup>101</sup>.

Table 3.2: Tauc's plot calculated from the DRS spectra, at the maximum intensity edge state.

Compounds	Calculated band gap (in eV)
<b>1</b> (2D)	3.25
<b>2</b> (2D)	3.50
<b>3</b> (2D)	3.77
<b>4</b> (0D)	3.80

Figure 3.14 shows the absorption and emission spectra for all the compounds for the ease of understanding. We also note a very high stokes shift for all the compounds, 1.19 eV (**1**), 1.08 eV (**2**), 1.06 eV (**3**) and 0.99eV (**4**), respectively. This can be attributed to trap mediated PL emission in 2D HOIP compounds.<sup>102</sup> The transition elements i.e. Mn<sup>2+</sup> and Cu<sup>2+</sup> respectively are acting as a deep trap centers.<sup>103</sup> We predict that when the electron-hole pairs in the compound are PL excited the electrons form a bound exciton on the transition metal sites. Especially for compounds **1** and **2** the band edge is not sharp in Figure 3.13, thus the Mn<sup>2+</sup> center acts like a deep trap which facilitates decay, hence the large stokes shift was observed.

To elucidate the stability of the compounds we have carried out PL measurements at 70-80% humidity (Figure 3.4). We have noticed a drastic change in PL for compound **3** indicating a complete loss of the perovskite structure. However, comparatively very low material degradation is noted for compound **1**. This is likely due to the fact that Mn<sup>2+</sup> has a larger ionic radius than Cu<sup>2+</sup>, which means that it can form stronger bonds with the surrounding ligands in the perovskite structure.<sup>105</sup> This results in a more stable crystal lattice, making the manganese-based 2D perovskites less prone to degradation in the presence of water. Furthermore, the stable electronic configuration for Mn<sup>2+</sup>, electronic configuration [Ar]4s0,3d5, configuration where d-block is half filled making the centre more stable as compared to compound **3**. These stronger metal-ligand bonds help to stabilize the crystal lattice and prevent water from attacking the perovskite.<sup>106</sup> In contrast, copper-based 2D perovskites are more susceptible to degradation in the presence of water due to weaker metal-ligand.<sup>107</sup> Copper also tends to undergo oxidation in

the presence of water, which can further destabilize the crystal lattice and lead to degradation. Therefore, the combination of a larger ionic radius and higher oxidation state of manganese compared to copper results in higher water stability in Mn-based 2D HOIPs.

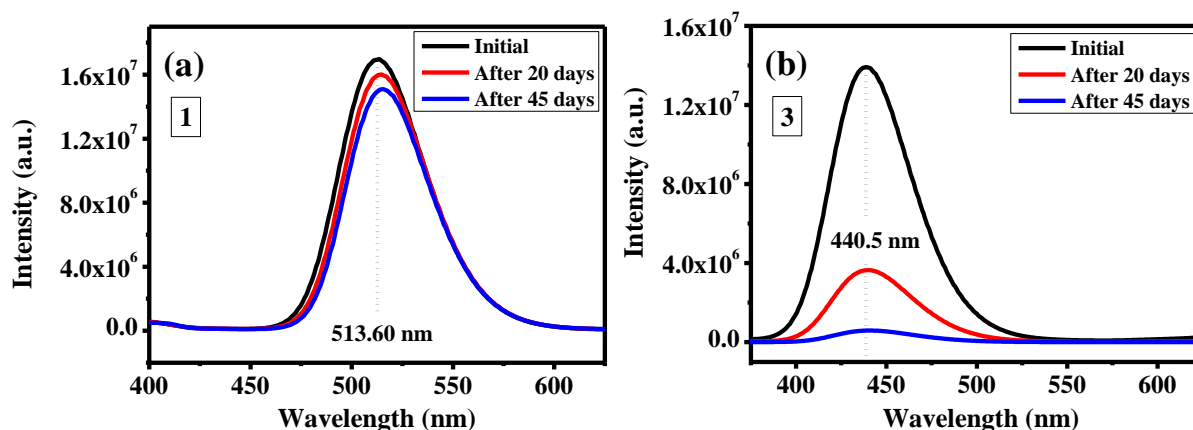


Figure 3.14: PL spectra of compounds **1** and **3** under 70-80% humidity conditions in solid state.

### 3.4. Metal Ion Detection

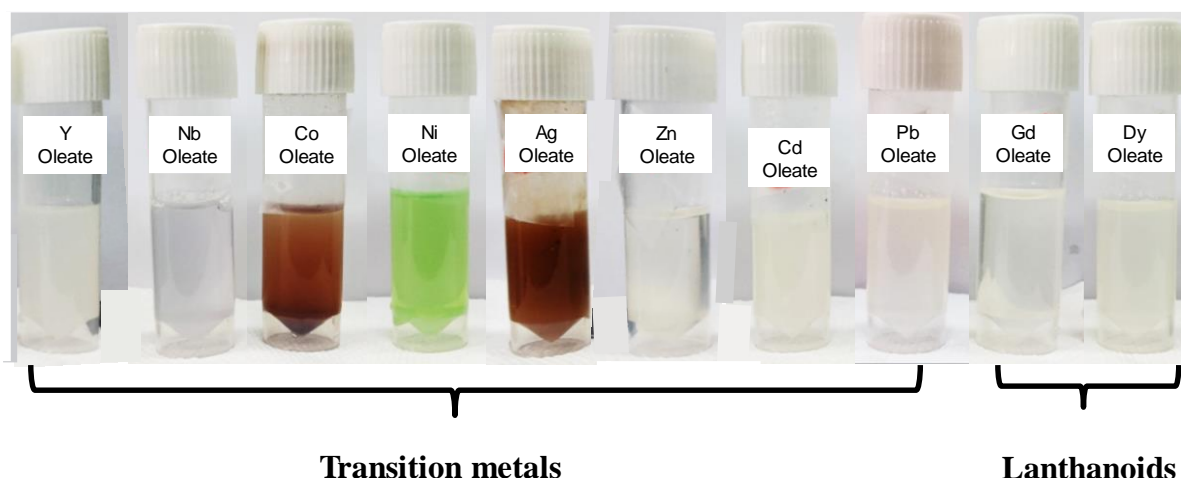


Figure 3.15: Digital photograph showing as prepared solutions of different metal-oleates of transition metalloids and lanthanides in toluene used for the metal ion detection experiments.

The superior stability of Mn-based HOIPs lead us to investigate fluorescence titration studies on compounds **1** and **2** for detecting metal cations using a signal transduction pathway by titration. Metal ion detection is essential in many fields such as medical diagnosis, environmental monitoring, and industrial quality control <sup>42</sup>.

Mn-based HOIPs offer a unique solution to this challenge due to their selective binding to specific metal ions, high sensitivity, cost-effectiveness, rapid response, and versatility. Despite

the several advantages of these Mn-LFHHPs their applicability for metal ion detection is limited.

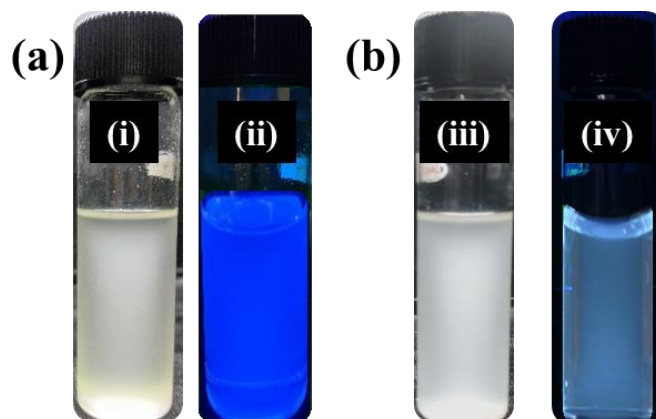


Figure 3.16: Digital photographs of solutions at concentration of 0.25 mg/ml of compounds (a) **1**, and (b) **2** in toluene; the left image in each panel is in ambient and the right image shows respective compounds under UV light, pictures for compounds **1** and **2** are recorded under 365 nm light.

We have carried out these studies in toluene as it is a high solubility solvent for HOIP-based metal ion detection which provides a favourable environment for the perovskite crystals to form and interact with metal ions keeping solvent based degradation to negligible levels.

Metal oleate solids were prepared by a previously reported methodology<sup>70</sup>. We have chosen transition metals and lanthanide ions such as,  $Y^{3+}$ ,  $Nb^{3+}$ ,  $Co^{2+}$ ,  $Ni^{2+}$ ,  $Ag^+$ ,  $Zn^{2+}$ ,  $Cd^{2+}$ ,  $Pb^{2+}$ ,  $Gd^{3+}$ , and  $Dy^{3+}$  respectively, to test the efficacy of as synthesized Mn-based HOIPs for fluorescence quenching studies. The toluene solutions of the respective metal-oleates are shown in Figure 3.15. The compounds were dispersed in toluene at a concentration of 0.25 mg/ml by sonicating for 10-15 minutes. Figure 3.16 shows dispersions of compounds **1**, and **2** and their respective emissions in dark under UV-lamp. This shifting from green emissive solid compound to blue emissive dispersions arises from the fact that as a solid goes to its nano-regime (later confirmed by HRTEM), a free-excitonic electron emission will arise at the band edge instead of trap mediated transitions in the bulk (Figure 3.17) accompanied by drastic reduction in Stokes shift to about 0.21 eV.<sup>105</sup>

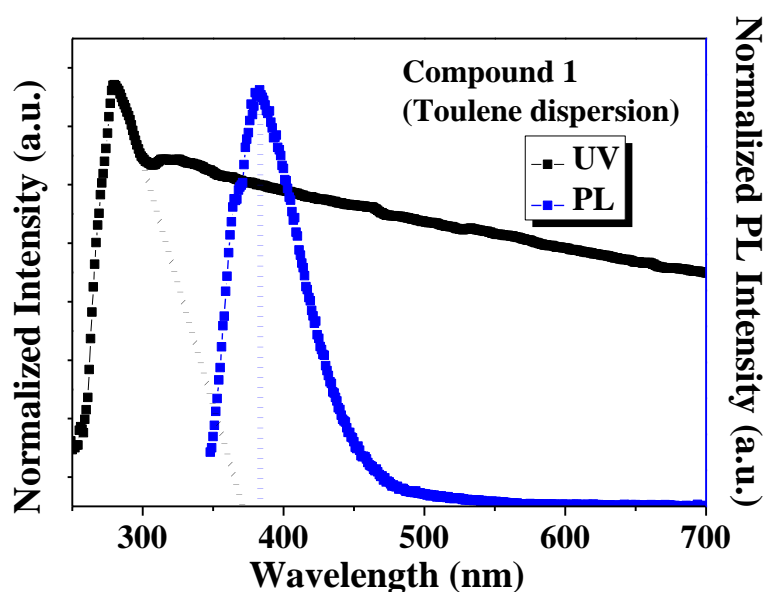


Figure 3.17: UV and PL spectra for solid as-synthesized compounds (a) **1**, (b) **2**, (c) **3** and (d) **4** indicating high Stokes shift for compounds in solid -state.

Fluorescence quenching performance of compounds **1** and **2** was carried out for detecting various above mentioned heavy metal ions. These investigations were carried out using a signal transduction pathway by titration. Fluorescence titration spectra were carried out in the presence of different  $\text{Pb}^{2+}$  concentrations ranging from  $0.25 \times 10^{-7} \text{ M}$  –  $2.0 \times 10^{-7} \text{ M}$ . The compounds **1** and **2** show PL emission at 383 nm in absence of  $\text{Pb}^{2+}$  ions [Figure 3.18(a, b)]. However, upon sequential addition of  $\text{Pb}^{2+}$  ions (concentration range  $0.25 \times 10^{-7} \text{ M}$  –  $2.0 \times 10^{-7} \text{ M}$ ) the peak intensity at  $\sim 383 \text{ nm}$  shows quenching behavior for both the compounds. Surprisingly, we note a sequential occurrence of a new emission peak at 552.28 nm for compound **1** and at 599.13 nm for compound **2**. Interestingly, the peak strength at 552.28 nm for compound **1** increases monotonically with maxima at  $2.0 \times 10^{-7} \text{ M}$  concentration of  $\text{Pb}^{2+}$  with a simultaneous quenching and peak minima for 383 nm emission at the same concentration [Figure 3.18(a)]. However, upon comparison of the initial results for compounds **1** and **2** [Figure (a, b)] it can be found that compound **1** is more sensitive towards the  $\text{Pb}^{2+}$  ion detection. Hence further analysis is carried out on compound **1** as Figure 3.18(a) shows a uniform reduction in PL intensity at of 383.01 nm which is the main peak. We carried out UV-vis absorbance spectroscopy [Figure 3.18(c)] to co-relate the changes in the emission spectra as identified by the appearance of a new peak at around 552.28. We noted a similar dual peak nature in the absorbance spectra. The peak initially at about 280 nm retained as the

concentration of  $\text{Pb}^{2+}$  increased along with the occurrence of a new peak around 350 nm. This can point towards the possibility of formation of a biphasic material within the solution.

Figure 3.18(d) plots the fluorescence intensity at around 383 nm for compound **1** as a function of the  $\text{Pb}^{2+}$  concentrations, the inset shows the  $\text{Pb}^{2+}$  concentration vs. emission intensity, demonstrating a linear relationship<sup>17</sup>. The titration method, which is superior to previous methods for detecting  $\text{Pb}^{2+}$  in solutions, was found to have a detection limit as low as  $2.0 \times 10^{-7}$  M. Also, because all of the fluorescence data were captured during the  $\text{Pb}^{2+}$  titration process, they implied a quick response, which was advantageous for quickly and quantitatively detecting  $\text{Pb}^{2+}$ .

The limit of detection (LOD) was determined to be  $2.43 \times 10^{-8}$  M using the equation,

$$\text{LOD} = 3\delta/s$$

(where  $\delta$  is the standard deviation of the signals and  $s$  is the slope of the linear calibration plot)<sup>17</sup>.

Selectivity towards various metal cations was tested under identical conditions while taking into consideration the interference of other metal cations. The fluorescence intensity rose by 100% at  $2.0 \times 10^{-7}$  M  $\text{Pb}^{2+}$  at 550 nm peak position, as shown in Figure 3.18(e), therefore this concentration was chosen to test compound **1**'s selectivity with the other 10 metal cations. Figure 3.18(e) shows how different metal cations have distinct effects on the fluorescence intensity at 339 nm. We can note that all the metal ions have changed the emission peak shape, broadened or multiple peaks are forming this can point to possible degradation. However, a change in the emission color was observed upon addition of  $\text{Pb}^{2+}$  along with nice evolution of two distinct peaks. This indicated that the compound **1** is unstable in the presence of other heavy metal cations used in this study, whereas the selectivity of compound **1** is extremely high towards  $\text{Pb}^{2+}$  metal ions indicated by a change in the emission of the solution.

The formula for determining a sample's selectivity to a certain metal cation ( $S_M$ ) is,

$$S_M = (F_0 - F)/F_0 \text{ 100\%}$$

where  $F$  and  $F_0$  are the fluorescence intensities in the presence and absence of the metal cation, respectively. Figure 3.18(f) illustrates the specific selectivity of **1** for other metal ions. With an  $S_{\text{Pb(II)}}$  value of 80.41%, the selectivity towards  $\text{Pb}^{2+}$  is significantly higher than that of other metal cations<sup>17</sup>.



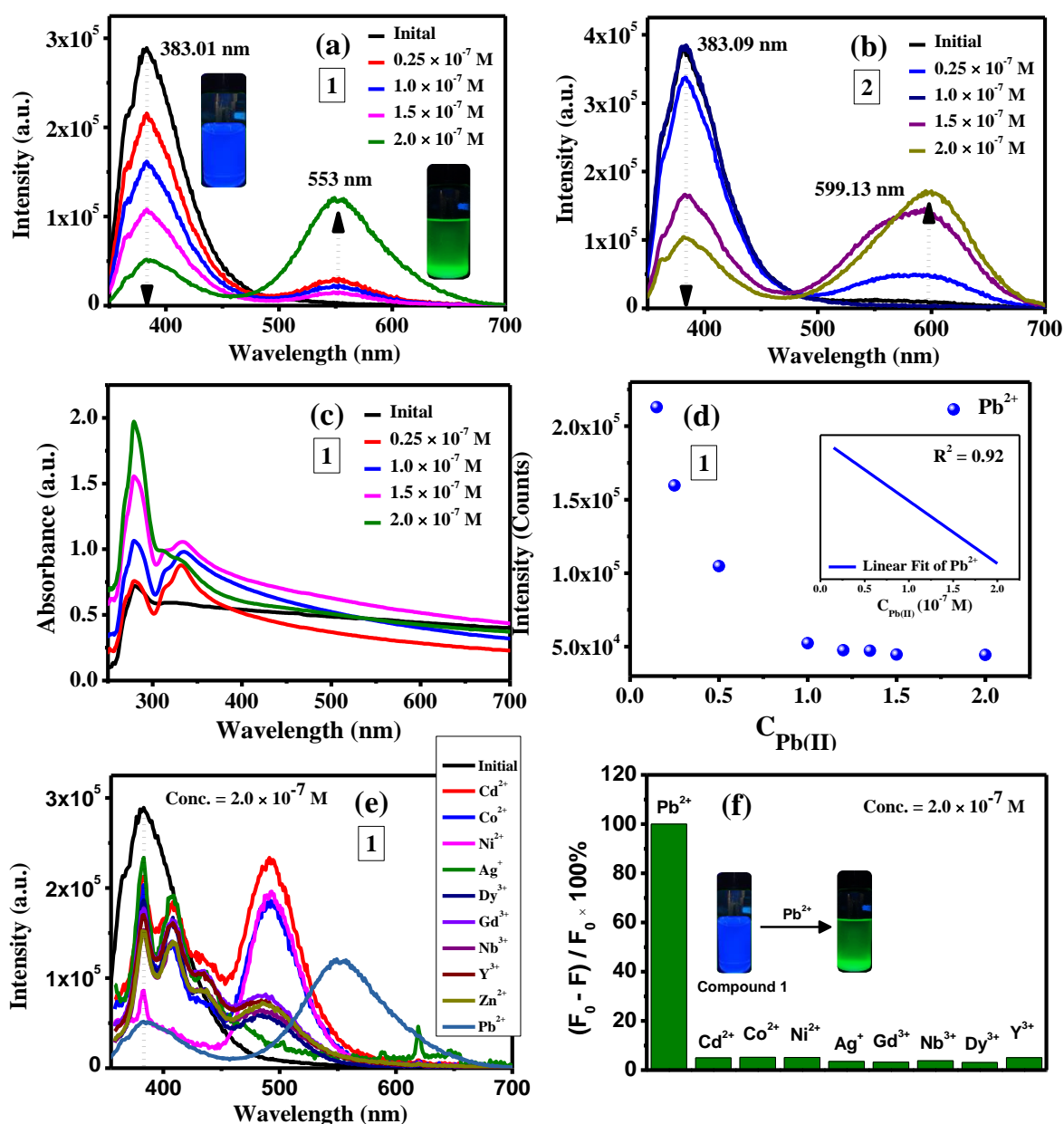


Figure 3.18: Compound dispersions: (a) fluorescence titration spectra for compound 1; (b) fluorescence titration spectra for compound 2; (c) Absorption spectra for compound 1 upon addition of  $Pb^{2+}$  ions; (d) Intensity v/s concentration of  $Pb^{2+}$  ions, inset is the corresponding calibration between the fluorescence intensity and  $Pb^{2+}$  concentration; Fluorescence results in blank and presence of various metal cations: (e) emission intensity spectra; (f) selectivity at  $\lambda = 552.28$ .

To test compound 1 for visual UV-lamp based  $Pb^{2+}$  detector we have fabricated thin film with compound 1. Compound 1 was solubilized at a concentration of 1 mg/ml in DMF solvent. The Compound 1 solution was coated using spin coater on a previously cleaned glass slide using a two-step programmed at 1000 RPM for 60 seconds and second step at 4000 RPM for 30

seconds. This was followed by annealing at 80 °C for 20 minutes. A calorimetric sensitivity test was performed by dipping the spin coated films of compound **1** in toluene solution of  $2.0 \times 10^{-7}$  M Pb-oleate for 2-4 seconds and the emission change was observed under a UV-lamp at  $\lambda = 365$  nm (Figure 3.19). We can note a clear change in emission of compound **1** [Figure 3.19(a)] upon partial dipping in the lead solution [Figure 3.19(b)] and upon complete dipping [Figure 3.19(c)] the change in emission colour from blue to green is as expected from the solution based metal ion detection experiments Figure 3.18(a).

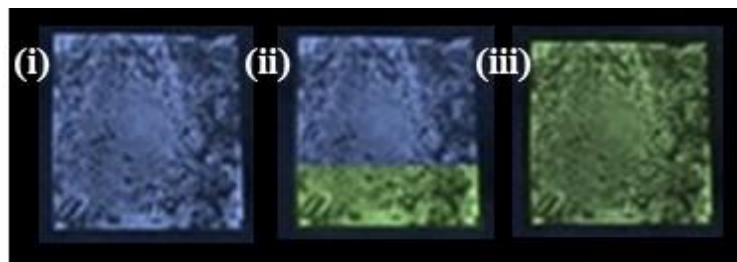


Figure 3.19: Photographic images of as casted film under  $\lambda = 365$  nm, (a) Compound **1** coated on a glass slide; Compound **1** coated on a glass slide after (b) 1/3 portion dipping in  $\text{Pb}^{2+}$  solution for 2-4 seconds; (c) completely dipping in  $\text{Pb}^{2+}$  solution for a shorter duration of time.

#### 3.4.1. Post - $\text{Pb}^{2+}$ detection Characterizations

In order to understand the correlation between the photophysical properties on compound **1** morphology in solid and dispersions states we carried out by HRTEM studies. The HRTEM images of compound **1** are shown in Figure 3.20 (a, b). Figure 3.20 (a) images corresponds to solid compound **1** after the mechanochemical synthesis method. We notice a clear 2D layered sheet-like structure with a d-spacing of 0.29 nm [Figure 3.21 (a)]. Figure 3.21 (b) corresponds to the nanoparticles (NPs) dispersions of compound **1** in toluene, with the average particle size distribution of  $\sim 5.45$  nm [Figure 3.21 (b)]. The d-spacing values of the NPs ( $\sim 0.27$  nm) are closely matching with the d-spacing value of solid compound **1** [Figure 3.21 (c)].

In order to quantify the occurrence of the very prominent peak at around 550 nm we carried out post application studies on the samples as shown in Figure 3.20. Figure 3.20 (c) shows the pXRD data for compound **1** upon gradual addition of  $\text{Pb}^{2+}$  ions. We can note evolution of a new peak at  $2\theta = 9^\circ$  along with peak intensity reduction at  $2\theta = 37.52^\circ$  indicated by the up and down arrows in Figure 3.20 (c) which we have ascertained to the formation of tetraethylammonium lead bromide. This is possible since HOIPs are ionic solids. When  $\text{Pb}^{2+}$  ions are introduced into the lattice of Mn-based hybrid organic-inorganic perovskites, compounds **1** it can replace some of the  $\text{Mn}^{2+}$  atoms in the lattice.

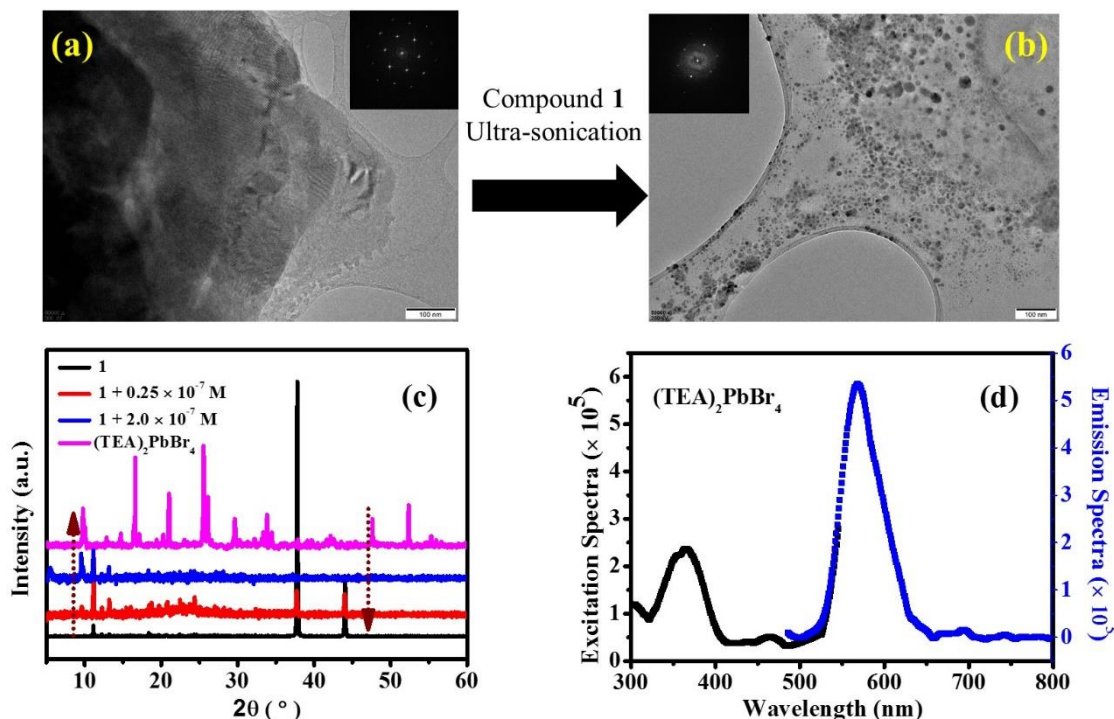


Figure 3.20: Post  $\text{Pb}^{2+}$  ion detection application studies for compound **1**, HRTEM images (a) As-synthesized solid powder, (b) After ultra-sonication of the solid power in Toluene solvent; Post  $\text{Pb}^{2+}$  ion detection application studies for compound **1**, (c) shows the XRD data for compound **1** in the presence of various concentrations of  $\text{Pb}^{2+}$  along with the possible formation of tetraethylammonium lead bromide; (d) PL Emission and PL excitation spectra for the tetraethylammonium lead bromide compound.

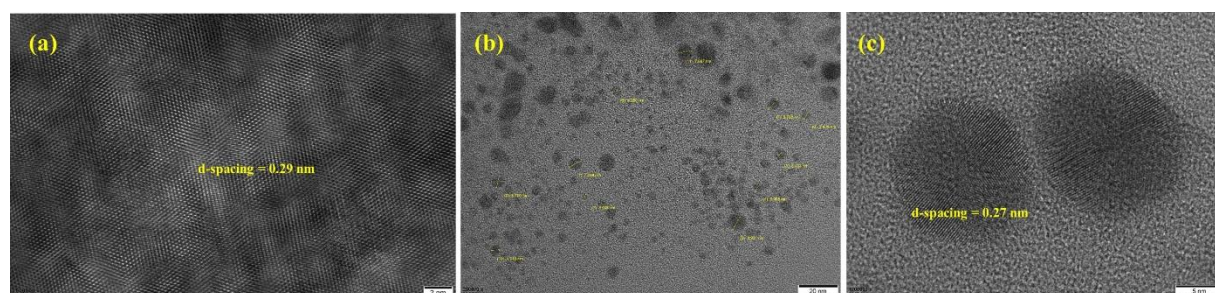
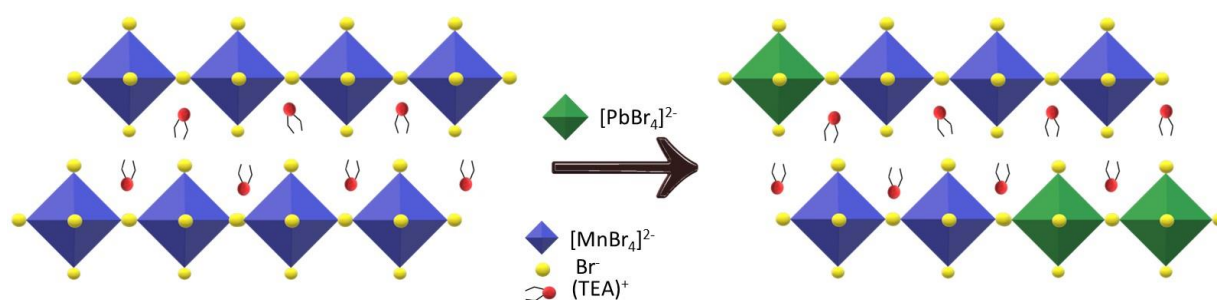


Figure 3.21: HRTEM images for toluene dispersion of compound **1**, (a) particle size distribution, (b) d-spacing calculations.

This is because  $\text{Pb}^{2+}$  has a similar size and electronic configuration to  $\text{Mn}^{2+}$ , and can fit into the lattice in a similar way.  $\text{Pb}^{2+}$  ions can also form bonds with the organic cation, TEA having  $\text{N}^+$  groups within the lattice, which can stabilize the crystal structure and improve the optical and electronic properties of the HLHPs material. We then carried out fluorescence emission

and excitation studies on  $(\text{TEA})_2\text{PbBr}_4$ , as represented in Figure 3.20 (d). These results clearly correlate to Figure 3.18 (a, b) wherein we can note the evolution of absorbance peak at  $\sim 350$  nm and a new PL peak at  $\sim 550$  nm which can now be assigned to the formation of an ion exchange *in-situ* compound of tetraethylammonium lead bromide.

#### 4.4.2. Proposed Mechanism



Scheme 3.2: Proposed mechanism for selective detection of  $\text{Pb}^{2+}$  by compound **1**. (For clarity, 2-ethyl chains have been represented in the  $(\text{TEA})^+$  molecule).

The conclusions drawn from the XRD, HRTEM and, PL studies lead to a proposed mechanism for the selective detection of  $\text{Pb}^{2+}$  by compound **1** is depicted in Scheme 3.2. There is an *in-situ* ion exchange reaction which goes on *in-situ*, leading to the formation of tetraethylammonium lead bromide NPs as confirmed from Figure 3.20. This new  $\text{TEAPbBr}$  compound causes the change in emission color and formation of a new peak ( $\sim 550$  nm) at the green wavelength. The LOD for this replacement reaction is obtained as  $5.28 \times 10^{-8}$  M. The  $\text{Pb}^{2+}$  detection by fluorescence titration is observed to be very fast, since the ion exchange reaction occurs within fraction of seconds.

### 3.5. Conclusion

To conclude, a novel, easy and energy efficient solid state methodology using KaKuHunter made planetary mixer under ambient conditions is proposed to synthesize Pb-free manganese- and copper-based HOIPs namely, compound **1**  $(\text{TEA})_2\text{MnBr}_4$ , compound **2**  $(\text{TBA})_2\text{MnBr}_4$ , compound **3**  $(\text{TEA})_2\text{CuBr}_4$  and compound **4**  $(\text{TBA})\text{CuBr}_2$ . Structural characterizations indicated that all the compounds are 2D except for  $(\text{TBA})\text{CuBr}_2$  which has crystallized in 0D lattice, supported by the Tauc's plot. All the compounds are phase pure and demonstrate a stable emission in solid state at room temperature. Furthermore, the stability of these compounds is studied under a relative humidity of 70% - 80% and the Mn-based HOIPs **1** and **2** showed reasonable stability when compared to the copper based HOIPs, this is ascertained to the stronger bonds for  $\text{Mn}^{2+}$  atoms in the lattice and its stable electronic configuration. As a result,

the Mn- based HOIPs were used for fluorescence titration studies using various heavy metal cations. Compounds **1** and **2** show good  $\text{Pb}^{2+}$  fluorescence quenching. However, compound **1** shows excellent fluorescence quenching performance as  $\text{Pb}^{2+}$  titration with a detection limit of  $5.28 \times 10^{-8}$  M including short reaction time, high sensitivity and reasonable selectivity. This detection is also possible visually at a  $\text{Pb}^{2+}$  concentration of  $2.0 \times 10^{-7}$  and hence compound **1** can be used for fabrication of a  $\text{Pb}^{2+}$  calorimetric sensor. This highly selective  $\text{Pb}^{2+}$  detection by compound **1** is brought about by the ability of  $\text{Pb}^{2+}$  ions to diffuse into the lattice and cause partial ion replacement within the lattice in order to form a biphasic material. Efficient and ultrafast detection of  $\text{Pb}^{2+}$  ions is of utmost environmental importance. Thus, this study reveals the ability of Pb-free HOIPs to detect oxidizing metal cations quantitatively.

### 3.6. References

1. A. Swarnkar, W. J. Mir, R. Chakraborty, M. Jagadeeswararao, T. Sheikh and A. Nag, , Chem. Mater. 2019, 31, 3, 565–575.
2. Y. Xie, H. Yu, J. Duan, L. Xu and B. Hu, ACS Appl. Mater. Interfaces, 2020, 12, 11190–11196.
3. J. You, Z. Hong, T. Bin Song, L. Meng, Y. Liu, C. Jiang, H. Zhou, W. H. Chang, G. Li and Y. Yang, Appl. Phys. Lett., , Applied Physics Letters 105(18):183902.
4. C. Ma, D. Shen, T. W. Ng, M. F. Lo and C. S. Lee, Adv. Mater., 2018, 30, 1800710.
5. H. Tsai, W. Nie, J.-C. Blancon, C. C. Stoumpos, R. Asadpour, B. Harutyunyan, A. J. Neukirch, R. Verduzco, J. J. Crochet, S. Tretiak, L. Pedesseau, J. Even, M. A. Alam, G. Gupta, J. Lou, P. M. Ajayan, M. J. Bedzyk, M. G. Kanatzidis and A. D. Mohite, Nature, 2016, 536, 312–316.
6. W. Zhang, M. Saliba, S. D. Stranks, Y. Sun, X. Shi, U. Wiesner and H. J. Snaith, Nano Lett., 2013, 130815103150002.
7. S. S. Mali and C. K. Hong, Nanoscale, 2017, 2, 3095–3104.
8. T. T. Ngo, I. Suarez, G. Antoncelli, D. Cortizo-Lacalle, J. P. Martinez-Pastor, A. Mateo-Alonso and I. Mora-Sero, Adv. Mater., Adv.Mater.2017, 29, 1604056.
9. M. Kar, R. Sarkar, S. Pal and P. Sarkar, J. Phys. Chem. C, 2021, 125, 74–81.
10. M. A. Green and A. Ho-Baillie, ACS Energy Lett., 2017, 2, 822–830.
11. T. M. A. Kojima, K. Teshima, Y. Shirai, J Am Chem Soc, 2009, 131, 6050–6051.
12. T. C. Sum and N. Mathews, Energy Environ. Sci., 2014, 7, 2518–2534.
13. H. J. Snaith, Nat. Mater., 2018, 17, 372–376.
14. T. Duong, A. T. John, H. Chen, H. Pham, K. Murugappan, T. Tran-Phu, A. Tricoli and K. Catchpole, Mater. Adv., 2022, 3, 1263–1271.
15. W. Xu, F. Li, Z. Cai, Y. Wang, F. Luo and X. Chen, J. Mater. Chem. C, 2016, 4, 9651–9655.
16. P. Kour, M. Chenna Reddy, S. Pal, S. Sidhik, T. Das, P. Pandey, S. P. Mukherjee, S. Chakraborty, A. D. Mohite and S. Ogale, Angew. Chemie - Int. Ed., 2021, 60, 18750–18760.
17. M. Y. Zhu, L. X. Zhang, J. Yin, J. J. Chen and L. J. Bie, Inorg. Chem. Commun., 2019, 109, 107562.
18. D. Zhang, Y. Xu, Q. Liu and Z. Xia, Inorg. Chem., 2018, 57, 4613–4619.
19. P. Pandey, A. Sengupta, S. Parmar, U. Bansode, S. Gosavi, A. Swarnkar, S. Muduli, A. D. Mohite and S. Ogale, ACS Appl. Nano Mater., 2020, 3, 3305–3314.
20. Y. Zhou, L. You, S. Wang, Z. Ku, H. Fan, D. Schmidt, A. Rusydi, L. Chang, L. Wang, P. Ren, L. Chen, G. Yuan, L. Chen and J. Wang, Nat. Commun., 2016, 7, 11193.
21. Z. Wang, Q. Lin, F. P. Chmiel, N. Sakai, L. M. Herz and H. J. Snaith, Nat. Energy, 2017, 2, 1–10.
22. S. Nagane and S. Ogale, J. Phys. Chem. Lett., 2016, 7, 4757–4762.

23. L. Mao, W. Ke, L. Pedesseau, Y. Wu, C. Katan, J. Even, M. R. Wasielewski, C. C. Stoumpos and M. G. Kanatzidis, *J. Am. Chem. Soc.* 2018, 140, 10, 3775–3783.
24. A. Krishna, S. Gottis and M. K. Nazeeruddin, 2018, 1806482, 1–20.
25. P. Kour, M. C. Reddy, R. Naphade and S. Ogale, *APL Mater.*, 2018, 6, 086107–7.
26. A. Basu, P. Kour, S. Parmar, R. Naphade and S. Ogale, *J. Phys. Chem. C*, 2018, 122, 4802–4808.
27. S. Krishnamurthy, P. Kour, A. Katre, S. Gosavi, S. Chakraborty and S. Ogale, *APL Mater.*, 2018, 6, 114204–8.
28. Z. Chen, X. Zheng, F. Yao, J. Ma, C. Tao and G. Fang, 2018, 17625–17632.
29. M. Shellaiah, K. Awasthi, S. Chandran, B. Azaad, K. W. Sun, N. Ohta, S.-P. Wu and M.-C. Lin, *ACS Appl. Nano Mater.*, 2022, 5, 2859–2874.
30. M. Kong, H. Hu, L. Wan, M. Chen, Y. Gan, J. Wang, F. Chen, B. Dong, D. Eder and S. Wang, *RSC Adv.*, 2017, 7, 35549–35557.
31. F. Xia, Y. Xu, B. Li, W. Hui, S. Zhang, L. Zhu, Y. Xia, Y. Chen and W. Huang, *ACS Appl. Mater. Interfaces*, 2020, 12, 15439–15445.
32. S. Aharon and L. Etgar, 2016, 6–11.
33. D. Amgar, S. Aharon and L. Etgar, *Adv. Funct. Mater.*, 2016, 26, 8576–8593.
34. C. M. M. Soe, C. C. Stoumpos, M. Kepenekian, B. Traoré, H. Tsai, W. Nie, B. Wang, C. Katan, R. Seshadri, A. D. Mohite, J. Even, T. J. Marks and M. G. Kanatzidis, *J. Am. Chem. Soc.*, 2017, 139, 16297–16309.
35. R. Guo, Z. Zhu, A. Boulesbaa, F. Hao, A. Puzos, K. Xiao, B. Jiming, Y. Yan and W. Li, *Small Methods*, 2017, 1, 1–6.
36. C. Quarti, N. Marchal and D. Beljonne, *J. Phys. Chem. Lett.*, 2018, acs.jpcclett.8b01309.
37. J. H. Kim and S. H. Kim, *Dye. Pigment.*, 2016, 133, 73–78.
38. J. H. Kim and S. H. Kim, *Dye. Pigment.*, 2016, 134, 198–202.
39. A. Senocrate, T. Acartürk, G. Y. Kim, R. Merkle, U. Starke, M. Grätzel and J. Maier, *J. Mater. Chem. A*, 2018, 6, 10847–10855.
40. S. H. Kim, A. Kirakosyan, J. Choi and J. H. Kim, *Dye. Pigment.*, 2017, 147, 1–5.
41. S. Cheng and H. Zhong, *J. Phys. Chem. Lett.*, 2022, 2281–2290.
42. Z. Zhu, Q. Sun, Z. Zhang, J. Dai, G. Xing, S. Li, X. Huang and W. Huang, *J. Mater. Chem. C*, 2018, 6, 10121–10137.
43. S. C. Hamel, J. R. Heckman, K. L. Shilke-Gartley and B. Hoskins, *Commun. Soil Sci. Plant Anal.*, 2003, v. v. 34.
44. S. J. Adjogri and E. L. Meyer, *Molecules*, DOI:10.3390/molecules25215039.
45. S. Chatterjee and A. J. Pal, *J. Mater. Chem. A*, 2018, 6, 3793–3823.
46. J. Jiang, C. K. Onwudinanti, R. A. Hatton, P. A. Bobbert and S. Tao, *J. Phys. Chem. C*, 2018, 122, 17660–17667.
47. B. Lei, X. Wu and W. Liu, *Crystals*, DOI:10.3390/cryst11060594.
48. E. Dynamics, T. Doped, J. Grimm, J. F. Suyver, E. Beurer, G. Carver and H. U. Gu, 2006, 2093–2101.
49. D. B. Mitzi and K. Liang, *Chem. Mater.*, 1997, 9, 2990–2995.
50. J. A. Barth, H.-J. Seifert and D. Haberhauer, *Z. anorg. allg. Chem.*, 1982, 491, 301–307.
51. V. M. Goldschmidt, *Naturwissenschaften*, 1926, 14, 477.
52. H. Peng, Y. Tian, Z. Zhang, X. Wang, T. Huang, T. Dong, Y. Xiao, J. Wang and B. Zou, *J. Phys. Chem. C*, DOI:10.1021/acs.jpcc.1c05065.
53. L. Lian, P. Zhang, G. Liang, S. Wang, X. Wang, Y. Wang, X. Zhang, J. Gao, D. Zhang, L. Gao, H. Song, R. Chen, X. Lan, W. Liang, G. Niu, J. Tang and J. Zhang, *ACS Appl. Mater. Interfaces*, 2021, 13, 22749–22756.
54. P. Pandey, N. Sharma, R. A. Panchal, S. W. Gosavi and S. Ogale, *ChemSusChem*, 2019, 12, 3742–3746.
55. X. Hei and J. Li, *Chem. Sci.*, 2021, 12, 3805–3817.
56. S. Charoensuk, J. Tan, M. Sain and H. Manuspiya, *Nanomaterials*, 2021, 11, 1–11.
57. A. Elattar, H. Suzuki, R. Mishima, K. Nakao, H. Ota, T. Nishikawa, H. Inoue, A. K. K. Kyaw and Y. Hayashi, *J. Mater. Chem. C*, 2021, 9, 3264–3270.
58. S. Chen, J. Gao, J. Chang, Y. Zhang and L. Feng, *Sensors Actuators, B Chem.*, 2019, 297, 1–8.

59. B. Su, G. Zhou, J. Huang, E. Song, A. Nag and Z. Xia, *Laser Photonics Rev.*, 2021, 15, 1–29.
60. F. Akrouf, F. Hajlaoui, K. Karoui, N. Audebrand, T. Roisnel and N. Zouari, *J. Solid State Chem.*, , *J. Solid State Chem.* 287, 2020, 121338.
61. T. Xuan and R. J. Xie, *Chem. Eng. J.*, 2020, 393, 124757.
62. P. Szklarz, R. Jakubas, W. Medycki, A. Gągor, J. Cichos, M. Karbowski and G. Bator, *Dalt. Trans.*, , *Dalton Trans.*, 2022, 51, 1850–1860.
63. S. N. Hsu, W. Zhao, Y. Gao, Akriti, M. Segovia, X. Xu, B. W. Boudouris and L. Dou, *Nano Lett.*, , *Nano Lett.* 2021, 21, 18, 7839–7844.
64. D. Han, H. Shi, W. Ming, C. Zhou, B. Ma, B. Saparov, Y. Z. Ma, S. Chen and M. H. Du, *J. Mater. Chem. C*, 2018, 6, 6398–6405.
65. F. Reyes-Pérez, J. J. Gallardo, T. Aguilar, R. Alcántara, C. Fernández-Lorenzo and J. Navas, *ChemistrySelect*, 2018, 3, 10226–10235.
66. M. Aamir, M. Sher, M. A. Malik, J. Akhtar and N. Revaprasadu, *New J. Chem.*, 2016, 40, 9719–9724.
67. X. Sheng, Y. Liu, Y. Wang, Y. Li, X. Wang, X. Wang, Z. Dai, J. Bao and X. Xu, *Adv. Mater.*, , *Adv. Mater.* 2017, 29, 1700150.
68. X. Sheng, Y. Liu, Y. Wang, Y. Li, X. Wang, X. Wang, Z. Dai, J. Bao and X. Xu, *Adv. Mater.*, 2017, 29, 1–7.
69. Y. Huang, F. Yan, J. Xu, Y. Bian, R. Zhang, J. Wang and X. Zhou, *Microchim. Acta*, 2017, 184, 3513–3519.
70. Y. Liu, X. Tang, T. Zhu, M. Deng, I. P. Ikechukwu, W. Huang, G. Yin, Y. Bai, D. Qu, X. Huang and F. Qiu, *J. Mater. Chem. C*, 2018, 6, 4793–4799.
71. C. Ma, M. F. Lo and C. S. Lee, *Chem. Commun.*, 2018, 54, 5784–5787.
72. N. Ding, D. Zhou, G. Pan, W. Xu, X. Chen, D. Li, X. Zhang, J. Zhu, Y. Ji and H. Song, *ACS Sustain. Chem. Eng.*, 2019, 7, 8397–8404.
73. Q. Li, W. Zhou, L. Yu, S. Lian and Q. Xie, *Mater. Lett.*, 2021, 282, 128654.
74. S. Ray, A. Mohapatra and S. Bhaumik, *Mater. Adv.*, 2022, 3, 4684–4692.
75. M. Shellaiah, K. Awasthi, S. Chandran, B. Aazaad, K. W. Sun, N. Ohta, S. P. Wu and M. C. Lin, *ACS Appl. Nano Mater.*, 2022, 5, 2859–2874.
76. L. Q. Lu, T. Tan, X. K. Tian, Y. Li and P. Deng, *Anal. Chim. Acta*, 2017, 986, 109–114.
77. I. Poli, S. Eslava and P. Cameron, *J. Mater. Chem. A*, 2017, 5, 22325–22333.
78. S. K. Abdel-Aal, G. Kocher-Oberlehner, A. Ionov and R. N. Mozhchil, *Appl. Phys. A Mater. Sci. Process.*, 2017, 123, 1–10.
79. K. Asokan, M. K. Patil, S. P. Mukherjee, S. B. Sukumaran and T. Nandakumar, *Chem. - An Asian J.*, , DOI:10.1002/asia.202201012.
80. Y. Liu, X. Tang, T. Zhu, M. Deng, I. P. Ikechukwu, W. Huang, G. Yin, Y. Bai, D. Qu, X. Huang and F. Qiu, *J. Mater. Chem. C*, 2018, 6, 4793–4799.
81. Y. El Ajjouri, F. Locardi, M. C. Gélvez-rueda, M. Prato, M. Sessolo, M. Ferretti, F. C. Grozema, F. Palazon and H. J. Bolink, 2019, 1900788, 1–9.
82. J. Breternitz, S. Levchenko, H. Hempel, G. Gurieva and A. Franz, .
83. G. K. Grandhi, N. S. M. Viswanath, H. Bin Cho, J. H. Han, S. M. Kim, S. Choi and W. Bin Im, , *J. Phys. Chem. Lett.* 2020, 11, 18, 7723–7729.
84. O. H. Perovskites, A. D. Jodlowski, Y. Ø. Alfonso, R. Luque, L. Camacho and G. De Miguel, 2016, 14972–14977.
85. C. Jiang, H. Fu, Y. Han, D. Li, H. Lin, B. Li and X. Meng, 2019, 1800236, 1–7.
86. H. Nagasaka, M. Yoshizawa-Fujita, Y. Takeoka and M. Rikukawa, *ACS Omega*, 2018, 3, 18925–18929.
87. S. F. Zhang, X. K. Chen, A. M. Ren, H. Li and J. L. Bredas, *ACS Energy Lett.*, 2019, 4, 17–25.
88. S. Kubota, S. Ozaki, J. Onishi, K. Kano and O. Shirai, *Anal. Sci.*, 2009, 25, 189–194.
89. Y. Zhou, Y. Huang, X. Xu, Z. Fan, J. B. Khurgin and Q. Xiong, *Appl. Phys. Rev.*, , *Applied Physics Reviews* 7, 041313, 2020.
90. J. Du, M. Zhang and J. Tian, *Int. J. Miner. Metall. Mater.*, 2022, 29, 49–58.
91. B. Smith, *Spectroscopy*, 2019, 34, 22–26.
92. Y. Singh, P. C. Sharpe, H. N. Hoang, A. J. Lucke, A. W. McDowall, S. P. Bottomley and D. P.

- Fairlie, Chem. - A Eur. J., 2011, 17, 151–160.
93. A. Srivastava, P. Arya, S. Goel, B. Kundu, P. Mishra and A. Fnu, PLoS ONE 10, 5, e0127011, 2015.
  94. P. A. Pieniazek and J. Stangret, Vib. Spectrosc., 2005, 39, 81–87.
  95. M. Najafi, A. Abbasi, M. Masteri-Farahani and J. Janczak, Dalt. Trans., 2015, 44, 6089–6097.
  96. Y. Zhao, C. Xie, Y. Song and P. Yang, J. Nanoparticle Res., , DOI:10.1007/s11051-020-04884-w.
  97. J. G. Zhang, Z. M. Li, Y. Zang, T. L. Zhang, Y. J. Shu, L. Yang and P. P. Power, J. Hazard. Mater., 2010, 178, 1094–1099.
  98. A. Drzewiecka-Antonik, W. Ferenc, B. Mirosław, D. Osypiuk and J. Sarzyński, Polyhedron, 207, 115370, 2021.
  99. P. Han, X. Zhang, C. Luo, W. Zhou, S. Yang, J. Zhao, W. Deng and K. Han, ACS Cent. Sci., 2020, 6, 566–572.
  100. S. Krishnamurthy, R. Naphade, W. J. Mir, S. Gosavi, S. Chakraborty, R. Vaidhyathan and S. Ogale, Adv. Opt. Mater., 2018, 6, 1800751.
  101. Q. Chen, N. De Marco, Y. Yang, T. Bin Song, C. C. Chen, H. Zhao, Z. Hong, H. Zhou and Y. Yang, Nano Today, 2015, 10, 355–396.
  102. M. Gong, B. Timalina, R. Sakidja, J. T. Douglas and J. Z. Wu, Adv. Opt. Mater., , DOI:10.1002/adom.202101012.
  103. M. B. Gawande, A. Goswami, F. X. Felpin, T. Asefa, X. Huang, R. Silva, X. Zou, R. Zboril and R. S. Varma, Chem. Rev., 2016, 116, 3722–3811.
  104. T. Density, A. F. Xu, R. T. Wang, L. W. Yang, E. E. Liu and G. Xu, Crystals, 2020, 10, 272.
  105. S. Kumar, J. Jagielski, T. Marcato, S. F. Solari and C. Shih, J. Phys. Chem. Lett. 2019, 10, 24, 7560–7567.
  106. M. B. Gawande, A. Goswami, F. X. Felpin, T. Asefa, X. Huang, R. Silva, X. Zou, R. Zboril and R. S. Varma, Chem. Rev., 2016, 116, 3722–3811.
  107. M. Ch, N. H. Pbcl and P. Nanocrystals, Crystals, 8,4, 2018.
  108. Y. J. Kim, D. Kim, Y. Kim, Y. Jeong, B. Jeong and J. Y. Park, mBio., 2021, 12, 1, e02583-20.
  109. S. Wu, L. Cheng and Q. Wang, Mater. Res. Express 4 085017, 2017.



*Appendix***Materials**

Copper bromide, CsBr	Sigma-Aldrich, 99%
Manganese bromide, MnBr	Sigma-Aldrich, 99%
Tetraethylammonium bromide, $C_8H_{20}N^+Br^-$	Hygeia Laboratories, A.R. grade
Tetrabutylammonium bromide, $C_{16}H_{36}N^+Br^-$	Sigma-Aldrich, 99.9%
1,4-dioxane	Sigma-Aldrich, 99.8%
Mesitylene	Sigma Aldrich, 99.8%
Acetic acid glacial, AA	SRL, extrapure 99.5%
Methyl Orange, MO	BDH Laboratory Reagent
DMF	AVRA, A.R. grade
Hexane	SRL, 99%
Toluene	SRL, 99%
Methanol	Thomas Baker, A.R. grade
Triethanolamine, TEOA	Loba Chemie, A.R. 99%
p-benzoquinone, PBZQ	98+%, Alfa Aesar
Isopropyl alcohol, IPA	SRL, UV and HPLC grade, 99.8%

**Characterizations**

*pXRD*: The phase identification of the as-synthesized samples were performed by Powder X ray diffraction (PXRD), recorded on a Panalytical X'pert PRO powder X-ray diffractometer with Cu K $\alpha$  radiation. Small Angle X-Ray Diffraction (SAXS) was performed on a Rigaku, Micromax-007HF with highintensity micro focus rotating anode X-Ray generator.

*FESEM*: The images were taken in a SEM NNS 450 instrument.

*TGA-DSC*: It was performed using SDT Q600 DSC-TGA instrument in Argon atmosphere at ramping rate 10 °C/min.

*XPS*: The surface properties of the as-synthesised samples were characterized by XPS using Thermo Scientific K-Alpha+ X-ray photoelectron spectrometer analyser chamber operating at  $2 \times 10^{-7}$  mbar pressure.

*FT-IR*: The spectra were recorded using Perkin Elmer 2000 FTIR spectrometer in the 400–4000  $cm^{-1}$  region.

*UV-Vis Spectroscopy:* The absorption spectra were collected using a Varian Carry 4000 UV–vis spectrophotometer.

*PL Spectroscopy:* The PL spectra were recorded using a Perkin Elmer LS 55 instrument.

## Chapter 4

### **3D/0D Perovskite@COF Nanocomposite for Photocatalysis of Model Molecule in Water**

In this chapter we have for the first time, synthesized all-inorganic CsPbBr<sub>3</sub>/Cs<sub>4</sub>PbBr<sub>6</sub> perovskite@COF nanocomposites under atmospheric conditions and tuned the crystal structures of the perovskite as well. The nanocomposite is reasonably stable and maintains its crystalline properties even when dipped into water for 60 minutes. The perovskite@COF nanocomposite shows efficient visible-light-driven photocatalytic performance to degrade Methyl orange (10 mL; 20–100 ppm). The rate of photodegradation was about 0.245 min<sup>-1</sup> with high catalytic activity and recyclability for three to six cycles.

Ref: This chapter is based on the thesis author's own publication, Prachi Kour and Shatabdi Porel Mukherjee, **J. Mater. Chem. A**, 2021, 9, 6819.

## 4.1. Introduction

All-inorganic cesium lead-halide perovskite nanocrystals (NCs) have recently attracted enormous attention due to their desirable photophysical properties.<sup>1-3</sup> Among them, cesium lead-bromide perovskites (CLBPs) have emerged as a prospective candidate in optoelectronic applications because of their strong photoluminescence (PL) with relatively narrow full width at half maximum (FWHM) and high PL quantum yields (PLQYs).<sup>4</sup> The networked perovskite NCs are essentially different from the usual low dimensional semiconductor NCs; instead, they are known as bulk quantum materials. In the case of perovskite NCs, charge carriers are localized within ordered metal halide sheets (2D), rods (1D), or clusters (0D), which are separated by cationic lattices. CLBPs are also known to exist in three-dimensional polymorphs, namely 3D CsPbBr<sub>3</sub> (cubic) formed by a cubo-octahedral (PbX<sub>6</sub><sup>-</sup>) network in all three directions, 2D CsPb<sub>2</sub>Br<sub>5</sub> (tetragonal) which possesses octahedral connectivity only in two directions and hence creates a layered structure and 0D Cs<sub>4</sub>PbBr<sub>6</sub> (hexagonal) which lacks octahedral connectivity in all the directions.<sup>4-10</sup> Therefore, for CLBPs, even in NCs and bulk, it is anticipated that the photo-excited charge carriers in these materials experience strong quantum confinement, and the exciton binding energy for 0D perovskites is much superior to that for 3D perovskites.<sup>11-13</sup> The PL intensity and efficiency of 0D Cs<sub>4</sub>PbBr<sub>6</sub> found to be much superior to those of 3D CsPbBr<sub>3</sub>.<sup>14,15</sup> Thus, strong excitons from Cs<sub>4</sub>PbBr<sub>6</sub> are likely to be very useful for various light-emitting devices, e.g., display technology, solar concentrators, lasers, LEDs, etc.<sup>4,16,17</sup> Current reports on the PL of Cs<sub>4</sub>PbBr<sub>6</sub> NCs are reasonably debatable; therefore, more investigations are necessary to understand the details and also the mechanism of the origin of PL. Few reports suggested that Cs<sub>4</sub>PbBr<sub>6</sub> NCs maintained strong and stable bright green luminescence.<sup>11-13</sup> In contrast, other reports acclaimed that Cs<sub>4</sub>PbX<sub>6</sub> NCs are almost non-emissive.<sup>18,19</sup> It has been claimed that the green emission of Cs<sub>4</sub>PbX<sub>6</sub> NCs originated from several phenomena, such as direct exciton recombination luminescence of Cs<sub>4</sub>PbBr<sub>6</sub>,<sup>16,20</sup> bromine vacancies,<sup>4</sup> and the impurities of CsPbBr<sub>3</sub> NCs embedded in Cs<sub>4</sub>PbBr<sub>6</sub> NCs.<sup>14,21,22</sup> It is also reported that the co-existence of CsPbBr<sub>3</sub> and Cs<sub>4</sub>PbBr<sub>6</sub> NCs was hard to suppress,<sup>23</sup> and Cs<sub>4</sub>PbBr<sub>6</sub> NCs can be easily transformed into CsPbBr<sub>3</sub> via an insertion reaction with additional PbBr<sub>2</sub>, physical or chemical extraction of CsBr, and ligand-mediated transformation.<sup>24-29</sup> Since, CsPbBr<sub>3</sub> has superior optical properties and Cs<sub>4</sub>PbBr<sub>6</sub> has higher moisture stability, their co-existence processed stability, and outstanding PLQY comparable to CsPbBr<sub>3</sub> NCs.<sup>30-36</sup> Several strategies have been adopted to form mixed-phase CLBP composites

and overcome the abhorrent obstacle of ambient instability, such as using polymer blends and inorganic passivators to solve these issues.<sup>37–40</sup>

Metal–organic frameworks (MOFs) are also used as effective encapsulations due to their framework structure and facile modulation features.<sup>41–44</sup> Covalent Organic Frameworks (COFs) are another sister class of MOFs in which light atoms bond covalently to form an open structure with high porosity.<sup>45,46</sup> These materials have similar properties to MOFs. Still, they possess a tunable pore size, structural predictability, lower density, and higher stability, making them an exciting class of encapsulations that have not been explored extensively to encapsulate perovskite systems as far as is known currently.<sup>46,47</sup>

In this work, we have synthesized a bromide cation containing covalent organic framework (EB-COF:Br) via a simple modified mechanochemical method and used it to fabricate a CLBP incorporated COF nanocomposite.<sup>48,49</sup> Interestingly, we have achieved both single-phase and mixed-phase CLBP systems, wherein 3D (CsPbBr<sub>3</sub>) and 3D/0D (CsPbBr<sub>3</sub>/Cs<sub>4</sub>PbBr<sub>6</sub>) crystal structures are encapsulated inside the EB-COF:Br framework. CsPbBr<sub>3</sub>/Cs<sub>4</sub>PbBr<sub>6</sub>@EB-COF:Br is found to be reasonably stable in a water medium for 60 minutes.

Using the CsPbBr<sub>3</sub>/Cs<sub>4</sub>PbBr<sub>6</sub>@EB-COF:Br nanocomposite, efficient visible-light-driven photocatalytic activity to degrade Methyl orange (MO) (10 mL; 20–100 ppm) is demonstrated. The CsPbBr<sub>3</sub>/Cs<sub>4</sub>PbBr<sub>6</sub>@EB-COF:Br nanocomposite material exhibited the highest photocatalytic activity reported to date with a photodegradation rate of about 0.245 min<sup>-1</sup> (for 100 ppm), using a perovskite composite material.<sup>41,50–62</sup> The recyclability of the photocatalyst is tested for three to six cycles.

We have specifically selected a cationic COF (EB-COF:Br) having Br-functionalization due to its chemical affinity and non-interference with the PL properties with the bromide containing perovskite, mainly CLBP.

## 4.2. Experimental Section

### 4.2.1. Synthesis of Ethidium Bromide COF (EB-COF:Br)

The EB-COF:Br was synthesized using a previously reported method in literature, with slight modifications. 1 In this method, 1,3,5-triformylphloroglucinol (TFP) (0.2 mmol), ethidium

bromide (EB) (0.3 mmol), 2 mL 1,4-dioxane–mesitylene (v/v, 1:1), 0.2 mL of 6M aqueous acetic acid were mixed together at room temperature for 2-3 hours by using DI water as the solvent till a dark brown paste was achieved. This paste was then transferred to a vial and heated in the oven at 90°C for 24 hours. The product was then washed thrice with methanol and THF solvents at 60°C for 12 hours each. Finally, the product was dried at 100°C under vacuum for 12 hours to get corresponding EB-COF:Br. The bulk phase purity of EB-COF:Br was confirmed by powder X-ray diffraction (XRD) measurements. The Brunauer–Emmett–Teller (BET) surface area was calculated from the measured N<sub>2</sub> adsorption-desorption isotherm at 77 K for the activated EB-COF:Br at 150 °C in vacuum for 12 h.

#### 4.2.2. Synthesis of CsPbBr<sub>3</sub>@EB-COF:Br

In a 30 mL glass vial, PbBr<sub>2</sub> (3.0 mmol) was dispersed in DMF (10.0 mL), and the mixture was stirred for 30 min at 60°C. Then, the as-prepared EB-COF:Br powder (1 mg/ml) and PbBr<sub>2</sub> solutions were mixed and stirred for 2-3 h at 60°C, followed by cooling to RT. The powder was separated by centrifugation under 10,000 rpm for 10 min. The sediment was collected and dispersed in toluene (10 mL). In a separate solution, CsBr (3.0 mmol) was dissolved in MeOH (10.0 mL) at 60 °C. Then, the CsBr/MeOH solution was quickly injected into the PbBr<sub>2</sub>/toluene precursor solution at 60°C. After 5 minutes of stirring the resulting CsPbBr<sub>3</sub>@EB-COF:Br composite powder was then centrifuged for 10 min at 10,000 rpm and then washed with hexane twice at 10,000 rpm for 10 minutes. All the above operations were performed under ambient atmospheric conditions.

#### 4.2.3. Synthesis of CsPbBr<sub>3</sub>/Cs<sub>4</sub>PbBr<sub>6</sub>@EB-COF:Br

The synthetic process was similar to the synthesis of CsPbBr<sub>3</sub>@EB-COF:Br, but the concentration of PbBr<sub>2</sub> and CsBr was 5.0 mmol each.

#### 4.2.4. Synthesis of CsPbBr<sub>3</sub>-Cs<sub>4</sub>PbBr<sub>6</sub> without COF

To synthesize the CsPbBr<sub>3</sub>/Cs<sub>4</sub>PbBr<sub>6</sub> nanocomposite a modified synthesis methodology of the previously reported method was used.<sup>2</sup> Briefly it was as follows, CsBr (1.6mmol) and PbBr<sub>2</sub> (0.4 mmol) (CsBr/PbBr<sub>2</sub> molar ratio of 4:1) were added to DMF (2 mL) in a centrifuge tube with a volume of 5 mL. The centrifuge tube was ultra-sonicated for 30 min until all the reactants were

converted to a light yellowish precipitate. The CsPbBr<sub>3</sub>-Cs<sub>4</sub>PbBr<sub>6</sub> nanocomposite powder was obtained by evaporating the solvent in an oven at 70 °C after centrifugation.

#### 4.2.5. Water stability

The stability of compounds in water was checked by initially storing the compounds under DI water for a fixed interval of 5, 10, 20, 30, 40, 50, and 60 minutes followed by centrifuge separation and vacuum drying before analysis.

#### 3.2.6. Photocatalytic experiments

The photocatalytic performances of the as-synthesized samples were analysed by degradation of Methyl Orange (MO) dye in an aqueous solution under a Xe-300W lamp in a Photo catalytic reactor cabinet by Lelesil Innovative Systems. 10 mg of the photocatalyst was added to an aqueous solution of MO (10 mL, 20-100 ppm) in a 2 port-quartz reaction vessel at room temperature. The suspended solution was kept in dark for 5 min with continuous stirring to reach an adsorption–desorption equilibrium of MB molecules on the photocatalyst surface. Thereafter, this suspension was irradiated with Xe-300W lamp ( $\lambda = 100\text{-}1800\text{ nm}$ ) and the solution temperature was monitored continuously by a thermocouple and stabilized to 24- 26°C to trigger the decomposition of MO molecules under constant magnetic stirring. Aliquots of solution (500  $\mu\text{L}$ ) were isolated from the reaction mixture at a specific irradiation time, and the suspended solids were separated by centrifugation. The photocatalytic degradation process was monitored by measuring the absorption spectrum in the range of 200–700 nm (the maximum absorption of MO at 467 nm) using UV-1800 Shimadzu spectrophotometer. For reactions in dark similar method was followed to the light experiments.

#### 4.3. Results and Discussion

Recently, mechanochemical synthesis has become an excellent alternative to the solution based classical synthesis of COFs.<sup>48</sup> Herein, we have used a modified mechanochemical method to synthesize EB-COF:Br avoiding the necessity of using typical inert atmosphere conditions in a Pyrex tube, as reported earlier.<sup>49</sup> In this method, 1,3,5-triformyl phloroglucinol (TFP) (0.2 mmol) and ethidium bromide (EB) (0.3 mmol) were ground together using a mortar and pestle followed by the addition of 2 mL 1,4-dioxane–mesitylene (v/v, 1 : 1) and 0.2 mL of 6 M aqueous acetic acid solutions at room temperature. The mixing was continued for 2–3 hours by using DI water as the

solvent till a dark brown paste was achieved. This paste was then transferred to a vial and heated in an oven at 90 ° C for 24 hours. The product was then washed and dried under vacuum for further use [Figure 4.1].

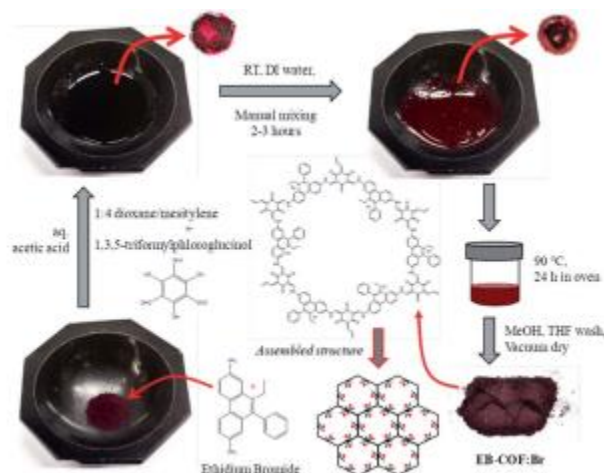


Figure 4.1: Schematic representation of the modified mechanochemical synthesis of EB-COF:Br through simple Schiff base reactions performed via mechanochemical grinding and mixing using a mortar and pestle, followed by heating.

In the following action, CLBP incorporated EB-COF:Br was synthesized via a two-step precursor addition strategy, wherein first  $\text{PbBr}_2$  was added, followed by  $\text{CsBr}$  addition to achieve the  $\text{CLBP@EB-COF:Br}$  nanocomposite [Figure 4.2].

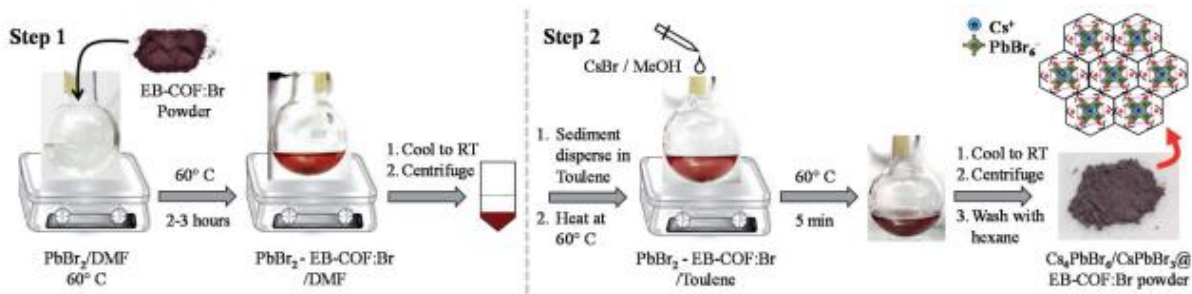


Figure 4.2: Schematic representation of the two-step solution-based synthesis of  $\text{CsPbBr}_3/\text{Cs}_4\text{PbBr}_6@EB-COF:Br$ .

The crystal structure of the products formed was investigated by XRD analysis. The existence of characteristic peaks at  $2.83^\circ$  and a broad peak at  $27^\circ$  corresponding to 100 and 001 planes confirmed the formation of EB-COF:Br (Fig. 4.3).<sup>49</sup> We were also able to tune the crystal



structures of the encapsulated perovskites by simply changing the mole ratios of CsBr and PbBr<sub>2</sub> (1 : 1) to COF concentration resulting in the formation of different crystal structures of CLBP.

Compound	PbBr <sub>2</sub>	CsBr	COF
CsPbBr <sub>3</sub> @EB-COF:Br	3 mmol	3 mmol	10 mg
CsPbBr <sub>3</sub> /Cs <sub>4</sub> PbBr <sub>6</sub> @EB-COF:Br	15 mmol	15 mmol	10 mg

Table 4.1: The concentration of precursors used to form the respective composites

### 4.3.1. Structural Characterizations

The PXRD patterns of the as synthesized sample were obtained using 15 mmol of PbBr<sub>2</sub> and CsBr, each [Figure 4.3]. The co-existence of cubic phase CsPbBr<sub>3</sub> and rhombohedral phase Cs<sub>4</sub>PbBr<sub>6</sub> is evident in Figure 4.3. The peaks at  $2\Theta = 15.17^\circ$ ,  $21.42^\circ$ ,  $26.39^\circ$ ,  $30.65^\circ$ ,  $34.43^\circ$  and  $37.70^\circ$  were respectively indexed to the (1 0 0), (1 1 0), (1 1 1), (2 0 0), (2 1 0) and (2 1 1) planes of cubic phase CsPbBr<sub>3</sub> with the lattice constant  $a = 5.83 \text{ \AA}$  (JCPDS no 54-0752),<sup>29,63</sup> while the peaks at  $2\Theta = 12.54^\circ$ ,  $12.83^\circ$ ,  $20.07^\circ$ ,  $22.39^\circ$ ,  $25.36^\circ$ ,  $27.47^\circ$ ,  $28.55^\circ$ ,  $30.66^\circ$ ,  $34.57^\circ$ ,  $37.61^\circ$ , and  $38.92^\circ$  were respectively indexed to the (0 1 2), (1 1 0), (1 1 3), (3 0 0), (0 2 4), (1 3 1), (2 1 4), (0 0 6), (4 1 0), (3 1 5), and (3 2 4) planes of Cs<sub>4</sub>PbBr<sub>6</sub> with lattice constants  $a = b = 13.73 \text{ \AA}$ ,  $c = 17.32 \text{ \AA}$ ,  $\alpha = \beta = 90^\circ$ , and  $\gamma = 120^\circ$  (JCPDS no 73-2478).<sup>29,63</sup> Therefore, the sample synthesized under the above conditions was named CsPbBr<sub>3</sub>/Cs<sub>4</sub>PbBr<sub>6</sub>@EB-COF:Br. When both PbBr<sub>2</sub> and CsBr were used in 3 mmol concentration while keeping the EB-COF:Br concentration constant, only cubic phase CsPbBr<sub>3</sub> was obtained. Peaks were observed at  $2\Theta = 21.61^\circ$ ,  $26.59^\circ$ , and  $30.79^\circ$  and indexed to the (1 1 0), (1 1 1), and (2 0 0), planes of cubic phase CsPbBr<sub>3</sub> with the lattice constant  $a = 5.64 \text{ \AA}$  (JCPDS no 54-0752)<sup>29,63</sup> and the corresponding sample was named CsPbBr<sub>3</sub>@EB-COF:Br [Figure 4.4].

For both the samples CsPbBr<sub>3</sub>/Cs<sub>4</sub>PbBr<sub>6</sub>@EB-COF:Br and CsPbBr<sub>3</sub>@EB-COF:Br, an intense diffraction peak at  $2.83^\circ$  and a broad peak at  $27^\circ$  were observed, which confirmed the presence of EB-COF:Br in the nanocomposites (Figure 4.3 and Figure 4.4).<sup>49</sup> Therefore, it was observed that the tuning of the crystal structures of CLBPs could be obtained by changing the mole concentration ratio of Cs and Pb to the COF while keeping all other reaction parameters constants.

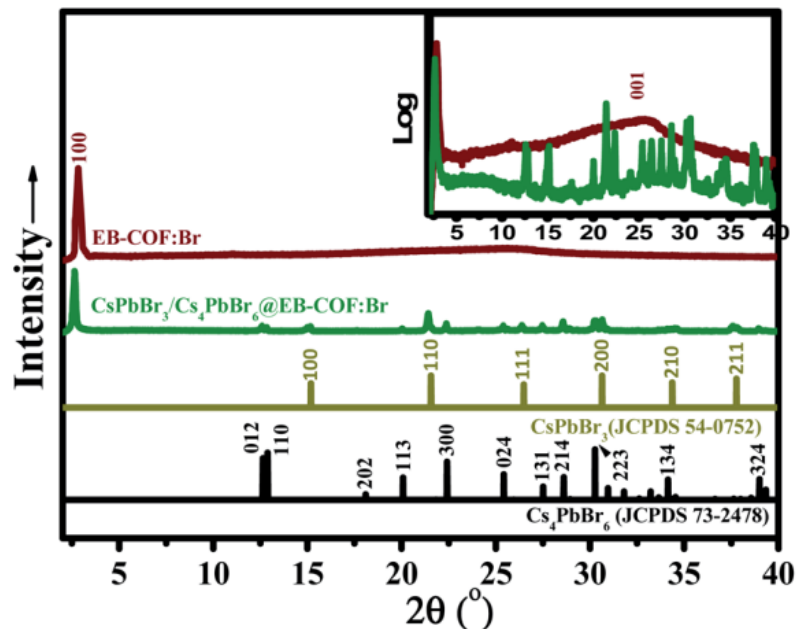


Figure 4.3: X-ray diffraction (XRD) pattern of the CsPbBr<sub>3</sub>/Cs<sub>4</sub>PbBr<sub>6</sub>@EB-COF:Br nanocomposite matched with JCPDS no 54-0752 for CsPbBr<sub>3</sub>, JCPDS no 73-2478 for Cs<sub>4</sub>PbBr<sub>6</sub> and EB-COF:Br (as per ref. 49). The inset shows the log of intensity to confirm the presence of a peak at 27° from EB-COF:Br.

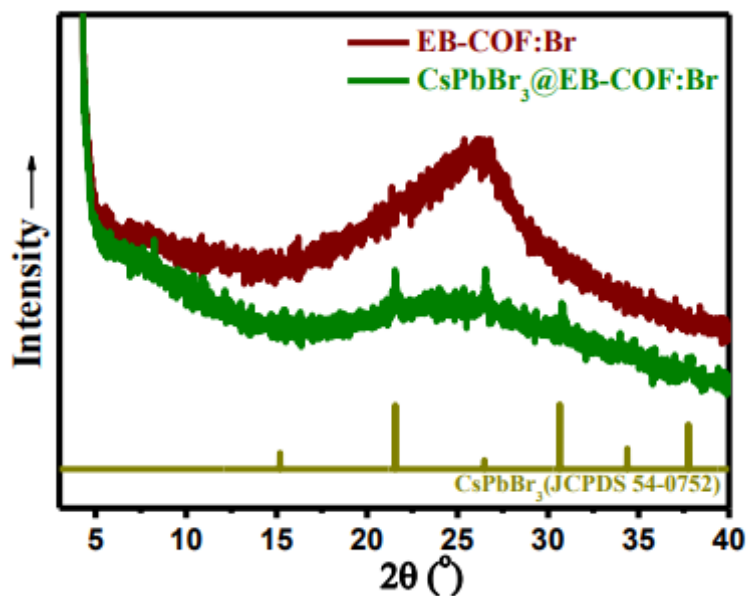


Figure 4.4: XRD pattern of EB-COF:Br and CsPbBr<sub>3</sub>@EB-COF:Br (matched with JCPDS no. 54-0752).

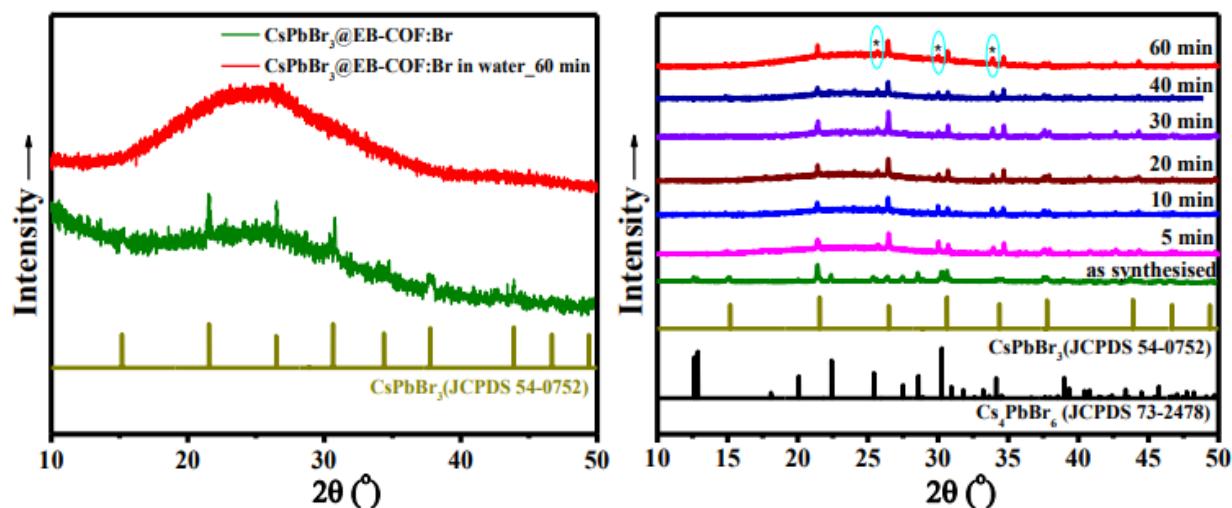


Figure 4.5: (a) XRD of CsPbBr<sub>3</sub>@EB-COF:Br compound before and after water stability test for 60 minutes; (b) Evolution of XRD with time within the duration of 60 minutes upon water stability test for CsPbBr<sub>3</sub>/Cs<sub>4</sub>PbBr<sub>6</sub>@EB-COF:Br compound, matched with JCPDS no. 54-0752 and 73-2478.

The water stability of both the COF encapsulated CLBP samples, CsPbBr<sub>3</sub>/Cs<sub>4</sub>PbBr<sub>6</sub>@EB-COF:Br and CsPbBr<sub>3</sub>@EB-COF:Br, was checked via time-dependent XRD analysis. 10 mg of the corresponding sample was immersed in DI water for a fixed time interval of 5, 10, 20, 30, 40, 50, and 60 minutes followed by complete vacuum drying before analysis. For the single-phase CsPbBr<sub>3</sub>@EB-COF:Br sample after being immersed in DI water for 60 min, only the peak from EB-COF:Br was prominently visible,<sup>49</sup> whereas the 2θ peaks from CsPbBr<sub>3</sub> were completely dispersed as represented in Figure 4.5(a). However for the sample CsPbBr<sub>3</sub>/Cs<sub>4</sub>PbBr<sub>6</sub>@EB-COF:Br, although a few very low intense peaks from the as-synthesized sample disappeared when dipped in water for 60 minutes, still the sample has retained its mixed phase composition, as represented in Figure 4.5(b). The peaks at 2θ of 21.41° , 26.43° , 30.68° , 34.66° and 37.94° correspond to the (1 1 0), (1 1 1), (2 0 0), (2 1 0) and (2 1 1) planes of cubic phase CsPbBr<sub>3</sub> (JCPDS no 54-0752), whereas the peaks at 2θ of 25.71° , 30.04° and 33.86° correspond to the (0 2 4), (0 0 6), and (4 1 0) planes of Cs<sub>4</sub>PbBr<sub>6</sub> (JCPDS no 73-2478).<sup>29,63</sup> The peaks for the Cs<sub>4</sub>PbBr<sub>6</sub> phase after water immersion show some shift in 2θ values probably because water induces strain effects. We have even compared the water stability of CsPbBr<sub>3</sub>/Cs<sub>4</sub>PbBr<sub>6</sub> materials synthesized using a reported protocol without encapsulation within the COF moiety.<sup>34</sup> It was noticed that for the CsPbBr<sub>3</sub>/Cs<sub>4</sub>PbBr<sub>6</sub> composite without COF encapsulation when dipped in water for 60 minutes, XRD shows complete reorganization of the crystal structure, along with the appearance of

precursor peaks ( $\text{CsBr}$  and  $\text{PbBr}_2$ ), indicating the instability of the mixed-phase composite without the COF encapsulation (Figure 4.6).

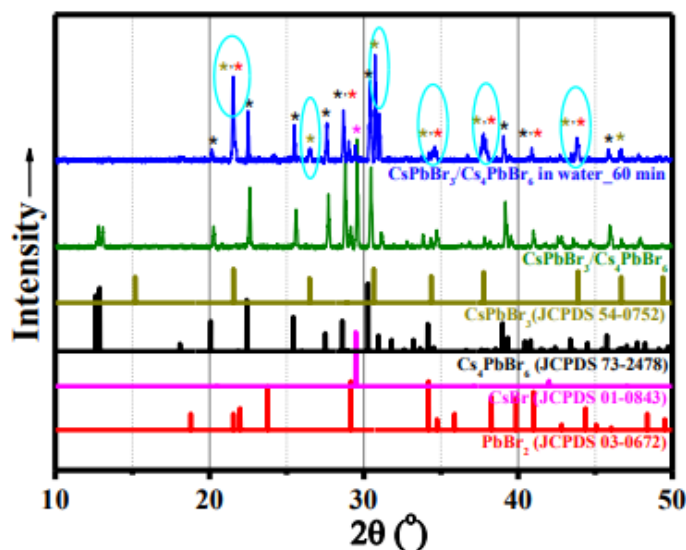


Figure 4.6: XRD of  $\text{CsPbBr}_3/\text{Cs}_4\text{PbBr}_6$  compound before and after water immersion for a duration of 60 minutes followed by vacuum drying before analysis. “\*” in the XRD shows the appearance of precursor peaks upon water immersion indicating instability of the composite without encapsulation.

Therefore, since the COF encapsulation prevented the degradation of the mixed-phase sample,  $\text{CsPbBr}_3/\text{Cs}_4\text{PbBr}_6@EB\text{-COF:Br}$ , into its precursors (e.g.,  $\text{CsBr}$  and  $\text{PbBr}_2$ ) even after the water immersion for 60 minutes, as observed from XRD analysis, we have continued with other characterization and water-based photocatalytic applications for the mixed-phase sample  $\text{CsPbBr}_3/\text{Cs}_4\text{PbBr}_6@EB\text{-COF:Br}$  only.

#### 4.3.2. Optical Spectroscopy

The  $\text{CsPbBr}_3/\text{Cs}_4\text{PbBr}_6@EB\text{-COF:Br}$  sample was investigated by UV-Vis absorption and PL spectroscopy, as shown in Figure 4.7. EB-COF:Br showed UV-Vis absorption around 314, 379, and 579 nm [Figure 4.7(a)], whereas one extra cliff around 510–515 nm was observed corresponding to the absorption of cubic-phase  $\text{CsPbBr}_3$  in the absorption spectra of the  $\text{CsPbBr}_3/\text{Cs}_4\text{PbBr}_6@EB\text{-COF:Br}$  nanocomposite, along with the peaks observed for EB-COF:Br.<sup>26,32,35</sup> Generally,  $\text{Cs}_4\text{PbBr}_6$  showed absorption spectra in the UV range around 313–315 nm,<sup>26,29,35</sup> but here due to the overlapping with absorption spectra in the UV region of EB-COF:Br,

the presence of the  $\text{Cs}_4\text{PbBr}_6$  absorption peak in the mixed-phase  $\text{CsPbBr}_3/\text{Cs}_4\text{PbBr}_6@EB\text{-COF:Br}$  nanocomposite cannot be concluded. Figure 4.7(b) shows the emission spectra recorded for the  $\text{CsPbBr}_3/\text{Cs}_4\text{PbBr}_6@EB\text{-COF:Br}$  nanocomposite with peak maxima at 516 nm,<sup>22,27</sup> indicating a low Stokes shift and hence the formation of defect-free nanocrystals, whereas EB-COF:Br was non-luminescent.<sup>64</sup>

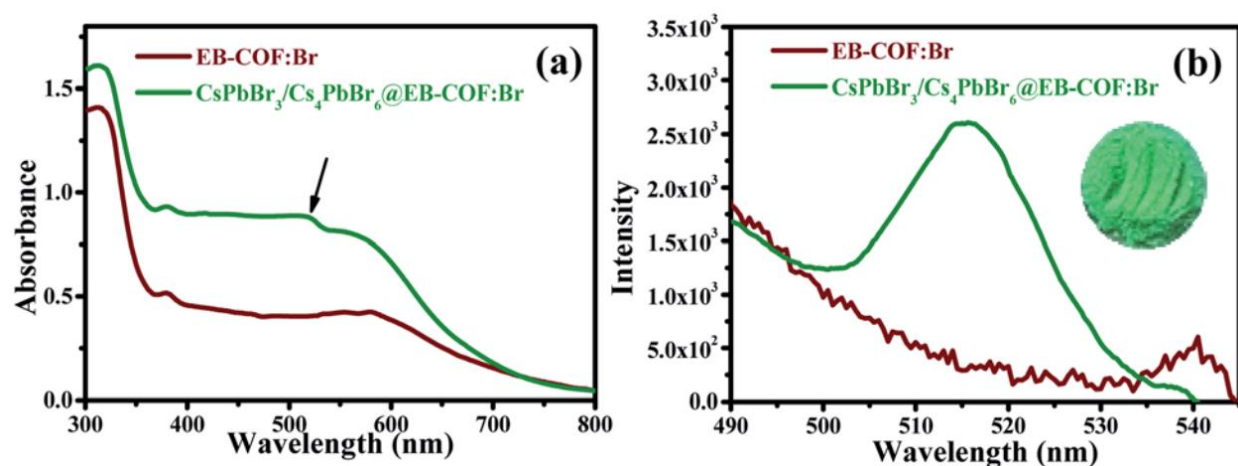


Figure 4.7: Photophysical properties of the  $\text{CsPbBr}_3/\text{Cs}_4\text{PbBr}_6@EB\text{-COF:Br}$  nanocomposite and EB-COF:Br; (a) UV-Vis spectra and (b) PL spectra [the inset shows the photograph of green emissive composite power under UV light (254 nm) irradiation].

### 4.3.3. IR Spectroscopy

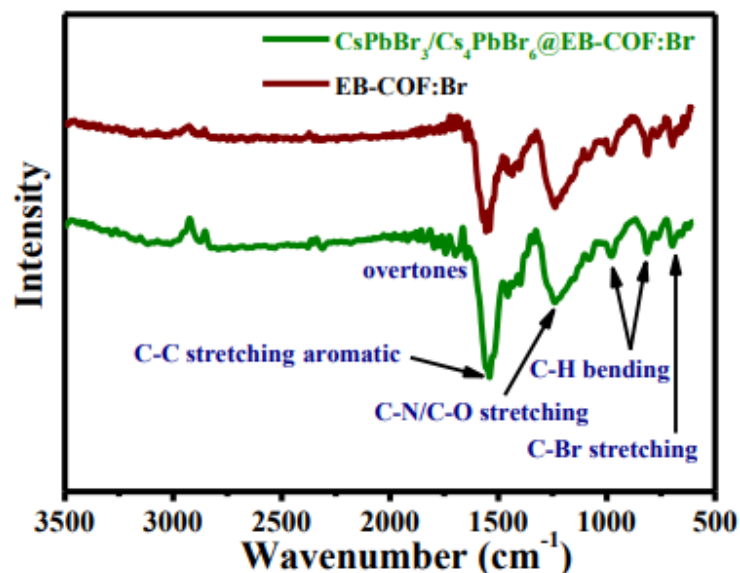


Figure 4.8: FTIR spectra for EB-COF:Br and  $\text{CsPbBr}_3/\text{Cs}_4\text{PbBr}_6@EB\text{-COF:Br}$ .

The IR spectra of EB-COF:Br and CsPbBr<sub>3</sub>/Cs<sub>4</sub>PbBr<sub>6</sub>@EB-COF:Br nanocomposite are shown in Figure 4.8. The disappearance of the N–H stretching bands of EB and the C=O stretching bands of TFP provided direct evidence for EB-COF:Br formation.<sup>49</sup> The dominant peak at 1539 cm<sup>-1</sup> resulting from the C=C stretching and the lack of O–H and C=N stretching demonstrate that EB-COF:Br was existed in the keto form in both the samples.<sup>49</sup>

#### 4.3.4. Brunauer–Emmett–Teller (BET)

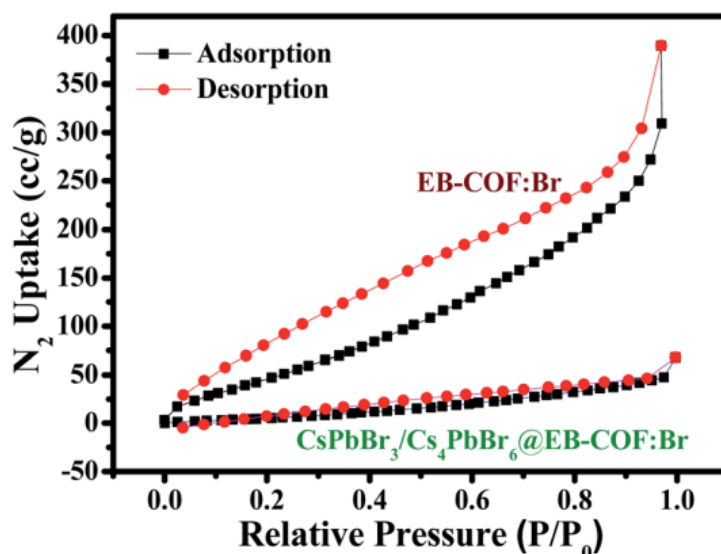


Figure 4.9: N<sub>2</sub> adsorption/desorption isotherm for EB-COF:Br and CsPbBr<sub>3</sub>/Cs<sub>4</sub>PbBr<sub>6</sub>@EB-COF:Br nanocomposite.

The BET surface area result was obtained to be 267.51 m<sup>2</sup> g<sup>-1</sup> for EB-COF:Br from nitrogen adsorption–desorption isotherms as represented in Figure 4.9. EB-COF:Br synthesized herein using a low synthesis temperature and less time resulted in a mesoporous network in the COF. Thus, the mechanochemically synthesized EB-COF:Br showed a type-IV isotherm with a hysteresis loop, whereas EB-COF:Br synthesized by a solvothermal method as reported earlier showed a type-I isotherm indicating a microporous network due to higher reaction temperature and time (120 ° C and 3 days).<sup>49</sup> These phenomena of mesoporous network formation in the COF as well as type-IV isotherm with a hysteresis loop when synthesized by a mechanochemical method are fully consistent with the reported literature.<sup>65–67</sup> The surface area obtained for the CsPbBr<sub>3</sub>/Cs<sub>4</sub>PbBr<sub>6</sub>@EB-COF:Br nanocomposite from the nitrogen adsorption–desorption

isotherm was  $49.83 \text{ m}^2 \text{ g}^{-1}$  [Figure 4.9]. The abrupt decrease of the surface area from the COF to the  $\text{CsPbBr}_3/\text{Cs}_4\text{PbBr}_6@\text{EB-COF:Br}$  nanocomposite confirms the successful encapsulation of  $\text{CsPbBr}_3/\text{Cs}_4\text{PbBr}_6$  NCs into the porous structures of EB-COF:Br.<sup>41,42</sup>

#### 4.3.5. CHN Analysis

Element	C [%]	N [%]	H [%]
Theoretical value of EB-COF:Br <sup>2</sup>	65.06	8.43	4.01
EB-COF:Br	58.82	7.76	4.21
$\text{CsPbBr}_3/\text{Cs}_4\text{PbBr}_6@\text{EB-COF:Br}$	38.69	5.40	2.64

Table 4.2: CHN analysis indicating the % of each element in  $\text{CsPbBr}_3/\text{Cs}_4\text{PbBr}_6@\text{EB-COF:Br}$  sample.

The CHN analysis is shown in Table 4.2 for  $\text{CsPbBr}_3/\text{Cs}_4\text{PbBr}_6@\text{EB-COF:Br}$  sample. The C, H, and N results of the synthesized EB-COF:Br sample show C, N and H content similar to the theoretical value. The calculated C: N: H ratio for synthesized EB-COF:Br was 1: 0.132: 0.072, whereas the ratio from the theoretical value was suggested as 1: 0.139: 0.068. For the sample  $\text{CsPbBr}_3/\text{Cs}_4\text{PbBr}_6$  loaded EB-COF:Br, the C: N: H ratio was calculated as 1: 0.129: 0.062. These CHN experiments suggested that the COF structure was remain intact in  $\text{CsPbBr}_3/\text{Cs}_4\text{PbBr}_6@\text{EB-COF:Br}$  composite. Indeed, the EDS elemental analysis of  $\text{CsPbBr}_3/\text{Cs}_4\text{PbBr}_6@\text{EB-COF:Br}$  composite shows the presence of Pb and Br in excess quantity (Cs: Pb: Br = 1:1.53:5.65), further confirming the existence of  $\text{CsPbBr}_3/\text{Cs}_4\text{PbBr}_6$  NCs inside EB-COF:Br cavities along with the elemental mapping.

#### 4.3.6. Nanoscale Microscopic Imaging

From HRTEM, EDS and CHN analyses, it was clear that  $\text{CsPbBr}_3/\text{Cs}_4\text{PbBr}_6$  NCs were encapsulated by EB-COF:Br and well dispersed inside it [Figure 4.10].

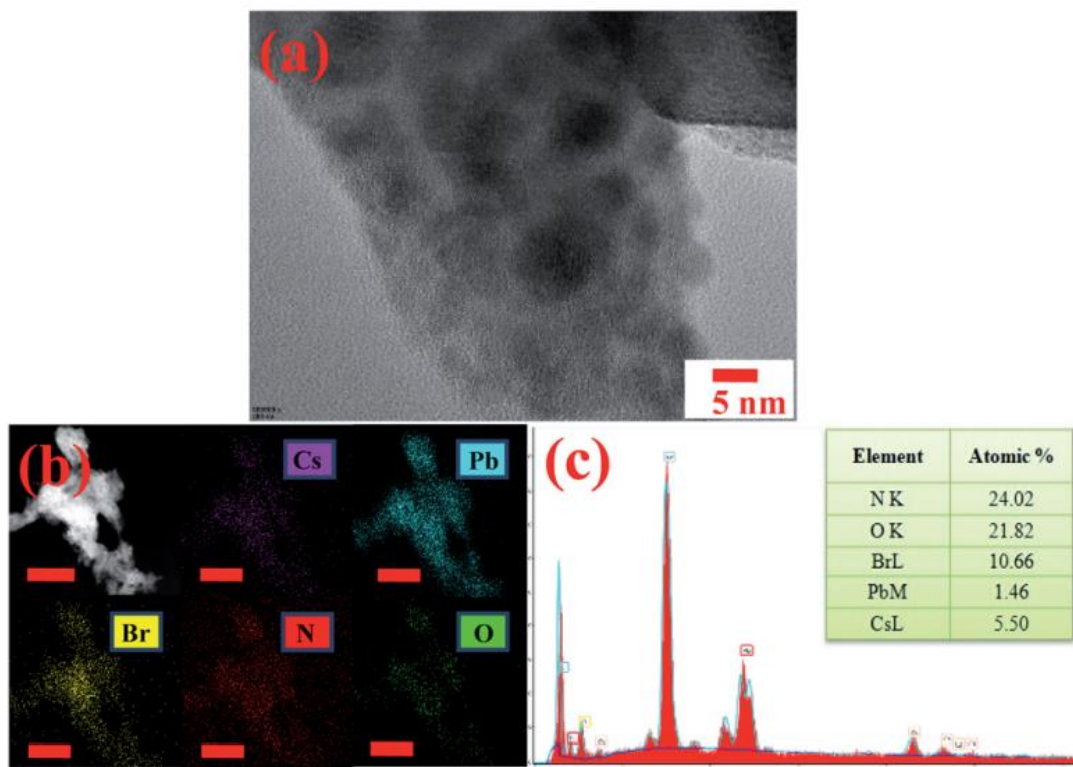


Figure 4.10: (a) HRTEM image, (b) HAADF-STEM image and elemental mapping of Cs, Pb, Br, N, and O (scale bar = 50 nm) and (c) STEM-EDS analysis with the atomic% table of the CsPbBr<sub>3</sub>/Cs<sub>4</sub>PbBr<sub>6</sub>@EB-COF:Br nanocomposite.

A graphene-sheet-like 2D layered structure was observed for EB-COF:Br in the HRTEM images [Figure 4.11], whereas, encapsulated CLBP NCs of size 4–7 nm were clearly observed in the HRTEM image of the CsPbBr<sub>3</sub>/Cs<sub>4</sub>PbBr<sub>6</sub>@EB-COF:Br nanocomposite sample [Figure 4.10(a), 11(b)].

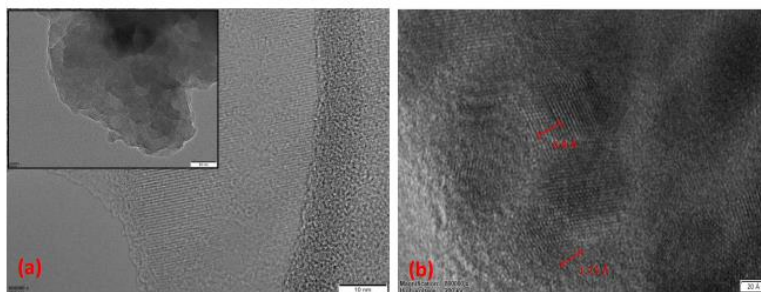


Figure 4.11: HRTEM images of (a) EB-COF:Br, and (b) CsPbBr<sub>3</sub>/Cs<sub>4</sub>PbBr<sub>6</sub>@EB-COF:Br composite showing lattice fringes and the corresponding d-spacing.



The appearance of larger size particles (few  $\sim 7$  nm) in the HRTEM images may be due to overlapping CLBP NCs. The high-angle annular electron microscopy (HAADF-STEM) images and elemental mappings of the nanocomposite revealed the presence of Cs, Pb, Br, N, and O [Figure 4.10(b)], supporting the encapsulation and uniform distribution of CsPbBr<sub>3</sub>/Cs<sub>4</sub>PbBr<sub>6</sub> NCs inside EB-COF:Br.

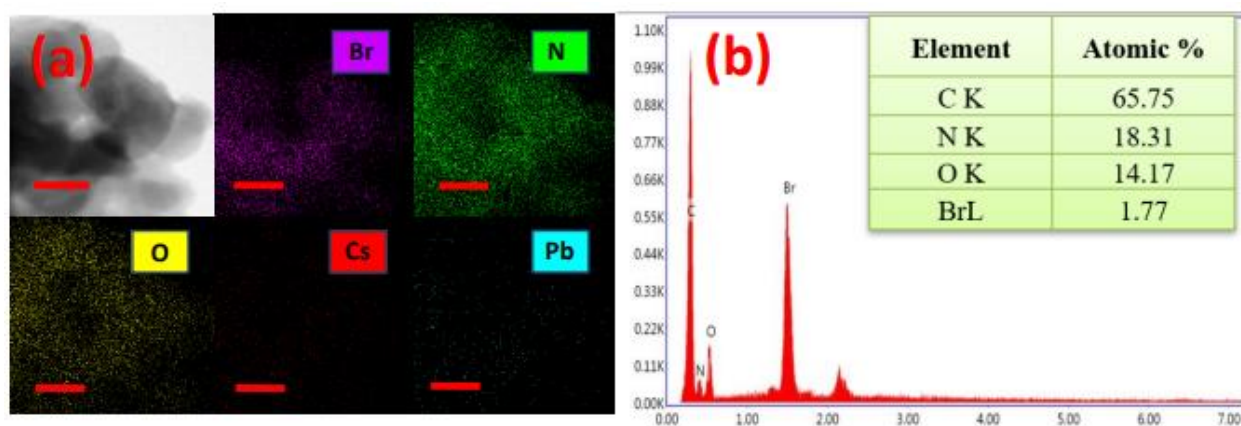


Figure 4.12: (a) STEM-HAADF mapping for EB-COF:Br (Scale bar = 100 nm) and (b) corresponding EDAX elemental analysis.

The EDS elemental analysis and C, H, and N analysis of the CsPbBr<sub>3</sub>/Cs<sub>4</sub>PbBr<sub>6</sub>@EB-COF:Br nanocomposite further confirmed the encapsulation of CLBP NCs inside the COF (Figure 4.10(c) and inset table). The excess of Cs concerning the Pb atomic% in the composite material (as Cs : Pb : Br ratio  $\frac{1}{4}$  3.76 : 1 : 7.30) from EDS analysis further suggests the formation of mixed-phase CLBP NCs. Further proof for successful encapsulation of nanocrystals was shown by the presence of two typical lattice structures found in the HRTEM fringes [Figure 4.11]. The interplanar distances of 2.9 Å and 1.75 Å could be attributed to the (200) and (315) planes of cubic CsPbBr<sub>3</sub> and the rhombohedral phase of Cs<sub>4</sub>PbBr<sub>6</sub>, respectively.<sup>64</sup>

In comparison, the elemental mappings and EDS analysis of the EB-COF:Br sample confirmed the presence of only C, N, O, and Br [Figure 4.12].

#### 4.3.7. XPS

The surface properties of EB-COF:Br and CsPbBr<sub>3</sub>/Cs<sub>4</sub>PbBr<sub>6</sub>@EB-COF:Br nanocomposite were investigated through X-ray photoelectron spectroscopy (XPS) analysis. All the spectra were

calibrated using the C 1s peak at 284.60 eV. The XPS survey spectrum for the CsPbBr<sub>3</sub>/Cs<sub>4</sub>PbBr<sub>6</sub>@EB-COF:Br nanocomposite confirmed the presence of Cs, Pb, Br, N, and O as the main components [Figure 4.13(a)].

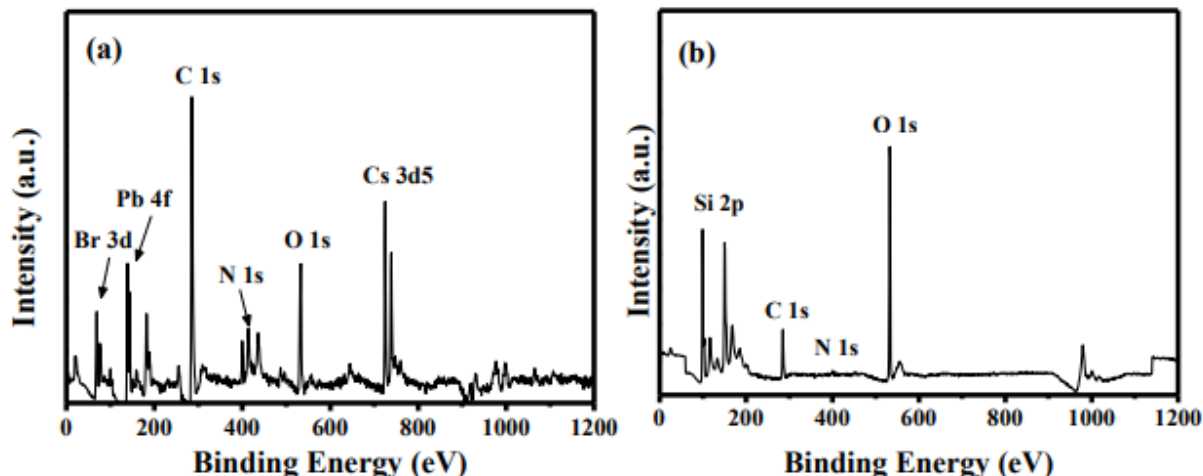
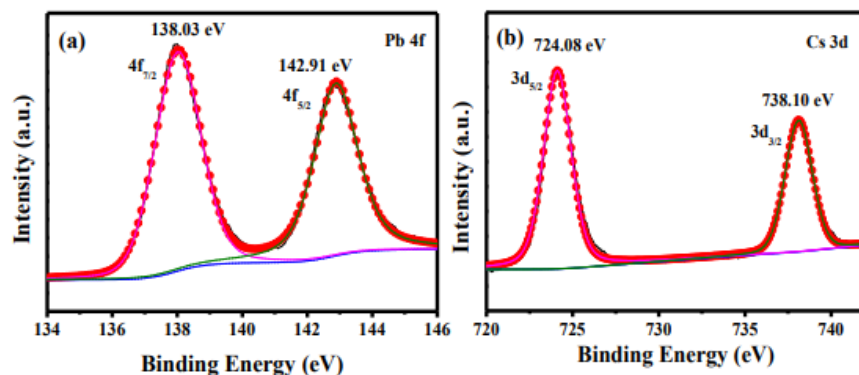


Figure 4.13: XPS survey scan (a) CsPbBr<sub>3</sub>/Cs<sub>4</sub>PbBr<sub>6</sub>@EB-COF:Br and (b) EB-COF:Br.

For the nanocomposite, two intense Pb 4f peaks without any shoulder at 138.03 and 142.91 eV corresponding to Pb 4f<sub>7/2</sub> and Pb 4f<sub>5/2</sub> [Figure 4.14 (a)] and Cs 3d peaks at 724.08 eV and 738.10 eV corresponding to Cs 3d<sub>5/2</sub> and Cs 3d<sub>3/2</sub> [Figure 4.14(b)] strongly support the formation of CLBP NCs in the COF matrix.<sup>31,41</sup>

Quantitative XPS analysis indicates that Cs : Pb : Br is 1.45 : 1 : 4.14 for the CsPbBr<sub>3</sub>/Cs<sub>4</sub>PbBr<sub>6</sub>@EB-COF:Br nanocomposite, which indicates excess Cs in the composition. Notably, the Br 3d peak of the CLBP@COF nanocomposite can be fitted into two peaks with binding energies of 67.80 eV and 68.90 eV, which were assigned to Br<sup>-</sup> ions from EB-COF:Br and CLBP [Figure 4.14(c)].<sup>14</sup>



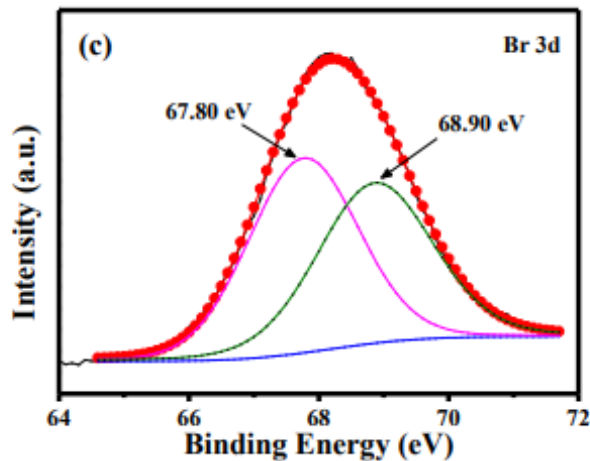


Figure 4.14: XPS spectrum of (a) Pb 4f, (b) Cs 3d and (c) Br 3d for CsPbBr<sub>3</sub>/Cs<sub>4</sub>PbBr<sub>6</sub>@EB-COF:Br.

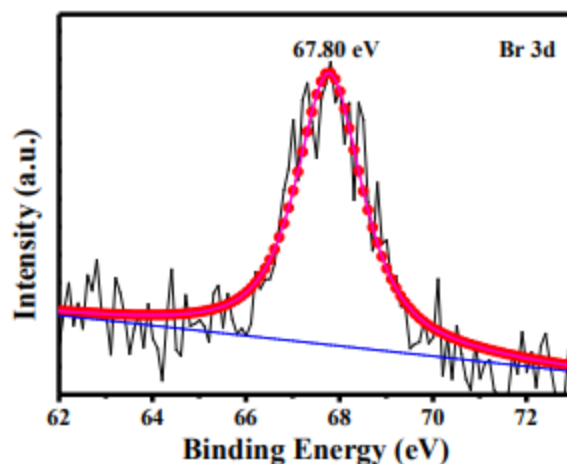


Figure 4.15: XPS spectrum of Br 3d for EB-COF:Br

On the other hand, the XPS survey spectrum of the EB-COF:Br sample confirmed the presence of N, O, and Br as the main components [Figure 4.13(b)] and the Br 3d peak can be fitted into one peak with a binding energy of 67.80 eV, which were assigned to Br<sup>-</sup> ions from the COF itself [Figure 4.15].

#### 4.3.8. TGA

The TGA shows that the decomposition of EB-COF:Br and CsPbBr<sub>3</sub>/Cs<sub>4</sub>PbBr<sub>6</sub>@EB-COF:Br nanocomposite started at ~400 °C (in Ar), as reported earlier [Figure 4.16].<sup>49</sup> A 15–25% weight loss for EB-COF:Br in TGA was observed in the low-temperature range (below ~200 °C). This could be ascribed to the removal of the trapped solvents in the EB-COF:Br nanocomposite.

Therefore, the TGA experiments indicated that the synthesized  $\text{CsPbBr}_3/\text{Cs}_4\text{PbBr}_6@\text{EB-COF:Br}$  nanocomposite possessed excellent thermal stability.

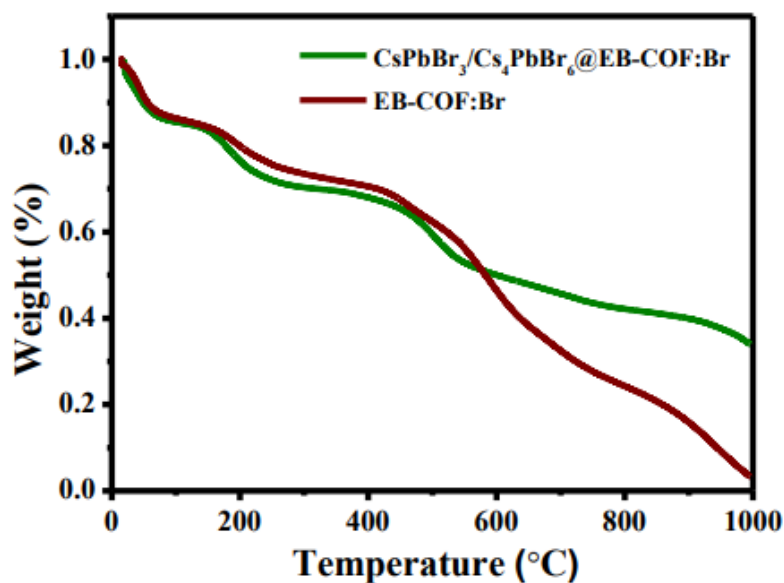


Figure 4.16: Comparative TGA for EB-COF:Br and  $\text{CsPbBr}_3/\text{Cs}_4\text{PbBr}_6@\text{EB-COF:Br}$  nanocomposite.

#### 4.4. Heterogeneous Photocatalytic Performance

These EB-COF:Br and  $\text{CsPbBr}_3/\text{Cs}_4\text{PbBr}_6@\text{EB-COF:Br}$  nanocomposites had excellent visible light absorption characteristics [Figure 4.7] and good water stability [Figure 4.5]. Therefore, the photocatalytic activities of the as-synthesized COF and  $\text{CsPbBr}_3/\text{Cs}_4\text{PbBr}_6@\text{COF}$  nanocomposite were examined by the degradation of MO in an aqueous solution (100 ppm), in the presence of visible light (xenon lamp, 300 W,  $\lambda = 100\text{--}1800$  nm, for photocatalytic measurements).

The photodegradation rates of the EB-COF:Br and  $\text{CsPbBr}_3/\text{Cs}_4\text{PbBr}_6@\text{EB-COF:Br}$  nanocomposite could not be compared with that of  $\text{CsPbBr}_3@\text{EB-COF:Br}$  or bulk  $\text{CsPbBr}_3/\text{Cs}_4\text{PbBr}_6$ , since both the samples were not stable in water [Figure 4.5 and Figure 4.6]. The factual photodegradation rates of the EB-COF:Br and  $\text{CsPbBr}_3/\text{Cs}_4\text{PbBr}_6@\text{EB-COF:Br}$  nanocomposite were compared under visible light irradiation.

A blank photolysis experiment without the photocatalyst does not show any noticeable decrease in the MO concentration with a similar time interval [Figure 4.17 (a)], demonstrating that the photocatalysts were the cause of MO's decomposition. Interestingly, it was found that both the EB-COF:Br and  $\text{CsPbBr}_3/\text{Cs}_4\text{PbBr}_6@\text{EB-COF:Br}$  nanocomposite show some MO adsorption in the

dark and after a particular time the absorbance intensity remained the same. EB-COF:Br shows a slightly better adsorption behavior of 32.5% than the CsPbBr<sub>3</sub>/Cs<sub>4</sub>PbBr<sub>6</sub>@EB-COF:Br nanocomposite with 29.5% (in the dark) [Figure 4.17 (b) and Figure 4.17 (c)], because of apparent COF pore site availability, as observed from the BET surface area measurement.

The degradation curves of MO over EB-COF:Br and CsPbBr<sub>3</sub>/Cs<sub>4</sub>PbBr<sub>6</sub>@EB-COF:Br photocatalysts as a function of visible light irradiation time are plotted in Figure 4.17 (d) and Figure 4.17 (e) respectively, at a specific time interval.

The CsPbBr<sub>3</sub>/Cs<sub>4</sub>PbBr<sub>6</sub>@EB-COF:Br nanocomposite exhibits superior photocatalytic activity to EB-COF:Br with a photodegradation efficiency of 100% and 77.5% in 25 min under visible light irradiation, respectively [Figure 4.17 (f)]. Practically the CsPbBr<sub>3</sub>/Cs<sub>4</sub>PbBr<sub>6</sub>@EB-COF:Br nanocomposite completely degraded 100 ppm MO solution within 25 min of visible light irradiation.

Assuming that the degradation process follows first-order kinetics,

$$C = C_0 e^{-\kappa t}, \text{ (}\kappa \text{ is the photodegradation rate constant) for MO degradation,}$$

the plots of  $-\ln(C/C_0)$  as a function of the visible light irradiation time  $t$  are shown in Figure 4.17 (g).<sup>41,68</sup>

The photodegradation rate constant of the EB-COF:Br and CsPbBr<sub>3</sub>/Cs<sub>4</sub>PbBr<sub>6</sub>@EB-COF:Br nanocomposite was about 0.057 min<sup>-1</sup> and 0.245 min<sup>-1</sup> respectively [Table 4.3], which were found to be considerably higher than the previously reported values for dye photodegradation with halide perovskites [Table 4.4].<sup>41,50-62</sup>

Table 4.3: Table for calculated photodegradation rate constant, using formula  $C=C_0e^{-\kappa t}$  (first order kinetics).

MO photodegradation condition	Rate constant (min <sup>-1</sup> )
No photocatalyst (in light)	5.995E-4
EB-COF:Br (in dark)	0.018
EB-COF:Br (in light)	0.057
CsPbBr <sub>3</sub> /Cs <sub>4</sub> PbBr <sub>6</sub> @EB-COF:Br (in dark)	0.014
CsPbBr <sub>3</sub> /Cs <sub>4</sub> PbBr <sub>6</sub> @EB-COF:Br (in light)	0.245

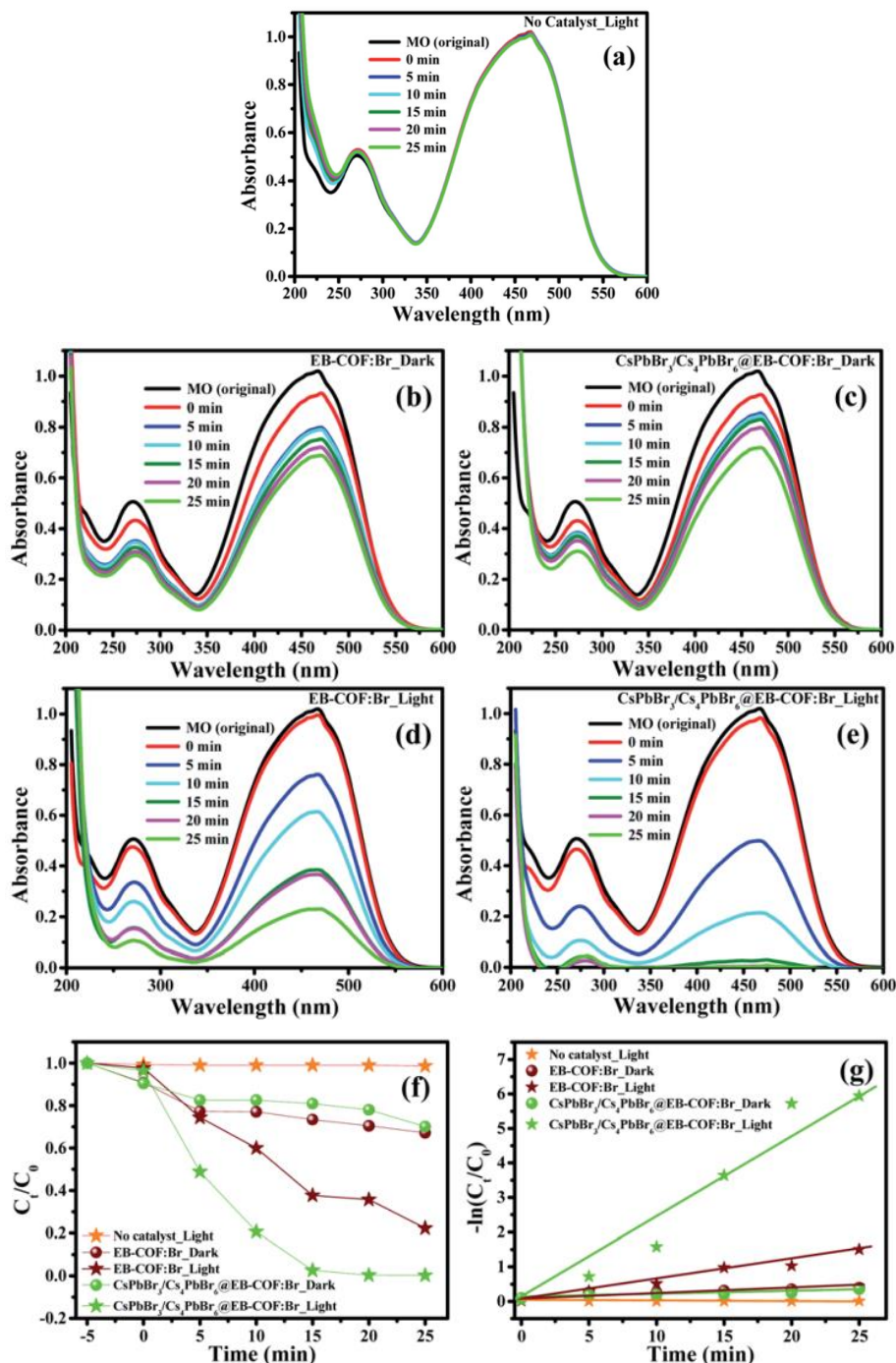


Figure 4.17: Photocatalytic performance of the as-synthesized EB-COF:Br and CsPbBr<sub>3</sub>/Cs<sub>4</sub>PbBr<sub>6</sub>@EB-COF:Br nanocomposite samples for 100 ppm MO aqueous solution; typical UV-Vis spectral change of MO solution as a function of time; (a) blank photolysis without photocatalysts: in the presence of (b) EB-COF:Br and (c) CsPbBr<sub>3</sub>/Cs<sub>4</sub>PbBr<sub>6</sub>@EB-COF:Br nanocomposites in the dark; in the presence of photocatalysts under visible light irradiation (d) EB-COF:Br and (e) CsPbBr<sub>3</sub>/Cs<sub>4</sub>PbBr<sub>6</sub>@EB-COF:Br

nanocomposite; (f) the plot of MO remaining in the solution ( $C/C_0$  measured from the absorbance at 467 nm); (g) the plots of  $-\ln(C/C_0)$  as a function of photo-irradiation time (min) in the presence of catalyst EB-COF:Br and CsPbBr<sub>3</sub>/Cs<sub>4</sub>PbBr<sub>6</sub>@EB-COF:Br nanocomposite, for the blank (without photocatalysts) and in the dark (without light irradiation).

Table 4.4: Comparative literature survey on degradation rates of organic pollutants under the action of different halide perovskite nanocatalysts to show the excellence of the CsPbBr<sub>3</sub>/Cs<sub>4</sub>PbBr<sub>6</sub>@EB-COF:Br nanocomposite photocatalyst reported.

Sr. No.	Photocatalyst	Light Source	Concentration and Volume of Dye Solution	Dye used	Degradation Time (minutes)	Efficiency / Rate constant	Reference
1.	CsPbBr <sub>3</sub> /Cs <sub>4</sub> PbBr <sub>6</sub> @EB-COF:Br (10 mg)	300W Xenon lamp	100 ppm (10 ml)	MO	25	0.245 min <sup>-1</sup> , 100%	This Work
2.	CH <sub>2</sub> NH <sub>3</sub> SnI <sub>3</sub> (80 mg)	300W Xenon lamp	10 ppm (80 ml)	Rhodamine B (RhB)	50	0.0066 min <sup>-1</sup> , 40%	50
3.	CsPbBr <sub>3</sub> NCs (1 mg)	500W Xenon lamp	10 ppm (3 ml)	MO	100	89%	51
	CsPbCl <sub>3</sub> NCs (2 mg)					90%	
4.	CsSnBr <sub>3</sub> (120 mg)	1 Sun Simulator (1kW/m <sup>2</sup> )	2 ppm (100 ml)	Crystal Violet Blue	120	73.1%	52
5.	CH <sub>2</sub> NH <sub>3</sub> PbBr <sub>3</sub> @MOF (2 mg)	LED	~ 18-30 ppm	MO	100	0.027 min <sup>-1</sup>	41
				Methyl Red (MR)		0.0145 min <sup>-1</sup>	
		Sunlight		Nitrofurazone		0.0071 min <sup>-1</sup>	
		MO		0.032 min <sup>-1</sup>			
6.	CH <sub>2</sub> NH <sub>3</sub> PbI <sub>3</sub> (0.5 mg)	150W Halogen lamp	20 ppm (50 ml)	RhB	180	65%	53
7.	Cs <sub>3</sub> Bi <sub>2</sub> Br <sub>9</sub> -OA NCs (7 mg)	Visible light	70 ppm	Methylene Blue (MB)	60	0.69 x 10 <sup>-2</sup> min <sup>-1</sup> , 26.6%	54
	Cs <sub>3</sub> Bi <sub>2</sub> I <sub>9</sub> -OA NCs (7 mg)					1.8 x 10 <sup>-2</sup> min <sup>-1</sup> , 62.1%	
8.	Cs <sub>2</sub> AgBiBr <sub>6</sub> (20 mg)	100 mW cm <sup>-2</sup> Xenon lamp	100 ppm (10 ml, ethanol)	RhB	120	~ 98%	55
				Rh110		~ 30% - 35%	
				MR			
				MO			
9.	CsPbI <sub>3</sub> NCs (0.07 g)	150 W Visible Light	5 ppm (100 ml)	Methyl Violet	120	81.7%	56
				RhB		61.5%	
				Malachite green		42.3%	

				Acid Black 1		33.0%	
				MO		50.8%	
10.	CsPbBrCl <sub>2</sub> (20 mg)	500 W Xenon Lamp	~ 3.2 ppm – 5.80 ppm (40 ml)	Eosin B	180	Negligible activity	57
				RhB			
				MO			
				MB			
11.	TiCdI <sub>3</sub> (0.005 mg)	125 W mercury lamp	~ 32 - 32.7 ppm	MO	120	27%	58
				MB		100%	
12.	CsPbBr <sub>3</sub> NCs (100 mg)	300 W Xenon Lamp	10 ppm (100 ml)	Tetracycline Hydrochloride	30	18%	59
13.	OHNH <sub>3</sub> PbCl <sub>3</sub> , Hydroxyl Ammonium Lead Chloride (20 mg)	Sunlight	5 ppm (40 ml)	Direct Yellow 27	5	82.19	60
	OHNH <sub>3</sub> PbI <sub>2</sub> Cl (20 mg)				20	93.98	
14	CsPbI <sub>3</sub> (20 mg)	500 W Xenon Lamp	5.80 ppm (40 ml)	Eosin B	210	73%	61
	CsPbBr <sub>3</sub> (20 mg)					82%	
	CsPbCl <sub>3</sub> (20 mg)				140	90%	

The actual photographs of visible light-driven photocatalytic degradation of MO with the CsPbBr<sub>3</sub>/Cs<sub>4</sub>PbBr<sub>6</sub>@EB-COF:Br nanocomposite photocatalyst are presented in Figure 4.18.

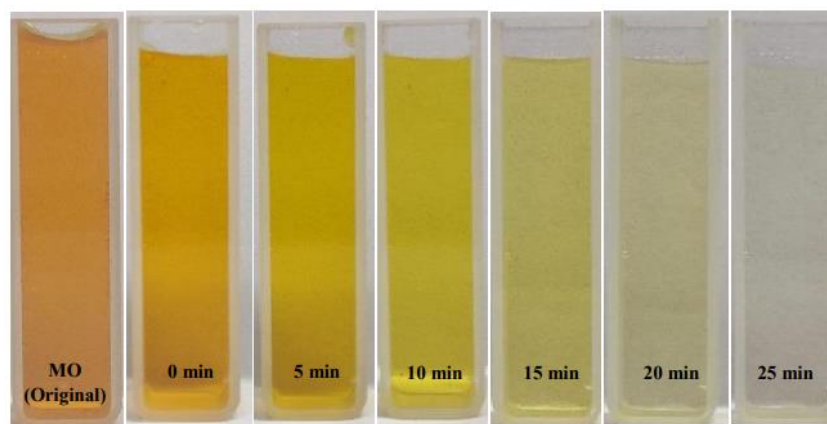


Figure 4.18: Photographs of 100 ppm MO solutions after photocatalytic degradation as a function of time in presence of CsPbBr<sub>3</sub>/Cs<sub>4</sub>PbBr<sub>6</sub>@EB-COF:Br nanocomposite photocatalyst.

The results, therefore, confirmed that the CsPbBr<sub>3</sub>/Cs<sub>4</sub>PbBr<sub>6</sub>@EB-COF:Br nanocomposite had a higher impact on the enhancement of photocatalytic activity even under room temperature conditions (24–26 °C). This is probably because the COF we have used herein to encapsulate the



CLBPs was also photoactive and the inherent porous structure of the EB-COF:Br, more coordination sites of  $\text{CsPbBr}_3/\text{Cs}_4\text{PbBr}_6$  were exposed to the solution, and therefore, reactant molecules could effectively access the active sites of the photocatalyst.

#### 4.4.1. Photocatalyst Recyclability

The recyclability of the  $\text{CsPbBr}_3/\text{Cs}_4\text{PbBr}_6@EB\text{-COF:Br}$  nanocomposite photocatalyst was examined with various concentrations of MO aqueous solution (20, 50 and 100 ppm) and the nanocomposite was collected after its first cycle usage to carry out the subsequent degradation.

It was found that for the photocatalysis of 20 ppm MO, the photocatalyst can be recycled up to six cycles, whereas for 50 and 100 ppm of MO, the photocatalyst can be recycled up to three cycles. The degradation efficiency for the sixth cycle of 20 ppm was 93.85%, and the third cycle of 50 ppm was 94.19%, whereas, for 100 ppm, the degradation efficiency for the third cycle was comparatively low 46.8% as presented in Figure 4.19.

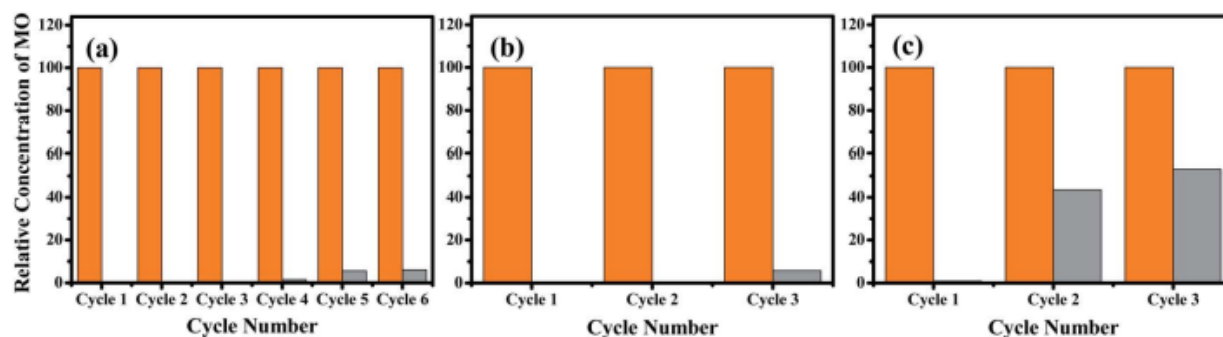


Figure 4.19: Recycling tests for the photocatalytic degradation of MO: (a) 20 ppm, (b) 50 ppm and (c) 100 ppm in the presence of the  $\text{CsPbBr}_3/\text{Cs}_4\text{PbBr}_6@EB\text{-COF:Br}$  nanocomposite photocatalyst under similar photoirradiation conditions

The recyclability test's actual photographs for 20–100 ppm MO using the  $\text{CsPbBr}_3/\text{Cs}_4\text{PbBr}_6@EB\text{-COF:Br}$  nanocomposite photocatalyst are presented in Figure 4.20-4.22. Herein, we have observed a concentration-dependent change in photocatalytic efficiency and change in the number of reusability cycles for the  $\text{CsPbBr}_3/\text{Cs}_4\text{PbBr}_6@EB\text{-COF:Br}$  nanocomposite photocatalyst. This phenomenon is quite common, as several parameters affect the efficiency of the photocatalyst.<sup>69</sup>

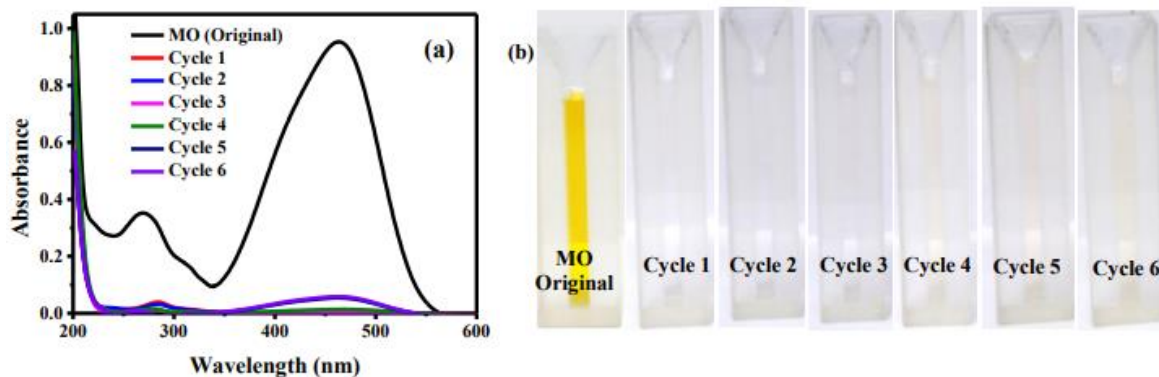


Figure 4.20: (a) UV-Vis spectra of recycling tests for the photocatalytic degradation for 20 ppm of MO in the presence of  $\text{CsPbBr}_3/\text{Cs}_4\text{PbBr}_6@\text{EB-COF}:\text{Br}$  nanocomposite, and (b) photographs of MO solutions after each recycling tests.

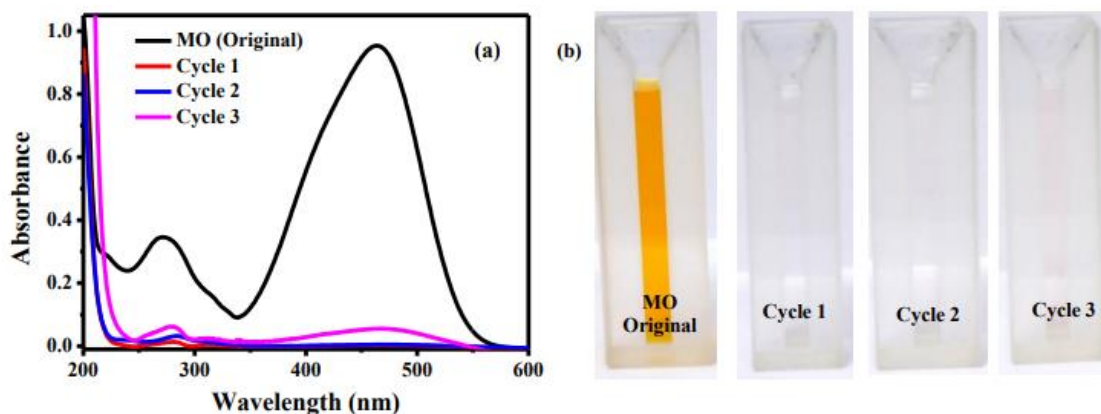


Figure 4.21: (a) UV-Vis spectra of recycling tests for the photocatalytic degradation for 50 ppm of MO in the presence of  $\text{CsPbBr}_3/\text{Cs}_4\text{PbBr}_6@\text{EB-COF}:\text{Br}$  nanocomposite, and (b) photographs of MO solutions after each recycling tests.

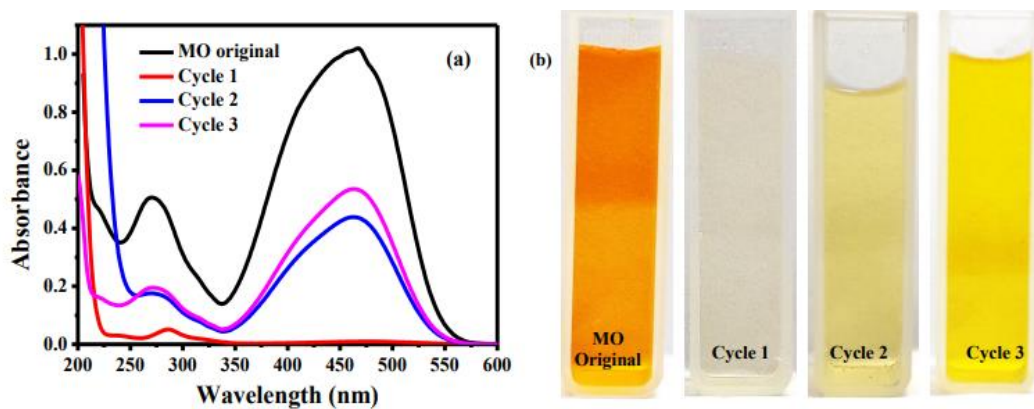


Figure 4.22: (a) UV-Vis spectra of recycling tests for the photocatalytic degradation for 100 ppm of MO in the presence of CsPbBr<sub>3</sub>/Cs<sub>4</sub>PbBr<sub>6</sub>@EB-COF:Br nanocomposite, and (b) photographs of MO solutions after each recycling tests.

#### 4.4.2. Post-catalysis Characterizations

We have carried out XRD analysis of the recycled photocatalyst samples to confirm the change in the nanocomposite's crystal structures [Figure 4.23 (a)]. There was no change in the  $2\theta$  peak value for 20 ppm and 50 ppm sixth and third time recycled photocatalysts, respectively. In contrast, a slight change was observed for the 100 ppm third time recycled photocatalyst, which is in line with the experimental observations (Figure 4.19). As shown in Figure 4.23 (b), changes in the CsPbBr<sub>3</sub>/Cs<sub>4</sub>PbBr<sub>6</sub> NCs' morphology, NC aggregation, were observed after the repeated photodegradation reactions. These results demonstrated that the synthesized CsPbBr<sub>3</sub>/Cs<sub>4</sub>PbBr<sub>6</sub>@EB-COF:Br nanocomposite remained stable, maintaining its framework integrity up to a particular time and acting as a photocatalyst for repeated usage under visible light irradiation.

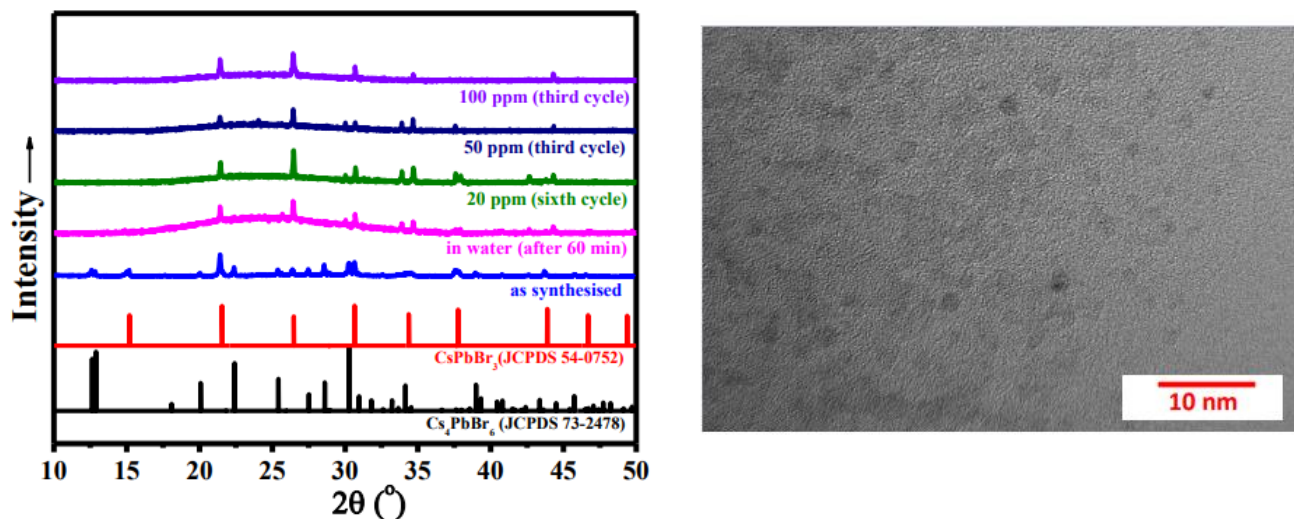


Figure 4.23: XRD analysis of the photocatalysts (CsPbBr<sub>3</sub>/Cs<sub>4</sub>PbBr<sub>6</sub>@EB-COF:Br) after completion of the recycling experiments for 20-100 ppm of MO solution; (b) HRTEM image for CsPbBr<sub>3</sub>/Cs<sub>4</sub>PbBr<sub>6</sub>@EB-COF:Br nanocomposite after MO recycling experiments of photocatalytic degradation for 100 ppm MO solution.

#### 4.4.3. Total Organic Carbon (TOC) Analysis and Measurement

The analytical measure known as total organic carbon (TOC) indicates how much organic carbon is contained in a sample<sup>70</sup>. Total inorganic carbon (IC), which represents the amount of non-organic carbon, such as carbon in carbonate minerals, is measured in addition to TOC in a typical examination of total carbon (TC). TOC is obtained by deducting IC from TC. Another typical approach to TOC analysis entails first eliminating the TIC component before measuring the residual carbon. Non-purgeable organic carbon (NPOC) is a more realistic name for this technique because it involves purging an acidified sample with carbon-free air or nitrogen prior to analysis<sup>70</sup>.

Herein, TOC analysis was carried out to check the organic content in the reaction after the photocatalytic degradation for 5 minutes and 25 minutes respectively, using EB-COF:Br and CsPbBr<sub>3</sub>/Cs<sub>4</sub>PbBr<sub>6</sub>@EB-COF:Br nanocomposite photocatalysts. Table 4.5 shows the values for the TOC analysis.

Table 4.5: TOC analysis for MO solutions at different time intervals during photocatalytic degradation reaction as a function of time in absence/presence of photocatalysts.

Sample		TOC (mg/L)	TC (mg/L)	IC (mg/L)
MO	After PC	23.67	23.67	0.00
EB-COF:Br	5 minutes	7.775	7.820	0.044
	25 minutes	5.758	5.767	0.0087
CsPbBr <sub>3</sub> /Cs <sub>4</sub> PbBr <sub>6</sub> @EB-COF:Br	5 minutes	7.119	7.172	0.0523
	25 minutes	0.814	0.814	0.000

The fundamental disadvantage of employing organic dye decolorization as a probe system to test photocatalysts, however, is that it has a propensity to undergo redox reactions with a progressive degradation of the organic molecule. To assess the overall degradation of the byproducts, a total organic carbon (TOC) examination of the mineralization must be carried out<sup>71</sup>. The TOC determined from 20 ppm MO solution amounts to 23.67 ppm and the TOC observed after the degradation using CsPbBr<sub>3</sub>/Cs<sub>4</sub>PbBr<sub>6</sub>@EB-COF:Br nanocomposite under Xe lamp for 25 min amounts to 0.814 ppm which has reduced from 7.119 ppm after 5 min photoreaction. This value is close to the total conversion of the organic matter, which demonstrates the true photocatalytic disappearance of MO<sup>71</sup>.

The results indicated that the maximum TOC removal rate was approximately 3.44% and 24.33% respectively by, CsPbBr<sub>3</sub>/Cs<sub>4</sub>PbBr<sub>6</sub>@EB-COF:Br nanocomposite and EB-COF:Br after 25 minutes. It was observed that for the CsPbBr<sub>3</sub>/Cs<sub>4</sub>PbBr<sub>6</sub>@EB-COF:Br nanocomposite sample as the irradiation time increases, TOC value decreases continuously, and after 25 min of irradiation, 3.44% of TOC removal, which suggests that the synthesized material is a very effective catalyst to treat MO-contaminated water under visible light source<sup>72</sup>. Hence we can say that the photocatalytic degradation was complete using CsPbBr<sub>3</sub>/Cs<sub>4</sub>PbBr<sub>6</sub>@EB-COF:Br nanocomposite photocatalyst for 20 PPM MO.

#### 4.5. Conclusions

In summary, this article reported a facile controlled synthesis of a CsPbBr<sub>3</sub>/Cs<sub>4</sub>PbBr<sub>6</sub>@EB-COF:Br nanocomposite, where perovskite NCs were well dispersed in the COF cavity.

Herein, we have also demonstrated a simple mechanochemical synthetic route to synthesize a cationic covalent organic framework EB-COF:Br with Br<sup>-</sup> as the counter ion, avoiding the necessity of using typical inert atmosphere conditions in a Pyrex tube. The Br<sup>-</sup> functionalized COF was selected because of its chemical affinity and non-interference with the photoluminescence properties of the bromide containing perovskite.

The synthesized products were characterized by XRD, UV-Vis, IR, CHN, BET, TGA, XPS, HRTEM, HAADF, and EDS analyses. It was shown that the concentration of Cs:Pb:COF played a significant role in controlling the crystal structure of the perovskite NCs. Therefore, both single-phase CsPbBr<sub>3</sub>@EB-COF:Br and mixed-phase CsPbBr<sub>3</sub>/Cs<sub>4</sub>PbBr<sub>6</sub>@EB-COF:Br nanocomposites were obtained by slightly tuning the synthesis protocol. The samples' water stability, e.g., CsPbBr<sub>3</sub>@EB-COF:Br, CsPbBr<sub>3</sub>/Cs<sub>4</sub>PbBr<sub>6</sub>@EB-COF:Br, CsPbBr<sub>3</sub>/Cs<sub>4</sub>PbBr<sub>6</sub> without COF encapsulation, was compared, and it was found that the CsPbBr<sub>3</sub>/Cs<sub>4</sub>PbBr<sub>6</sub>@EB-COF:Br nanocomposite has remained reasonably stable in water for 60 minutes.

Furthermore, the CsPbBr<sub>3</sub>/Cs<sub>4</sub>PbBr<sub>6</sub>@EB-COF:Br nanocomposite showed efficient visible-light-driven photocatalytic activity to degrade Methyl orange (MO) (10 mL; 100 ppm) in aqueous media with a photodegradation rate of about 0.245 min<sup>-1</sup>. The CsPbBr<sub>3</sub>/Cs<sub>4</sub>PbBr<sub>6</sub>@EB-COF:Br photocatalyst also exhibited water and photo-stability up to three to six cycles for 20–100 ppm of MO solution, while showing some aggregation of NCs during the recycling experiments.

Although Pb's toxic nature is of great concern, to be used as a photocatalyst, the encapsulation method provided by us will offer an opportunity to consider COFs as encapsulating materials to improve the stability of unstable nanomaterials via nanocomposite fabrication. This study should also lead to various opportunities to design and synthesize proficient nanocomposite based photocatalysts with other nontoxic alternative perovskites as promising materials for applications in the photodegradation of organic contaminants and wastewater treatment under visible light, a topic of vital significance as well as universal apprehension.

#### 4.6. References

1. Q. Zhang and Y. Yin, *ACS Cent. Sci.*, 2018, 4, 668–679.
2. U. Thumu, M. Piotrowski, B. Owens-Baird and Y. V. Kolen'ko, *J. Solid State Chem.*, 2019, 271, 361–377.
3. T. Yang, F. Li and R. Zheng, *ACS Appl. Electron. Mater.*, 2019, 1, 1348–1366.
4. Y. Jiang, B. Li, T. Zhang, Y. Shi and Q.-H. Xu, *ChemNanoMat.*, 2020, 6, 327–335.
5. M. De Bastiani, I. Dursun, Y. Zhang, B. A. Alshankiti, X. H. Miao, J. Yin, E. Yengel, E. Alarousu, B. Turedi, J. M. Almutlaq, M. I. Saidaminov, S. Mitra, I. Gereige, A. Alsaggaf, Y. Zhu, Y. Han, I. S. Roqan, J. L. Bredas, O. F. Mohammed and O. M. Bakr, *Chem. Mater.*, 2017, 29, 7108–7113.
6. A. Ray, D. Maggioni, D. Baranov, Z. Dang, M. Prato, Q. A. Akkerman, L. Goldoni, E. Caneva, L. Manna and A. L. Abdelhady, *Chem. Mater.*, 2019, 31, 7761–7769.
7. L. A. T. Nguyen, D. N. Minh, D. Zhang, L. Wang, J. Kim and Y. Kang, *J. Phys. Chem. C*, 2020, 124, 22291–22297.
8. R. Wang, Z. Li, S. Li, P. Wang, J. Xiu, G. Wei, H. Liu, N. Jiang, Y. Liu and M. Zhong, *ACS Appl. Mater. Interfaces*, 2020, 12, 41919–41931.
9. Z. Bao, Y. J. Tseng, W. You, W. Zheng, X. Chen, S. Mahlik, A. Lazarowska, T. Lesniewski, M. Grinberg, C. Ma, W. Sun, W. Zhou, R. S. Liu and J. P. Attfield, *J. Phys. Chem. Lett.*, 2020, 11, 7637–7642.
10. M. Li, X. Zhang, T. Dong, P. Wang, K. Matras-Postolek and P. Yang, *J. Phys. Chem. C*, 2018, 122, 28968–28976.
11. J. Almutlaq, J. Yin, O. F. Mohammed and O. M. Bakr, *J. Phys. Chem. Lett.*, 2018, 9, 4131–4138.
12. M. I. Saidaminov, J. Almutlaq, S. Sarmah, I. Dursun, A. A. Zhumekenov, R. Begum, J. Pan, N. Cho, O. F. Mohammed and O. M. Bakr, *ACS Energy Lett.*, 2016, 1, 840–845.
13. Y. Zhang, M. I. Saidaminov, I. Dursun, H. Yang, B. Murali, E. Alarousu, E. Yengel, B. A. Alshankiti, O. M. Bakr and O. F. Mohammed, *J. Phys. Chem. Lett.*, 2017, 8, 961–965.
14. X. Chen, F. Zhang, Y. Ge, L. Shi, S. Huang, J. Tang, Z. Lv, L. Zhang, B. Zou and H. Zhong, *Adv. Funct. Mater.*, 2018, 28, 1706567.
15. G. K. Grandhi, N. S. M. Viswanath, H. B. Cho, S. M. Kim and W. Bin Im, *Nanoscale*, 2019, 11, 21137–21146.
16. D. Chen, Z. Wan, X. Chen, Y. Yuan and J. Zhong, *J. Mater. Chem. C*, 2016, 4, 10646–10653.
17. J. H. Cha, J. H. Han, W. Yin, C. Park, Y. Park, T. K. Ahn, J. H. Cho and D. Y. Jung, *J. Phys. Chem. Lett.*, 2017, 8, 565–570.
18. J. Yin, Y. Zhang, A. Bruno, C. Soci, O. M. Bakr, J. L. Brédas and O. F. Mohammed, *ACS Energy Lett.*, 2017, 2, 2805–2811.

19. Z.Zhang, Y.Zhu, W.Wang, W.Zheng, R.Lin, X.Li, H.Zhang, D.Zhong and F.Huang, *Cryst. Growth Des.*, 2018, 18, 6393–6398.
20. H. Zhang, Q. Liao, Y. Wu, J. Chen, Q. Gao and H. Fu, *Phys. Chem. Chem. Phys.*, 2017, 19, 29092–29098.
21. C. De Weerd, J. Lin, L. Gomez, Y. Fujiwara, K. Suenaga and T. Gregorkiewicz, *J. Phys. Chem. C*, 2017, 121, 19490–19496.
22. T. Xuan, S. Lou, J. Huang, L. Cao, X. Yang, H. Li and J. Wang, *Nanoscale*, 2018, 10, 9840–9844.
23. K. Huang, D. Li, L. Yang, S. Liu and F. Yang, *J. Alloys Compd.*, 2017, 710, 244–252.
24. Q. A. Akkerman, S. Park, E. Radicchi, F. Nunzi, E. Mosconi, F. De Angelis, R. Brescia, P. Rastogi, M. Prato and L. Manna, *Nano Lett.*, 2017, 17, 1924–1930.
25. M. Liu, J. Zhao, Z. Luo, Z. Sun, N. Pan, H. Ding and X. Wang, *Chem. Mater.*, 2018, 30, 5846–5852.
26. Y. Li, H. Huang, Y. Xiong, S. V. Kershaw and A. L. Rogach, *CrystEngComm*, 2018, 20, 4900–4904.
27. X. Chen, D. Chen, J. Li, G. Fang, H. Sheng and J. Zhong, *Dalt. Trans.*, 2018, 47, 5670–5678.
28. G. Almeida, L. Goldoni, Q. Akkerman, Z. Dang, A. H. Khan, S. Marras, I. Moreels and L. Manna, *ACS Nano*, 2018, 12, 1704–1711.
29. L. Wu, H. Hu, Y. Xu, S. Jiang, M. Chen, Q. Zhong, D. Yang, Q. Liu, Y. Zhao, B. Sun, Q. Zhang and Y. Yin, *Nano Lett.*, 2017, 17, 5799–5804.
30. B. Kang and K. Biswas, *J. Phys. Chem. Lett.*, 2018, 9, 830–836.
31. G. Tong, H. Li, Z. Zhu, Y. Zhang, L. Yu, J. Xu and Y. Jiang, *J. Phys. Chem. Lett.*, 2018, 9, 1592–1599.
32. Y. M. Chen, Y. Zhou, Q. Zhao, J. Y. Zhang, J. P. Ma, T. T. Xuan, S. Q. Guo, Z. J. Yong, J. Wang, Y. Kuroiwa, C. Moriyoshi and H. T. Sun, *ACS Appl. Mater. Interfaces*, 2018, 10, 15905–15912.
33. L. Xu, J. Li, T. Fang, Y. Zhao, S. Yuan, Y. Dong and J. Song, *Nanoscale Adv.*, 2019, 1, 980–988.
34. W. Wang, D. Wang, F. Fang, S. Wang, G. Xu and T. Zhang, *Cryst. Growth Des.* 2018, 2018, 18, 6133–6141.
35. M. He, C. Wang, J. Li, J. Wu, S. Zhang, H. C. Kuo, L. Shao, S. Zhao, J. Zhang, F. Kang and G. Wei, *Nanoscale*, 2019, 11, 22899–22906.
36. L. N. Quan, R. Quintero-Bermudez, O. Voznyy, G. Walters, A. Jain, J. Z. Fan, X. Zheng, Z. Yang and E. H. Sargent, *Adv. Mater.*, 2017, 29, 1605945.
37. J. K. Nam, S. U. Chai, W. Cha, Y. J. Choi, W. Kim, M. S. Jung, J. Kwon, D. Kim and J. H. Park, *Nano Lett.*, 2017, 17, 2028–2033.
38. Y. Xin, H. Zhao and J. Zhang, *ACS Appl. Mater. Interfaces*, 2018, 10, 4971–4980.
39. H. Wu, W. Zhang, J. Wu and Y. Chi, *ACS Appl. Mater. Interfaces*, 2019, 11, 16713–16719.
40. P. Song, B. Qiao, D. Song, J. Cao, Z. Shen, G. Zhang, Z. Xu, S. Zhao, S. Wageh and A. Al-Ghamdi, *J. Mater. Sci.*, 2020, 55, 9739–9747.
41. S. Mollick, T. N. Mandal, A. Jana, S. Fajal, A. V. Desai and S. K. Ghosh, *ACS Appl. Nano Mater.*, 2019, 2, 1333–1340.
42. J. H. Cha, K. Noh, W. Yin, Y. Lee, Y. Park, T. K. Ahn, A. Mayoral, J. Kim, D. Y. Jung and O. Terasaki, *J. Phys. Chem. Lett.*, 2019, 10, 2270–2277.
43. S. Bhattacharyya, D. Rambabu and T. K. Maji, *J. Mater. Chem. A*, 2019, 7, 21106–21111.
44. Z. Chen, Z. G. Gu, W. Q. Fu, F. Wang and J. Zhang, *ACS Appl. Mater. Interfaces*, 2016, 8, 28737–28742.
45. E. Ploetz, H. Engelke, U. Lächelt and S. Wuttke, *Adv. Funct. Mater.*, 2020, 1909062.
46. J. Hu, S. K. Gupta, J. Ozdemir and M. H. Beyzavi, *ACS Appl. Nano Mater.*, 2020, 3, 6239–6269.
47. Y. Liu, Y. Zhu, S. B. Alahakoon and E. Egap, *ACS Materials Lett.* 2020, 2, 1561–1566.
48. B. P. Biswal, S. Chandra, S. Kandambeth, B. Lukose, T. Heine and R. Banerjee, *J. Am. Chem. Soc.*, 2013, 135, 5328–5331.
49. H. Ma, B. Liu, B. Li, L. Zhang, Y. G. Li, H. Q. Tan, H. Y. Zang and G. Zhu, *J. Am. Chem. Soc.*, 2016, 138, 5897–5903.

50. W. Zhang, Q. Zhao, X. Wang, X. Yan, J. Xu and Z. Zeng, *Catal. Sci. Technol.*, 2017, 7, 2753–2762.
51. G. Gao, Q. Xi, H. Zhou, Y. Zhao, C. Wu, L. Wang, P. Guo and J. Xu, *Nanoscale*, 2017, 9, 12032–12038.
52. F. Reyes-Pérez, J. J. Gallardo, T. Aguilar, R. Alcántara, C. Fernández-Lorenzo and J. Navas, *ChemistrySelect*, 2018, 3, 10226–10235.
53. B. M. Bresolin, S. Ben Hammouda and M. Sillanpää, *Nanomaterials*, 2020, 10, 1–17.
54. S. Bhattacharjee, S. P. Chaudhary and S. Bhattacharyya, *ChemRxiv* 2019.
55. Z. Zhang, Y. Liang, H. Huang, X. Liu, Qi Li, L. Chen, and D. Xu, *Angew. Chem. Int. Ed.*, 2019, 58, 7263–7267.
56. M. Karamia, M. Ghanbaria, O. Amirib and M. S. Niasaria, *Sep. Purif. Technol.*, 2020, 253, 117526.
57. T. Paula, D. Dasa, B. K. Dasb, S. Sarkarb, S. Maitic and K. K. Chattopadhyay, *J. Hazard. Mater.*, 2019, 380, 120855.
58. M. Ghanbari, F. Ansari and M. S. Niasari, *Inorg. Chim. Acta*, 2017, 455, 88–97
59. X. Qian, Z. Chen, X. Yang, W. Zhao, C. Liu, T. Sun, D. Zhou, Q. Yang, G. Wei and M. Fan, *J. Clean. Prod.*, 2019, 249, 119335.
60. M. Aamir, Z. Hussain, M. Sher and A. Iqbal, *Mater. Sci. Semicond. Process*, 2017, 63, 6–11.
61. S. Das, T. Paul, S. Maiti and K. K. Chattopadhyay, *Materials Letters*, 2020, 267, 127501.
62. L. Romani, A. Bala, V. Kumar, A. Speltini, A. Milella, F. Fracassi, A. Listorti, A. Profumo and L. Malavasi, *J. Mater. Chem. C*, 2020, 8, 9189.
63. X. Peng, J. Chen, F. Wang, C. Zhang and B. Yang, *Optik (Stuttg.)*, 2020, 208, 1–6.
64. M. C. Brennan, J. E. Herr, T. S. Nguyen-Beck, J. Zinna, S. Draguta, S. Rouvimov, J. Parkhill and M. Kuno, *J. Am. Chem. Soc.*, 2017, 139, 12201–12208.
65. D. B. Shinde, H. B. Aiyappa, M. Bhadra, B. P. Biswal, P. Wadge, S. Kandambeth, B. Garai, T. Kundu, S. Kurungot and R. Banerjee, *J. Mater. Chem. A*, 2016, 4, 2682–2690.
66. G. Das, D. B. Shinde, S. Kandambeth, B. P. Biswal and R. Banerjee, *Chem. Commun.*, 2014, 50, 12615.
67. H. Lv, X. Zhao, H. Niu, S. He, Z. Tang, F. Wu and J.P. Giesy, *J Hazard Mater.*, 2019;369, 494-502
68. S. H. Gaikwad, A. Koratti and S. P. Mukherjee, *Appl. Surf. Sci.*, 2019, 465, 413–419.
69. K. M. Reza, ASW Kurny and F. Gulshan, *Appl. Water Sci.*, 2017, 7, 1569–1578.
70. H. S. Lee, J. Hur, Y. H. Hwang, and H. S. Shin, *Int J Environ Res Public Health*. 2020, 17, 11, 3901.
71. C. D. V. Lopez, M. Z. Calvo, M. J. M. Vidales, V. B. Gutierrez, E. A. Sanchez, N. Merayo, F. F. Martinez, A. N. Marquez and A. J. D. Garcia, *Inorganics*, 2018, 6, 98.
72. I. Hasan, M. A. Albaejan, A. A. Alshayiqi, W. S. Nafaei, and F. A. Alharthi, *Molecules* 2023, 28, 3, 1140.



---

*Appendix***Materials**

Cesium bromide, CsBr	Sigma-Aldrich, 99%
Lead bromide, PbBr <sub>2</sub>	Sigma-Aldrich, 99%
1,3,5-triformylphloroglucinol, TFP	Hygeia Laboratories, A.R. grade
Ethidium bromide, EB	Sigma-Aldrich, 99.9%
1,4-dioxane	Sigma-Aldrich, 99.8%
Mesitylene	Sigma Aldrich, 99.8%
Acetic acid glacial, AA	SRL, extrapure 99.5%
Methyl Orange, MO	BDH Laboratory Reagent
DMF	AVRA, A.R. grade
Hexane	SRL, 99%
Toluene	SRL, 99%
Methanol	Thomas Baker, A.R. grade
Triethanolamine, TEOA	Loba Chemie, A.R. 99%
p-benzoquinone, PBZQ	98+%, Alfa Aesar
Isopropyl alcohol, IPA	SRL, UV and HPLC grade, 99.8%

**Characterizations**

*pXRD*: The phase identification of the as-synthesized samples were performed by Powder X ray diffraction (PXRD), recorded on a Panalytical X'pert PRO powder X-ray diffractometer with Cu K $\alpha$  radiation. Small Angle X-Ray Diffraction (SAXS) was performed on a Rigaku, Micromax-007HF with highintensity micro focus rotating anode X-Ray generator.

*Environmental Scanning Electron Microscopy*: The morphologies of the as-synthesised products were investigated using a scanning electron microscope (FEI, ESEM Quanta 200-3D) and High Resolution Transmission Electron Microscope (FEI, Tecnai 20 ST with an accelerating voltage of 200 kV) along with energy dispersive X-ray spectroscopy (EDX) and STEM-HAADF imaging.

*High-Resolution Transmission Electron Microscopy:* The samples were prepared by drop casting the sample from hexane on carbon-coated copper grids (TED PELLA INC., 200 mesh and SPI, lacey carbon 300 mesh).

*Thermo-Gravimetric Analysis:* TGA was performed using SDT Q600 DSC-TGA instrument in Argon atmosphere at ramping rate 10 °C/min.

*X-ray Photoelectron Spectra:* The surface properties of the as-synthesised samples were characterized by XPS using Thermo Scientific K-Alpha+ Xray photoelectron spectrometer analyser chamber operating at  $2 \times 10^{-7}$  mbar pressure.

*Fourier transform-infrared:* FTIR spectra were recorded using Perkin Elmer 2000 FTIR spectrometer in the 400–4000  $\text{cm}^{-1}$  region. The Brunauer–Emmett–Teller (BET) surface area of the samples were estimated by the nitrogen gas adsorption–desorption method on a NOVA 1200 (Quantachrome) instrument.

*Ultraviolet Spectroscopy:* UV spectra for all solutions were recorded using UV-1800 Shimadzu spectrophotometer.

*CHN analysis:* C, H, N contents were measured using ThermoFinnigan Flash EA1112 Series.

---

**ABSTRACT**

---

**Name of the Student:** Prachi Prasad Kour  
**Faculty of Study:** Chemical Science  
**AcSIR academic centre/CSIR Lab:**  
CSIR-National Chemical Laboratory, Pune

**Registration No. :** 10CC19J26009  
**Year of Submission:** 2023  
**Name of the Supervisor(s):** Dr. Shatabdi  
Porel Mukherjee

**Title of the thesis: Rational Design and Synthesis of Low-Dimensional Halide Perovskites with Improved Ambient Air Stability for Optoelectronic Applications**

---

Oxide perovskites ( $ABO_3$ ) discovered in the 90s were followed by the realization of halide perovskites (HPs) and Hybrid Organic and Inorganic Perovskites (HOIPs). These materials have become leading candidates for photovoltaic and optoelectronic device applications due to exceptional properties. However, their ionic lattice structure and intrinsic defects make them unstable to ambient conditions, and lead-based compounds limit their environmental and bio-medical fluorescence applications due to their high toxicity.

Considering this, the thesis entitled “Rational Design and Synthesis of Low-Dimensional Halide Perovskites with Improved Ambient Air Stability for Optoelectronic Applications”, aims to address the issue of ambient stability, which limits the applicability of the fantastic HOIP materials by synthesizing novel low dimensional structures. HOIP crystallization using 2-aminoethanethiol resulted in two stable compounds, (cysteammonium) $_7$ Pb $_4$ I $_{15}$  and (cysteammonium) $_2$ PbI $_4$ . The intermediate compound was used in a self-powered photodetector and for Ni $^{2+}$  ion detection. Long chain alkylammonium groups with Mn- and Cu- metal cations were synthesized using solid-state mechanochemical method, resulting in (TEA) $_2$ MnBr $_4$ , (TBA) $_2$ MnBr $_4$ , (TEA) $_2$ CuBr $_4$  and (TBA)CuBr $_2$  lead-free HOIPs. (TEA) $_2$ MnBr $_4$  and (TBA) $_2$ MnBr $_4$  were used for Pb $^{2+}$  ion detection due to their excellent stability under high humidity conditions. We have also synthesized a water-tolerant nanocomposite of perovskite and COF. The resulting compounds were CsPbBr $_3$ /Cs $_4$ PbBr $_6$ @EB-COF:Br and CsPbBr $_3$ @EB-COF:Br, with CsPbBr $_3$ /Cs $_4$ PbBr $_6$ @EB-COF:Br showing good tolerance to water and demonstrating state-of-the-art performance as a photocatalyst for methyl orange dye in water.

---

**List of Publications and Patents Emanating from the Thesis Work*****Publications***

1. **Prachi Kour** and Shatabdi Porel Mukherjee\*,  
CsPbBr<sub>3</sub>/Cs<sub>4</sub>PbBr<sub>6</sub> Perovskite@COF Nanocomposites for Visible-Light-Driven Photocatalytic Application in Water.  
*J. Mater. Chem. A* **2021**, 9, 6819. (IF: 14.51)
2. **Prachi Kour**, Mallu Chenna Reddy, Shiv Pal, Siraj Sidhik, Tisita Das, Padmini Pandey, Shatabdi Porel Mukherjee\*, Sudip Chakraborty\*, Aditya D Mohite\*, Satishchandra Ogale\*,  
An Organic-Inorganic Perovskitoid with Zwitterion Cysteamine Linker and Its Crystal-Crystal Transformation to Ruddlesden-Popper Phase.  
*Angew. Chem. Int. Ed.* **2021** 60, 18750. (IF: 16.82)
3. **Prachi Kour**, Neha Dambhare, Arup Kumar Rath and Shatabdi Porel Mukherjee\*  
Low-Dimensional Mn- and Cu- based Organic-Inorganic Perovskites for Metal Ion Detection.  
*Manuscript under submission*

***Patent***

1. CsPbBr<sub>3</sub>/Cs<sub>4</sub>PbBr<sub>6</sub> Perovskite@COF Nanocomposites for Visible-Light-Driven Photocatalytic Applications.  
Provisional filing Record no. 202211009056 dated 18-02-2022, Country: India; NCL No. 2021-INV-057, CSIR No. 2022-NF-0038.  
Inventors: Shatabdi Porel Mukherjee\* and **Prachi Kour**.

**Publication other than the Thesis Work**

1. Abhijit Biswas, Abhishek Swarnkar, Padmini Pandey, **Prachi Kour**, Swati Parmar, Satishchandra Ogale,  
Dynamics of Photo-Generated Carriers across the Interface between CsPbBr<sub>3</sub> Nanocrystals and Au–Ag Nanostructured Film, and Its Control via Ultrathin MgO Interface Layer.  
*ACS Omega* **2020**, 5, 21, 11915. (IF: 4.132)

### **List of Conferences and Awards**

#### **1. Prachi Kour**

Solar Energy Technologies for Sustainable Rural Development - SUNRISE,

Date of conference: Sep 07, 2020 to Sep 11, 2020.

**Awarded: 1<sup>st</sup> runner up in PhD Oral presentation competition**

**Title:** An Organic-Inorganic Perovskitoid with Zwitterion Cysteamine Linker and Its Crystal-Crystal Transformation to Ruddlesden-Popper Phase.

**Abstract:** Using zwitterion cysteamine, we demonstrate the synthesis of a novel low-D hybrid perovskitoid with a perovskite-like hybrid halide structure and yellow crystals (2-aminoethanethiol) linkage and its amazing crystal-to-crystal transformation to the Ruddlesden-Popper phase under the direction of molecular diffusion (Red crystals, Pnma space group). By having a special staggered arrangement of holes in the puckered 2D configuration with a facesharing connection between the corrugated-1D double chains, our stable intermediate perovskitoid significantly differs from all previous findings. When compared to the red phase, the yellow phase's PL intensity is 5 orders higher, and the yellow phase's average duration is likewise quite long (143 ns). The experimental band gap data and first principles DFT computations are extremely well in agreement. We show the novel perovskitoid yellow phase's and Black phosphorous is used as the active layer in a self-powered photodetector and for the selective detection of Ni<sup>2+</sup> via On-Off-On photoluminescence (PL) based on its composite.

#### **2. Prachi Kour**

Dr. K.V. Rao Scientific Society (KVRSS) - Research Awards 2021-22,

Date of Journal Paper Presentation: June 18, 2022.

**Awarded: 1st Runner up in Rasayanam – Chemistry category.**

**Title:** CsPbBr<sub>3</sub>/Cs<sub>4</sub>PbBr<sub>6</sub> Perovskite@COF Nanocomposites for Visible-Light-Driven Photocatalytic Application in Water.

3. **Prachi Kour**

InSc (Institute of Scholars), Govt. of India – 2022-23,

**Awarded: Young Researcher Award 2022.**

**Title:** CsPbBr<sub>3</sub>/Cs<sub>4</sub>PbBr<sub>6</sub> Perovskite@COF Nanocomposites for Visible-Light-Driven Photocatalytic Application in Water.

**Abstract:** We have created all-inorganic CsPbBr<sub>3</sub>/Cs<sub>4</sub>PbBr<sub>6</sub> perovskite@COF nanocomposites under air circumstances for the first time, and we have also fine-tuned the perovskite's crystal structures. Even after being submerged in water for 60 minutes, the nanocomposite is comparatively stable and retains its crystalline characteristics. Perovskite@COF nanocomposite exhibits effective photocatalytic degradation of methyl orange driven by visible light (10 mL; 20–100 ppm). With a high catalytic activity and cyclability of three to six cycles, the rate of photodegradation was approximately 0.245 min<sup>-1</sup>.

4. **Prachi Kour**

NCL-RF, NCLRF Awards for Research Scholars for the Year 2022, Interdisciplinary Research (Woman Research Scholar).

**Title:** Rational Design and Synthesis of Low-Dimensional Halide Perovskites with Improved Ambient Air Stability for Optoelectronic Applications.

**Abstract:**

Summary of the work: In the present thesis work, the challenges associated with the halide perovskite structures is solved by utilizing novel organic cations, by formation of nanocomposites and by utilizing lead free cations to solve the issue of toxicity to some extent.

Originality of the work: Initially, oxide perovskites were discovered in the 90s with the general formula  $ABO_3$  where, A monovalent cation, B divalent cation. However, halide perovskites and organic-inorganic perovskites also exist. Hybrid Organic and Inorganic Perovskites HOIPs,  $ABX_3$  (A=  $Cs^+$ ,  $MA^+$ ; B=  $Pb^{2+}$ ,  $Cu^{2+}$ ; X=  $Cl^-$ ,  $Br^-$ ,  $I^-$ ) and the halide perovskites (HPs) have an inorganic A site cation such as Cs, Na, etc. These have rapidly emerged as the leading photovoltaic and optoelectronic device materials in the past decade owing to their exceptional properties such as low exciton binding energy, high absorption coefficient, high carrier lifetime, bandgap tunability, dimensionality control, scalability, and low cost of fabrication due to solution processability. The main problem with these fascinating structures is their intrinsic instability to ambient conditions such as air, oxygen, and moisture. This is because they have an ionic lattice, and the intrinsic defects formed on the surface during thin film fabrication and other device applications. Also, another problem that exists till now is that the champion materials for solar cell applications and other practical applications are generally lead-based. To solve the aforementioned problems of instability within these materials, I have synthesizing low-dimensional halide perovskite structures. These structures have shown more stability in the ambient conditions owing to their network, which has long chain alkylammonium groups. These are hydrophobic in nature, thus resisting the attack of the environment on the structure and hence making it tolerant. Another strategy adopted to solve the problem of instability is nanocomposite formation. Halide perovskite nanocomposites have been reported previously with different polymers, metal oxides, MOF etc.



**Perovskite Phases**

# An Organic–Inorganic Perovskitoid with Zwitterion Cysteamine Linker and its Crystal–Crystal Transformation to Ruddlesden-Popper Phase

Prachi Kour, Mallu Chenna Reddy,\* Shiv Pal, Siraj Sidhik, Tisita Das, Padmini Pandey, Shatabdi Porel Mukherjee,\* Sudip Chakraborty,\* Aditya D. Mohite,\* and Satishchandra Ogale\*

**Abstract:** We demonstrate synthesis of a new low-*D* hybrid perovskitoid (a perovskite-like hybrid halide structure, yellow crystals,  $P21/n$  space group) using zwitterion cysteamine (2-aminoethanethiol) linker, and its remarkable molecular diffusion-controlled crystal-to-crystal transformation to Ruddlesden-Popper phase (Red crystals,  $Pnma$  space group). Our stable intermediate perovskitoid distinctly differs from all previous reports by way of a unique staggered arrangement of holes in the puckered 2D configuration with a face-sharing connection between the corrugated-1D double chains. The PL intensity for the yellow phase is 5 orders higher as compared to the red phase and the corresponding average lifetime is also fairly long (143 ns). First principles DFT calculations conform very well with the experimental band gap data. We demonstrate applicability of the new perovskitoid yellow phase as an excellent active layer in a self-powered photodetector and for selective detection of  $Ni^{2+}$  via On-Off-On photoluminescence (PL) based on its composite with few-layer black phosphorous.

## Introduction

Hybrid Organic and Inorganic Perovskites (HOIPs),  $ABX_3$  ( $A = Cs^+$ ,  $CH_3NH_3^+$ ,  $C_8H_9NH_3^+$ ,  $CH_5N_2^+$ ;  $B = Pb^{+2}$ ,  $Sn^{+2}$ ,  $Sb^{+2}$ ,  $Cu^{+2}$ ;  $X = I^-$ ,  $Br^-$ ,  $Cl^-$ ,  $BF_4^-$ ) have rapidly emerged as the leading photovoltaic and optoelectronic device materials in the past decade owing to their exceptional properties such as low exciton binding energy, high absorption coefficient, high carrier lifetime, band gap tunability, dimensionality control, scalability, and low cost of fabrication due to

solution processability.<sup>[1–10]</sup> The conversion of 3D HOIP to 2D HOIP is achieved by increasing the length of the organic cation (two or more carbon atoms), thus pushing the inorganic ( $PbI_6^-$ ) octahedral layers farther apart and creating a quantum well like structure with sequentially increasing band gaps. 2D HOIPs have gained considerable attention following the work of Mohite and co-workers, wherein they developed a hot casting technique for better charge transport leading to highly efficient perovskite solar cells and light emitting diodes.<sup>[11,12]</sup> Indeed, these 2D systems have already been demonstrated to possess several unique properties such as moisture stability, thermal stability, self-trapping of excitonic features, and long carrier lifetimes. These properties make them highly applicable for LEDs, lasing, and white-light emission applications as well.<sup>[13–20]</sup> The 2D lead based HOIPs (tolerance factor,  $t > 1$ ) can form Ruddlesden Popper (RP) type phase (general formula:  $A_{n+1}B_nX_{3n+1}$ ), Dion-Jacobson type perovskite phase (general formula:  $A'A_{n-1}Pb_nX_{3n+1}$ ) or alternating cation type phase (general formula:  $(A'A)_{n+1}B_nX_{3n+1}$ ) by incorporation of long alkyl/aryl-organic monovalent or divalent cations, respectively.<sup>[21]</sup> Also, in some cases some degree of strain is imparted to the  $MX_6^-$  octahedra from the organic cations, which leads to distorted octahedra, giving rise to some uniquely interesting electronic density of states and properties. Mao et al. have reported a corrugated 2D hybrid perovskite (DMEN)PbBr<sub>4</sub> (2-(Dimethylamino)ethylamine lead bromide), which exhibited broadband white light emission with an impressive colour rendering index (CRI) value of 73.<sup>[22]</sup> Recently, Tremblay et al. have demon-

[\*] P. Kour, Dr. M. Chenna Reddy, Dr. S. Pal, Dr. P. Pandey, Prof. S. Ogale  
Department of Physics and Centre for Energy Science Indian Institute of Science Education and Research (IISER), Pune  
Dr. Homi Bhabha Road, Pune 411008 (India)  
E-mail: mchenna@students.iiserpune.ac.in  
satishogale@iiserpune.ac.in



P. Kour, Dr. S. P. Mukherjee  
Physical and Materials Chemistry Division, CSIR-National Chemical Laboratory  
Dr. Homi Bhabha Road, Pune 411008 (India)  
and  
Academy of Scientific and Innovative Research (AcSIR)  
Ghaziabad 201002 (India)  
E-mail: sp.mukherjee@ncl.res.in

S. Sidhik, Prof. A. D. Mohite  
Department of Chemical and Biomolecular Engineering, Rice University  
6100 Main Street, MS-362, Houston, TX 77005 (USA)

E-mail: adm4@rice.edu

T. Das, Prof. S. Chakraborty  
Harish-Chandra Research Institute (HRI) Allahabad, HBNI  
Chhatnag Road, Jhansi, Prayagraj 211019 (India)  
E-mail: sudipchakraborty@hri.res.in

Prof. S. Ogale  
Research Institute for Sustainable Energy (RISE), TCG Centres for Research and Education in Science and Technology (TCG-CREST)  
Kolkata 700091 (India)  
E-mail: satish.ogale@tcgcrest.org

 Supporting information and the ORCID identification number(s) for the author(s) of this article can be found under:  
 <https://doi.org/10.1002/anie.202105918>.

strated successful incorporation of a mono-cation to form  $(4\text{NPEA})_2\text{PbI}_4$  (4-nitrophenyl ethyl ammonium lead iodide) as a  $3 \times 3$  corrugated 2D HOIP, containing regular as well as distorted  $\text{PbI}_6^-$  octahedra rendering optical properties similar to the systems containing distorted octahedra.<sup>[23]</sup> Other than the 2D corrugated systems, recently C. C. Stoumpus et al. have described the existence of the hexagonal perovskite polytypes in tin iodide hybrid perovskites by incorporation of various cations/ mixed cation by interesting synthetic strategies of halo acid reaction of the precursor tin iodide ( $\text{SnI}_2$ ) with varied organic linkers of primary, secondary, tertiary, and quaternary amines.<sup>[24]</sup> Kanatzidis and co-workers have also reported some other interesting perovskite-like hybrid halide structure with combinations of the corner, face, or edge sharing octahedral chains, termed as perovskitoids recently.<sup>[25,26]</sup> The organic molecules, which minimize the octahedral distortion and maximize the interlayer charge transport in 2D HOIPs are generally preferred for their favourable optoelectronic applications.<sup>[27]</sup> Several reports on the incorporation of organic cations containing a few carbon atoms such as methylammonium (MA), formamidinium (FA), phenyl-ethyl ammonium (PEA), ethylenediamine (en), and 2- aminoethanethiol (AET) highlight the importance of such small molecules in this context.<sup>[28–30]</sup> Recently, W. Ke et al. enhanced the air stability of the formamidinium tin iodide ( $\text{FASnI}_3$ ) perovskite by the introduction of ethylenediammonium {en} in its 3D  $\text{FASnI}_3$  structure and were able to tune the band gap of the new system by the incorporation of several defects within the 3D framework, thereby retaining its dimensionality. They also showed the champion solar cell efficiency of {en} $\text{FASnI}_3$  to be 7.14%.<sup>[31]</sup> Spanopoulos et al. showed a similar {en}-concentration dependent band gap tuning in MAPI ( $\text{CH}_3\text{NH}_3\text{PbI}_3$ ) while retaining the 3D framework of  $\text{MAPbI}_3$ .<sup>[32]</sup> Rath et al. showed a 5.0% efficiency of  $\text{MA}_{0.75}\text{FA}_{0.15}\text{PEA}_{0.1}\text{SnI}_3$  perovskite system retaining this efficiency for 5000 h under glove-box conditions and an impressive 87% initial PCE retention.<sup>[33]</sup> The long chain organic cations have drawbacks such as they act as barriers to electron transport due to the absence of  $\pi$ -electron conjugations and also they are liable to moisture attack when incorporated in the HOIP framework.<sup>[34,35]</sup> Several benefits of thiol incorporation in HOIP have also been highlighted.<sup>[36]</sup> Recently, Cao et al. showed an efficiency of 14.1% under ambient conditions in a mesoporous configuration, with  $\text{HOOC-Ph-SH}$  modifications at the mesoporous- $\text{TiO}_2$ /MAPI and MAPI/spiro-OMeTAD interfaces.<sup>[37]</sup> They showed that the Pb-S coordination post-thiol-treatment of the HOIP leads to the formation of a hydrophobic barrier, which prevents the infusion of water molecules, thereby preventing degradation. Halder et al. examined the incorporation of thiocyanate anion ( $\text{SCN}^-$ ) in MAPI<sup>[38]</sup> and found that these  $\text{MAPbI}_{3(1-x)}(\text{SCN})_x$  films show an enhancement in emission quantum yield suggesting a reduction in the non-radiative channels. Li et al. showed the incorporation of 2-AET in  $\text{MAPbI}_3$  as a bridging ligand to facilitate the formation of highly uniform and water stable (> 10 minutes)  $\text{MAPbI}_{3(x)}\text{-AET}$  thin films.<sup>[39]</sup> Although thiol conjugations have been explored, to the best of our knowledge, the incorporation of zwitterionic moieties to

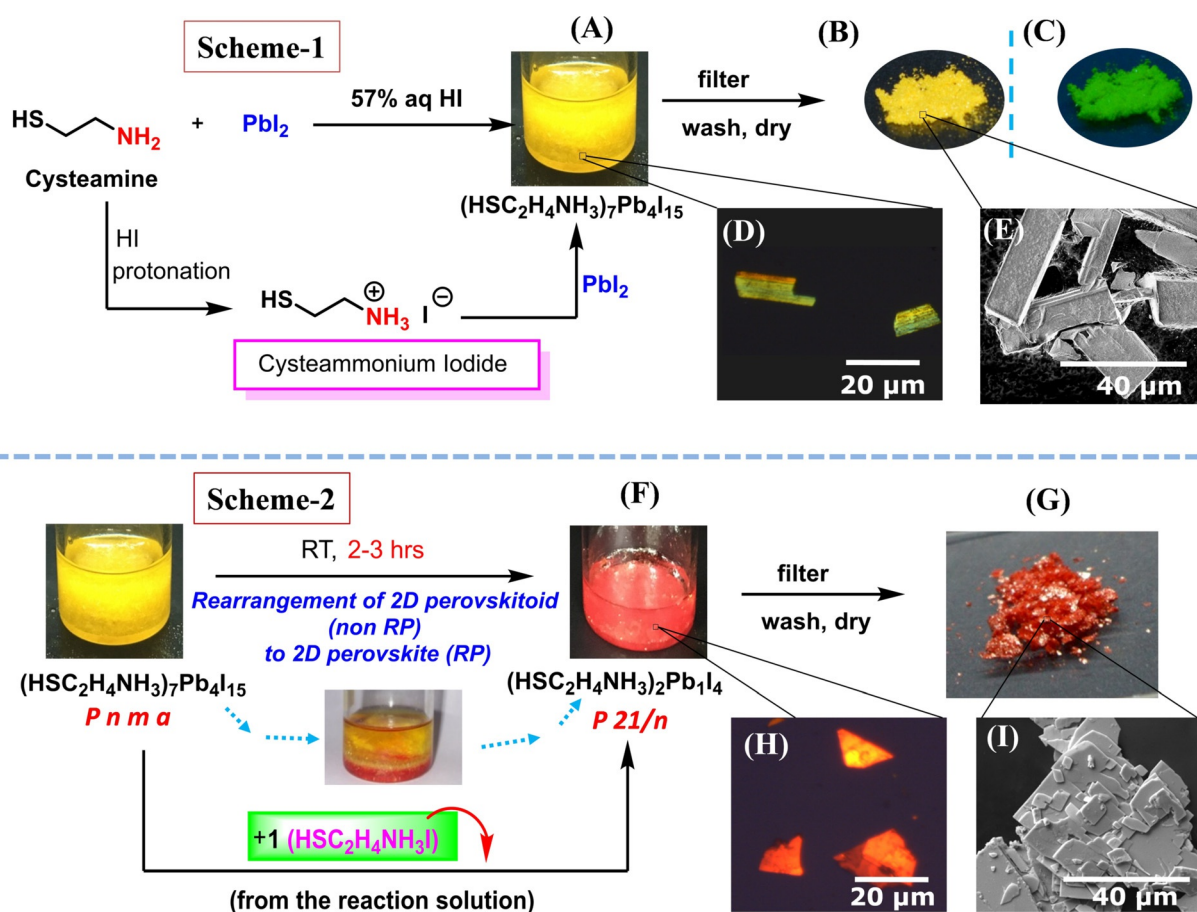
form 2D hybrid perovskite has not been studied to date, which sets the goal for the present work.

The molecule used in this study for synthesizing structurally and optoelectronically interesting HOIP single crystals is cysteamine (2-aminoethanethiol). This hetero-bifunctional cation (or zwitterion) contains an ammonium group at one end and thiol functional group at the other end of an ethyl chain. The ammonium group derived from amine of cysteamine can be incorporated into HOIP to make cysteamine ammonium cation based hybrids. In addition, thiol is a versatile and selective functional group that can involve in several functionalization reactions with different organic, inorganic reagents, bio, nanosystems which makes a huge difference vis a vis the traditional mostly amino group-containing molecules. The selective functionalization of the free thiol group of the zwitterion cysteamine could be utilized for connecting or conjugating the perovskite systems with other materials (Au, Ag) to form new material systems with interesting features.

Herein, we study the incorporation of zwitterion cysteamine or 2-AET  $\{\text{NH}_3\text{-CH}_2\text{-CH}_2\text{-SH}\}$  to form a robust perovskitoid and 2D RP phase of HOIP. We have successfully isolated the intermediate single crystals referred to as the yellow phase  $(\text{HSC}_2\text{H}_4\text{NH}_3)_7\text{Pb}_4\text{I}_{15}$ , compound **1**, which further converts to the red phase  $(\text{HSC}_2\text{H}_4\text{NH}_3)_2\text{PbI}_4$ , compound **2** when left undisturbed in the mother solution for 2–3 hours. We further propose a mechanism for this phase transformation (yellow to red), as limited by the in-diffusion of the organic cation. The compound **1** perovskitoid structure (layered 2D crystal structure with structural units of perovskite structure) has a unique puckered  $\text{PbI}_6^-$  framework comprising of both corner and face sharing octahedra. Interestingly, under visible excitation of 470 nm, compound **1** is highly luminescent with a large Stokes shift of 47 nm (FWHM 45 nm), while compound **2** is weakly luminescent with a Stokes shift of 38 nm (FWHM 55 nm). The PL intensity of compound **1** is 5 orders of magnitude higher than that of compound **2**, and compound **1** also has an impressively long carrier lifetime component, as revealed by time-resolved photoluminescence (TRPL). First principles DFT calculations match very well with the experimental band gap data. We further demonstrate that compound **1** (perovskitoid) works as an excellent active layer in a self-powered photodetector when sandwiched between PEDOT:PSS and PCBM (optoelectronic functionality) and a composite of compound **1** with few layer black phosphorous (FLBP) is a very effective On-Off-On photoluminescence (PL) probe for selective detection of  $\text{Ni}^{2+}$ .

## Results and Discussion

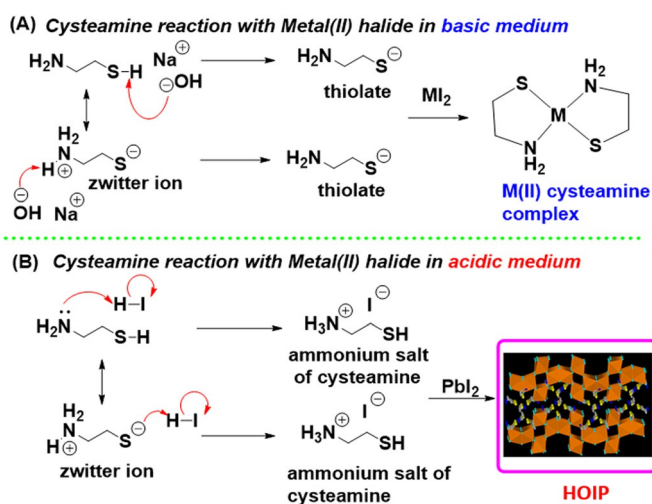
With the aim of incorporating the thiol-functional group containing ammonium cation into the organic-inorganic hybrid system, the reaction of  $\text{PbI}_2$  (1 equivalent) with cysteamine (3 equivalent) in HI solution was carried out at 250°C resulting in the growth of yellow crystals of  $(\text{HSC}_2\text{H}_4\text{NH}_3)_7\text{Pb}_4\text{I}_{15}$  (**1**). The details of the synthesis process are presented in supporting information (SI, page 4). The synthesis Scheme along with the physical appearance of



**Figure 1.** Scheme 1: the reaction and formation of  $(\text{HSC}_2\text{H}_4\text{NH}_3)_7\text{Pb}_4\text{I}_{15}$  (**1**); Crystals of **1** formed in the reaction solution (A); compound **1** in the ambient (B), under the 265 nm UV lamp showing green emission (C); polarized microscopy images (D); FESEM image for **1** (E); Scheme 2: the conversion of yellow crystals **1** ( $(\text{HSC}_2\text{H}_4\text{NH}_3)_7\text{Pb}_4\text{I}_{15}$  (2D perovskitoid)) into red crystals **2** ( $(\text{HSC}_2\text{H}_4\text{NH}_3)_2\text{PbI}_4$  (2D perovskite)) in the mother solution; RP phase crystals **2** in solution (F); Compound **2** crystals under ambient light after filtration (G); polarized microscopy images (H), FESEM image for **2** (I).

yellow crystals before and after filtration is shown in Figure 1 (A,B), Scheme 1. Compound **1** is green-emitting, as seen under the UV light (Figure 1C) initially and studied later in this work. Figure 1D shows the confocal microscopy images obtained under polarised microscopy indicating well-faceted single crystals for further analysis. Following the appearance of the yellow crystals in the solution, it was allowed to settle for 2–3 hours without any changes in the environmental conditions or additives. An interesting transformation of the yellow crystals into the red crystals was observed in the solution at room temperature after 2–3 hours, as shown in Figure 1, Scheme 2. Our analysis showed that the non-Ruddlesden Popper (RP) 2D perovskitoid gradually got converted into RP-like 2D perovskite ( $n=1$ ) ( $(\text{HSC}_2\text{H}_4\text{NH}_3)_2\text{PbI}_4$ ). Recently, Kanatzidis and co-workers have reported the transformation of RP ( $n=1$ ) perovskite to a corrugated structure by using *N,N*-dimethylethylenediamine (DMEN) cation, wherein both phases maintained the perovskite structure without losing corner-sharing. The important distinction in our case is that along with the structural change, the perovskitoid form (which is a non-perovskite) got transformed into a RP perovskite structure indicating crystal-to-crystal rearrangements in HOIP systems. Moreover, in the

work of Kanatzidis and co-workers, the molecular formula of the two phases  $\beta$ -(DMEN) $\text{PbBr}_4$  and  $\alpha$ -(DMEN) $\text{PbBr}_4$  before and after conversion is the same.<sup>[22]</sup> Such phase changes ( $\alpha$ ,  $\beta$ ,  $\gamma$ ,  $\delta$ ) have been reported in the colloidal state by varying the temperature.<sup>[36]</sup> However, quite surprisingly, as explained below, in our case the molecular formula is also changed upon conversion, which indicates that this is an incorporative transformation via molecular in-diffusion, which is distinctly different from a stoichiometry-preserving phase change, as previously reported.<sup>[22,40–42]</sup> We further solved the crystal structure (SI, page 5–7) to obtain the molecular formula of **1**,  $(\text{HSC}_2\text{H}_4\text{NH}_3)_7\text{Pb}_4\text{I}_{15}$  [CCDC No. 1951646] which is short by one cysteammonium iodide *vis a vis* the four formula units of the red crystallites of compound **2**,  $(\text{HSC}_2\text{H}_4\text{NH}_3)_2\text{PbI}_4$  [CCDC No. 1951645]. This suggests that the cysteammonium iodide diffusing slowly from the solution into the (intermediate) yellow crystal renders the crystal-to-crystal rearrangement leading to the transformation of compound **1** to compound **2**. The physical appearance of red crystals before and after filtration, and the confocal microscopy images obtained under polarised microscopy are illustrated in Figure 1 (F,G,H). FESEM images show thin rectangular platelet-like and sheet-like morphology for com-



**Figure 2.** The variation between cysteamine reaction with metal(II) halide in basic medium (A) and acidic medium (B) with the possible mechanism; cysteamine with base (NaOH) generates thiolate intermediate which forms  $M^{II}$  cysteamine complex with  $Ml_2$  (A); cysteamine with acid (HI) generates cysteammonium iodide salt, which forms HOIP with  $Pbl_2$  (B).

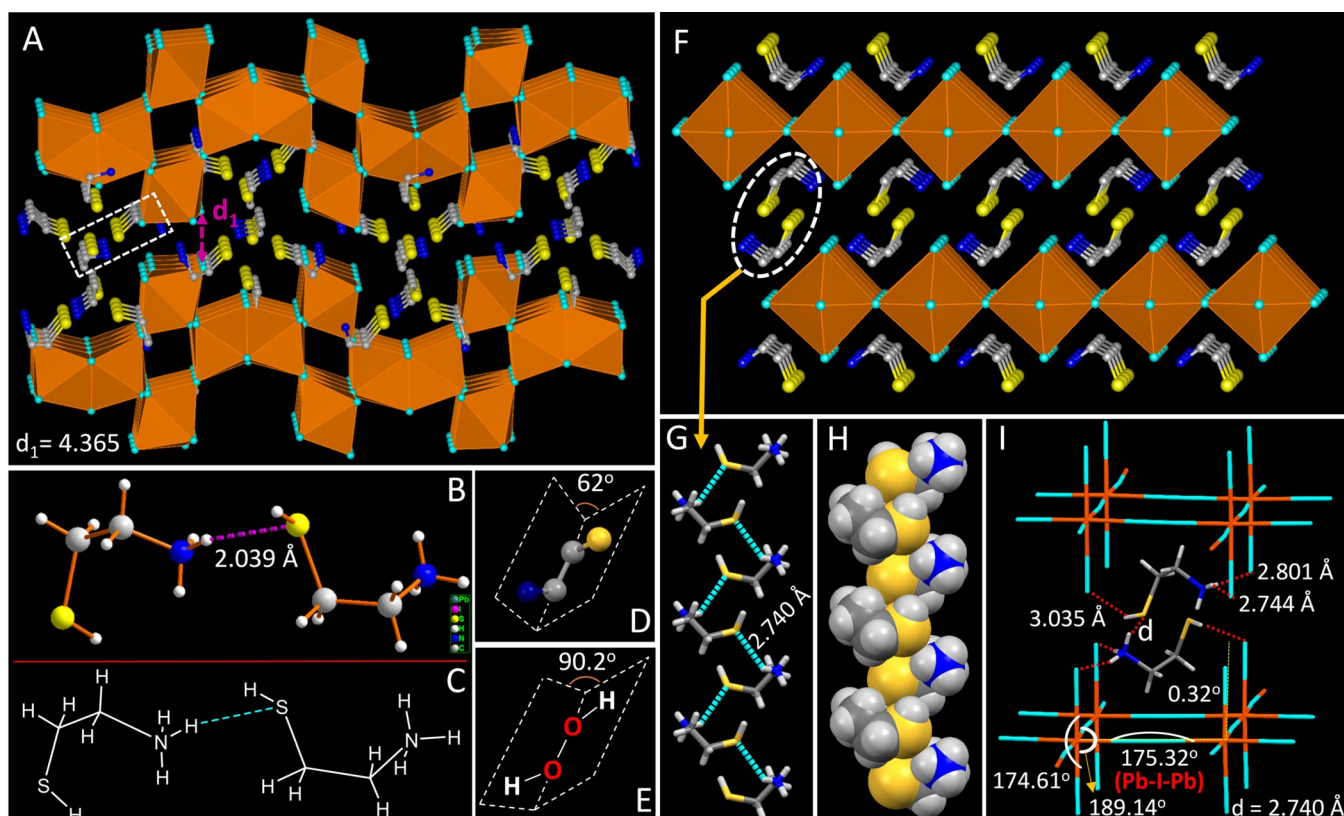
pounds **1** and **2** (Figure 1E,I). The experimental and simulated X-ray diffraction patterns of **1** and **2** were matched to check the purity of the dried compounds (Figure S1A,B). The PXRD patterns matched well with the simulated pattern with no detectable impurity peaks. Thus, the crushed crystalline powder faithfully retains its original crystal structure. The I: Pb stoichiometric ratio of crystals of **1** from SEM (EDAX) data is 3.75 (Figure S2A) and that for **2** it is 4.00 (Figure S2B) which approximately matches with the corresponding single crystal composition. In general, the reaction of metal (II) halide ( $MX_2$ ) with cysteamine leads to the formation of organometallic complexes, which are involved in the formation of the thiolate in the presence of base NaOH and this is followed by halide replacement and coordination of  $NH_2$  to the metal as shown in Figure 2A. This is a competitive reaction for the growth of the organic-inorganic hybrid structure with cysteamine incorporation. The reactive behaviour of cysteamine is very interesting and varies from basic to acidic medium. In the acidic medium (in HI solution), it generates cysteammonium iodide (cysteaminehydroiodide) salt from zwitterion by protonation of thiolate group or neutral molecule by the neutralization of the amine group. The mechanism showing the formation of cysteammonium ion from the zwitterion and neutral molecule of cysteamine is shown in Figure 2B. In the following step, the in situ formed cysteammonium iodide in the reaction mixture reacts with  $Pbl_2$  to form a new cysteamine incorporated HOIP, the compound **2** ( $HSC_2H_4NH_3)_7Pb_4I_{15}$ . This schematic of the diffusion of cysteammonium is presented in Figure 2B.

### Crystal Structure Discussion

The structural features obtained from single crystal data of **1** are illustrated in Figure 3A. The complete crystallo-

graphic data for compound **1** is given in Table S1. Analysis reveals that compound **1** crystallizes with a centrosymmetric monoclinic P system in the  $P21/n$  space group with lattice parameters  $a = 26.768(9)$  Å,  $b = 9.238(3)$  Å, and  $c = 27.595(11)$  Å, respectively. The asymmetric unit consists of seven cysteammonium cations along with one  $Pb_4I_{15}$  inorganic moiety (Figure S3), and it shows a clear charge balancing framework, where  $Pb_4I_{15}$  contributes +7 charge and 7 cysteammonium cations contribute -7 charge. Our newly synthesized hybrid structure **1** features  $PbI_6^-$  octahedra that are uniquely connected in both face and corner sharing moieties. This configuration is different from the perovskites that configure only corner sharing  $PbI_6^-$  octahedra. Hence the nomenclature used to describe our structure is perovskitoid, as indicated in some recent papers.<sup>[24,43]</sup> Interestingly, our structure has an additional peculiar feature that separates it from all the previous reports on perovskitoids. We have a peculiar staggered arrangement of holes in the puckered 2D configuration as shown in Figure 3A, S4 (A,B). The 2D net-like puckered structure is thus uniquely formed with the face sharing connection between corrugated-1D double chains, as shown in Figure S4D. The  $PbI_6^-$  octahedra connected with two adjacent octahedra through corner-sharing are seen to form a 1D zigzag chain. This is further connected (chain 1 in Figure S4D) to another 1D zigzag chain (chain 2 in Figure S4D) to form a nanowire, which can be considered as a corrugated-1D double chain structure.<sup>[24,44]</sup> The alternate octahedra of the two zigzag chains participate in face sharing connectivity, while the other alternating free octahedra lead to the formation of a unique inorganic network with small cave/cup type of arrangement, with the caves alternating in opposite directions to each other throughout the 2D net (Figure S4A). All the other alternate octahedra stand free without connection; bringing a uniquely interesting look to the total framework (Figure S4D). The adjacent nanowires are twisted with a twisting angle of  $64.92^\circ$  at face sharing. To give a clear view and understanding of the inorganic layer, a model was made and is presented in Figure S5. The inorganic puckered layer with cups directed in and out alternately as in the present 2D perovskitoid structure mimics a model reflected by a typical egg box with rows arranged alternatively opposite to each other, as shown in Figure S5. The other organic part formed between two inorganic puckered layers consists of two types of cysteammoniums, that is, dimeric units of cysteammonium through hydrogen bonding with hydrogen bonding distance of 2.039 Å, and isolated cysteammonium units as shown in Figure 3B, 3C. Moreover, the cation size, length of alkyl groups, and shape of the cation skeleton structure, all play an important role in rendering a new type structure of HOIPs with interesting structural and optoelectronic properties.<sup>[24,45,46]</sup>

The interesting feature of cysteammonium ion is that it has a peculiar structural shape that is, like an open book type structure of  $N_1C_2C_1S_1$  skeleton with  $\approx 65^\circ$  angle between two covers containing  $N_1$  and  $S_1$  on each side, connected with  $C_1C_2$  bond on the spine (Figure 3D). So far this special structural shape is limited to only a few molecules; one well known example being  $H_2O_2$  which exhibits open book structure with  $90.2^\circ$  between covers in the crystal (Figure 3E). The structural

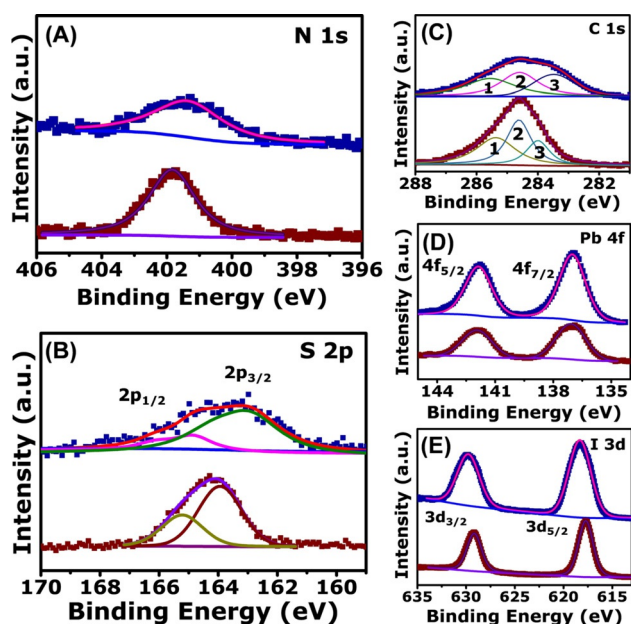


**Figure 3.** The crystal structure of **1**,  $(\text{HSC}_2\text{H}_4\text{NH}_3)_7\text{Pb}_4\text{I}_{15}$  featuring with  $\text{PbI}_6^-$  octahedra are uniquely connected in both face and corner sharing moieties to form 2D perovskitoid HOIP with 4.365 Å of a minimum distance between two inorganic layers (A); the dimeric cysteamine unit present between  $\text{Pb}_4\text{I}_{15}^{7-}$  puckered layers with hydrogen bonding distance of 2.039 Å (B); chemical structure representation of dimeric cysteamine unit (C); open book structure of  $\text{H}_2\text{O}_2$  (D); slightly open book structure of  $\text{N}_1\text{C}_2\text{C}_1\text{S}_1$  skeleton of cysteamine (E); The crystal structure of **2**,  $(\text{HSC}_2\text{H}_4\text{NH}_3)_2\text{PbI}_4$  featuring the  $\text{PbI}_4^{2-}$  plat inorganic sheets are separated by two consecutive organic cysteammonium layers (F); The unique helical-type of polymeric organic network with hydrogen bonds of cysteamine in capped sticks model (G) and space fill model (H); H-bonding interactions between organic and inorganic layers, I-Pb-I angles and out of plane distortion ( $0.32^\circ$ ) (I).

features extracted from the single crystal data for compound **2** are presented in Figure 3 F. Table S1 gives complete crystallographic data for compound **2**. The phase transformation changes the crystal system from a monoclinic  $P$  system in the  $P21/n$  space group to an orthorhombic  $P$  system in the  $Pnma$  space group with lattice parameters  $a = 12.9729(5)$  Å,  $b = 20.6291(9)$  Å and  $c = 6.4366(3)$  Å, respectively. Most interestingly, the yellow to red (perovskitoid to RP) solid state crystal-crystal transformation changes all the structural features of inorganic as well as organic part. The puckered inorganic layer with corner- and face-shared connectivity gets changed into a planar layered structure. Compound **2** adopts a structure where the layer is formed with corner-shared octahedra and the cysteammonium acts as a spacer between the two layers, stabilizing the total framework by electrostatic forces (between negatively charged head, namely the terminal iodide, and the positively charged head, namely  $\text{NH}_3$ ) and van der Waals interactions between the organic molecules (Figure S6). Upon diffusion of the cysteammonium iodide into the crystallites of **1**, the cysteammonium dimers and isolated cysteammonium units of **2** get nicely rearranged into a unique helical-type of polymeric organic network which is formed through the intermolecular interactions between S and H of  $\text{NH}_3$  groups @ 2.740 Å (weak hydrogen bonding), as

shown in Figure 3 (G,H). In the 2-(dimethylamino)ethylamine (DMEN) case, RP 2D perovskite with flat inorganic sheets is a kinetically favoured product.<sup>[22]</sup> On the other hand, the use of cysteammonium cation changes the phenomenon drastically and the RP 2D perovskite containing planar inorganic sheets acts as a thermodynamically stable product. Interestingly, the yellow crystals after filtration do not get converted into red crystals, due to the absence of reaction solution (excess molecules to impart required small but important stoichiometry change). Thus, it is a stable material for utilization in any viable application. This is an additional benefit of the present work, where two different and interesting materials are synthesized, starting with one set of precursor materials and using a single method with time domain control (Figure S7).

The XPS spectra for both the compounds **1** and **2** were recorded to identify the subtle changes in the chemical environments of cysteamine molecules. In N1s spectra, we can observe only a single peak assigned to  $\text{NH}_3^+$  for both the crystal systems (Figure 4 A).<sup>[47,48]</sup> There is a shift of the peak at 401.44 eV noted for compound **1** to 401.86 eV in the case of compound **2** resulting from the change in the state of  $\text{NH}_3^+$  moiety from being relaxed in **1** to more ordered state in **2**.<sup>[49]</sup> The S2p spectra, for compound **2** have the standard thiol



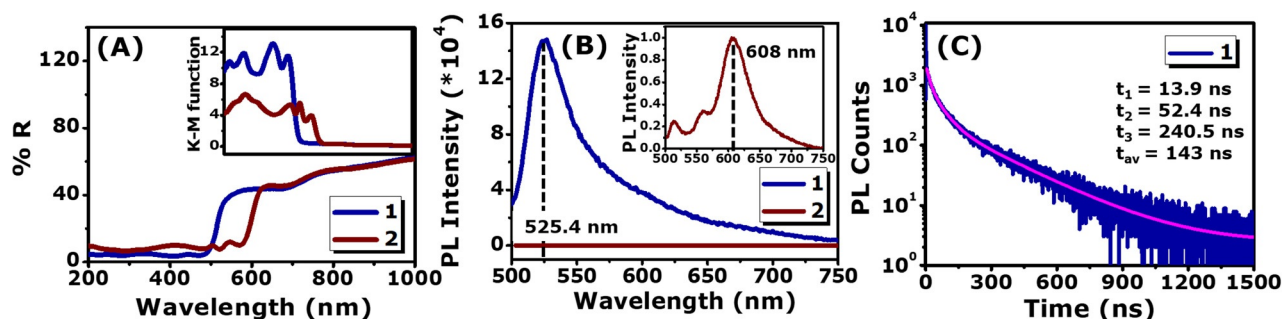
**Figure 4.** XPS core level spectra for compound **1** and compound **2** the Carbon correction C1s = 284.6 eV for all spectra, N1s (A); S2p (B); C1s (C); Pb4f (D) and I3d (E).

binding energies (BE) (Figure 4B). But the S2p spectra for compound **1** has slight shifting for these peaks to lower B.E. due to the more distorted bonds in this crystal system. Surface oxidation is more likely to occur in **1** since out of the two types of -SH bonds one is attracted to N by weak van der Waals attraction, whereas the other type of thiol is free to undergo oxidation during the course of the experiment which can be pointed out by the appearance of 2 peaks in the spectra.<sup>[50]</sup> The C1s spectra for compound **1** can be deconvoluted into 3 peaks, at 285.56 eV (C-N) (1) 284.6 eV (C-C) (2) and 283.48 eV (C-S) (3) (Figure 4C). The corresponding spectra for compound **2** show a 0.5 eV shift to higher B.E. for C-S bond indicating a lower bond electronegativity resulting from the vander Waals interaction with its more electronegative neighbouring N {N.S atomic distance 3.39 Å}. The C-N bond shows a shift to lower B.E. by 0.18 eV due to its electrostatic attraction with adjacent  $\text{PbI}_6^-$  octahedron. Out of the Pb4f (Figure 4D) and I3d (Figure 4E) spectra, it can be seen that the I3d spectrum concurs with a higher order of shifting due to

the more protected environment of  $\text{Pb}^{+2}$  cation in the octahedron.<sup>[51]</sup> The corrugated arrangement of  $\text{PbI}_6^-$  octahedron in compound **1** implies a weaker Pb-I interaction therein. The inclusion of cysteamine molecules in both the crystal systems was further examined by ATR-IR spectroscopy (Figure S8). The cysteamine peaks are present in both the spectra as reflected by the vibrations for the N-H stretching at  $3735.42\text{ cm}^{-1}$ , C-H stretching at  $2999.13\text{ cm}^{-1}$ , S-H stretching at  $2329.31\text{ cm}^{-1}$ , and N-H bending at  $1698.21\text{ cm}^{-1}$ . Surprisingly only the C-H stretching peak showed a major difference due to changes in the dipole moment of the bonds attributed to their differential interactions with the neighbouring  $\text{PbI}_6^-$  octahedra as reflected in the XPS discussion. To examine the thermal stability properties of the newly synthesized crystals **1** and **2**, thermogravimetric analysis (TGA) was performed from room temperature (RT) up to  $600^\circ\text{C}$  under nitrogen flow and the results are shown in Figure S9.<sup>[52]</sup> The decomposition temperatures of compound **1** and **2** are almost same because it is directly related to the acidity of the organic cation, which is same in both compounds; they being stable up to  $252^\circ\text{C}$ . However, interestingly, despite the organic cation being the same in both the compounds, the decomposition of cysteammonium iodide in **1** occurred from  $252^\circ\text{C}$  to  $330^\circ\text{C}$ , while that of **2** occurred from  $252^\circ\text{C}$  to  $415^\circ\text{C}$ ; a huge difference of around  $85^\circ\text{C}$ . This can be attributed to the polymeric helical structural arrangement of the cation in **2** which requires a higher temperature range to decompose; while the cation arrangement in **1** is in the form of dimeric and monomeric units. Further details about the TGA results are presented on SI, page 12.

#### Photo-Physical Properties

Figure 5A compares the diffuse reflectance spectroscopy (DRS) data for compounds **1** and **2** and the inset shows the Kubelka-Munk (K-M) function values. It can be seen that there is a significant change in the band gap (Figure S10) from about 2.27 eV for **1** to about 2.02 eV for **2**. The reason for significant difference in the band gaps of **1** and **2** lies in the structural orientation of the cysteamine cation within the crystal, depicted in Figure S11. The orientation of the bifunctional organo-ammonium cations with respect to the  $\text{PbX}_6^-$



**Figure 5.** DRS (%R) data with K-M function shown as an inset for the compounds **1** and **2** (A); Comparative PL spectra for compounds **1** and **2**, inset shows the PL for compound **2** (B) at 470 nm excitation; TRPL data for compounds **1** (C). Note: All optical measurements are performed on compound **1** and compound **2** powders.

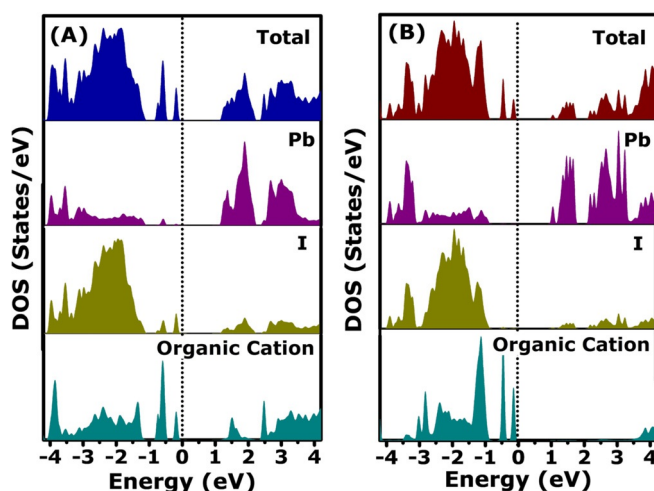
(X = I, Br, Cl) octahedral layers controls the type of hydrogen bonding and X-Pb-X (in and out of plane) distortions, finally influencing the band gap for the 2D perovskite systems. Generally, for the case of  $Y(\text{CH}_2)_2\text{NH}_3^+$  (Y = OH, Cl, Br, I, CN, SH) cation in the  $(Y(\text{CH}_2)_2\text{NH}_3^+)_2\text{PbI}_4$  perovskite, as the size of the Y cation increases, the I-Pb-I bond distortion increases for halide 2D systems.<sup>[45]</sup> In 2D Chloro and Bromo 2D halide cases, the ammonium cation heads are located out of the inorganic chain giving lower H-bonding. For the 2D Iodo systems, the amino heads are inside leading to higher H-bonding and consequently, the band gap is higher.<sup>[45]</sup> However, for **2** crystallites the ammonium cation head lies out of the perovskite layer whereas ethyl parts are located in the inorganic framework (Figure S11A,B), leading to weaker hydrogen bonding interaction and weaker distortions in the I-Pb-I layers. This explains the band gap reduction for our **2** crystallites RP perovskite. The PL data for both compounds are shown in Figure 5 B, respectively, for excitation @ 470 nm. Interestingly, **1** is highly luminescent (peak @ 525 nm) while **2** crystallites exhibit only a feeble PL intensity (with peak @ 608 nm) for the 470 nm excitation condition. We briefly address this intensity aspect below, following the discussion of the results of DFT calculations. We have also done excitation wavelength dependent PL experiment and it was observed that PL intensity for both compounds is realized under UV excitation (near 350 nm). Even then the intensity for the compound **2** is orders of magnitude lower than that for the compound **1** (Figure S12).

The Stokes shift is also found to be small in both compounds **1** and **2**. The PL intensity being feeble in compound **2** case, the time resolved PL (TRPL) data for this case was noisy and hence is not analysed. Finally, we also looked at the time resolved PL for the yellow crystal for which significant PL intensity was observed and the same is shown in Figure 5 C. The same was fitted into three relaxation time components with short (13.9 ns), medium (52.4 ns), and very long (240.5 ns) time scales (Table S2). Further detailed studies will be required to pinpoint the mechanisms of the relaxations rendering these time domains. Possible mechanisms may include polaronic effects and strong screening as discussed in some reports.<sup>[53,54]</sup>

#### Analysis and Insights based on Density Functional Theory

In order to validate the experimental outcome, we have rigorously performed electronic structure calculations based on Density Functional Theory (DFT) formalism<sup>[55]</sup> for the newly synthesized crystal structures of compound **1** and compound **2** respectively. The computational details are provided in SI, page 15.

Figure 6 (A,B) shows the results for the total and projected density of states (DOS) for compound **1** and compound **2** crystals based on the first principles electronic structure calculations within the framework of density functional theory (DFT) formalism. We note that the continuum of valence band states for both compounds starts below about  $-1$  eV with a few localized sharp density of states separated out from the continuum and located just below the Fermi



**Figure 6.** Density of states calculation for **1** (A) and **2** (B) by DFT (For clarity an enlarged image is shown in the Supporting Information, Figure S13).

energy. The continuum of states belonging to the conduction band for both the compounds, on the other hand, starts just above 1 eV. Thus, the band gap values for both compounds that would be reflected in optical measurements are expected to be over 2 eV, as is indeed confirmed experimentally (Figure 5 A and related discussion), while the sharp states below the Fermi energy would contribute to the band tailing effects in the absorbance. Therefore, considering the continuum states into account, the DFT-calculated values turn out to be about 2.46 eV (2.276 eV) for compound **1** and 2.27 eV (2.085 eV) for compound **2**, if we consider the mid-points of the leading edges (edges) of the valence and conduction bands. The agreement with the experimental values for **1** (**2**) of 2.27 eV (2.02 eV) is thus quite good.

We have also determined the projected density of states in order to find the elemental contributions of the constituents towards the total DOS of compounds **1** and **2**, while having a profound understanding of the hybridization. In case of compound **1**, we can observe Pb-6p contributions in the valence band regime of DOS, similar to I-5p contribution with comparatively larger intensity. This leads to the hybridization between Pb-6p and I-5p, which provides the inherent stability of the  $\text{PbI}_6^-$  octahedra in the structure. Similar observations have been found in case of compound **2**, while the contributions from I-5p are negligible near the Fermi vicinity of valence band maxima (VBM) as compared to compound **1**. It is also worth to mention the different contribution of Pb-6p orbitals in valence band regime corresponding to the two compounds, in compound **1**, there is finite density of states around  $-0.5$  eV, which can act as defect states, which is not present in the compound **2**. This particular defect-like state is certainly unique to the perovskitoid structure as compared to compound **2**.

The difference in the Pb-6p contributions in both the compounds is also visible in the conduction band regime, where the density of states corresponding to Pb-6p appear below 1 eV in case of compound **2**, while the same appeared above 1 eV in compound **1**. The density of states correspond-

ing to I-6p orbitals is having more intensity as it prevailed in the conduction band regime in case of perovskitoid structure as compared to the compound **2**. The electronic contribution corresponding to the organic cation also bears the difference of less intensity in case of RP system, as compared to the perovskitoid one. Additionally, the organic contribution in the conduction band regime has been prevailed more in perovskitoid as compared to compound **2**.

Thus, based on the combined analysis of the experimental results on absorbance and PL and the total DOS calculated from DFT calculations one can understand as to why the luminescence is bright for the **1** and weak for **2**, along with the corresponding energy maxima. Moreover, from the projected density of states analysis, we have observed the states in the Fermi vicinity, while this exciting signature can be envisaged further from the perspective of band edge alignment and non-linear optical features, having a direct implication in the electronic transport phenomena. This would certainly pave the way to a series of investigations for probing the combination of Wannier and Frenkel excitons.

### Applications of the new Perovskitoid phase

With the impressive optical properties of the new perovskitoid phase as discussed above, we further endeavoured to explore its efficacy for optoelectronic and sensing applications. In the first application, we could demonstrate its applicability for an interesting design of a self-powered photodetector with the perovskitoid layer sandwiched between PEDOT:PSS and PCBM. In another application we integrated the perovskitoid with few layer black phosphorous (FLBP) in a functional composite and demonstrated the ability of the composite for selective detection of Ni<sup>2+</sup> ion via on-off-on photoluminescence (PL) probe.

### Self-powered photodetector using (HSC<sub>2</sub>H<sub>4</sub>NH<sub>3</sub>)<sub>7</sub>Pb<sub>4</sub>I<sub>15</sub> crystals

We explored the optoelectronic functionality of the new perovskitoid (HSC<sub>2</sub>H<sub>4</sub>NH<sub>3</sub>)<sub>7</sub>Pb<sub>4</sub>I<sub>15</sub> crystals, the thin films of the same were deposited by hot casting method.<sup>[11]</sup> Figure 7A shows the absorbance of the thin films of (HSC<sub>2</sub>H<sub>4</sub>NH<sub>3</sub>)<sub>7</sub>Pb<sub>4</sub>I<sub>15</sub> which establishes that its band gap lies in optically interesting region.

The X-ray diffraction pattern of the film confirms that the perovskitoid phase seen in the crystal is retained in the film grown by the hot casting method (Figure 7B). Figure 7C shows the band diagram upon which the design of our self-powered photodetector was based. The device three-layer configuration was deposited by the procedure detailed in the SI, page 5. The I-V curves of the device in the dark and under illumination with light intensity of 1.5 mW cm<sup>-2</sup> using a broadband source are shown in Figure 7D (Note the log scale on both axes).

Clearly, over the full voltage range, more than a factor of 10 change is seen in the current upon illumination. Figure 7E shows the current vs. time curves for the photodetector under bias voltage of 0 V using a broad band light source. An

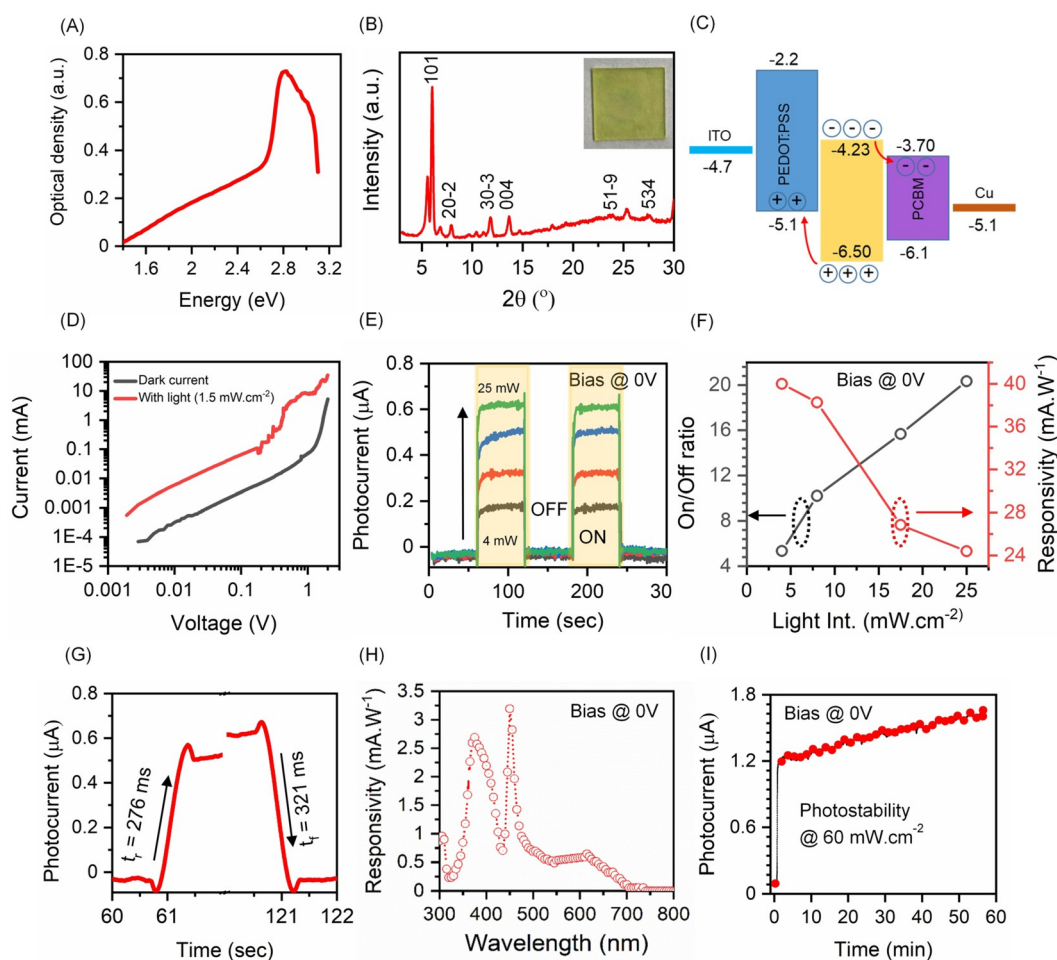
impressive power dependence is noted with fast rise and fall times. The on-off ratio and responsivity values measured at 0 V bias, plotted in Figure 7F as a function of the incident light intensity, show the expected trends with fairly impressive numbers. The plot showing the response time of the self-powered photodetector at 25 mW cm<sup>-2</sup> light intensity under 0 bias is shown in Figure 7G. The observed rise and fall times are commensurate with the regime reflected in other reports.<sup>[56,57]</sup> Figure 7H shows the responsivity spectra of the fabricated photodetector at 0 V bias; the sharp peak at about 450 nm corresponds to photon energy of 2.755 eV which is near the absorbance peak in Figure 7A. We also examined the photostability of the photodetector at a rather high light intensity of 60 mW cm<sup>-2</sup> and the data are shown in Figure 7I. The photostability of the self-powered photodetector clearly appears to be good for the duration of time it is tested.

### Perovskitoid/FLBP interfacing and metal ion detection

With the impressive optical properties of the new perovskitoid (compound **1**) as discussed above, we further endeavour its integration with few layers of black phosphorous (FLBP) to investigate the electronic coupling and charge transfer between the duo, and possible heavy metal ion sensing application. This was achieved by mixing compound **1** (2 mg) with FLBP (0.8 mg) in 2 mL anhydrous toluene and sonicating together to achieve the integration. The XRD pattern of compound **1** + FLBP shown in Figure S15 confirms the coexistence of both perovskitoid and FLBP, without the formation of any other phase. The high-resolution transmission electron microscopy (HRTEM) image (Figure 8A) reveals the surface decoration of compound **1** on FLBP. It shows the lattice spacing of  $d=3.3 \text{ \AA}$  corresponding to the (534) plane of compound **1**. The absorption spectra of compound **1** and compound **1** + FLBP as-prepared composite in toluene are shown in Figure S16. With the addition of FLBP, the absorption spectral nature of compound **1** is maintained, although with a slight shift, and the absorption above the band edge of compound **1** (> about 410 nm) represents the contribution of FLBP.

Figure 8B represents the PL of compound **1** and its quenching upon FLBP addition. The multi-peak structure of PL of the perovskitoid quantum dots (with the peaks separated roughly equally on the energy scale) is quite intriguing and will be addressed and pursued in future work. The PL quenching observed for **1** + FLBP case can be assigned to the charge transfer from compound **1** to FLBP. This electron transfer from compound **1** to FLBP can be understood from the band alignment shown in Figure 8C. The locations of the conduction and valence bands of FLBP have been reported.<sup>[58]</sup> In order to obtain the same for the case of compound **1**, we first recorded the ultraviolet photoelectron spectrum (UPS) for **1** (Figure S18) and the work function was calculated using the relationship between the incident photon energy ( $h\nu$ ) and the secondary edge position (cut off), as described in eq  $\{\Phi = h\nu - \text{cutoff}\}$ <sup>[59]</sup> which yields the work function 5.02 eV for compound **1**. From this the location of valence band maximum was found to be  $-6.5 \text{ eV}$  which is



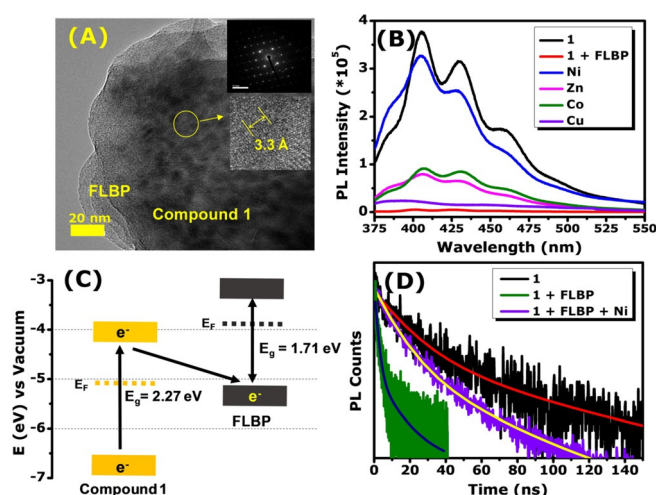


**Figure 7.** Absorbance of the thin films of compound **1** fabricated by hot-casting technique (A); X-ray diffraction of the thin films of compound **1** fabricated by hot-casting technique (B); Band diagram showing the self-powered photodetector with the synthesized crystals (C);  $I$ - $V$  curves of the device in the dark and under illumination with light intensity of  $1.5 \text{ mW cm}^{-2}$  using a broadband source at  $0 \text{ V}$  (D); current versus time curves of the PD under bias voltage of  $0 \text{ V}$  using a broad band light source (E); Variation in the ON/OFF ratio and responsivity with the intensity of light at  $0 \text{ V}$  bias (F); Plot showing the response time of the self-powered photodetector at  $25 \text{ mW cm}^{-2}$  light intensity under  $0 \text{ V}$  bias (G); Responsivity spectra of the fabricated photodetector at  $0 \text{ V}$  bias (H); Photostability of the self-powered photodetector at high light intensity of  $60 \text{ mW cm}^{-2}$  (I). (For clarity an enlarged image is shown in the Supporting Information, Figure S14.)

indicated in Figure 8C. The location of the conduction band was then found from the optically determined band gap. When a photon of energy  $3.2 \text{ eV}$  ( $\lambda = 350 \text{ nm}$ ) is incident on the composite system, the photogenerated electrons from the perovskitoid can be easily transferred to FLBP as shown and therefore the PL is dramatically quenched. The time resolved PL (TRPL) data shown in Figure 8D is consistent with this observation, as expected. The corresponding fitted data for relaxation times are provided in Table S3. It may be seen from Table S3 that the average life time of compound **1** reduced from  $37.84 \text{ ns}$  to  $12.34 \text{ ns}$  with the addition of FLBP (Figure 8D). The exceptional properties and versatility of such hybrid systems can facilitate their applicability as a PL On-Off-On probe for heavy metal ion detection.<sup>[60–63]</sup>

Herein we therefore examined the use of perovskitoid/FLBP composite as a PL On-Off-On probe for 3d transition element ion detection. The preparation procedure of metal-oleates for this study was adopted from the reported literature.<sup>[62]</sup> The PL modification by the addition of different

metal-oleate compounds of  $\text{Ni}^{2+}$ ,  $\text{Zn}^{2+}$ ,  $\text{Co}^{2+}$  and  $\text{Cu}^{2+}$  to the solution containing compound **1** + FLBP composite was then studied. The corresponding PL spectra are shown in Figure 8B for various cases of interest. It was noted that  $\text{Ni}^{2+}$  renders a remarkable (almost full) recovery of PL, while the recovery is either negligible ( $\text{Cu}^{2+}$ ) or small ( $\text{Zn}^{2+}$  and  $\text{Co}^{2+}$ ) for other transition elements. Since for all the cases the nature of PL is similar to that of the parent compound **1**, the transition element interaction with the perovskitoid is of primary importance for PL changes. Also, the average life time (Figure 8D) of compound **1** which was reduced from  $37.84 \text{ ns}$  to  $12.34 \text{ ns}$  with the addition of FLBP showed a significant recovery back to  $29.97 \text{ ns}$  (Table S3) upon addition of  $1.79 \times 10^{-3} \text{ M}$  concentration of  $\text{Ni}^{2+}$ . The bi-exponentially fitted slow component (for radiative recombination)<sup>[64]</sup> of compound **1** reduced from  $39.11 \text{ ns}$  (52.8%) to  $16.80 \text{ ns}$  (21.0%) upon compositing with FLBP, which upon addition of  $\text{Ni}^{2+}$  ions is seen to recover to  $32.70 \text{ ns}$  (62.2%). These findings corroborate well with the PL quenching and



**Figure 8.** HRTEM image depicting the formation of nanocomposite of compound 1 and FLBP, inset depicts SAED pattern (top) and d-spacing (bottom) (A); PL spectra at 350 nm excitation for perovskitoid/FLBP composite with  $1.79 \times 10^{-2}$  M concentration of various metal ions in toluene (B); Energy-band diagram showing excitonic charge transfer between compound 1 and FLBP (C); TRPL data depicting subsequent recovery of lifetime after addition of  $1.79 \times 10^{-3}$  M  $\text{Ni}^{2+}$  ions in solution (D). (For clarity an enlarged image is shown in the Supporting Information, Figure S17.)

recovery discussed above. We briefly discuss the  $\text{Ni}^{2+}$  concentration dependence (Figure S19) and possible mechanism of selective  $\text{Ni}^{2+}$  detection by the Perovskitoid/FLBP composite (Figure S20) in the SI, page 19–20. Highly selective  $\text{Ni}^{2+}$  detection is an important result because humans exposed to nickel inhalation or Ni internalization via oral, and dermal routes can cause several severe health problems if nickel exposure exceeds certain limit.<sup>[65–67]</sup>

## Conclusion

A zwitterion cysteamine linker is used for the first time to synthesize unique organic-inorganic single crystal perovskitoid structure with face sharing and corner sharing octahedra. It is further shown that if left in the reaction medium, this yellow phase gradually (kinetically) transforms into a red-coloured compound with Ruddlesden-Popper structure via incorporative crystal-to-crystal transformation. This involves a change in the overall formula of the HOIP compound from the initial phase  $(\text{HSC}_2\text{H}_4\text{NH}_3)_7\text{Pb}_4\text{I}_{15}$  (1) to the final phase  $(\text{HSC}_2\text{H}_4\text{NH}_3)_2\text{PbI}_4$  (2). Photo-physical properties are also examined and analysed via comparison with the results of DFT calculations. Two appealing applications of the optoelectronically interesting compound 1 are demonstrated which include a self-powered photodetector exhibiting impressive performance features and selective detection of  $\text{Ni}^{2+}$  ion via on-off-on PL probe measurements.

## Acknowledgements

The authors gratefully acknowledge funding under the UK-India SUNRISE and UKIERI (DST/INT/UK/P-148/2016) (DST-British Council) programs. PK thanks CSIR for the award of Senior Research fellowship.

## Conflict of Interest

The authors declare no conflict of interest.

**Keywords:** crystal growth · organic–inorganic hybrid composites · perovskite phases · photodetectors · zwitterions

- [1] D. H. Cao, C. C. Stoumpos, O. K. Farha, J. T. Hupp, M. G. Kanatzidis, *J. Am. Chem. Soc.* **2015**, *137*, 7843–7850.
- [2] Q. Dong, J. Song, Y. Fang, Y. Shao, S. Ducharme, J. Huang, *Adv. Mater.* **2016**, *28*, 2816–2821.
- [3] W. Zhang, X. Yan, W. Gao, J. Dong, R. Ma, L. Liu, M. Zhang, *Org. Electron.* **2019**, *65*, 56–62.
- [4] A. Z. Chen, M. Shiu, J. H. Ma, M. R. Alpert, D. Zhang, B. J. Foley, D. Smilgies, S. Lee, J. J. Choi, *Nat. Commun.* **2018**, *9*, 1336.
- [5] T. Zuo, X. He, P. Hu, H. Jiang, *ChemNanoMat* **2019**, *5*, 278–289.
- [6] C. C. Stoumpos, D. H. Cao, D. J. Clark, J. Young, J. M. Rondinelli, J. I. Jang, J. T. Hupp, M. G. Kanatzidis, *Chem. Mater.* **2016**, *28*, 2852–2867.
- [7] Y. Yu, D. Zhang, P. Yang, *Nano Lett.* **2017**, *17*, 5489–5494.
- [8] A. Basu, P. Kour, S. Parmar, R. Naphade, S. Ogale, *J. Phys. Chem. C* **2018**, *122*, 4802–4808.
- [9] P. Kour, M. C. Reddy, R. Naphade, S. Ogale, *APL Mater.* **2018**, *6*, 086107-7.
- [10] R. Naphade, S. Nagane, U. Bansode, M. Tathavadekar, A. Sadhanala, S. Ogale, *ChemSusChem* **2017**, *10*, 3722–3739.
- [11] H. Tsai, W. Nie, J.-C. Blancon, C. C. Stoumpos, R. Asadpour, B. Harutyunyan, A. J. Neukirch, R. Verduzco, J. J. Crochet, S. Tretiak, L. Pedesseau, J. Even, M. A. Alam, G. Gupta, J. Lou, P. M. Ajayan, M. J. Bedzyk, M. G. Kanatzidis, A. D. Mohite, *Nature* **2016**, *536*, 312–316.
- [12] H. Tsai, W. Nie, J. C. Blancon, C. C. Stoumpos, C. M. M. Soe, J. Yoo, J. Crochet, S. Tretiak, J. Even, A. Sadhanala, G. Azzellino, R. Brenes, P. M. Ajayan, V. Bulović, S. D. Stranks, R. H. Friend, M. G. Kanatzidis, A. D. Mohite, *Adv. Mater.* **2018**, *30*, 1704217.
- [13] X. Liu, F. Gao, *J. Phys. Chem. Lett.* **2018**, *9*, 2251–2258.
- [14] Z. Yuan, Y. Shu, B. Ma, *Chem. Commun.* **2016**, *52*, 3887–3890.
- [15] R. Guo, Z. Zhu, A. Boulesbaa, F. Hao, A. Puretzky, K. Xiao, B. Jiming, Y. Yan, W. Li, *Small Methods* **2017**, *1*, 1700245.
- [16] “Excitonics in 2D Perovskites”: W. K. Chong, D. Giovanni, T. C. Sum, *Halide Perovskites*, pp. 55–79, Wiley, Weinheim, **2018**.
- [17] D. Yu, B. Cai, F. Cao, X. Li, X. Liu, Y. Zhu, J. Ji, Y. Gu, H. Zeng, *Adv. Mater. Interfaces* **2017**, *4*, 1700441.
- [18] S. Krishnamurthy, P. Kour, A. Katre, S. Gosavi, S. Chakraborty, S. Ogale, *APL Mater.* **2018**, *6*, 114204–8.
- [19] S. Krishnamurthy, R. Naphade, W. J. Mir, S. Gosavi, S. Chakraborty, R. Vaidyanathan, S. Ogale, *Adv. Opt. Mater.* **2018**, *6*, 1800751.
- [20] S. Parmar, S. Pal, A. Biswas, S. Gosavi, S. Chakraborty, M. C. Reddy, S. Ogale, *Chem. Commun.* **2019**, *55*, 7562–7565.
- [21] C. M. M. Soe, C. C. Stoumpos, M. Kepenekian, B. Traoré, H. Tsai, W. Nie, B. Wang, C. Katan, R. Seshadri, A. D. Mohite, J. Even, T. J. Marks, M. G. Kanatzidis, *J. Am. Chem. Soc.* **2017**, *139*, 16297–16309.

- [22] L. Mao, Y. Wu, C. C. Stoumpos, M. R. Wasielewski, M. G. Kanatzidis, *J. Am. Chem. Soc.* **2017**, *139*, 5210–5215.
- [23] M. H. Tremblay, F. Thouin, J. Leisen, J. Bacsa, A. R. S. Kandada, J. M. Hoffman, M. G. Kanatzidis, A. D. Mohite, C. Silva, S. Barlow, S. R. Marder, *J. Am. Chem. Soc.* **2019**, *141*, 4521–4525.
- [24] C. C. Stoumpos, L. Mao, C. D. Malliakas, M. G. Kanatzidis, *Inorg. Chem.* **2017**, *56*, 56–73.
- [25] X. Li, Y. He, M. Kepenekian, P. Guo, W. Ke, J. Even, C. Katan, C. C. Stoumpos, R. D. Schaller, M. G. Kanatzidis, *J. Am. Chem. Soc.* **2020**, *142*, 6625–6637.
- [26] Q. Sun, Y. Xu, H. Zhang, B. Xiao, X. Liu, J. Dong, Y. Cheng, B. Zhang, W. Jie, M. G. Kanatzidis, *J. Mater. Chem. A* **2018**, *6*, 23388–23395.
- [27] C. Ma, D. Shen, T. W. Ng, M. F. Lo, C. S. Lee, *Adv. Mater.* **2018**, *30*, 1800710.
- [28] Y. Xie, H. Yu, J. Duan, L. Xu, B. Hu, *ACS Appl. Mater. Interfaces* **2020**, *12*, 11190–11196.
- [29] Y. Liu, S. Akin, A. Hinderhofer, F. T. Eickemeyer, H. Zhu, J. Y. Seo, J. Zhang, F. Schreiber, H. Zhang, S. M. Zakeeruddin, A. Hagfeldt, M. I. Dar, M. Grätzel, *Angew. Chem. Int. Ed.* **2020**, *59*, 15688–15694; *Angew. Chem.* **2020**, *132*, 15818–15824.
- [30] F. Xia, Y. Xu, B. Li, W. Hui, S. Zhang, L. Zhu, Y. Xia, Y. Chen, W. Huang, *ACS Appl. Mater. Interfaces* **2020**, *12*, 15439–15445.
- [31] W. Ke, C. C. Stoumpos, M. Zhu, L. Mao, I. Spanopoulos, J. Liu, O. Y. Kontsevoi, M. Chen, D. Sarma, Y. Zhang, M. R. Wasielewski, M. G. Kanatzidis, *Sci. Adv.* **2017**, *3*, e1701293.
- [32] I. Spanopoulos, W. Ke, C. C. Stoumpos, E. C. Schueller, O. Y. Kontsevoi, R. Seshadri, M. G. Kanatzidis, *J. Am. Chem. Soc.* **2018**, *140*, 5728–5742.
- [33] T. Rath, J. Handl, S. Weber, B. Friesenbichler, P. Fürk, L. Troi, T. Dimopoulos, B. Kunert, R. Resel, G. Trimmel, *J. Mater. Chem. A* **2019**, *7*, 9523–9529.
- [34] S. F. Zhang, X. K. Chen, A. M. Ren, H. Li, J. L. Bredas, *ACS Energy Lett.* **2019**, *4*, 17–25.
- [35] M. H. Tremblay, J. Bacsa, S. Barlow, S. R. Marder, *Mater. Chem. Front.* **2020**, *4*, 2023.
- [36] T. Kollek, D. Wurmbrand, S. T. Birkhold, E. Zimmermann, J. Kalb, L. Schmidt-Mende, S. Polarz, *ACS Appl. Mater. Interfaces* **2017**, *9*, 1077–1085.
- [37] J. Cao, J. Yin, S. Yuan, Y. Zhao, J. Li, N. Zheng, *Nanoscale* **2015**, *7*, 9443–9447.
- [38] A. Halder, R. Chulliyil, A. S. Subbiah, T. Khan, S. Chatteraj, A. Chowdhury, S. K. Sarkar, *J. Phys. Chem. Lett.* **2015**, *6*, 3483–3489.
- [39] B. Li, C. Fei, K. Zheng, X. Qu, G. Cao, J. Tian, *J. Mater. Chem. A* **2016**, *4*, 17018–17024.
- [40] W. A. Saidi, J. J. Choi, *J. Chem. Phys.* **2016**, *145*, 144702.
- [41] S. Sidhik, A. C. Pasarán, C. Rosiles Pérez, T. López-Luke, E. De La Rosa, *J. Mater. Chem. C* **2018**, *6*, 7880–7889.
- [42] M. Saliba, T. Matsui, J. Y. Seo, K. Domanski, J. P. Correa-Baena, M. K. Nazeeruddin, S. M. Zakeeruddin, W. Tress, A. Abate, A. Hagfeldt, M. Grätzel, *Energy Environ. Sci.* **2016**, *9*, 1989–1997.
- [43] N. Marchal, W. Van Gompel, M. C. Gélvez-Rueda, K. Vandewal, K. Van Hecke, H. G. Boyen, B. Conings, R. Herckens, S. Maheshwari, L. Lutsen, C. Quarti, F. C. Grozema, D. Vanderzande, D. Beljonne, *Chem. Mater.* **2019**, *31*, 6880–6888.
- [44] H. Lin, C. Zhou, J. Neu, Y. Zhou, D. Han, S. Chen, M. Worku, M. Chaaban, S. Lee, E. Berkwits, T. Siegrist, M. H. Du, B. Ma, *Adv. Opt. Mater.* **2019**, *7*, 1801474.
- [45] B. Saparov, D. B. Mitzi, *Chem. Rev.* **2016**, *116*, 4558–4596.
- [46] M. E. Kamminga, G. A. De Wijs, R. W. A. Havenith, G. R. Blake, T. T. M. Palstra, *Inorg. Chem.* **2017**, *56*, 8408–8414.
- [47] Y. Xue, J. Yuan, J. Liu, S. Li, *Nanomaterials* **2018**, *8*, 591.
- [48] P. Chen, Y. Bai, S. Wang, M. Lyu, J. H. Yun, L. Wang, *Adv. Funct. Mater.* **2018**, *28*, 1706923.
- [49] Y. Li, P. Li, Z. H. Lu, *AIP Adv.* **2018**, *8*, 035218.
- [50] Z. Zheng, X. Zhang, C. Neumann, D. Emmrich, A. Winter, H. Vieker, W. Liu, M. Lensen, A. Götzhäuser, A. Turchanin, *Nanoscale* **2015**, *7*, 13393–13397.
- [51] S. Chen, T. W. Goh, D. Sabba, J. Chua, N. Mathews, C. H. A. Huan, T. C. Sum, *APL Mater.* **2014**, *2*, 081512–7.
- [52] A. Dualeh, P. Gao, S. Il Seok, M. K. Nazeeruddin, M. Grätzel, *Chem. Mater.* **2014**, *26*, 6160–6164.
- [53] T. Chen, W. L. Chen, B. J. Foley, J. Lee, J. P. C. Ruff, J. Y. P. Ko, C. M. Brown, L. W. Harriger, D. Zhang, C. Park, M. Yoon, Y. M. Chang, J. J. Choi, S. H. Lee, *Proc. Natl. Acad. Sci. USA* **2017**, *114*, 7519–7524.
- [54] Y. Chen, H. T. Yi, X. Wu, R. Haroldson, Y. N. Gartstein, Y. I. Rodionov, K. S. Tikhonov, A. Zakhidov, X. Y. Zhu, V. Podzorov, *Nat. Commun.* **2016**, *7*, 12253.
- [55] C. H. Chu, C. W. Leung, *Integr. Equations Oper. Theory* **2001**, *40*, 391–402.
- [56] Y. Wang, T. Zhang, P. Zhang, D. Liu, L. Ji, H. Chen, Z. D. Chen, J. Wu, S. Li, *Org. Electron.* **2018**, *57*, 263–268.
- [57] Y. Li, Z. F. Shi, X. J. Li, C. X. Shan, *Chin. Phys. B* **2019**, *28*, 017803.
- [58] S. K. Muduli, E. Varrla, Y. Xu, S. A. Kulkarni, A. Katre, S. Chakraborty, S. Chen, T. C. Sum, R. Xu, N. Mathews, *J. Mater. Chem. A* **2017**, *5*, 24874–24879.
- [59] N. Cheng, J. Tian, Q. Liu, C. Ge, A. H. Qusti, A. M. Asiri, A. O. Al-Youbi, X. Sun, *ACS Appl. Mater. Interfaces* **2013**, *5*, 6815–6819.
- [60] D. Zhang, Y. Xu, Q. Liu, Z. Xia, *Inorg. Chem.* **2018**, *57*, 4613–4619.
- [61] Y. Liu, X. Tang, T. Zhu, M. Deng, I. P. Ikechukwu, W. Huang, G. Yin, Y. Bai, D. Qu, X. Huang, F. Qiu, *J. Mater. Chem. C* **2018**, *6*, 4793–4799.
- [62] P. Pandey, A. Sengupta, S. Parmar, U. Bansode, S. Gosavi, A. Swarnkar, S. Muduli, A. D. Mohite, S. Ogale, *ACS Appl. Nano Mater.* **2020**, *3*, 3305–3314.
- [63] M.-Y. Zhu, L.-X. Zhang, J. Yin, J.-J. Chen, L.-J. Bie, *Inorg. Chem. Commun.* **2019**, *109*, 107562.
- [64] A. Biswas, A. Swarnkar, P. Pandey, P. Kour, S. Parmar, S. Ogale, *ACS Omega* **2020**, *5*, 11915–11922.
- [65] G. Genchi, A. Carocci, G. Lauria, M. S. Sinicropi, *Int. J. Environ. Res. Public Health* **2020**, *17*, 679.
- [66] <https://apps.who.int/iris/handle/10665/107335>, World Heal. Organ. Reg. Off. Eur. (2000). Air Qual. Guidel. Eur. Second Ed. World Heal. Organ. Reg. Off. Eur. **2000**, 11–23.
- [67] K. K. Das, R. C. Reddy, I. B. Bagoji, S. Das, S. Bagali, L. Mullur, J. P. Khodnapur, M. S. Biradar, *J. Basic Clin. Physiol. Pharmacol.* **2019**, *30*, 141–152.

Manuscript received: May 1, 2021

Accepted manuscript online: June 24, 2021

Version of record online: July 14, 2021

Cite this: *J. Mater. Chem. A*, 2021, 9, 6819Received 8th January 2021  
Accepted 19th February 2021

DOI: 10.1039/d1ta00201e

rsc.li/materials-a

## CsPbBr<sub>3</sub>/Cs<sub>4</sub>PbBr<sub>6</sub> perovskite@COF nanocomposites for visible-light-driven photocatalytic applications in water†

Prachi Kour<sup>ab</sup> and Shatabdi Porel Mukherjee \*<sup>ab</sup>

For the first time, we have synthesized all-inorganic CsPbBr<sub>3</sub>/Cs<sub>4</sub>PbBr<sub>6</sub> perovskite@COF nanocomposites under atmospheric conditions and tuned the crystal structures of the perovskite as well. The nanocomposite is reasonably stable and maintains its crystalline properties even when dipped into water for 60 minutes. The perovskite@COF nanocomposite shows efficient visible-light-driven photocatalytic performance to degrade Methyl orange (10 mL; 20–100 ppm). The rate of photodegradation was about 0.245 min<sup>-1</sup> with high catalytic activity and recyclability for three to six cycles.

Recently, all-inorganic cesium lead-halide perovskite nanocrystals (NCs) have attracted enormous attention due to their desirable photophysical properties.<sup>1–3</sup> Among them, cesium lead-bromide perovskites (CLBPs) have emerged as a prospective candidate in optoelectronic applications because of their strong photoluminescence (PL) with a relatively narrow full width at half maximum (FWHM) and high PL quantum yields (PLQYs).<sup>4</sup> The networked perovskite NCs are essentially different from the usual low dimensional semiconductor NCs; instead, they are known as bulk quantum materials. In the case of perovskite NCs, charge carriers are localized within ordered metal halide sheets (2D), rods (1D), or clusters (0D), which are separated by cationic lattices. CLBPs are also known to exist in three-dimensional polymorphs, namely 3D CsPbBr<sub>3</sub> (cubic) formed by a cubo-octahedral (PbX<sup>6-</sup>) network in all three directions, 2D CsPb<sub>2</sub>Br<sub>5</sub> (tetragonal) which possesses octahedral connectivity only in two directions and hence creates a layered structure and 0D Cs<sub>4</sub>PbBr<sub>6</sub> (hexagonal) which lacks octahedral connectivity in all the directions.<sup>4–10</sup> Therefore, for CLBPs, even in NCs and bulk, it is anticipated that the photo-excited charge carriers in these materials experience strong quantum confinement and the exciton binding energy for 0D

perovskites is much superior to that for 3D perovskites.<sup>11–13</sup> The PL intensity and efficiency of 0D Cs<sub>4</sub>PbBr<sub>6</sub> found to be much superior to those of 3D CsPbBr<sub>3</sub>.<sup>14,15</sup> Thus, strong excitons from Cs<sub>4</sub>PbBr<sub>6</sub> are likely to be very useful for various light-emitting devices, *e.g.*, display technology, solar concentrators, lasers, LEDs, *etc.*<sup>4,16,17</sup> Current reports on the PL of Cs<sub>4</sub>PbBr<sub>6</sub> NCs are reasonably debatable; therefore, more investigations are necessary to understand the details and also the mechanism of the origin of PL. Few reports suggested that Cs<sub>4</sub>PbBr<sub>6</sub> NCs maintained strong and stable bright green luminescence.<sup>11–13</sup> In contrast, other reports acclaimed that Cs<sub>4</sub>PbX<sub>6</sub> NCs are almost non-emissive.<sup>18,19</sup> It has been claimed that the green emission of Cs<sub>4</sub>PbX<sub>6</sub> NCs originated from several phenomena, such as direct exciton recombination luminescence of Cs<sub>4</sub>PbBr<sub>6</sub>,<sup>16,20</sup> bromine vacancies,<sup>4</sup> and the impurities of CsPbBr<sub>3</sub> NCs embedded in Cs<sub>4</sub>PbBr<sub>6</sub> NCs.<sup>14,21,22</sup> It is also reported that the co-existence of CsPbBr<sub>3</sub> and Cs<sub>4</sub>PbBr<sub>6</sub> NCs was hard to suppress,<sup>23</sup> and Cs<sub>4</sub>PbBr<sub>6</sub> NCs can be easily transformed into CsPbBr<sub>3</sub> *via* an insertion reaction with additional PbBr<sub>2</sub>, physical or chemical extraction of CsBr, and ligand-mediated transformation.<sup>24–29</sup> Since, CsPbBr<sub>3</sub> has superior optical properties, and Cs<sub>4</sub>PbBr<sub>6</sub> has higher moisture stability, their co-existence processed stability as well as outstanding PLQY comparable to CsPbBr<sub>3</sub> NCs.<sup>30–36</sup> Several strategies have been adopted to form mixed-phase CLBP composites and overcome the abhorrent obstacle of ambient instability, such as using polymer blends and inorganic passivators to solve these issues.<sup>37–40</sup> Metal-organic frameworks (MOFs) are also being used as effective encapsulators due to their framework structure and facile modulation features.<sup>41–44</sup> Covalent Organic Frameworks (COFs) are another sister class of MOFs in which light atoms bond covalently to form an open structure with high porosity.<sup>45,46</sup> These materials have similar properties to MOFs. Still, they possess a tunable pore size, structural predictability, lower density, and higher stability, making them an exciting class of encapsulators that have not been explored extensively to encapsulate perovskite systems as far as is known currently.<sup>46,47</sup>

<sup>a</sup>Physical and Materials Chemistry Division, CSIR-National Chemical Laboratory, Dr Homi Bhabha Road, Pune, 411008, India. E-mail: sp.mukherjee@ncl.res.in

<sup>b</sup>Academy of Scientific and Innovative Research (AcSIR), Ghaziabad-201002, India

† Electronic supplementary information (ESI) available. See DOI: 10.1039/d1ta00201e

Herein, we have synthesized a bromide cation containing covalent organic framework (EB-COF:Br) *via* a simple modified mechanochemical method and used it to fabricate a CLBP incorporated COF nanocomposite.<sup>48,49</sup> Interestingly, we have achieved both single-phase and mixed-phase CLBP systems, wherein 3D (CsPbBr<sub>3</sub>) as well as 3D/0D (CsPbBr<sub>3</sub>/Cs<sub>4</sub>PbBr<sub>6</sub>) crystal structures are encapsulated inside the EB-COF:Br framework. CsPbBr<sub>3</sub>/Cs<sub>4</sub>PbBr<sub>6</sub>@EB-COF:Br is found to be reasonably stable in water medium for 60 minutes. To the best of our knowledge, this is the first report of fabrication of all-inorganic perovskite@COF composite nanomaterials with tunable crystalline properties. Using the CsPbBr<sub>3</sub>/Cs<sub>4</sub>PbBr<sub>6</sub>@EB-COF:Br nanocomposite, efficient visible-light-driven photocatalytic activity to degrade Methyl orange (MO) (10 mL; 20–100 ppm) is demonstrated. The CsPbBr<sub>3</sub>/Cs<sub>4</sub>PbBr<sub>6</sub>@EB-COF:Br nanocomposite material exhibited the highest photocatalytic activity reported to date with a photodegradation rate of about 0.245 min<sup>-1</sup> (for 100 ppm), using a perovskite composite material.<sup>41,50–62</sup> The recyclability of the photocatalyst is tested for three to six cycles.

We have specifically selected a cationic COF (EB-COF:Br) having Br-functionalization due to its chemical affinity and

non-interference with the PL properties with the bromide containing perovskite, mainly CLBP. Recently, mechanochemical synthesis has become an excellent alternative to the solution-based classical synthesis of COFs.<sup>48</sup> Herein, we have used a modified mechanochemical method to synthesize EB-COF:Br avoiding the necessity of using typical inert atmosphere conditions in a Pyrex tube, as reported earlier.<sup>49</sup> In this method, 1,3,5-triformyl phloroglucinol (TFP) (0.2 mmol) and ethidium bromide (EB) (0.3 mmol) were ground together using a mortar and pestle followed by the addition of 2 mL 1,4-dioxane–mesitylene (v/v, 1 : 1) and 0.2 mL of 6 M aqueous acetic acid solutions at room temperature. The mixing was continued for 2–3 hours by using DI water as the solvent till a dark brown paste was achieved. This paste was then transferred to a vial and heated in an oven at 90 °C for 24 hours. The product was then washed and dried under vacuum for further use [Fig. 1; also see the ESI†].

In the next action, CLBP incorporated EB-COF:Br was synthesized *via* a **two-step precursor addition strategy**, wherein first PbBr<sub>2</sub> was added, followed by CsBr addition to achieve the CLBP@EB-COF:Br nanocomposite (Fig. 2). The crystal structure of the products formed was investigated by XRD analysis. The existence of characteristic peaks at 2.83° and a broad peak at 27° corresponding to 100 and 001 planes confirmed the formation of EB-COF:Br (Fig. 3).<sup>49</sup> As discussed in the ESI,† by changing the mole ratios of CsBr and PbBr<sub>2</sub> (1 : 1) to COF concentration, different crystal structures of CLBP were obtained (Table S1, see the ESI†). Fig. 3 displays the typical XRD patterns of the as-synthesized sample obtained using 15 mmol of PbBr<sub>2</sub> and CsBr, each. **The co-existence of cubic phase CsPbBr<sub>3</sub> and rhombohedral phase Cs<sub>4</sub>PbBr<sub>6</sub> is evident from Fig. 3.** The peaks at  $2\theta = 15.17^\circ, 21.42^\circ, 26.39^\circ, 30.65^\circ, 34.43^\circ$  and  $37.70^\circ$  were respectively indexed to the (1 0 0), (1 1 0), (1 1 1), (2 0 0), (2 1 0) and (2 1 1) planes of cubic phase CsPbBr<sub>3</sub> with the lattice constant  $a = 5.83 \text{ \AA}$  (JCPDS no 54-0752),<sup>29,63</sup> while the peaks at  $2\theta = 12.54^\circ, 12.83^\circ, 20.07^\circ, 22.39^\circ, 25.36^\circ, 27.47^\circ, 28.55^\circ, 30.66^\circ, 34.57^\circ, 37.61^\circ, \text{ and } 38.92^\circ$  were respectively indexed to the (0 1 2), (1 1 0), (1 1 3), (3 0 0), (0 2 4), (1 3 1), (2 1 4), (0 0 6), (4 1 0), (3 1 5), and (3 2 4) planes of Cs<sub>4</sub>PbBr<sub>6</sub> with lattice constants  $a = b = 13.73 \text{ \AA}$ ,  $c = 17.32 \text{ \AA}$ ,  $\alpha = \beta = 90^\circ$ , and  $\gamma = 120^\circ$  (JCPDS no 73-2478).<sup>29,63</sup> Therefore, the sample synthesized under the above conditions was named CsPbBr<sub>3</sub>/Cs<sub>4</sub>PbBr<sub>6</sub>@EB-COF:Br. When both PbBr<sub>2</sub> and CsBr were used in 3 mmol concentration while

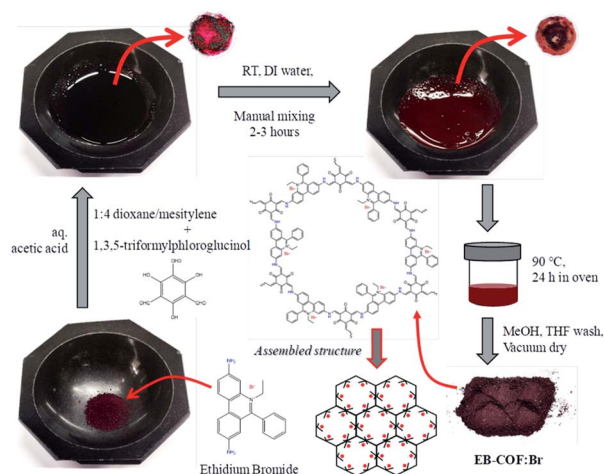


Fig. 1 Schematic representation of the modified mechanochemical synthesis of EB-COF:Br through simple Schiff base reactions performed via mechanochemical grinding and mixing using a mortar and pestle, followed by heating.

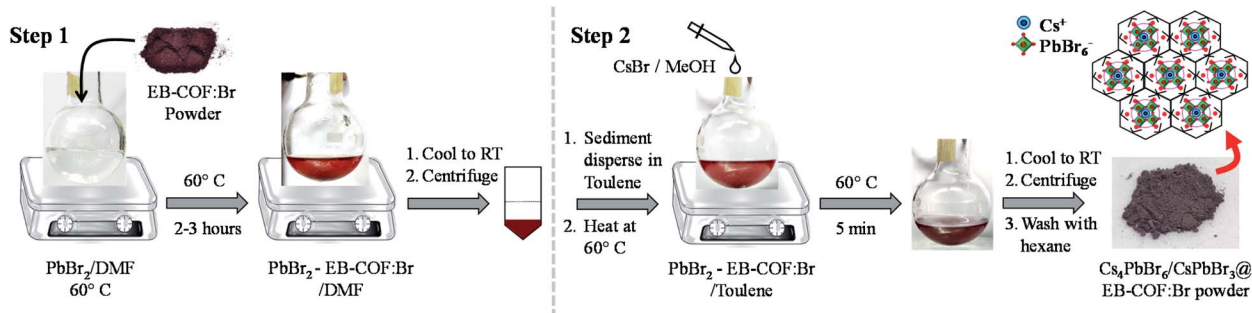


Fig. 2 Schematic representation of the two step solution-based synthesis of CsPbBr<sub>3</sub>/Cs<sub>4</sub>PbBr<sub>6</sub>@EB-COF:Br.

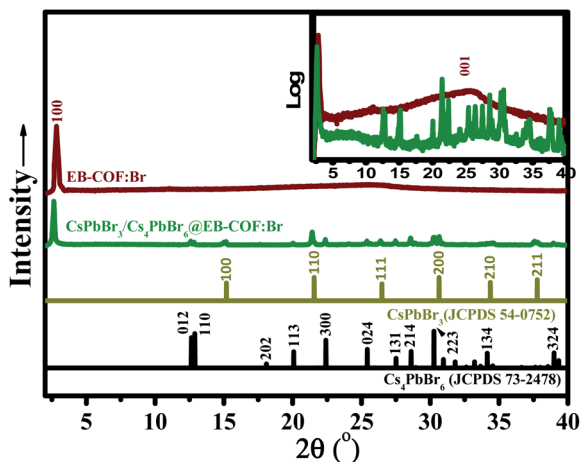


Fig. 3 X-ray diffraction (XRD) pattern of the CsPbBr<sub>3</sub>/Cs<sub>4</sub>PbBr<sub>6</sub>@EB-COF:Br nanocomposite matched with JCPDS no 54-0752 for CsPbBr<sub>3</sub>, JCPDS no 73-2478 for Cs<sub>4</sub>PbBr<sub>6</sub> and EB-COF:Br (as per ref. 49). The inset shows the log of intensity to confirm the presence of a peak at 27° from EB-COF:Br.

keeping the EB-COF:Br concentration constant, only cubic phase CsPbBr<sub>3</sub> was obtained. Peaks were observed at  $2\theta = 21.61^\circ$ ,  $26.59^\circ$ , and  $30.79^\circ$  and indexed to the (1 1 0), (1 1 1), and (2 0 0), planes of cubic phase CsPbBr<sub>3</sub> with the lattice constant  $a = 5.64 \text{ \AA}$  (JCPDS no 54-0752)<sup>29,63</sup> and the corresponding sample was named CsPbBr<sub>3</sub>@EB-COF:Br (Fig. S1, see the ESI†). For both the samples CsPbBr<sub>3</sub>/Cs<sub>4</sub>PbBr<sub>6</sub>@EB-COF:Br and CsPbBr<sub>3</sub>@EB-COF:Br, an intense diffraction peak at  $2.83^\circ$  and a broad peak at  $27^\circ$  were observed, which confirmed the presence of EB-COF:Br in the nanocomposites (Fig. 3, S1†).<sup>49</sup> Therefore, it was observed that the tuning of the crystal structures of CLBPs could be obtained by changing the mole concentration ratio of Cs and Pb to the COF while keeping all the reaction parameters constant.

The water stability of both the COF encapsulated CLBPs samples, CsPbBr<sub>3</sub>/Cs<sub>4</sub>PbBr<sub>6</sub>@EB-COF:Br and CsPbBr<sub>3</sub>@EB-COF:Br, was checked *via* time-dependent XRD analysis. 10 mg of the corresponding sample was immersed in DI water for a fixed time interval of 5, 10, 20, 30, 40, 50, and 60 minutes followed by complete vacuum drying before analysis. For the single-phase CsPbBr<sub>3</sub>@EB-COF:Br sample after being immersed in DI water for 60 min, only the peak from EB-COF:Br was prominently visible,<sup>49</sup> whereas the  $2\theta$  peaks from CsPbBr<sub>3</sub> were completely dispersed as represented in Fig. S2 (see the ESI†). However for the sample CsPbBr<sub>3</sub>/Cs<sub>4</sub>PbBr<sub>6</sub>@EB-COF:Br, although a few very low intense peaks from the as-synthesized sample disappeared when dipped in water for 60 minutes, still the sample has retained its mixed phase composition, as represented in Fig. S3 (see the ESI†). The peaks at  $2\theta$  of  $21.41^\circ$ ,  $26.43^\circ$ ,  $30.68^\circ$ ,  $34.66^\circ$  and  $37.94^\circ$  correspond to the (1 1 0), (1 1 1), (2 0 0), (2 1 0) and (2 1 1) planes of cubic phase CsPbBr<sub>3</sub> (JCPDS no 54-0752), whereas the peaks at  $2\theta$  of  $25.71^\circ$ ,  $30.04^\circ$  and  $33.86^\circ$  correspond to the (0 2 4), (0 0 6), and (4 1 0) planes of Cs<sub>4</sub>PbBr<sub>6</sub> (JCPDS no 73-2478).<sup>29,63</sup> The peaks for the Cs<sub>4</sub>PbBr<sub>6</sub> phase after water immersion show some shift in  $2\theta$  values

probably because water induces strain effects. We have even compared the water stability of CsPbBr<sub>3</sub>/Cs<sub>4</sub>PbBr<sub>6</sub> materials synthesized using a reported protocol without the encapsulation within the COF moiety.<sup>34</sup> It was noticed that for the CsPbBr<sub>3</sub>/Cs<sub>4</sub>PbBr<sub>6</sub> composite without COF encapsulation when dipped in water for 60 minutes, XRD shows complete reorganization of the crystal structure, along with the appearance of precursor peaks (CsBr and PbBr<sub>2</sub>), indicating the instability of the mixed-phase composite without the COF encapsulation (Fig. S4, see the ESI†). Therefore, since the COF encapsulation prevented the degradation of the mixed-phase sample, CsPbBr<sub>3</sub>/Cs<sub>4</sub>PbBr<sub>6</sub>@EB-COF:Br, into its precursors (*e.g.* CsBr and PbBr<sub>2</sub>) even after the water immersion for 60 minutes, as observed from XRD analysis, we have continued with other characterization and water-based photocatalytic applications for the mixed-phase sample CsPbBr<sub>3</sub>/Cs<sub>4</sub>PbBr<sub>6</sub>@EB-COF:Br only.

The CsPbBr<sub>3</sub>/Cs<sub>4</sub>PbBr<sub>6</sub>@EB-COF:Br sample was investigated by UV-Vis absorption and PL spectroscopy, as shown in Fig. 4. EB-COF:Br showed UV-Vis absorption around 314, 379, and 579 nm (Fig. 4a), whereas one extra cliff around 510–515 nm was observed corresponding to the absorption of cubic-phase CsPbBr<sub>3</sub>, in the absorption spectra of the CsPbBr<sub>3</sub>/Cs<sub>4</sub>PbBr<sub>6</sub>@EB-COF:Br nanocomposite, along with the peaks observed for EB-COF:Br.<sup>26,32,35</sup> Generally, Cs<sub>4</sub>PbBr<sub>6</sub> showed absorption spectra in the UV range around 313–315 nm,<sup>26,29,35</sup> but here due to the overlapping with absorption spectra in the UV region of EB-COF:Br, the presence of the Cs<sub>4</sub>PbBr<sub>6</sub> absorption peak in the mixed-phase CsPbBr<sub>3</sub>/Cs<sub>4</sub>PbBr<sub>6</sub>@EB-COF:Br nanocomposite cannot be concluded. Fig. 4b shows the emission spectra recorded for the CsPbBr<sub>3</sub>/Cs<sub>4</sub>PbBr<sub>6</sub>@EB-COF:Br nanocomposite with peak maxima at 516 nm,<sup>22,27</sup> indicating a low Stokes shift and hence the formation of defect-free nanocrystals, whereas EB-COF:Br was non-luminescent.<sup>64</sup>

The IR spectra of EB-COF:Br and CsPbBr<sub>3</sub>/Cs<sub>4</sub>PbBr<sub>6</sub>@EB-COF:Br nanocomposite are shown in Fig. S5 (see the ESI†). The disappearance of the N–H stretching bands of EB and the C=O stretching bands of TFP provided direct evidence for EB-COF:Br formation.<sup>49</sup> The dominant peak at  $1539 \text{ cm}^{-1}$  resulting from the C=C stretching and the lack of O–H and C=N stretching demonstrate that EB-COF:Br was existed in the keto form in both the samples.<sup>49</sup> The BET surface area result was obtained to be  $267.51 \text{ m}^2 \text{ g}^{-1}$  for EB-COF:Br from nitrogen adsorption–desorption isotherms as represented in Fig. 5. EB-

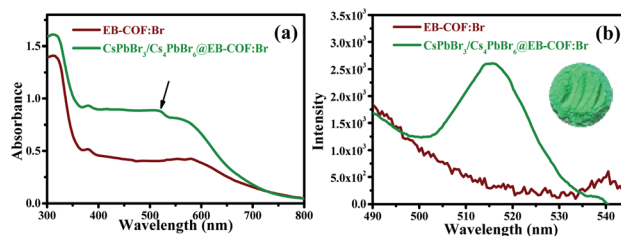


Fig. 4 Photophysical properties of the CsPbBr<sub>3</sub>/Cs<sub>4</sub>PbBr<sub>6</sub>@EB-COF:Br nanocomposite and EB-COF:Br; (a) UV-Vis spectra and (b) PL spectra [the inset shows the photograph of green emissive composite power under UV light (254 nm) irradiation].

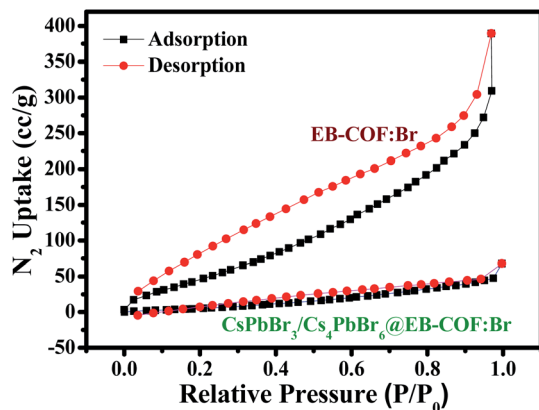


Fig. 5  $N_2$  adsorption/desorption isotherm for EB-COF:Br and  $CsPbBr_3/Cs_4PbBr_6@EB-COF:Br$  nanocomposite.

COF:Br synthesized herein using a low synthesis temperature and less time resulted in a mesoporous network in the COF. Thus, the mechanochemically synthesized EB-COF:Br showed a type-IV isotherm with a hysteresis loop, whereas EB-COF:Br synthesized by a solvothermal method as reported earlier showed a type-I isotherm indicating a microporous network due to higher reaction temperature and time (120 °C and 3 days).<sup>49</sup> These phenomena of mesoporous network formation in the COF as well as type-IV isotherm with a hysteresis loop when synthesized by a mechanochemical method are fully consistent with the reported literature.<sup>65–67</sup> The surface area obtained for the  $CsPbBr_3/Cs_4PbBr_6@EB-COF:Br$  nanocomposite from the nitrogen adsorption-desorption isotherm was  $49.83 \text{ m}^2 \text{ g}^{-1}$  (Fig. 5). The abrupt decrease of the surface area from the COF to the  $CsPbBr_3/Cs_4PbBr_6@COF$  nanocomposite confirms the successful encapsulation of  $CsPbBr_3/Cs_4PbBr_6$  NCs into the porous structures of EB-COF:Br.<sup>41,42</sup>

From HRTEM, EDS and CHN analyses, it was clear that  $CsPbBr_3/Cs_4PbBr_6$  NCs were encapsulated by EB-COF:Br and well dispersed inside it (Fig. 6, S6, Table S2, see the ESI†). A graphene-sheet-like 2D layered structure was observed for EB-COF:Br in the HRTEM images (Fig. S6a, see the ESI†), whereas, encapsulated CLBP NCs of size 4–7 nm were clearly observed in the HRTEM image of the  $CsPbBr_3/Cs_4PbBr_6@EB-COF:Br$  nanocomposite sample [Fig. 6a, S6b (ESI†)]. The appearance of larger size particles (few  $\sim 7$  nm) in the HRTEM images may be due to overlapping CLBP NCs. The high-angle annular electron microscopy (HAADF-STEM) images and elemental mappings of the nanocomposite revealed the presence of Cs, Pb, Br, N, and O (Fig. 6b), supporting the encapsulation and uniform distribution of  $CsPbBr_3/Cs_4PbBr_6$  NCs inside EB-COF:Br. The EDS elemental analysis and C, H, and N analysis of the  $CsPbBr_3/Cs_4PbBr_6@EB-COF:Br$  nanocomposite further confirmed the encapsulation of CLBP NCs inside the COF (Fig. 6c and inset table). The excess of Cs concerning the Pb atomic% in the composite material (as Cs : Pb : Br ratio = 3.76 : 1 : 7.30) from EDS analysis further suggests the formation of mixed-phase CLBP NCs. Further proof for successful encapsulation of nanocrystals was shown by the presence of two

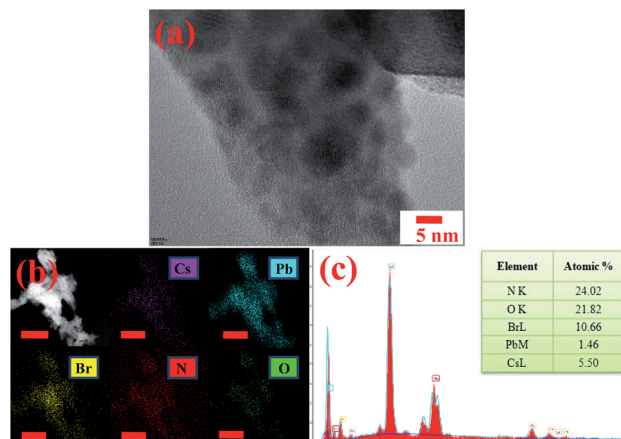


Fig. 6 (a) HRTEM image, (b) HAADF-STEM image and elemental mapping of Cs, Pb, Br, N, and O (scale bar = 50 nm) and (c) STEM-EDS analysis with the atomic% table of the  $CsPbBr_3/Cs_4PbBr_6@EB-COF:Br$  nanocomposite.

typical lattice structures found in the HRTEM fringes (Fig. S6b, ESI†). The interplanar distances of 2.9 Å and 1.75 Å could be attributed to the (200) and (315) planes of cubic  $CsPbBr_3$  and the rhombohedral phase of  $Cs_4PbBr_6$ , respectively.<sup>64</sup> In comparison, the elemental mappings and EDS analysis of the EB-COF:Br sample confirmed the presence of only C, N, O, and Br (Fig. S7, see the ESI†).

The surface properties of EB-COF:Br and  $CsPbBr_3/Cs_4PbBr_6@EB-COF:Br$  nanocomposite were investigated through X-ray photoelectron spectroscopy (XPS) analysis (Fig. S8–S10, see the ESI†). All the spectra were calibrated using the C 1s peak at 284.60 eV. The XPS survey spectrum for the  $CsPbBr_3/Cs_4PbBr_6@EB-COF:Br$  nanocomposite confirmed the presence of Cs, Pb, Br, N, and O as the main components (Fig. S8a, see the ESI†). For the nanocomposite, two intense Pb 4f peaks without any shoulder at 138.03 and 142.91 eV corresponding to Pb 4f<sub>7/2</sub> and Pb 4f<sub>5/2</sub> (Fig. S9a, see the ESI†) and Cs 3d peaks at 724.08 eV and 738.10 eV corresponding to Cs 3d<sub>5/2</sub> and Cs 3d<sub>3/2</sub> (Fig. S9b, see the ESI†) strongly support the formation of CLBP NCs in the COF matrix.<sup>31,41</sup> Quantitative XPS analysis indicates that Cs : Pb : Br is 1.45 : 1 : 4.14 for the  $CsPbBr_3/Cs_4PbBr_6@EB-COF:Br$  nanocomposite, which indicates excess Cs in the composition. Notably, the Br 3d peak of the CLBP@COF nanocomposite can be fitted into two peaks with binding energies of 67.80 eV and 68.90 eV, which were assigned to Br<sup>-</sup> ions from EB-COF:Br and CLBP (Fig. S9c, ESI†).<sup>14</sup> On the other hand, the XPS survey spectrum of the EB-COF:Br sample confirmed the presence of N, O, and Br as the main components (Fig. S8b, see the ESI†) and the Br 3d peak can be fitted into one peak with a binding energy of 67.80 eV, which were assigned to Br<sup>-</sup> ions from the COF itself (Fig. S10, see the ESI†).

The thermogravimetric analysis (TGA) shows that the decomposition of EB-COF:Br and  $CsPbBr_3/Cs_4PbBr_6@EB-COF:Br$  nanocomposite started at  $\sim 400$  °C (in Ar), as reported earlier (Fig. S11, see the ESI†).<sup>49</sup> A 15–25% weight loss for EB-COF:Br in TGA was observed in the low-temperature range

(below  $\sim 200$  °C). This could be ascribed to the removal of the trapped solvents in the EB-COF:Br nanocomposite. Therefore, the TGA experiments indicated that the synthesized CsPbBr<sub>3</sub>/Cs<sub>4</sub>PbBr<sub>6</sub>@EB-COF:Br nanocomposite possessed excellent thermal stability.

## Heterogeneous photocatalytic performance

These EB-COF:Br and CsPbBr<sub>3</sub>/Cs<sub>4</sub>PbBr<sub>6</sub>@EB-COF:Br nanocomposite had excellent visible light absorption characteristics (Fig. 4a) and good water stability (Fig. S2, ESI†). Therefore, the photocatalytic activities of the as-synthesised COF and CsPbBr<sub>3</sub>/Cs<sub>4</sub>PbBr<sub>6</sub>@COF nanocomposite were examined by the degradation of MO in an aqueous solution (100 ppm), in the presence of visible light (xenon lamp, 300 W,  $\lambda = 100$ –1800 nm, for photocatalytic measurements, see the ESI†). The photodegradation rates of the EB-COF:Br and CsPbBr<sub>3</sub>/Cs<sub>4</sub>PbBr<sub>6</sub>@EB-COF:Br nanocomposite could not be compared with that of CsPbBr<sub>3</sub>@EB-COF:Br or bulk CsPbBr<sub>3</sub>/Cs<sub>4</sub>PbBr<sub>6</sub>, since both the samples were not stable in water (Fig. S3 and S4, ESI†).

The factual photodegradation rates of the EB-COF:Br and CsPbBr<sub>3</sub>/Cs<sub>4</sub>PbBr<sub>6</sub>@EB-COF:Br nanocomposite were compared under visible light irradiation. A blank photolysis experiment without the photocatalyst does not show any noticeable decrease in the MO concentration with a similar time interval (Fig. 7a), demonstrating that the photocatalysts were the cause of MO's decomposition. Interestingly it was found that both the EB-COF:Br and CsPbBr<sub>3</sub>/Cs<sub>4</sub>PbBr<sub>6</sub>@EB-COF:Br nanocomposite show some MO adsorption in the dark and after a particular time the absorbance intensity remained the same. EB-COF:Br shows a slightly better adsorption behavior of 32.5% than the CsPbBr<sub>3</sub>/Cs<sub>4</sub>PbBr<sub>6</sub>@EB-COF:Br nanocomposite with 29.5% (in the dark) (Fig. 7b and c), because of apparent COF pore site availability, as observed from the BET surface area measurement. The degradation curves of MO over EB-COF:Br and CsPbBr<sub>3</sub>/Cs<sub>4</sub>PbBr<sub>6</sub>@EB-COF:Br photocatalysts as a function of visible light irradiation time are plotted in Fig. 7d and e respectively, at a specific time interval. The CsPbBr<sub>3</sub>/Cs<sub>4</sub>PbBr<sub>6</sub>@EB-COF:Br nanocomposite exhibits superior photocatalytic activity to EB-COF:Br with a photodegradation efficiency of 100% and 77.5% in 25 min under visible light irradiation, respectively (Fig. 7f). Practically the CsPbBr<sub>3</sub>/Cs<sub>4</sub>PbBr<sub>6</sub>@EB-COF:Br nanocomposite completely degraded 100 ppm MO solution within 25 min of visible light irradiation. Assuming that the degradation process follows first-order kinetics ( $C = C_0 e^{-\kappa t}$ ,  $\kappa$  is the photodegradation rate constant) for MO degradation, the plots of  $-\ln(C_t/C_0)$  as a function of the visible light irradiation time  $t$  are shown in Fig. 7g.<sup>41,68</sup> The photodegradation rate constant of the EB-COF:Br and CsPbBr<sub>3</sub>/Cs<sub>4</sub>PbBr<sub>6</sub>@EB-COF:Br nanocomposite was about  $0.057 \text{ min}^{-1}$  and  $0.245 \text{ min}^{-1}$  respectively (Table S3, see the ESI†), which were found to be considerably higher than the previously reported values for dye photodegradation with halide perovskites (Table S4, see the ESI†).<sup>41,50–62</sup> The actual photographs of visible-light-driven photocatalytic degradation of MO with the

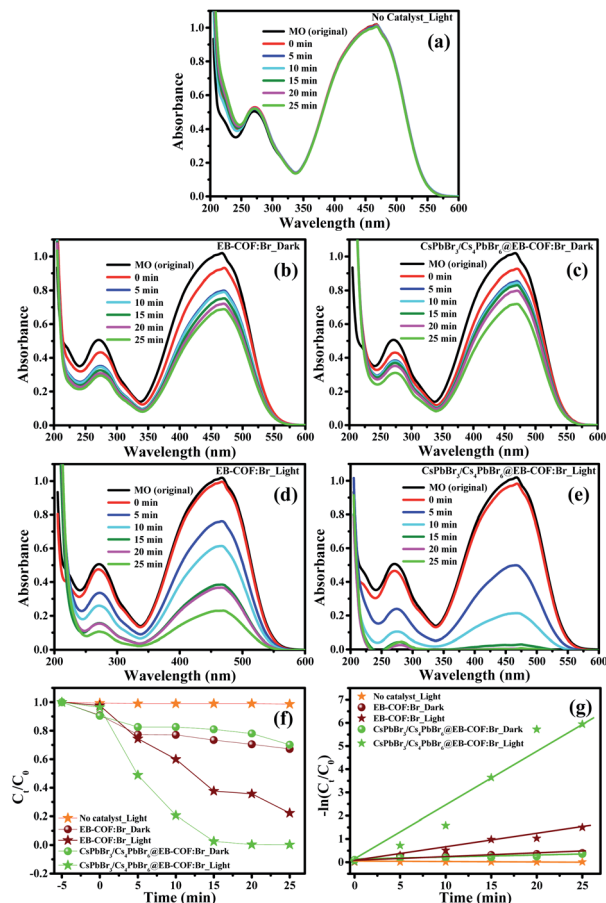


Fig. 7 Photocatalytic performance of the as-synthesized EB-COF:Br and CsPbBr<sub>3</sub>/Cs<sub>4</sub>PbBr<sub>6</sub>@EB-COF:Br nanocomposite samples for 100 ppm MO aqueous solution; typical UV-Vis spectral change of MO solution as a function of time; (a) blank photolysis without photocatalysts: in the presence of (b) EB-COF:Br and (c) CsPbBr<sub>3</sub>/Cs<sub>4</sub>PbBr<sub>6</sub>@EB-COF:Br nanocomposites in the dark; in the presence of photocatalysts under visible light irradiation (d) EB-COF:Br and (e) CsPbBr<sub>3</sub>/Cs<sub>4</sub>PbBr<sub>6</sub>@EB-COF:Br nanocomposite; (f) the plot of MO remaining in the solution ( $C/C_0$ ) measured from the absorbance at 467 nm; (g) the plots of  $-\ln(C_t/C_0)$  as a function of photo-irradiation time (min) in the presence of catalyst EB-COF:Br and CsPbBr<sub>3</sub>/Cs<sub>4</sub>PbBr<sub>6</sub>@EB-COF:Br nanocomposite, for the blank (without photocatalysts) and in the dark (without light irradiation).

CsPbBr<sub>3</sub>/Cs<sub>4</sub>PbBr<sub>6</sub>@EB-COF:Br nanocomposite photocatalyst are presented in Fig. S12 (see the ESI†). The results, therefore, confirmed that the CsPbBr<sub>3</sub>/Cs<sub>4</sub>PbBr<sub>6</sub>@EB-COF:Br nanocomposite had a higher impact on the enhancement of photocatalytic activity even under room temperature conditions (24–26 °C). This is probably because the COF we have used herein to encapsulate the CLBPs was also photoactive and the inherent porous structure of the EB-COF:Br, more coordination sites of CsPbBr<sub>3</sub>/Cs<sub>4</sub>PbBr<sub>6</sub> were exposed to the solution, and therefore, reactant molecules could effectively access the active sites of the photocatalyst.

The recyclability of the CsPbBr<sub>3</sub>/Cs<sub>4</sub>PbBr<sub>6</sub>@EB-COF:Br nanocomposite photocatalyst was examined with various concentrations of MO aqueous solution (20, 50 and 100 ppm)



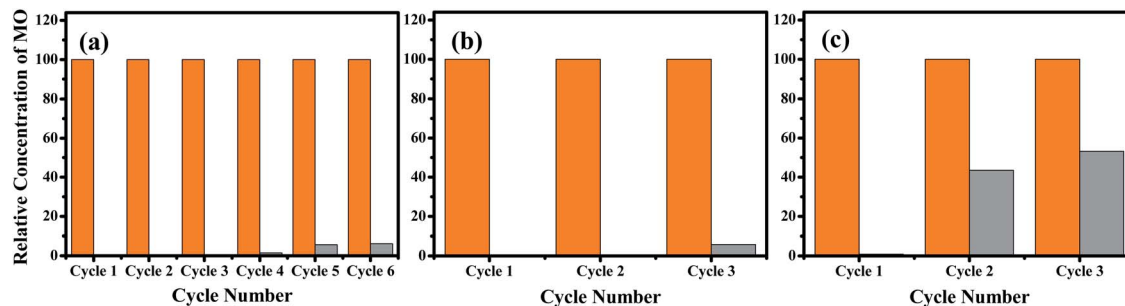


Fig. 8 Recycling tests for the photocatalytic degradation of MO: (a) 20 ppm, (b) 50 ppm and (c) 100 ppm in the presence of the CsPbBr<sub>3</sub>/Cs<sub>4</sub>PbBr<sub>6</sub>@EB-COF:Br nanocomposite photocatalyst under similar photoirradiation conditions.

and the nanocomposite was collected after its first cycle usage to carry out the subsequent degradation. It was found that for the photocatalysis of 20 ppm MO, the photocatalyst can be recycled up to six cycles, whereas for 50 and 100 ppm of MO, the photocatalyst can be recycled up to three cycles. The degradation efficiency for the sixth cycle of 20 ppm was 93.85%, and the third cycle of 50 ppm was 94.19%, whereas, for 100 ppm, the degradation efficiency for the third cycle was comparatively low 46.8% as presented in Fig. 8. The recyclability test's actual photographs for 20–100 ppm MO using the CsPbBr<sub>3</sub>/Cs<sub>4</sub>PbBr<sub>6</sub>@EB-COF:Br nanocomposite photocatalyst are presented in Fig. S13–S15 (see the ESI†). Herein, we have observed a concentration-dependent change in photocatalytic efficiency and change in the number of reusability cycles for the CsPbBr<sub>3</sub>/Cs<sub>4</sub>PbBr<sub>6</sub>@EB-COF:Br nanocomposite photocatalyst. This phenomenon is quite common, as several parameters affect the efficiency of the photocatalyst.<sup>69</sup> We have carried out XRD analysis of the recycled photocatalyst samples to confirm the change in the nanocomposite's crystal structures (Fig. S16, see the ESI†). There was no change in the  $2\theta$  peak value for 20 ppm and 50 ppm sixth and third time recycled photocatalysts, respectively. In contrast, a slight change was observed for the 100 ppm third time recycled photocatalyst, which is in line with the experimental observations (Fig. 8). As shown in Fig. S17 (see ESI†), changes in the CsPbBr<sub>3</sub>/Cs<sub>4</sub>PbBr<sub>6</sub> NCs' morphology, NC aggregation, were observed after the repeated photodegradation reactions. These results demonstrated that the synthesized CsPbBr<sub>3</sub>/Cs<sub>4</sub>PbBr<sub>6</sub>@EB-COF:Br nanocomposite remained stable, maintaining its framework integrity up to a particular time and acting as a photocatalyst for repeated usage under visible light irradiation.

## Conclusions

In summary, this article reported a facile controlled synthesis of a CsPbBr<sub>3</sub>/Cs<sub>4</sub>PbBr<sub>6</sub>@EB-COF:Br nanocomposite, where perovskite NCs were well dispersed in the COF cavity. Herein, we have also demonstrated a simple mechanochemical synthetic route to synthesize a cationic covalent organic framework EB-COF:Br with Br<sup>-</sup> as the counter ion, avoiding the necessity of using typical inert atmosphere conditions in a Pyrex tube. The Br-functionalized COF was selected because of its chemical affinity and non-interference with the photoluminescence

properties of the bromide containing perovskite. The synthesized products were characterized by XRD, UV-Vis, IR, CHN, BET, TGA, XPS, HRTEM, HAADF, and EDS analyses. It was shown that the concentration of Cs:Pb:COF played a significant role in controlling the crystal structure of the perovskite NCs. Therefore, both single-phase CsPbBr<sub>3</sub>@EB-COF:Br and mixed-phase CsPbBr<sub>3</sub>/Cs<sub>4</sub>PbBr<sub>6</sub>@EB-COF:Br nanocomposites were obtained by slightly tuning the synthesis protocol. The samples' water stability, e.g., CsPbBr<sub>3</sub>@EB-COF:Br, CsPbBr<sub>3</sub>/Cs<sub>4</sub>PbBr<sub>6</sub>@EB-COF:Br, CsPbBr<sub>3</sub>/Cs<sub>4</sub>PbBr<sub>6</sub> without COF encapsulation, was compared, and it was found that the CsPbBr<sub>3</sub>/Cs<sub>4</sub>PbBr<sub>6</sub>@EB-COF:Br nanocomposite has remained reasonably stable in water for 60 minutes. Furthermore, the CsPbBr<sub>3</sub>/Cs<sub>4</sub>PbBr<sub>6</sub>@EB-COF:Br nanocomposite showed efficient visible-light-driven photocatalytic activity to degrade Methyl orange (MO) (10 mL; 100 ppm) in aqueous media with a photodegradation rate of about  $0.245 \text{ min}^{-1}$ . The CsPbBr<sub>3</sub>/Cs<sub>4</sub>PbBr<sub>6</sub>@EB-COF:Br photocatalyst also exhibited water and photo-stability up to three to six recycles for 20–100 ppm of MO solution, while showing some aggregation of NCs during the recycling experiments. Although Pb's toxic nature is of great concern, to be used as a photocatalyst, the encapsulation method provided by us will offer an opportunity to consider COFs as encapsulating materials to improve the stability of unstable nanomaterials *via* nanocomposite fabrication. This study should also lead to various opportunities to design and synthesize proficient nanocomposite based photocatalysts with other nontoxic alternative perovskites as promising materials for applications in the photodegradation of organic contaminants and wastewater treatment under visible light, a topic of vital significance as well as universal apprehension.

## Conflicts of interest

There are no conflicts to declare.

## Acknowledgements

The authors would like to acknowledge the NCL start-up grant (MLP031526) for financial and infrastructure support, and Centre for Materials Characterization (CMC, NCL, Pune) for SEM, HRTEM, and XPS analyses. We thank the Polymer Science and Engineering Division, NCL, and Pune for helping us with

small-angle XRD measurements and Mr Manoj Patil for his help with BET measurements. We would also like to thank Ms Swati Dilwale and Dr Sreekumar Kurungot for their timely help with TGA analysis, and Prof. S. Ogale, IISER, Pune, for providing the XRD instrumentation facility for the stability studies. PK thanks CSIR, New Delhi, for a senior research fellowship.

## References

- Q. Zhang and Y. Yin, *ACS Cent. Sci.*, 2018, **4**, 668–679.
- U. Thumu, M. Piotrowski, B. Owens-Baird and Y. V. Kolen'ko, *J. Solid State Chem.*, 2019, **271**, 361–377.
- T. Yang, F. Li and R. Zheng, *ACS Appl. Electron. Mater.*, 2019, **1**, 1348–1366.
- Y. Jiang, B. Li, T. Zhang, Y. Shi and Q.-H. Xu, *ChemNanoMat*, 2020, **6**, 327–335.
- M. De Bastiani, I. Dursun, Y. Zhang, B. A. Alshankiti, X. H. Miao, J. Yin, E. Yengel, E. Alarousu, B. Turedi, J. M. Almutlaq, M. I. Saidaminov, S. Mitra, I. Gereige, A. Alsaggaf, Y. Zhu, Y. Han, I. S. Roqan, J. L. Bredas, O. F. Mohammed and O. M. Bakr, *Chem. Mater.*, 2017, **29**, 7108–7113.
- A. Ray, D. Maggioni, D. Baranov, Z. Dang, M. Prato, Q. A. Akkerman, L. Goldoni, E. Caneva, L. Manna and A. L. Abdelhady, *Chem. Mater.*, 2019, **31**, 7761–7769.
- L. A. T. Nguyen, D. N. Minh, D. Zhang, L. Wang, J. Kim and Y. Kang, *J. Phys. Chem. C*, 2020, **124**, 22291–22297.
- R. Wang, Z. Li, S. Li, P. Wang, J. Xiu, G. Wei, H. Liu, N. Jiang, Y. Liu and M. Zhong, *ACS Appl. Mater. Interfaces*, 2020, **12**, 41919–41931.
- Z. Bao, Y. J. Tseng, W. You, W. Zheng, X. Chen, S. Mahlik, A. Lazarowska, T. Lesniewski, M. Grinberg, C. Ma, W. Sun, W. Zhou, R. S. Liu and J. P. Attfield, *J. Phys. Chem. Lett.*, 2020, **11**, 7637–7642.
- M. Li, X. Zhang, T. Dong, P. Wang, K. Matras-Postolek and P. Yang, *J. Phys. Chem. C*, 2018, **122**, 28968–28976.
- J. Almutlaq, J. Yin, O. F. Mohammed and O. M. Bakr, *J. Phys. Chem. Lett.*, 2018, **9**, 4131–4138.
- M. I. Saidaminov, J. Almutlaq, S. Sarmah, I. Dursun, A. A. Zhumeckenov, R. Begum, J. Pan, N. Cho, O. F. Mohammed and O. M. Bakr, *ACS Energy Lett.*, 2016, **1**, 840–845.
- Y. Zhang, M. I. Saidaminov, I. Dursun, H. Yang, B. Murali, E. Alarousu, E. Yengel, B. A. Alshankiti, O. M. Bakr and O. F. Mohammed, *J. Phys. Chem. Lett.*, 2017, **8**, 961–965.
- X. Chen, F. Zhang, Y. Ge, L. Shi, S. Huang, J. Tang, Z. Lv, L. Zhang, B. Zou and H. Zhong, *Adv. Funct. Mater.*, 2018, **28**, 1706567.
- G. K. Grandhi, N. S. M. Viswanath, H. B. Cho, S. M. Kim and W. Bin Im, *Nanoscale*, 2019, **11**, 21137–21146.
- D. Chen, Z. Wan, X. Chen, Y. Yuan and J. Zhong, *J. Mater. Chem. C*, 2016, **4**, 10646–10653.
- J. H. Cha, J. H. Han, W. Yin, C. Park, Y. Park, T. K. Ahn, J. H. Cho and D. Y. Jung, *J. Phys. Chem. Lett.*, 2017, **8**, 565–570.
- J. Yin, Y. Zhang, A. Bruno, C. Soci, O. M. Bakr, J. L. Brédas and O. F. Mohammed, *ACS Energy Lett.*, 2017, **2**, 2805–2811.
- Z. Zhang, Y. Zhu, W. Wang, W. Zheng, R. Lin, X. Li, H. Zhang, D. Zhong and F. Huang, *Cryst. Growth Des.*, 2018, **18**, 6393–6398.
- H. Zhang, Q. Liao, Y. Wu, J. Chen, Q. Gao and H. Fu, *Phys. Chem. Chem. Phys.*, 2017, **19**, 29092–29098.
- C. De Weerd, J. Lin, L. Gomez, Y. Fujiwara, K. Suenaga and T. Gregorkiewicz, *J. Phys. Chem. C*, 2017, **121**, 19490–19496.
- T. Xuan, S. Lou, J. Huang, L. Cao, X. Yang, H. Li and J. Wang, *Nanoscale*, 2018, **10**, 9840–9844.
- K. Huang, D. Li, L. Yang, S. Liu and F. Yang, *J. Alloys Compd.*, 2017, **710**, 244–252.
- Q. A. Akkerman, S. Park, E. Radicchi, F. Nunzi, E. Mosconi, F. De Angelis, R. Brescia, P. Rastogi, M. Prato and L. Manna, *Nano Lett.*, 2017, **17**, 1924–1930.
- M. Liu, J. Zhao, Z. Luo, Z. Sun, N. Pan, H. Ding and X. Wang, *Chem. Mater.*, 2018, **30**, 5846–5852.
- Y. Li, H. Huang, Y. Xiong, S. V. Kershaw and A. L. Rogach, *CrystEngComm*, 2018, **20**, 4900–4904.
- X. Chen, D. Chen, J. Li, G. Fang, H. Sheng and J. Zhong, *Dalton Trans.*, 2018, **47**, 5670–5678.
- G. Almeida, L. Goldoni, Q. Akkerman, Z. Dang, A. H. Khan, S. Marras, I. Moreels and L. Manna, *ACS Nano*, 2018, **12**, 1704–1711.
- L. Wu, H. Hu, Y. Xu, S. Jiang, M. Chen, Q. Zhong, D. Yang, Q. Liu, Y. Zhao, B. Sun, Q. Zhang and Y. Yin, *Nano Lett.*, 2017, **17**, 5799–5804.
- B. Kang and K. Biswas, *J. Phys. Chem. Lett.*, 2018, **9**, 830–836.
- G. Tong, H. Li, Z. Zhu, Y. Zhang, L. Yu, J. Xu and Y. Jiang, *J. Phys. Chem. Lett.*, 2018, **9**, 1592–1599.
- Y. M. Chen, Y. Zhou, Q. Zhao, J. Y. Zhang, J. P. Ma, T. T. Xuan, S. Q. Guo, Z. J. Yong, J. Wang, Y. Kuroiwa, C. Moriyoshi and H. T. Sun, *ACS Appl. Mater. Interfaces*, 2018, **10**, 15905–15912.
- L. Xu, J. Li, T. Fang, Y. Zhao, S. Yuan, Y. Dong and J. Song, *Nanoscale Adv.*, 2019, **1**, 980–988.
- W. Wang, D. Wang, F. Fang, S. Wang, G. Xu and T. Zhang, *Cryst. Growth Des.*, 2018, **18**, 6133–6141.
- M. He, C. Wang, J. Li, J. Wu, S. Zhang, H. C. Kuo, L. Shao, S. Zhao, J. Zhang, F. Kang and G. Wei, *Nanoscale*, 2019, **11**, 22899–22906.
- L. N. Quan, R. Quintero-Bermudez, O. Voznyy, G. Walters, A. Jain, J. Z. Fan, X. Zheng, Z. Yang and E. H. Sargent, *Adv. Mater.*, 2017, **29**, 1605945.
- J. K. Nam, S. U. Chai, W. Cha, Y. J. Choi, W. Kim, M. S. Jung, J. Kwon, D. Kim and J. H. Park, *Nano Lett.*, 2017, **17**, 2028–2033.
- Y. Xin, H. Zhao and J. Zhang, *ACS Appl. Mater. Interfaces*, 2018, **10**, 4971–4980.
- H. Wu, W. Zhang, J. Wu and Y. Chi, *ACS Appl. Mater. Interfaces*, 2019, **11**, 16713–16719.
- P. Song, B. Qiao, D. Song, J. Cao, Z. Shen, G. Zhang, Z. Xu, S. Zhao, S. Wageh and A. Al-Ghamdi, *J. Mater. Sci.*, 2020, **55**, 9739–9747.
- S. Mollick, T. N. Mandal, A. Jana, S. Fajal, A. V. Desai and S. K. Ghosh, *ACS Appl. Nano Mater.*, 2019, **2**, 1333–1340.

- 42 J. H. Cha, K. Noh, W. Yin, Y. Lee, Y. Park, T. K. Ahn, A. Mayoral, J. Kim, D. Y. Jung and O. Terasaki, *J. Phys. Chem. Lett.*, 2019, **10**, 2270–2277.
- 43 S. Bhattacharyya, D. Rambabu and T. K. Maji, *J. Mater. Chem. A*, 2019, **7**, 21106–21111.
- 44 Z. Chen, Z. G. Gu, W. Q. Fu, F. Wang and J. Zhang, *ACS Appl. Mater. Interfaces*, 2016, **8**, 28737–28742.
- 45 E. Ploetz, H. Engelke, U. Lächelt and S. Wuttke, *Adv. Funct. Mater.*, 2020, 1909062.
- 46 J. Hu, S. K. Gupta, J. Ozdemir and M. H. Beyzavi, *ACS Appl. Nano Mater.*, 2020, **3**, 6239–6269.
- 47 Y. Liu, Y. Zhu, S. B. Alahakoon and E. Egap, *ACS Mater. Lett.*, 2020, **2**, 1561–1566.
- 48 B. P. Biswal, S. Chandra, S. Kandambeth, B. Lukose, T. Heine and R. Banerjee, *J. Am. Chem. Soc.*, 2013, **135**, 5328–5331.
- 49 H. Ma, B. Liu, B. Li, L. Zhang, Y. G. Li, H. Q. Tan, H. Y. Zang and G. Zhu, *J. Am. Chem. Soc.*, 2016, **138**, 5897–5903.
- 50 W. Zhang, Q. Zhao, X. Wang, X. Yan, J. Xu and Z. Zeng, *Catal. Sci. Technol.*, 2017, **7**, 2753–2762.
- 51 G. Gao, Q. Xi, H. Zhou, Y. Zhao, C. Wu, L. Wang, P. Guo and J. Xu, *Nanoscale*, 2017, **9**, 12032–12038.
- 52 F. Reyes-Pérez, J. J. Gallardo, T. Aguilar, R. Alcántara, C. Fernández-Lorenzo and J. Navas, *ChemistrySelect*, 2018, **3**, 10226–10235.
- 53 B. M. Bresolin, S. Ben Hammouda and M. Sillanpää, *Nanomaterials*, 2020, **10**, 1–17.
- 54 S. Bhattacharjee, S. P. Chaudhary and S. Bhattacharyya, *ChemRxiv*, 2019 [https://chemrxiv.org/articles/preprint/Lead-Free\\_Metal\\_Halide\\_Peroovskite\\_Nanocrystals\\_for\\_Photocatalysis\\_in\\_Water/9794270/1?file=17572175](https://chemrxiv.org/articles/preprint/Lead-Free_Metal_Halide_Peroovskite_Nanocrystals_for_Photocatalysis_in_Water/9794270/1?file=17572175).
- 55 Z. Zhang, Y. Liang, H. Huang, X. Liu, Q. Li, L. Chen and D. Xu, *Angew. Chem., Int. Ed.*, 2019, **58**, 7263–7267.
- 56 M. Karamia, M. Ghanbaria, O. Amirib and M. S. Niasaria, *Sep. Purif. Technol.*, 2020, **253**, 117526.
- 57 T. Paula, D. Dasa, B. K. Dasb, S. Sarkarb, S. Maitic and K. K. Chattopadhyay, *J. Hazard. Mater.*, 2019, **380**, 120855.
- 58 M. Ghanbari, F. Ansari and M. S. Niasari, *Inorg. Chim. Acta*, 2017, **455**, 88–97.
- 59 X. Qian, Z. Chen, X. Yang, W. Zhao, C. Liu, T. Sun, D. Zhou, Q. Yang, G. Wei and M. Fan, *J. Cleaner Prod.*, 2019, **249**, 119335.
- 60 M. Aamir, Z. Hussain, M. Sher and A. Iqbal, *Mater. Sci. Semicond. Process.*, 2017, **63**, 6–11.
- 61 S. Das, T. Paul, S. Maiti and K. K. Chattopadhyay, *Mater. Lett.*, 2020, **267**, 127501.
- 62 L. Romani, A. Bala, V. Kumar, A. Speltini, A. Milella, F. Fracassi, A. Listorti, A. Profumo and L. Malavasi, *J. Mater. Chem. C*, 2020, **8**, 9189.
- 63 X. Peng, J. Chen, F. Wang, C. Zhang and B. Yang, *Optik*, 2020, **208**, 1–6.
- 64 M. C. Brennan, J. E. Herr, T. S. Nguyen-Beck, J. Zinna, S. Draguta, S. Rouvimov, J. Parkhill and M. Kuno, *J. Am. Chem. Soc.*, 2017, **139**, 12201–12208.
- 65 D. B. Shinde, H. B. Aiyappa, M. Bhadra, B. P. Biswal, P. Wadge, S. Kandambeth, B. Garai, T. Kundu, S. Kurungot and R. Banerjee, *J. Mater. Chem. A*, 2016, **4**, 2682–2690.
- 66 G. Das, D. B. Shinde, S. Kandambeth, B. P. Biswal and R. Banerjee, *Chem. Commun.*, 2014, **50**, 12615.
- 67 H. Lv, X. Zhao, H. Niu, S. He, Z. Tang, F. Wu and J. P. Giesy, *J. Hazard. Mater.*, 2019, **369**, 494–502.
- 68 S. H. Gaikwad, A. Koratti and S. P. Mukherjee, *Appl. Surf. Sci.*, 2019, **465**, 413–419.
- 69 K. M. Reza, A. S. W. Kurny and F. Gulshan, *Appl. Water Sci.*, 2017, **7**, 1569–1578.





